FERMILAB P803 PROPOSAL

October, 1990

MUON NEUTRINO TO TAU NEUTRINO OSCILLATIONS

K. Kodama and N. Ushida
Aichi University of Education, Kariya 448, JAPAN

G. S. Tzanakos
University of Athens, Athens, GREECE

P. M. Yager
University of California (Davis), Davis CA 95616

Wonyong Lee
Columbia University, New York NY 10027

A. D. Bross, G. Koizumi and A. J. Malensek
Fermilab, Batavia IL 60510

K. Nakazawa and S. Tasaka
Gifu University, Gifu 501-11, JAPAN

S. Kuramata
Hirosaki University, Hirosaki 036, JAPAN

M. Chikawa
Kinki University, Higashi-Osaka 577, JAPAN

T. Abe, H. Fukushima, T. Hara, Y. Tsuzuki and C. Yokoyama
Kobe University, Kobe 657, JAPAN

Jae Kwan Kim
Korea Advanced Institute of Science and Technology, KOREA

J. S. Kang and C. O. Kim
Korea University, Seoul, KOREA

Y. Isokane and Y. Tsuneoka
Nagoya Institue of Technology, Nagoya 466, JAPAN

S. Aoki, K. Hoshino, H. Kitamura, M. Kobayashi, M. Miyanishi, M. Nakamura,
Y. Nakamura, S. Nakanishi, K. Niu, K. Niwa, M. Nomura, K. Saito, H. Tajima,
K. Teraoka and S.Yoshida
Nagoya University, Nagoya 464-01, JAPAN

N. W. Reay*, K. Reibel, R. A. Sidwell and N. R. Stanton
The Ohio State University, Columbus OH 43210

K. Moriyama and H. Shibata
Okayama University, Okayama 700, JAPAN

T. Okusawa, M. Teranaka, T. Tominaga, T. Yoshida and T. Watanabe
Osaka City University, Osaka 558, JAPAN

G. Fujioka and Y. Takahashi
Osaka University of Commerce, Higashi-Osaka 577, JAPAN

R. W. Rusack
Rockefeller University, New York, NY 10021

H. Okabe and J. Yokota
Science Education Institute of Osaka Prefecture, Osaka 558, JAPAN

O. Kusumoto
Soai University, Osaka 559, JAPAN

Jewan Kim
Seoul National University, Seoul, KOREA

F.T. Avignone and C. Rosenfeld
University of South Carolina, Columbia SC 29208

M. Adachi, M. Kazuno, Y. Kobayashi, F. Minakawa, E. Niu, S. Ono, H. Shibuya
Y. Umezawa and S. Watanabe
Toho University, Funabashi 274, JAPAN

A. Napier, T. Kafka and J. Schneps
Tufts University, Medford MA 02155

Y. Maeda
Yokohama National University, Yokohama 240,JAPAN

Y. Sato and I. Tezuka
Utsunomiya University, Utsunomiya 350, JAPAN

*Contact person.

FERMILAB P803 PROPOSAL

MUON NEUTRINO TO TAU NEUTRINO OSCILLATIONS

I. RATIONALE

The primary goal of the experiment is to push the limits on $\nu_\mu \leftrightarrow \nu_\tau$ mixing well below the mixing angles in the quark sector, or to observe a positive τ signal if one exist at this level of sensitivity. The secondary goal, which will be achieved with modest additional effort, is to use the low-energy behavior of neutrino-produced charm and anticharm cross sections to measure the Kobayashi-Maskawa matrix element V_{cd} to a precision comparable to unitary estimates.

A. Oscillations

It has been suggested [1] that the tau neutrino, if massive, is the only known particle which could provide sufficient mass to close the universe. A see-saw mechanism [1] in its simplest version relates masses of the leptons to quark masses in the same generation as follows:

$$M_{\nu_e} : M_{\nu_\mu} : M_{\nu_\tau} = \frac{m_u^2}{M} : \frac{m_c^2}{M} : \frac{m_t^2}{M} \qquad (1)$$

where m_q are the respective up, charm and top quark masses and M is a very massive decoupled neutrino. Thus, the ν_μ could be 6×10^4 times heavier than ν_e, and in turn the ν_τ could be 6×10^3 times heavier than ν_μ, for a 100 GeV top mass. If the top quark mass is greater than 100 GeV, a tau-neutrino mass in the range 10-60 eV (sufficient to close the universe) could be generated and still maintain $\nu_e \leftrightarrow \nu_\mu$ oscillations in the 10^{-4} to 10^{-7} eV^2 range required by the MSW [2], [3] solution to the solar neutrino problem. Preliminary results from SLC and LEP [4] indicate that there are only three generations of neutrinos. In this case, the tau neutrino becomes an even more attractive candidate for closing the universe.

The present world limits for $\nu_\mu \leftrightarrow \nu_\tau$ oscillations are given in Fig. 1. These limits are determined by Fermilab experiment E531 [5] and the CERN CDHSW experiment [6]. Oscillations with a coupling greater than 0.5×10^{-2} have been ruled out for δM^2 greater than 20 eV^2. However, the assumption that lepton mixing angles are comparable to K-M matrix quark mixing angles leads to the conclusion that $\sin^2(2\alpha)$ must be larger than 4×10^{-4}, just ten times smaller than existing limits. We discuss here the preliminary design of an experiment that can access 40 times smaller couplings in the mixing parameter, $\sin^2(2\alpha) \leq 1 \times 10^{-4}$, with an estimated background of a fraction of an event; it could clearly establish a signal if one were present at 4–5 times this limit. P803 can also improve the existing limits on $\nu_e \leftrightarrow \nu_\tau$ oscillations by a similar factor, to $\sin^2(2\alpha) \leq 5 \times 10^{-3}$, comparable to the old ν_μ limit.

The apparatus is also well-suited to serve as a flux monitor for proposed long-baseline oscillation experiments if one or more of these experiments are approved. P803 would then share a neutrino beamline with the long-baseline effort(s).

B. Standard Model

1. Measurement of $|V_{cd}|$. Because this new experiment would have excellent muon identification and topological identification of charm, the same apparatus could simultaneously make definitive measurements both of the "slow rescaling" of charm production and of the Kobayashi-Maskawa matrix element V_{cd} [7]. "Slow rescaling," which refers to the low-energy suppression of the neutrino charm-production cross section due to the massiveness of the charm quark, is parameterized in terms of the charm quark mass m_c, and is one of the main limiting systematic errors in the extraction of $\sin^2(\theta_W)$ from deep-inelastic scattering of neutrinos[7]. P803 would measure m_c to better than ± 0.05 GeV/c^2, as compared to the present determination of 1.5 ± 0.4 GeV/c^2. This would be sufficient to test QCD charm-production models and to eliminate this source of error from the determination of $\sin^2(\theta_W)$. Graphs indicating the constraints imposed by 500 topologically-identified charm and 200 similarly identified anti-charm decays are shown in Figs. 2a and 2b.

The present state of measurement of V_{cd} depends on interpretation of systematic errors. If statistical and several systematic errors are summed in quadrature, V_{cd} is now known to 8% from analysis of charm production in deep inelastic scattering [8]. However, if the conservative approach is taken of combining errors linearly, V_{cd} is known only to 13%. Large systematic errors result from the fact that charm production now is inferred through analysis of dimuon data, and thus extraction of this K-M matrix element is model dependent.

On the theoretical side, V_{cd} can be inferred to 1.1% at the one standard deviation level from the unitarity of the K-M matrix [9]. The proposed experiment plans to make a $\pm$ 2.5% direct measurement, approaching a precision where a difference between direct and inferred values could indicate new physics. More detail on standard model measurements is presented in Appendix A.

2. Precision QCD measurements at low Q^2. Neutrino scattering traditionally has played a leading role in the extraction both of quark and gluon structure functions, and shows promise of providing precision tests of QCD. Recently, however, controversies have arisen because the size of contributions from "nonperturbative" effects is not calculable and could be large [10] [11]. Since most nonperturbative effects are worse at low energies and smaller Q^2, one way to estimate their size experimentally is to measure the full gamut of structure functions using intense low-energy neutrino beams from the main injector.

In the initial emulsion run we expect to achieve the same number of ν_μ and $\overline{\nu_\mu}$ charged current interactions as obtained by Fermilab experiments E744 and E770 (1.4×10^6 and 0.3×10^6, respectively). Using a low-Z aluminum target

instead of emulsion, this experiment could obtain twice this number of events in another similar running period.

The spectrometer is particularly well set up to measure both hadronic energy and energy flow, and will measure the momentum of most muons to better than 6%. The ability to separate neutral current from charged current interactions is better than for any previous neutrino detector. Further, methods applied for relative normalization of neutrino to antineutrino data in the more conventional neutrino experiments [12] also could be applied here. Analysis would be all-electronic, not depending in any way on results from scanning of emulsion. Though the main thrust of this experiment has been to measure oscillations and V_{cd}, the ability to study conventional structure functions and QCD processes at low energies and Q^2 will receive increasing attention throughout the forthcoming year.

II. HOW THE EXPERIMENT IS DONE

The proposed experiment is intended to increase the sensitivity for detecting $\nu_\mu \leftrightarrow \nu_\tau$ oscillations by a factor of 40 over E531.

Like E531, P803 is a hybrid emulsion experiment in which τ decay candidates are observed in an active emulsion target. An electronic spectrometer selects and locates the events to be scanned in the emulsion, and provides momentum, energy and particle identification information for reconstruction of each event.

The large increase in sensitivity over E531 comes mainly from an eightfold increase in emulsion target mass, an eighteen-fold increase (in one running period) of protons on target provided by the rapid-cycling 120 GeV beam from the new Main Injector. The yield of neutrinos per proton has also been significantly increased. Target and beam parameters for E531 and P803 are compared in Table 1. The P803 yields in this proposal are based on one 8-month running period.

TABLE 1.
Comparison of Target and Beam Parameters for E531 and P803

Item	E531	P803
Volume of emulsion	23 liters	200 liters
Mass of emulsion	0.10 ton	0.84 ton
Area of emulsion	0.9 m×0.7 m	1.8 m×1.8 m
Thickness of emulsion	5.0 cm	7.5 cm
Primary proton energy	400 GeV	120 GeV
Protons per pulse	1.3×10^{13}	4×10^{13}
Cycle time	8 sec	2.0 sec
Number of pulses†	1×10^6	6×10^6
Total protons on target	1.3×10^{19}	2.4×10^{20}
Average CC interaction energy	30 GeV	16 GeV
CC interactions in target (all E_ν)	6×10^3	1.5×10^6
NC interactions in target (all E_ν)	0.2×10^3	4.4×10^5

† Assumes one 8-month run at 100 useful hours/week.

Not all of the increase in number of interactions is reflected in an increase in sensitivity, for several reasons.

1. The ν_τ interaction cross section is suppressed at low energy by kinematic and helicity effects (see Fig. 3a). Neutrinos of energy below about 10 GeV (which produce 56% of the interactions) are not useful for making detectable τ's (see Fig. 3b). Furthermore, the beam-averaged ν_τ cross-section is only 55% of that in E531.

2. Because of the large number of interactions, it is not possible to scan the emulsion for every neutrino interaction as in E531, even though the event-handling capacity of the emulsion groups has increased by more than an order of magnitude since that experiment was done. The present capability is a scan load of 30,000 events per year. A potentially τ-rich subset of interactions must be selected from the spectrometer data, implying detection efficiency losses from the necessary cuts. It is clear that the spectrometer must be designed to perform these cuts efficiently.

3. No τ decay candidates were observed in E531, while the estimated expected background [13] was 1 event. Using the same acceptance criteria for candidates in P803 would result in an estimated background of > 100 events, clearly unacceptable for the intended increase in sensitivity. Since most interactions and charm decays are multiprong, a major reduction in background results from limiting the search to single-prong decay modes of τ^- (see Table 2 below), in events in which there is no muon or electron from the primary vertex.

TABLE 2.
Single-Prong Decay Modes of τ^-

Label	Decay Mode	Branching Ratio
1	$\mu^-\nu_\tau\overline{\nu_\mu}$	17.8%
2	$e^-\nu_\tau\overline{\nu_e}$	17.5%
3	$\pi^-\nu_\tau$, $K^-\nu_\tau$	11.5%
4	$\rho^-\nu_\tau$	22.6%
5	$\pi^-\nu_\tau$ multi-γ	16.2%
	Total one-prongs	85.6%

A. Summary of Procedure

The experimental procedure is as follows: triggered events recorded on tape are reconstructed in the spectrometer, and a subset for emulsion scanning is selected. The primary neutrino interaction vertex is found by linking one track (the "leading track") from the spectrometer tracking chambers to the downstream face of the emulsion, and following it back to the primary.

The features of a tau decay candidate in the emulsion are indicated schematically in Fig. 4. Because of the relatively large mass of the τ, it is produced at relatively small laboratory angles: 98% of real τ's will be at angles less than 15°. One-prong decay candidates are located by following down all primary tracks within a cone of 15° from the beam direction for a distance of 2.5 mm, searching for a kink of more than 10 mrad. (Note that $c\tau$ for τ's is 0.091 mm, and γ's are of the order of 5, so that 2.5 mm is more than adequate.)

For events in which a kink is found, the kink secondary must be followed all the way to the exit of the emulsion and linked to the spectrometer so that its

charge and momentum can be determined. Positively-charged kinks are rejected at this stage, as are those which are too soft (momentum $p < 1.0$ GeV/c) or have insufficient transverse momentum ($p_T < 0.30$ GeV/c) relative to the candidate τ direction. For events meeting these criteria, it must be established that none of the tracks from the primary vertex are identified as muons (ν_μ CC event) or electrons (ν_e CC event). Many such tracks can be matched between emulsion and spectrometer without followdown, but ambiguous matches must followed out. Finally, the τ decay modes consistent with the event must be identified, and the event must pass the particle identification and kinematic cuts for at least one of these modes.

Backgrounds to τ decays are discussed in detail in Section V. We mention the most serious of them here, because the experimental design described in Section IV is motivated in part by the need to reduce them. They turn out to be one-prong decays of anticharm produced by the $\overline{\nu_\mu}$ contamination of the beam, and one-prong interactions with no indication of nuclear breakup ("white star kinks").

B. Important Details of Procedure

1. Linking of lead track. Timely analysis of the experiment depends in large measure on the speed and efficiency of linking the leading track and following it back to the primary. This track should be an identified hadron or muon, since following electrons back wastes time – they almost always lead to dead-end gamma conversions. For quick followback it should have a small polar angle ($< 15°$ mrad) and not be too soft (p$>$ 1 GeV/c).

There is an inherent bad match between tracking chambers and emulsion which results from the small field of view of the scanning microscope, about 150 microns on a side; this is a scale similar to the rms error in good wire chambers. When reconstructed wire chamber tracks are projected back to the emulsion, high efficiency demands making a search window which is 3 or 4 times the rms error (including that from multiple scattering) in the extrapolation. This search window can easily encompass 30 fields of view, which slows down the linking procedure and increases the chance of an accidental match to an unrelated track, leading to a large waste of time while a false trail is followed and rejected.

In past hybrid experiments by members of this collaboration special devices have been used to solve this problem: the "changeable emulsion sheet" [14] in E531, and silicon microstrips, an emulsion sheet, and a moving emulsion tape [15] in E653. The proposed solution here is small-diameter scintillating fibers which are interspersed with the emulsion layers, together with interface sheets similar to those used in E531.

2. Selection of events for scanning. To maximize the τ sensitivity in the $\approx$ 30,000 events per year which can be scanned by the emulsion physicists, the following offline selection criteria based on spectrometer information seem at present to be optimal:

- At least one leading track which is not identified as an electron, with $p >$ 1.0 GeV/c and production angle $\theta < 15°$. This is necessary for finding the primary vertex.

- Visible energy $E_{vis} > 12$ GeV. Simulated τ events have a higher average E_{vis} than neutral current events.

- A measured p_T imbalance about the beam direction of at least 0.20 GeV/c in the event. This eliminates a substantial fraction of charged current events in which the muon is unidentified.

- If an identified muon is present, a reconstructed inelasticity $y \geq 0.4$, and a measured p_T imbalance about the beam direction $\geq$ 1.0 GeV/c. This selection maintains the sensitivity to the $\tau \rightarrow \mu^- \nu_\tau \overline{\nu_\mu}$ mode at about half that for the $e^- \nu_\tau \overline{\nu_e}$ mode at an affordable cost in events to be scanned.

Simulations indicate that for the beam flux in Table 1, the above selection criteria will yield 6.0×10^4 neutral-current candidates, 1.5×10^4 charged-current candidates in which the muon escapes identification, and 0.6×10^4 candidates with an identified muon, for a total of 8.1×10^4 events. A three-year scanning effort will be needed to realize the full sensitivity of the experiment (see Appendix C).

Additional scanning of a smaller number of neutrino and antineutrino charged-current events will be required both to investigate backgrounds and to study "Standard Model" physics (Section IB). The scan load for this portion of the experiment has not yet been determined, but can be bounded from above: if no special kinematic selection criteria are used, about 2.5×10^4 events must be scanned for charm. Kinematic selection appears to reduce this number by about a factor of 2, but more study in this area is needed.

In scanning for charm, the follow-down distance will be increased to 6 mm, and a scanback technique similar to that in E531 will also be incorporated. In this latter method, electronic detector tracks whose slopes do not match emulsion track slopes measured near the production vertex will be located in the downstream face of the emulsion block, then followed upstream in an attempt to locate neutral charm decays. Based on the handling of 15,000 events per year in E653, it would take roughly 4 months to reach full efficiency, then an additional 8 months to finish scanning the charm sample.

III. NEUTRINO BEAM

Considerable progress has been made by the Neutrino Areas Working Group during calendar 1990 in understanding and optimizing the high intensity neutrino beam from the 120 GeV Main Injector. The beam described here has a high energy ($\geq$ 15 GeV) flux per proton 2.5 times greater than the one presented in a draft of this proposal (March, 1990). Equally important for this experiment, the background fluxes of $\overline{\nu_\mu}$ and $\overline{\nu_e}$, which give rise to anticharm background to τ's, are respectively 7 times and 36 times smaller than the November estimates. These design results have been confirmed by agreement among four independent simulation programs. Effects such as interactions in the horn material, previously ignored, have been studied and understood.

Particle production data for two of these programs have been parametrized using data from the Fermilab Single Arm Spectrometer (SAS)[16],[17] for 100 and 175 GeV protons. Agreement with the older 400 GeV parametrization formerly used, extrapolated to 120 GeV, is good to 10%-15% in most kinematic regions of interest.

The production target (inspired by a CERN design) is a series of thin graphite cylinders 3.0 mm in radius, totalling 2.0 interaction lengths, and separated by gaps to give an average density half the normal value. Preliminary heat load studies by A. Malensek indicate that this design is indeed practical. Most of the secondary flux from this target escapes out the sides of the cylinder rather than being reabsorbed; it gains more than a factor 2 in flux per proton over the 1.1 interaction length Be targets employed in past Fermilab neutrino experiments. If the proton beam has a Gaussian area density of standard deviation 1.3 mm, 80% of the primary beam interacts in the target, and only 24% of the useful secondaries are absorbed.

The horn for the new beam (Fig. 5), designed by Malensek, is significantly more efficient than previous double-horn implementations, achieving nearly 50% of the flux from a "perfect" horn (one which puts all particles on-axis) for neutrinos above 15 GeV. It will run at a current of 140 to 160 kA.

At this time, there are two possible locations for P803: a) sharing a beam line with the conventional Tevatron neutrino beam; b) sharing a beam with one or more long-baseline oscillation experiments. Fluxes and spectrum shapes from the two beams are similar but not identical. For the sake of concreteness we base the yield and sensitivity in this proposal on alternative a), which has a 500 m decay region. Nearly the same sensitivity can be achieved with beam b), which would have a 300 m decay space, but the optimizing cuts for event candidates are slightly different. Beam a) is shown schematically in Fig. 6. The 500 m decay space is followed by 65 m of iron and 30 m of earth, with the emulsion located 605 m from the production target.

The energy spectra for ν_μ, $\overline{\nu_\mu}$, ν_e, and $\overline{\nu_e}$ expected from this beam (weighted by E_ν and expressed as charged current interactions/ton/GeV) are shown in Fig. 7. The yields come from a Monte Carlo program which uses the SAS particle production data, and includes absorption of secondaries in the target and horn but

does not simulate the additional flux from tertiaries. This buildup effect has been studied using another (GEANT-based) Monte Carlo; it shows an enhancement by 30-50% of the ν_μ flux below 10 GeV, which is below our effective anticharm threshold and therefore harmless.

The ν_μ spectrum peaks around 8 GeV, slightly below the effective threshold for ν_τ interactions; the huge flux per unit real time available from this beam (Table 1) more than compensates for its low energy. The total ν_μ charged current (CC) interaction rate in the P803 detector is 6.0×10^3 per 10^{18} protons. The ν_e CC rate is 0.8% of that for ν_μ but peaks at higher energy since it comes predominantly from K^- decays. This flux will be measured and used to set a limit for $\nu_e \leftrightarrow \nu_\tau$ oscillations.

The background $\overline{\nu_\mu}$ CC rate is only 0.56% of that for ν_μ, 7 times smaller than our previous estimate. The $\overline{\nu_\mu}$ flux above 10 GeV is dominated by decays of π^- and K^- which pass through the horn apertures undeflected. Estimating this rate correctly requires knowledge of the small p_T dependence of production cross sections, which is helped greatly by the newer data[16],[17]. The excellent efficiency of the horn for ν_μ's also reduces the relative contamination of $\overline{\nu_\mu}$, which are not focussed. The $\overline{\nu_e}$ CC rate is shown by the Monte Carlos to be dominated by K^0_L decays; the CC rate for this background component relative to ν_μ is only 4×10^{-4}, which means that the anticharm background from $\overline{\nu_e}$ is negligible compared to the already small background from $\overline{\nu_\mu}$.

Most of the running for P803 would require neutrinos rather than antineutrinos. The antineutrino running is important, however, for both the standard model physics (production of anticharm from the sea by antineutrinos), and for understanding the cuts necessary to remove the anticharm background to τ decays. The $\overline{\nu_\mu}$ charged current interaction rate, with the horn set for negatives, is somewhat less than half of the ν_μ rate given above.

IV. DETECTOR DESIGN

The hybrid emulsion spectrometer is drawn schematically in Figs. 8a and 8b. LUND-GEANT simulations of some typical events in the spectrometer are shown in Figs. 9a–9d. We discuss below the requirements and essential features of each spectrometer component.

A. Emulsion Target

The emulsion target has a volume of 200 liters, a mass of 0.84 tons, a cross-sectional area of 180 cm×180 cm, and a thickness of 7.5 cm. It consists of 12 modules of the "vertical" type [14] in which particle track directions are nearly perpendicular to the emulsion sheets; this configuration is well-suited to rapid semiautomatic and fully automatic scanning techniques [15] developed at Nagoya University. As shown in Fig. 10, each module is composed of 25 emulsion sheets 1 mm thick and 90 cm square, vacuum-packed into a stack 2.5 cm deep in the beam direction. Each sheet is constructed of two 450 micron emulsion layers bonded on opposite sides of a 100 micron plastic base which increases rigidity and minimizes emulsion warpage due to shrinking during the development process. Three such $180\times180\times2.5$ cm^3 layers are separated by layers of scintillating fibers and interface sheets (see below). Mounting details are provided in Appendix C.

It can be reasonably argued that this target is about as large as a single-target design will allow without serious losses of effectiveness in added material. The radial distribution of high-energy neutrinos falls off rapidly beyond a radius of 1 meter. The radiation length of emulsion is only 2.89 cm, so that many neutrino interactions in the upstream portion of the target produce well-developed electromagnetic showers in the emulsion, which the tracking system must be designed to deal with.

Emulsion analysis is based on techniques developed in more than a decade of previous Fermilab experiments. After exposure, sheets will be sliced into 5 cm × 5 cm squares. As indicated in Fig. 10, squares from succeeding sheets will be stuck onto a plastic backing prior to developing, forming a "tower geometry" of an event which can be scanned without changing plates on the microscope stage. The microscope stages are driven to the electronically-predicted event positions under computer control; events are located and charged track slopes measured using semiautomatic techniques with minimal human intervention.

B. Magnet

The hybrid spectrometer is built into an existing large-aperture superconducting magnet (the former 15 foot bubble chamber magnet). Because of the low average energy of the interaction tracks produced, it is planned to run with a 0.5 Tesla field. The magnet coils are shown in Figs. 8a, 8b; the configuration is essentially open Helmholz coils, with no iron. Access to the emulsion and spectrometer detectors will be primarily from above. The fringe field of this magnet is large and far-reaching, which will mandate the use of special photomultiplier

tubes and preamplifiers in the trigger and muon veto counters. The Hamamatsu R2490 high-gain photomultiplier, for example, is designed for magnetic environments; it has a gain of approximately 5×10^5 in a field of 0.5 Tesla.

C. Wire Tracking

The purposes of the tracking system are:

1. For all recorded events, to reconstruct the leading track (ideally, highest momentum small-angle track) which will be linked to the emulsion and followed back to the primary interaction.

2. For all recorded events, to reconstruct and obtain momenta for all charged tracks stiffer than about 0.15 GeV/c (radius of curvature > 1.0 m). This is for computing the visible energy E_{vis} and transverse momentum vector for kinematic reconstruction and selection of events for scanning. Note that the tracking will be often called upon to act as a pair spectrometer for γ conversions in the emulsion; see the simulated events in Fig. 9.

3. For events with an emulsion kink, to link and reconstruct the secondary track from each emulsion kink, establish its charge and momentum, and to follow it into the calorimeters for particle identification as a possible muon or electron.

4. For events with an emulsion kink, to link all tracks from the primary vertex and project them into the calorimeters for particle identification as possible electrons or muons; this must be done to eliminate $\nu_\mu, \overline{\nu_\mu}$ and $\nu_e, \overline{\nu_e}$ charged-current events.

5. To serve as an important component of the trigger (see subsection H below).

Since typical track momenta are on the order of 0.5 to 10 GeV/c, the tracking chambers need not deliver the state-of-the-art in momentum resolution. However, multitrack separation is challenging because of the well-developed electromagnetic showers which frequently emerge from the relatively thick emulsion target (Figs. 9a–9d). This problem is handled by leaving a 25 cm drift space between the emulsion and the tracking chambers, by using small drift cells, and by designing for high redundancy, with 56 samples in four projections.

The wire chambers for this experiment will have a structure similar to those used successfully in the AMY detector [18] at KEK in a magnetic field of 3 Tesla. They will have an average area of 2.7×2.7 m^2, and will use a hexagonal cell structure (Fig. 11) with a sense wire spacing of 1.2 cm. Each chamber will be 4 cells deep in the beam direction, providing a local minivector for connecting tracks between modules.

The tracking modules are arranged to give four 4-layer samples each in the bend view (x) and in a u-view rotated 10° from x, and three 4-layer samples each in the nonbend view (y) and in a v-view rotated 10° from y. When tracks are

close together in one projection, the staggered cells in each layer of 4 (see Fig. 11) should catch two hits on each track, on the average; further, if the tracks are only nearby in one projection, the small angle stereo has a good chance of resolving them cleanly. Examples of this are apparent in the simulated events in Fig. 9. Assuming a conservative position resolution of 0.25 mm from the hexagonal cells, the momentum resolution in the 0.5 Tesla field is $\delta p/p = \sqrt{(0.006p)^2 + (.022)^2}$.

Layout of Tracking Chambers

xxxx uuuu yyyy vvvv xxxx uuuu yyyy vvvv xxxx uuuu yyyy vvvv xxxx uuuu

In addition to the 14 tracking chambers, there will be a pair of xxxx and yyyy chambers on either side of the emulsion target, used principally for forming the trigger (subsection H). The xxxx, yyyy doublet just downstream of the target will also be helpful in picking up soft tracks at wide angles. The complete system will have approximately 1.3×10^4 sense wires in the tracking chambers, and an additional 2.5×10^3 sense wires in the trigger chambers.

The tracking chambers will be constructed as (xxxx, uuuu) or (yyyy, vvvv) doublets sharing a common rectangular frame, with the u or v wires strung at an angle between the drilled endplates (this leaves small dead spots at the corners of the angled views). Each doublet chamber will be approximately 10.4 cm thick, allowing seven doublets to fit in 75 cm of depth. Many of the proven AMY construction techniques[18] and hardware items (e.g., wire-holding pins) could probably be used. We plan to fill the chambers with nonflammable HRS gas (89% Ar, 10% CO_2, 1% CH_4) at atmospheric pressure.

Because of the large number of sense wires, it is desirable to reduce cabling by using electronics which stores outputs locally and multiplexes the outputs. Whether this is done in analogue or digital form depends on availability of commercial components. The time-to-digital converters need not be able to handle multiple hits per wire, but they must be able to buffer two or more events (subsection H). The electronics must also be capable of providing a fast output from each cell in the trigger chambers for use in the trigger logic.

An additional component of the tracking system will be planes of scintillators immediately downstream of the target, and just downstream of the wire chambers. Timing information from these scintillators in combination with a signal derived from the accelerator RF will generate a stop pulse for the TDC system. The stop pulse will be phase locked to the RF-derived signal, so its jitter will be 1–2 ns. The resolution of the scintillator pulse only has to be good enough to select the RF bucket responsible for an event. The RF period will be 19 ns, and 5 ns resolution (sigma) from the scintillator will be adequate and feasible even considering the difficulty created by the magnetic field.

D. Scintillating Fibers

The purpose of the scintillating fibers is to provide an interface between tracks extrapolated from the wire chambers and the emulsion, especially for the two upstream emulsion modules. If a neutrino interaction occurs in the most upstream module, for example, it would save considerable time if the leading track could be extrapolated from the chambers across the intervening emulsion layers to the fibers, and then into the emulsion, rather than having to follow it from sheet to sheet through 5 cm of emulsion.

Ideally, the fibers should provide at least two hits per track in each of two projections as close to the emulsion as possible, with a resolution comparable to the size of the field of view of an emulsion microscope (0.15 mm$\times$0.15 mm). The system shown schematically here is based on arrays of square fibers 0.50 mm $\times$0.50 mm in size. A complete fiber module will have two x-layers and two y-layers, with each layer 3 fibers (1.5 mm) deep. With present technology, the expected yield is 1.2 photoelectrons per mm, so that an average of 1.8 photoelectrons is expected from each 3-fiber layer; from Poisson statistics, the efficiency of each x- or y-layer layer is 87%, or 98% for each x,x or y,y pair of layers. It is not practical to use fibers in the coincidence mode unless the light yield is improved by at least a factor 2. Prospects for such an improvement are good (see below).

The fibers will be coupled to image intensifier tubes of a new design recently developed by Hamamatsu, Inc. (see Appendix E). The Hamamatsu design uses existing techniques, so that a prototype can be built quickly. This image intensifier uses no electron lens, and operates with a small distance between the photocathode and the microchannel plate; it should work well in a 0.5 Tesla field. This is very important for this experiment because of the ubiquitous fringe field of the magnet; running long fibers to a field-free region would extract a large penalty in light attenuation. The readout of the image intensifier will be via CCD cameras recorded digitally, so that the fiber data will be available on tape with the wire chamber data for track reconstruction. This fiber data will be very useful in estimating the transverse vertex position in high-multiplicity events to about $\pm$0.5 cm, a desirable first step in finding roads for trackfinding involving curved tracks.

Tracks must be linked efficiently from the wire chambers to the fibers. The extrapolation is about 300 mm from the center of the most upstream (x,u) tracking point to the most downstream fibers. The error in this extrapolation in the bend plane is roughly

$$\Delta x = \sqrt{(0.14\text{ mm})^2 + [(.0006)^2 + (.0008/\text{p})^2](300\text{ mm})^2}$$

which gives $\Delta x = 0.26$ mm for a momentum $p = 2$ GeV/c, a good match to 0.5 mm fibers. Tracks must also be extrapolated through each 2.5 cm emulsion layer (0.87 radiation lengths). The rms projected deflection due to multiple scattering will be $\Delta\theta_{proj} = .014/p$ in angle, and $\Delta x = (13\text{ mm})(.014)/\text{p} = 0.2$ mm in position, comparable to the extrapolation from the drift chambers to the fibers. For fibers spaced 2 cm from the emulsion, multiple hits occur about 20% of the time; however, a large fraction of these are merely unresolved electron pairs.

Recent developments in scintillating fiber technology are very encouraging. Tests of different wavelength shifters are in progress in Japan, and a promising technique of butting short fibers with different wavelength sensitivity is being explored in the U.S. [19]. At Fermilab, a different approach[20] has used 0.5 mm diameter 3HF plastic scintillating fiber with PMMA cladding in conjunction with solid state photomultipliers (SSPM) to obtain an average yield of 8 photoelectrons per mm for fibers 60 cm in length; the SSPM's are virtually insensitive to magnetic fields, but require individual amplifiers on each channel, and cooling to liquid helium temperatures. Clearly another factor of 2–4 in photoelectron yield would be most welcome for this experiment, and a period of R&D is needed to find the optimum solution.

E. Interface Sheets

Interface sheets have been used successfully in Fermilab hybrid emulsion experiments E531[14] and E653[15]. They consist of thin layers of emulsion on both sides of a plastic base 0.5 mm thick; the emulsion track coordinates in the separated layers act as high-precision verniers between electronic detectors and emulsion, providing three-dimensional vectors pointing into the emulsion with 2 milliradian accuracy. The use of a changeable interface sheet in E531 is illustrated schematically in Fig. 12.

The interface sheets for this experiment will be located just upstream of each scintillating fiber module. They will be scanned with the fully automatic system[21] for tracks in the window predicted by the wire chambers and fibers. If the sheets are close to the fibers, this window should be ± 0.25 mm for tracks cleanly resolved by the fibers. Automatic scanning is efficient and fast for tracks with angles between 0.1 and 0.2 radians to the perpendicular. Tracks with larger slope take more time, by a factor of 2 to 3. Small-angle tracks (less than 0.1 radians) are difficult if the background of small-angle tracks is high; this was the case for E653 (600 and 800 GeV hadron beams) and in E531 (stiff muons from the shielding). However, it will probably not be true here (see below).

The muon flux from the iron shielding at the end of the neutrino beam is dominated by charged-current interactions in the last 5 or 10 meters of shielding; this will be about 50 muons per m^2 per pulse. If we assume 6×10^6 pulses per run, this gives $3 \times 10^4/cm^2$ integrated exposure, or 75 integrated muon tracks in a square 0.5 mm on a side. For effective use of the interface sheet, the accidental background after angle matching to a few milliradians should be less than 10%. This is the criterion for deciding whether the interface sheets must be changed several times during the run, as was done in E531.

At present it appears that changing will not be required. Muon tracks from the shielding will in general be soft (a few GeV), and will all have been swept in the same sense by the large fringe field of the magnet upstream of the detector, approximately 1.0 Tesla-meter, or 0.15 radians for a 2 GeV muon. Thus these muons will have a rather broad distribution in bend-plane slopes, and will be a much less severe background than the beam tracks and muons in E653 and E531.

F. Electromagnetic Calorimeter

The purposes of the electromagnetic calorimeter are:

1. For all recorded events, to obtain the electromagnetic component of E_{vis} and of the transverse momentum vector for the event, to be used for selection of events for scanning. This information can also be used in making kinematic cuts on event candidates.

2. For all events with negative kink candidates, to determine whether the kink is an electron and hence a candidate for $\tau \rightarrow e\overline{\nu_e}\nu_\tau$.

3. For all events with negative kink candidates, to determine whether any tracks from the primary vertex are positrons, in which case the candidate must be rejected as an ordinary charged-current interaction.

4. For all events with negative kink candidates, to measure the energy and direction of candidate showers from the the decay $\tau^- \rightarrow \rho^-\nu_\tau$, with $\rho^- \rightarrow \pi^-\pi^0$.

5. To measure the flux of ν_e charged current interactions, for use in establishing a limit on $\nu_e \rightarrow \nu_\tau$.

Because of the importance of identifying individual tracks, tracking aspects have been emphasized in the calorimeter design. Gas tracking is used because of the difficulties in using large numbers of photomultipliers in the magnetic field. Although occasional high-energy showers occur (especially from real ν_τ events), most tracks and showers are soft. The device must perform fairly well in separating electrons and pions, with rejection ratios of 5 to 10 down to energies of 1 GeV or so. It should pick up photon showers down to 0.3 GeV. This leads to rather fine longitudinal segmentation in the upstream layers.

The calorimeter has an area of 3.77×3.77 m^2 and a depth of 40 cm. It consists of alternating layers of lead and 1 cm square proportional resistive plastic tubes (Figs. 13, 14). Many details of its construction have been borrowed from the AMY barrel calorimeter[22] which works in a 3 Tesla magnetic field, and covers a similar energy regime. Some of these details are presented in Appendix F.

The total depth of the calorimeter is 22 radiation lengths (0.73 collision lengths). The sampling is every 0.5 radiation lengths for the first 4 radiation lengths, 1 radiation length for the following 12 radiation lengths, and 2 radiation lengths for the last 6 radiation lengths, a total of 23 layers of tubes, 8.7×10^3 tubes in all. Each extruded resistive plastic tube is designed (Fig. 14) to be read out from capacitively coupled 1 cm x-strips (x-readout in the bend plane) and y- or u-strips in the nonbend or stereo planes; this scheme is shown in exploded view in Fig. 15.

The calorimeter's 23 alternate layers of absorber, conducting plastic tubes and readout board are epoxied together to form one right module and one left module.

Each module fits inside a gas container which provides support, gas tightness and mounting of gas fittings and feedthrus to the detector (Appendix F). Dividing the calorimeter into two modules avoids the difficulty of obtaining and handling of the heavy lead absorber in one large piece. To reduce the number of readout channels, the readouts are ganged 2 tubes deep, as shown in Fig. 16, with the exception of the last three layers which are ganged 3 tubes deep. This gives 11 samples in x, 12 in y (6 left and 6 right), and 5 in u, resulting in 12×10^4 analogue readouts.

All charged tracks to be identified will have been momentum-analyzed in the tracking system before they enter the calorimeter. Based on the AMY experience, we can expect a pion rejection factor of 20 at 3 GeV based on energy-momentum comparison alone. Information on shower shape improves this discrimination as much as sixfold. Energy resolution for isolated showers is expected[22] to be approximately $\Delta E/E = \sqrt{(0.10)^2 + (0.29)^2/E}$, for E in GeV; the real resolution will probably often be dominated by the ability of the software to untangle overlapping showers.

G. Hadron Calorimeter

The main purpose of the hadron calorimeter (Fig. 17) is to identify muons; a secondary purpose is to record the energy of high-energy neutral hadrons. The design is conceptually similar to that of the electromagnetic calorimeter, emphasizing tracking capability: alternating layers of nonmagnetic (zinc) absorber and gas tubes, with x- and y- or u-coordinate readout from strips.

Identifying muons is important both in reducing the emulsion-scanning load of events from ordinary charged current interactions, and for reducing the potential background from anticharm produced in antineutrino charged-current interactions. Good muon-identification efficiency must be maintained at rather low energies and at large angles due to the low average energy of the beam. Tracks identified as muons will be those having no evidence of interactions or of anomalous energy loss after traversing N_I interaction lengths of material; to first approximation, the identification efficiency of such a track is $\epsilon_\mu = 1 - e^{-N_I}$. The misidentification of hadrons as muons ("false positives") is not a serious problem unless it is large enough to make an appreciable reduction in the event sample. In calculating efficiencies for this proposal, we make the conservative assumptions that no muon identification will be attempted below 1.0 GeV/c, and that the identification efficiency never exceeds 99%.

The hadron calorimeter will behave as a range stack for low energies and as a calorimeter at higher energies. It is assumed that most charged-particle momenta will be known from magnetic analysis to better than 10%; these particles will have been followed through the electromagnetic calorimeter from the tracking chambers. Then, muon/hadron separation will be performed by range for momenta below 1.5 GeV/c, by range and energy deposition pattern for momenta 1.5 to 5 GeV/c, and by hadron calorimetry above 5 GeV/c.

For example, a 1.0 GeV/c muon has a range of 4.4 pion interaction lengths;

the identification efficiency from range alone is nearly 99% if the muon does not leave the calorimeter. At somewhat higher momenta, detected energy deposition from pion interactions can reduce the inefficiency by another factor of 3-5. In the interval 1.5 to 5 GeV/c, muons will appear in the detector as minimum-ionizing particles, with a single hit per plane, which penetrate the whole stack. Most pions will interact, giving clusters of deposited energy. At energies above 5 GeV there will be several criteria for muon identification, including penetration, minimum-ionizing appearance, etc. Discriminant analysis [23] can be used to optimize muon separation at the 99% level, with an expected hadron energy resolution of approximately $\Delta E/E = 0.8/\sqrt{E}$ (E in GeV).

Inefficiencies in muon identification arise mainly from pions which do not suffer an interaction which changes their direction or energy significantly; this will occur principally for tracks with short paths in the absorber, either because of short range due to very low momentum, or because the track clips a corner of the calorimeter. These sources of inefficiency have been modeled, and are included in the calculated efficiencies. False positives (misidentification of pions as muons) will come mainly from pion decays. These should occur at a level smaller than 4% in the low-energy regime, and smaller than 3% for energies between 1.5 and 5 GeV.

The hadron calorimeter has 24 layers with an average area of 4.0 m $\times$ 4.0 m, each with a converter of 5 cm (0.26 interaction lengths) of zinc; the total depth is 6.3 interaction lengths. The gas tubes will employ limited streamer readout (Iarocci tubes). Details of their operation and construction are given in Appendix G; the total number of tubes is 9.8×10^3. These tubes have cathodes transparent to high-frequency signals, and are read out from both sides by pads in the form of 2 cm strips: a set of x-strips on one side, and alternating y- and u-strips on the other, giving a total of 9.8×10^3 analogue readouts.

Electronics for the electromagnetic and hadron calorimeters can be in large part identical, differing only in the gains of the front ends. A preliminary design is presented in Appendix I; it emphasizes onboard digitization, local storage, all-digital readout, and storage of multiple events before readout.

Because of the relatively thick absorber between the sampling planes, this device is not efficient for neutrons much below 5 GeV. Preliminary studies indicate that this shortcoming is not very damaging, since primary neutrons tend to be considerably softer than this, and missing them contributes relatively little to the transverse momentum error; on the other hand, detecting them reliably would require heroic efforts.

Both calorimeters will be calibrated with electrons, pions, and muons in a test beam, where test modules identical in structure with the real calorimeters will be installed. In addition, the calorimeters will be continously calibrated on line with external electron, pion, and muon beams brought to the detector (Appendix I).

H. Trigger

The problem in designing a trigger for this experiment is that the emulsion target has a much smaller mass than other objects in the vicinty, and triggers from these other objects can cause serious loss of sensitivity due to deadtime. Furthermore, we would like to trigger efficiently on the simplest possible event configuration: nothing into the emulsion, and at least one stiff ($p > 1.0$ GeV/c), small angle ($\theta < 15°$) track emerging from it.

An additional constraint is that the trigger decision must be made in less than 2 microseconds, and in one microsecond if possible. This arises from the temporary storage of scintillating fiber hits in a secondary phosphor of the cascaded image intensifier; the last stage of the image intensifier is gated by the trigger. A long delay in the trigger decision forces the use of a slow phosphor, and hence more accidental background in the fiber hits.

The interaction rate (both charged and neutral current) in the emulsion target is about 0.3 per pulse (Table 1), with a beam pulse duration of 1.0 msec. The interaction rate in the portion of the magnet coil immediately upstream of the emulsion is about 20 times greater, or 6 per pulse; the flux of muons into the target from neutrino interactions in the shielding upstream of the experiment is roughly 50 per pulse. Although the trigger scheme described below is designed to reduce the trigger rate below one per pulse, prudence dictates use of electronics capable of handling more than one event per spill, with event recording time ≈ 25 μsec. In rate calculations for this proposal it is assumed that trigger deadtime has been reduced below 10%.

The first level of the trigger will demand a coincidence between two scintillators inside the magnet, in anticoincidence with a large, efficient muon veto wall several feet upstream of the magnet. The two inside scintillators will be located just downstream of the emulsion and just upstream of the calorimeters. This first level will eliminate triggers from muons from the shielding, but will retain those from the coil.

The most straightforward solution to the problem of events from the magnet coil (see Fig. 18 for examples) is to place a veto counter between the emulsion and the coil. However, Monte Carlo studies have shown that an unacceptably large fraction (18%) of good emulsion interactions would be rejected by backsplash. This backsplash is mainly soft electrons swept backward by the magnetic field, but also includes some tracks produced backward in the laboratory. Since most of this backsplash has been found to intersect such a veto plane at transverse distances ≥ 12 cm from the primary vertex, trigger elements with crude tracking information are needed. The AMY pattern-recognition logic[24] uses static random-access memory chips to recognize various patterns of hit cells as containing track-like objects ("blobs") in single 4-layer drift chambers using allowed patterns of struck cells. It can be extended to require multiplicities and correlations of blobs in different chambers.

The second-level trigger recognizes these blobs. It uses two (x and y) 4-layer "veto" chambers between the emulsion and the coil, and two similar chambers just

downstream of the emulsion. In addition, the most downstream x and y tracking chambers are instrumented with the same pattern-recognition logic. The trigger requires a multiplicity cut on the blobs in the veto chambers, and at least one tracklike object crossing the wire chambers which has no blobs behind it in the veto chambers. Selection of events with stiff, small-angle track candidates is done most effectively in the nonbend (y) view, since no allowance must be made for displacement due to the field. If the separation of the most upstream and most downstream y planes is 80 cm, the criterion of $\theta < 15°$ implies that there must be a downstream blob separated from an upstream blob by less than 20 cm in this view.

The first level (scintillation counter) trigger will deal with an input rate of about 50 shielding muons per msec, or one every 20 μsec on the average. It reduces this rate to the approximately 6 per msec characteristic of interactions in the coil, and issues stop pulses to the TDC system at this rate. The second level trigger operates in about 600 ns, and resetting TDC's and ADC's may require an additional 600 ns. Therefore the dead time incurred by each first level trigger is 1.0 to 1.5 μs; it will be adequate even if its output rate is does not greatly exceed 60 per spill, 10 times the design rate. The second level trigger must make a decision about 6 times per msec. It should reject essentially all of the target-out background. Studies of the most efficient blob-logic criteria are in progress.

V. SENSITIVITY TO OSCILLATIONS

A. General Issues

The sensitivity of the experiment to the probability of $\nu_\mu \leftrightarrow \nu_\tau$ oscillations depends both on the estimated background and on the number of τ's which would be detected if the ν_μ beam were to be entirely converted to ν_τ. The latter number is most conveniently expressed relative to the equivalent ideal yield of charged-current interactions in the target, i.e. the integrated spectrum of Fig. 7 multiplied by the target mass:

$$N_{CC} = \int dE_\nu \, [dN_{cc}/dE_\nu] \, ,$$

where dN_{cc}/dE_ν = Number of ν_μ interactions per GeV in the target. From Table 1, $N_{CC} = 1.5 \times 10^6$.

Now suppose the same beam has oscillated with 100% probability to ν_τ. The yield of τ's would be

$$N_\tau(100\%) = \int dE_\nu \, [dN_{cc}/dE_\nu] \cdot \sigma_{\nu_\tau}/\sigma_{\nu_\mu} \cdot \epsilon(E_\nu)$$

where

$\sigma_{\nu_\tau}/\sigma_{\nu_\mu}$ = Energy-dependent cross-section ratio (Fig. 3a);

$\epsilon(E_\nu)$ = Energy-dependent τ detection efficiency. $\epsilon(E_\nu)$ includes the efficiency factors listed in Section B below, and also the branching ratios and energy-dependent acceptances of all detected τ modes (Fig. 3b).

There is thus a correction factor C for the sensitivity which is the weighted average of the σ and ϵ factors over the charged-current interaction spectrum, $C = N_\tau(100\%)/N_{CC}$. If no τ signal is seen, but rather an upper limit N_τ at 90% confidence level is set, the corresponding limit on oscillation probability (integrated over all energies) is

$$P(\nu_\mu \rightarrow \nu_\tau) \leq \frac{N_\tau}{C \cdot N_{CC}}.$$

If no candidates are observed, the 90% confidence level N_τ is 2.3 events. If however the expected background is not zero and events are observed, the situation is more complicated; it is summarized in Fig. 19 (reproduced from Ref. [25]). If, for example, the expected background is 3 events, and 3 events are actually observed, from Fig. 19 the 90% confidence level limit is 4.3 events above background.

Above an estimated background of about 2-3 events, the sensitivity decreases quite slowly with expected number of background events for fixed $C \cdot N_{CC}$. For estimated background levels well below 1 event, the sensitivity is nearly linear in $C \cdot N_{CC}$. These considerations are important in deciding whether to make cuts to remove background, since this almost always reduces the τ detection efficiency, and therefore C, as well.

B. Efficiency Factors Affecting Both Signal and Background

Event losses due to detection efficiencies ϵ which affect signal and background in the same way are estimated below. These factors must be applied to all background estimates. (An event is not backgound if it is never found.) No efficiencies due to event selection or kinematic cuts are included here, since they affect signal and background differently.

1. Trigger efficiency (deadtime and veto overkill)	0.85
2. Emulsion fiducial volume	0.90
3. Efficiency in scanning back to the primary vertex	0.93
4. Efficiency for seeing kink (some occur in plastic backing)	0.90
Product of efficiencies	0.64

C. Estimate of Backgrounds

Candidates for charged current interactions of tau neutrinos consist of events with no primary muon or electron which have a negative kink track with a production angle less than 15 degrees. Possible sources of background consist of tau neutrinos coming from the primary proton beam dump, charged hyperon and kaon decays, single-prong decays of charm antiparticles, and ordinary interacting tracks which scatter without leaving evidence for nuclear breakup in the emulsion.

Note that all sources of background except direct ν_τ are inherently measurable, and will be measured in this experiment. For example, one can scan a subset of non-muon tracks for several centimeters in emulsion. The number of kink interactions and strange decays per unit length will be roughly uniform over this distance, while all real τ decays would occur in the first few millimeters of path. The number of anti-charm particles produced in $\overline{\nu}$ interactions can be determined by searching for their decays in events with a primary μ^+.

The geometry of the calorimeters creates high efficiencies for detecting muons and electrons from the primary vertex over a wide range of angles and energies. Muon efficiency is presented as a function of neutrino energy in Fig. 20 both for μ^- from all charged-current neutrino events, and also for μ^+ from antineutrino-produced anticharm. The high μ^- efficiency of the calorimeter described in Section IV is important in reducing the number of events to be scanned, and is essential for reducing the background of kinks from anticharm decays found in the emulsion.

Note that a small percentage of pions will penetrate the range material without interacting and will be identified as muons, reducing the apparent number of neutral current interactions. Also, neutrons from neutrino interactions in surrounding material can interact in the emulsion, increasing the apparent number of neutral current interactions. These effects have little impact on the proposed measurements.

In discussing individual backgrounds, we use the kink-selection criteria listed in Table 3, which have been chosen to optimize the sensitivity for a tolerable scan load. As will be shown below, they reduce the estimated background to well below one event.

TABLE 3.

Kink Selection Criteria

Kink Attribute	Requirement
Maximum track angle	$< 15°$
Minimum kink angle	> 10 mrad
Minimum momentum of secondary	> 1.0 GeV/c
Minimum p_T relative to parent direction	> 0.30 GeV/c
Maximum decay length	< 1.5 mm

In the sections below, we discuss individual sources of background in increasing order of severity.

1. Decays of strange particles. Background from one-prong hadronic decays of negatively-charged strange particles was studied with LUND-generated neutral current interactions. (Muonic decays are suppressed by at least an order of magnitude by identification of the μ from the kink). Candidate decays were required to occur in events meeting the scan selection criteria described in Section IIB, and in addition, the secondary track from the kink was required to meet the kink selection criteria of Table 3 with the exception of the p_T cut. The background under these conditions would be about 1 event. The distributions in the transverse momentum p_T relative to the measured parent direction for strange and τ decays are shown in Figs. 21 and 22. The ability to measure the direction of a short-lived parent to obtain a good measurement of p_T is a major strength of emulsion experiments. The p_T cut actually used, 0.3 GeV/c, is 30% greater than the maximum p_T available in any strange decay. This cut should suppress the strange background by at least a factor of 100, giving < 0.01 event.

2. Tau neutrinos from the proton dump. Only 80% of the primary proton beam fails to interact in the long production target for the neutrino horn. Those protons which do not interact are stopped in an iron beam dump 105 m from the emulsion. Real ν_τ's from the decay chain

$$\overline{D_s} \rightarrow \tau + \overline{\nu_{\tau 1}}, \qquad \tau \rightarrow \nu_{\tau 2} + X$$

are a potential background to ν_τ's resulting from oscillation of ν_μ's.

This source of background has been carefully simulated with a Monte Carlo program; details of the calculation are described in Appendix B. Known production properties of charmed particles and Monte Carlo simulations of charm and τ decays are used to scale the results of the Fermilab beam dump experiment E613 [26] from 400 to 120 GeV protons. The calculation is certified by reproducing the absolute yield of charged current interactions from prompt neutrinos in E613.

The major uncertainties in the calculation are in the unmeasured charm cross section at 120 GeV, and in the assumed x_F dependence of D_s production at that energy, parametrized as $(1 - x_F)^n$. The results are summarized below, assuming the beam flux from Table 1. Even within the limits of uncertainty in production, direct ν_τ's are not a serious source of background, due in large part to the low energy of the proton beam.

TABLE 4.

Calculated Yield of Direct ν_τ Events

Assumed n-value	P803 Acceptance	$\overline{E_\nu}$ (GeV)	$\sigma_{\nu_\tau}/\sigma_{\nu_\mu}$	$\overline{x_F}$	P803 Yield/ 2.4×10^{20} p
2.0	0.030	28	0.48	0.66	0.096 events
2.5	0.022	27	0.47	0.60	0.067 events
3.2	0.015	26	0.46	0.55	0.043 events

The energy-weighted spectrum of ν_τ's for $n = 2.5$ is shown in Fig. B2 of Appendix B; the low- and high-energy peaks from the two sources (1) of ν_τ are evident. Using this best-guess value of n, we obtain 0.067 background events from the beam dump.

3. Backgrounds from charm production. There are three types of charm background events: single and associated charm coming from neutrino interactions and anti-charm coming from interactions of anti-neutrinos.

Single charged charm generated by neutrinos is positive; a τ lepton coming from a charged-current interaction would be negatively charged. For an average neutrino energy of 16 GeV (Table 1), the expected yield of charm per event (Fig. A3, Appendix A) is 2%. The primary muon will be found in 95% of the ν_μ interactions producing charm, and any single charged charm produced will have the wrong sign of charge. The background from single charm can thus be made arbitrarily small by rejecting kinks with an ambiguously-determined sign.

Associated production of charm is extremely small compared to single charm production at these low neutrino energies. However, all events containing tau candidates would be scanned for a second vertex with an efficiency experimentally determined to be greater than of 80%.

The most serious source of charm decay background comes from anticharm production by antineutrino interactions in which a negative single-prong anticharm decay occurs, and in addition the primary charged-current muon or electron is missed. In the estimates below, we use the background $\overline{\nu_\mu}$ and $\overline{\nu_e}$ fluxes discussed in Section III and shown in Fig. 7. The $\overline{\nu_\mu}$ anticharm decay background may then be calculated as a product of the following factors:

a. Number of charged-current interactions in the target	1.5×10^6
b. Fraction of interactions from $\overline{\nu}_\mu$	0.0056
c. Efficiencies affecting both signal and background	0.64
d. Beam-weighted average of anticharm cross section multiplied by muon detection inefficiency	0.99×10^{-3}
e. Ratio of charged anticharm to total anticharm	0.40
f. Branching ratio for charged charm to 1-prongs	0.43
g. Fraction passing scan and kink criteria	0.105
Number of $\overline{\nu_\mu}$ anticharm events	0.093

Entry (d) in this list is $\int dE_\nu \left[dN_{c\overline{c}}/dE_\nu\right] \cdot \left[\sigma_{\overline{C}}/\sigma_{\nu_\mu}\right] \cdot (1 - \epsilon_\mu)$,

with the relative anticharm cross section as shown in Fig. A3 of Appendix A and the muon efficiency as shown in Fig. 20. Note that there is negligible anti-Λ_c production in a low-energy antineutrino beam. The detection efficiency for charm background is only 40% of that for τ's, due mainly to the event p_T and decay length cuts; the decay length cut of 1.5 mm is effective in reducing the background of long-lived D^- relative to τ's. Decay length distributions for τ^- and D^- passing the other cuts are compared in Fig. 24.

A similar calculation may be done of the anticharm production by the $\overline{\nu_e}$ contamination in the beam, which from Section III is only 0.04%. If the identification inefficiency for electrons from the primary vertex is about the same as that for muons, this source of background adds only 0.007 events, bringing the total anticharm decay background to 0.10 events.

4. Background from interactions. The most serious source of background to hadronic τ decays will be single-prong interactions of tracks from the primary vertex which show no evidence of nuclear breakup, called white star kinks (WSK's). The important issues here are both the mean free path (mfp) and the p_T dependence of these interactions. For example, if they occur mostly through coherent scattering off the nucleus as a whole, they will have a very steep falloff in p_T, and a modest kink p_T cut can virtually eliminate them. If, on the other hand, WSK events are scattering off individual nucleons with a typical dependence of $e^{-8t} \approx e^{-8p_T^2}$, any reasonable p_T cut will have little effect.

Published quantitative information on WSK's is rather sketchy[27], indicating a mfp of about 30 m with an unknown p_T cutoff. This 30 m mfp, used in previous drafts of this proposal, is now known to be much too pessimistic. Members of this collaboration have exposed emulsion modules at KEK to π^- beams of 2.0 and 4.0 GeV/c, and are performing an efficient scan for kinks; this experiment is described in Appendix D. Another measurement at Fermilab is planned, with momenta of 10 and 15 GeV/c.

Preliminary results now available for half of the 4 GeV/c data are summarized in Fig. 23. This figure shows the p_T distribution both for all kinks, which includes those with breakup tracks or short "blobs" at the vertex, and for the WSK component. In this preliminary analysis the momentum information for the kink has not yet been incorporated, and the p_T for each event is inferred from the kink angle under the assumption that the momentum of the kink secondary is the same as that of the beam; later use of this information will remove a WSK background from bremsstrahlung of the 3% electron contamination of the beam which is still present in the data of Fig. 23.

From Fig. 23 it is clear that white star kinks do have a significantly steeper p_T dependence than the total sample. The falloff of the WSK sample is approximately e^{-20p_T} (dashed line in Fig. 23) for $p_T \geq$ 0.1 GeV/c. There are 8 WSK events with $p_T \geq$ 0.2 GeV/c, which corresponds (Appendix D) to a mfp of (50 $\pm$ 18) m; the exponential falloff in p_T then gives a (370 $\pm$ 130) m mfp for $p_T \geq$ 0.3 GeV/c. The fractional mfp per scanned track with a 0.3 GeV/c p_T cut is then 1.5×10^{-3} m/370 m = 4×10^{-6}.

The rapid falloff in p_T is very important; the WSK backgound decreases by about $1/e$ for each 0.05 GeV/c increase of the p_T cut in this region, while the corresponding signal losses are about 10%. This is illustrated in Fig. 22.

The background from white star kinks depends on the number of negatively-charged tracks from the primary vertex in the sample of events selected for scanning. This has been determined from LUND simulations of ν_μ neutral- and charged-current events which pass the scan cuts. The background is then found from multiplying the following factors:

a. Number of neutral-current interactions in the target	4.4×10^5
b. Efficiencies affecting both signal and background	0.64
c. Fraction of NC interactions passing scan cuts	0.18
d. Negative tracks per scanned event with $\theta < 15°$, $p > 0.5$ GeV/c	1.21
e. (Scan distance per track)/(mfp for WSK's)	4×10^{-6}
Number of WSK's from neutral current events	0.24

A similar calculation for the charged-current events which have no identified muon adds another 0.06 events, bringing the total WSK interaction background to 0.30 events.

There is a good possibility of reducing this WSK background even further, based on a promising approach now under study in Japan. WSK events are studied under very high magnification, looking for evidence of very short tracks from nuclear breakup or Auger electrons. This minute scrutiny will be possible in P803 because of the very small number of final candidates. Preliminary studies indicate that an additional reduction factor of as much as 7 in WSK background may be obtained in this manner.

5. Summed backgrounds. The estimated backgrounds from all sources with the specified set of cuts are summarized in Table 6. The total estimated background

is 0.47 events; from Fig. 19, if this many events are seen and subtracted, the 90% confidence level on a null signal is 2.8 events.

TABLE 6.

Estimated Background Contributions

Source of Background	# Events
Strange particle decays	< 0.01
Direct ν_τ	0.07
Anticharm decays	0.10
White star kinks	0.30
TOTAL	0.47

D. Oscillation Limits

The detection efficiency ϵ for τ decay events which meet the scan and kink selection criteria depends on the decay mode. Multiprong modes are rejected completely; the efficiencies for the remaining kink modes, averaged over the energy spectrum of produced τ's, are summarized below. The energy dependence of the detection efficiency of the sum of these modes is shown in Fig. 3b, and the neutrino energy spectrum for detected τ's is shown in Fig. 25. The $\mu^-\nu_\tau\overline{\nu_\mu}$ mode has a low efficiency because of the additional cuts needed to suppress the number of charged current events to be scanned.

TABLE 7.

Efficiency for Detected τ^- Decay Modes

Decay Mode	**Branching Ratio**	**Efficiency**	**BR×Effic.**
$\mu^-\nu_\tau\overline{\nu_\mu}$	0.178	0.106	0.0189
$e^-\nu_\tau\overline{\nu_e}$	0.175	0.232	0.0406
$\pi^-\nu_\tau$, $K^-\nu_\tau$	0.115	0.391	0.0450
$\rho^-\nu_\tau$	0.226	0.274	0.0619
$\pi^-\nu_\tau$ multi-γ	0.162	0.257	0.0416
Total			0.21

The factor C in Section A is the product of the common constant efficiency factors (0.64) and the beam-averaged product of relative τ production cross section (0.29) and detection efficiency (0.21), giving $C = 0.039$, $C \cdot N_{CC} = (0.039) \cdot (1.5 \times 10^6) = 5.8 \times 10^4$.

Using the 90% confidence level limit of 2.8 events above the estimated background, we find

$$P(\nu_\mu \rightarrow \nu_\tau) \leq \frac{N_\tau}{C \cdot N_{CC}} = \frac{2.8}{5.8 \times 10^4} = 4.8 \times 10^{-5}.$$

This is a factor of 40 more sensitive than the E531 limit [5] of 2×10^{-3}.

A similar calculation can be done for $\nu_e \leftrightarrow \nu_\tau$ oscillations, using the beam-simulation estimate of 0.82% ν_e in the beam; in the actual experiment, the ν_e flux will be measured. Because the average energy of ν_e's is higher than that of ν_μ, we obtain a larger C, $C_{\nu_e} = 0.097$, and

$$P(\nu_e \rightarrow \nu_\tau) \leq= \frac{2.8}{(0.097) \cdot (0.0082) \cdot (1.5 \times 10^6)} = 2.3 \times 10^{-3}.$$

This is 30 times as sensitive as the corresponding E531 limit.

$P(\nu_\mu \rightarrow \nu_\tau)$ may be interpreted in terms of a two-component representation of neutrino oscillations:

$$P(\nu_\mu \rightarrow \nu_\tau) = \sin^2(2\alpha) \int \rho(\frac{L}{E}) \sin^2(1.27 \delta M^2 \frac{L}{E}) d\frac{L}{E}$$

where ρ gives the normalized flux of neutrinos in terms of the variable (L/E), L is the neutrino flight path in meters, E the neutrino energy in MeV and δM^2 the neutrino mass difference squared in $(eV)^2$. For large δM^2 the oscillation length is small compared to the variation in neutrino flight length, and the (L/E) integral has an approximate value of 0.5; the P803 mixing angle sensitivity for $\nu_\mu \leftrightarrow \nu_\tau$ in the large-mass limit is then 9.6×10^{-5} at 90% CL. The corresponding plots of P803 $\sin^2(2\alpha)$ sensitivity versus δM^2 for both ν_μ and ν_e are shown in Fig. 1 along with existing ν_μ limits.

E. Observing a Signal

Because the estimated background is so small (0.5 event), and because all sources of background except beam dump ν_τ's are directly measureable, this experiment has an excellent opportunity to establish a signal if one exists at a level a few times higher than this limit. The scatterplots in Fig. 26 illustrate the power of the two-dimensional decay length and kink p_T distributions in separating a signal from the dominant WSK background. If 4 or 5 events are actually observed in the rectangle marked in that figure (which delineates the cuts of Table 3), most of these candidates should remain when the rectangle is shrunk to reduce the background by a factor of 5 or more.

VI. RESOURCES

A preliminary estimate of costs is given in the next section. We comment on some items here.

A. Fiber Development

Although no item is included in the cost estimates, a program in optical fiber development complementary to that in Japan would be most useful both for this experiment and for others.

B. Computing

Online data acquisition is rather trivial; present computing and acquisition techniques are more than adequate to log two events per spill. Offline requirements are similarly modest by present-day standards. To achieve the desired rate of much less than one triggered event per spill, the overall number of triggers must be well under 3 million. Most non-data triggers can be deleted quickly, leaving perhaps a million events which will require detailed processing. Typically, these events will have far fewer tracks than in E653, a previous hybrid emulsion-electronic experiment, but will have additional complications due to curvature in a magnetic field. If we assume the same per-event level of difficulty, 5 user-owned VAX3200 workstations could reconstruct the entire experiment in 2-3 months.

However, computing would be labor intensive. Developing offline software would require at least 5 man-years over a two year period of calendar time.

C. Emulsion Processing

It will be important to reconstitute the Fermilab Emulsion Pouring and Processing Laboratory used during E653. Some fraction of the emulsion must be analyzed during exposure in order to monitor emulsion quality, track backgrounds, etc., as a function of time.

D. Civil Construction

This issue will be addressed fully in an upcoming Fermilab Conceptual Design Report for Main Injector neutrino experiments. A preliminary layout for civil construction in one of the possible P803 locations is provided in Fig. 27.

VII. PRELIMINARY COST ESTIMATES

(Costs are preliminary estimates made by proponents, and will be reviewed in the Conceptual Design Report)

A. FERMILAB COSTS

1. Costs for Neutrino Beam and Experimental Area:

(These costs will be included in a Fermilab Conceptual Design Report which will include all proposed neutrino experiments)

2. Data acquisition and PREP costs:

a)	Miscellaneous PREP electronics	$ 300K
	SUBTOTAL	$ 300K

3. Upgrading Emulsion Pouring Facility:

a)	Restoring E653 capacity	$ 100K
	SUBTOTAL	$ 100K
	FERMILAB NONBEAM AND EXPT'L AREA	$ 400K
	30% CONTINGENCY	$ 120K
	TOTAL FERMILAB NONBEAM AND EXPT'L AREA	$ 520K

B. EXPERIMENTAL APPARATUS COSTS:

1)	**Emulsion**; Two hundred liters @$12K/liter, incl. processing and developing.	$ 2400K
2)	**Scintillating fibers**; 1.8 $\times 10^6$ channels.	$ 750K
	Readout; 6 image intensifier tubes @$25K/tube ($150K) Fibers; 4 $\times 10^6$ meters of fibers @$0.10/meter ($400K) R & D ($200K)	
3)	**Drift chambers**, 18 @$25K each	$ 450K

4) **Drift chamber electronics** $ 766K

(The cost of $50/channel for 15324 channels is based on those for E653, a previous experiment, as the present design is not yet complete)

5) **Emcal chamber construction** $ 216K

Lead ($26K)
Plastic tubings ($22K)
Readout boards ($18K)
Hardware ($12K)
Container ($24K)
Tooling ($12K)
Labor ($90K)
Misc. ($12K)

6) **Emcal electronics**, 12440 Channels@$40/Channel $ 498K

Item and price per 16 channels

Preamp Hybrid ($160)
AD684 ($94)
AD508AKN ($8)
faster version of AD7672 ($60)
IDT7200 ($18)
XC3030 ($90)
Misc. parts ($15)
Circuit Board ($90)
Stuffing ($40)
Power Supplies ($50)
Cables ($15)

Cost/channel ($40)

7) **Hadcal chamber construction** $ 540K

Zinc, 300,000lb @ $1.1/lb. ($330K)
Plastic inner and outer sleeves ($18K)
Plastic profiles ($15K)
Readout boards ($35K)
Hardware ($15K)
Tooling ($15K)
Labor ($100K)
Misc. ($12K)

8) **Hadcal Electronics** $ 393K

9832 Channels @ $40/channel

9)	**Overall mechanical support structure**	\$ 60K
10)	**24 veto hodoscope scintillating counters**	\$ 47K
	(Each 6 in × 12 ft with tubes at each end, plus \$5K for stand)	
11)	**First hodoscope plane inside field, 20 counters**	\$ 65K
	(Each 4 in × 78 in with tubes at each end and Winston cone lightpipes, plus \$5K for stand)	
12)	**Second hodoscope plane inside field, 37 counters**	\$ 127K
	(Each 4 in × 145 in with tubes at each end and Winston cone lightpipes, plus \$5K for stand)	
13)	**Smart Trigger and Data Acquisition**	\$ 100K
14)	**On-line Computing**	\$ 80K
	(VAX3200 or equivalent with 16 MB memory, a gigabyte of disk storage and two magnetic tape units)	
15)	**Off-line computing,** 5 existing VAX3200's, or equivalent.	(\$ 150K)
	SUBTOTAL, NEW COSTS	\$ 6492K
	30% Contingency	\$ 1948K
	TOTAL NEW EXPT'L APPARATUS COSTS	\$ 8440K

Note on ADC and TDC systems: Analogue signals from the calorimeters will be amplified and stretched; resulting analogue outputs will be sampled and held locally to the detectors. Local analogue multiplexing and daisy-chaining of digital outputs will be employed to minimize cabling. The design for drift chamber electronics is less well developed. Outputs also will be stored locally, but whether this will be done in analogue or digital format depends on the availability of commercial components.

Note on funding: We request that Fermilab play a substantial role in the funding for experimental apparatus costs.

References

[1] See, e.g., H. Harari, Phys. Lett. B216, 413 (1989).

[2] L. Wolfenstein, Phys. Rev. D17, 2369 (1978).

[3] S. P. Mikheyev and A. Yu. Smirnov, Sov. J. Nucl. Phys. 42, 913 (1985).

[4] G. S. Abrams, *et al.*, Phys. Rev. Lett. **63**, 2173 (1989); LEP results in press.

[5] N. Ushida, *et al.*, Phys. Rev. Lett. **57**, 2897 (1986).

[6] F. Dydak, *et al.*, Phys. Lett. **134B**, 281 (1984).

[7] The possibility of making these measurements was suggested to the proponents of P803 by R. Brock. In his review presentation at the 1989 Fermilab Workshop at Breckenridge, Brock also stated that slow rescaling uncertainties were a limiting systematic uncertainty in present determinations of $\sin^2(\theta_W)$ from deep inelastic scattering of neutrinos.

[8] C. Foudas, *et al.*, Phys. Rev. Lett. **64**, 1207 (1990); M. Shaevitz, Lectures at the 1989 SLAC Summer Institute.

[9] J. Cudell, F Halzen and S. Pakvasa, Phys. Rev. **40D**, 1562 (1989).

[10] G. Altarelli, "Tests of QCD", Ann. Rev. Nucl. Part. **39**, 366 (1989).

[11] S.R. Mishra and F. Sciulli, "Deep Inelastic Lepton-Nucleon Scattering", Ann. Rev. Nucl. Part., **39**, 259 (1989).

[12] S. R. Mishra, *et al.*, "Improved Measurement of Inverse Muon Decay at the Fermilab Tevatron", Nevis Preprint 1424 (1990).

[13] A. Gauthier, Ph.D. thesis, The Ohio State University, (1987).

[14] N. Ushida, *et al.*, Nuc. Instr. and Meth. **224**, 50 (1984).

[15] K. Kodama, *et al.*, Nuc. Instr. and Meth. **A289**, 146 (1990).

[16] A. E. Brenner, *et al.*, Phys. Rev. D26, 1497 (1982).

[17] D. S. Barton, *et al.*, Phys. Rev. D27, 2580 (1983).

[18] (AMY collaboration) K. Ueno, *et al.*, preprint (1990).

[19] R. Rusack, private communication.

[20] M. Atac, to be presented at the Atlanta SSC Conference (1990), and private communication.

[21] S. Aoki, Ph.D. Thesis, Nagoya University (1990); S. Aoki, *et al.*, submitted to Nuclear Instruments and Methods.

[22] A. Abashian, *et al.*, "The AMY Barrel Electromagnetic Shower Counter at TRISTAN", draft preprint (1990); A. Abashian, private communication.

[23] R. Baldini, *et al.*, Nuc. Instr. and Meth. **A251**, 449 (1986).

[24] C. Rosenfeld, private communication.

[25] Particle Data Group, Phys. Lett. **B204**, (1988).

[26] M. Duffy, *et al.*, Phys. Rev. **D38**, 2032 (1988).

[27] S. Hasegawa, *et al.*, Prog. Theor. Phys. Suppl. **47**, 126 (1971).

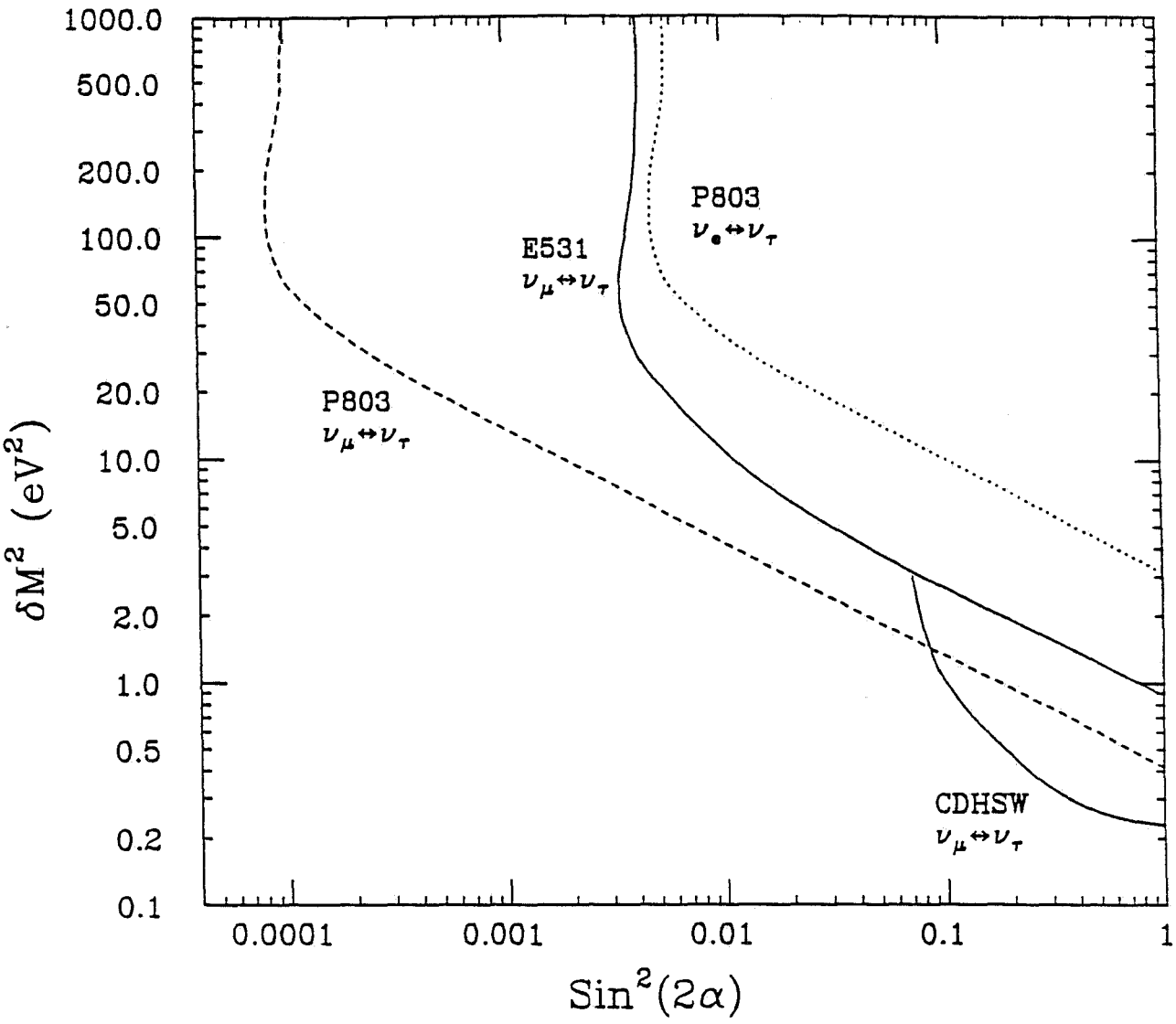

FIGURE 1. δM^2 versus $\sin^2(2\alpha)$ plane showing the previous limits for $\nu_\mu \leftrightarrow \nu_\tau$ oscillation (solid curves), and the improved limits on $\nu_\mu \leftrightarrow \nu_\tau$ (dashed) and $\nu_e \leftrightarrow \nu_\tau$ (dotted) which can be obtained from P803. The regions to the right of the appropriate curves are excluded at the 90% confidence level.

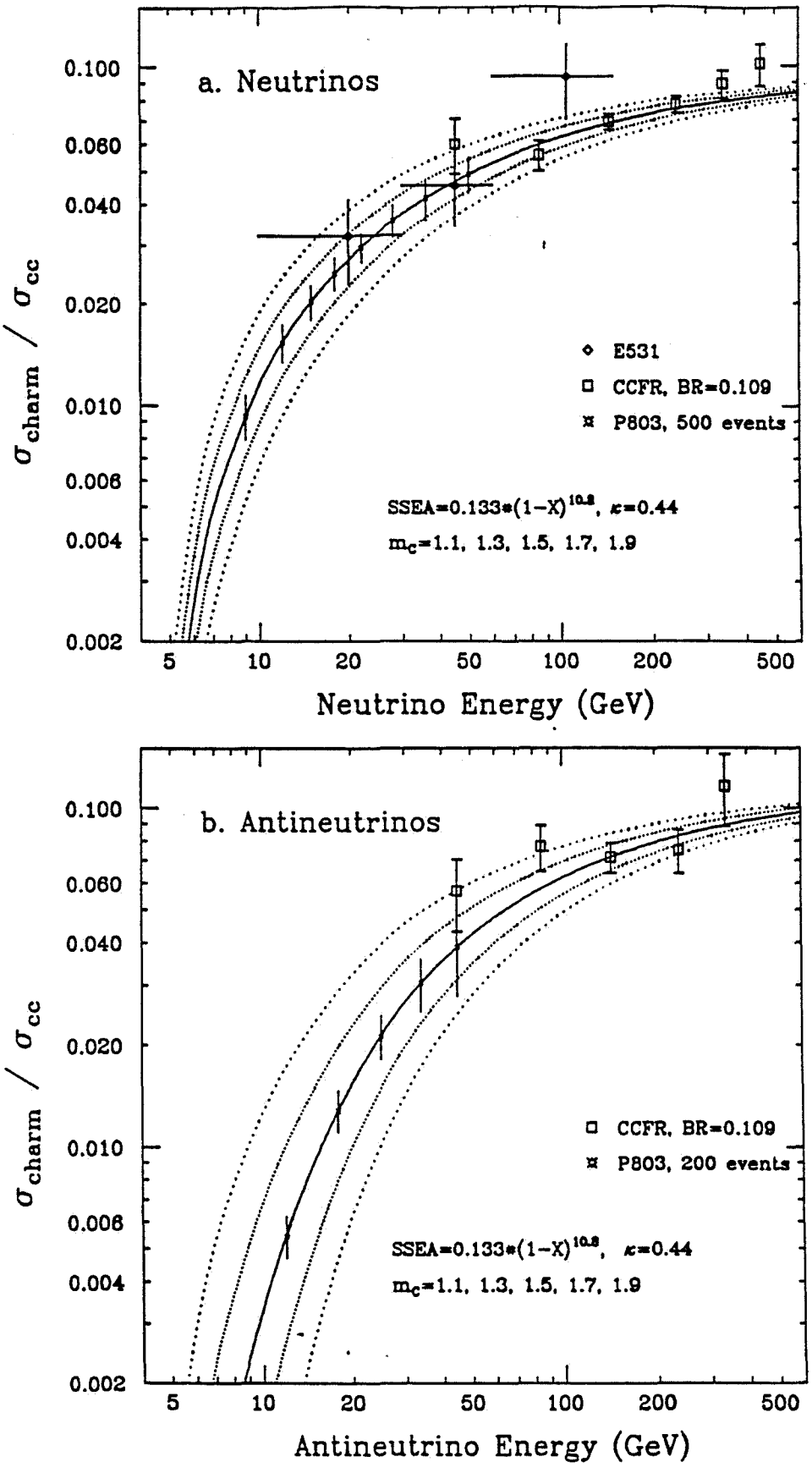

FIGURE 2. The ratio of charm production to charged-current interactions for (a) neutrino, and (b) antineutrino interactions. The impact of 500 neutrino charm events and 200 anti-charm events from P803 is shown.

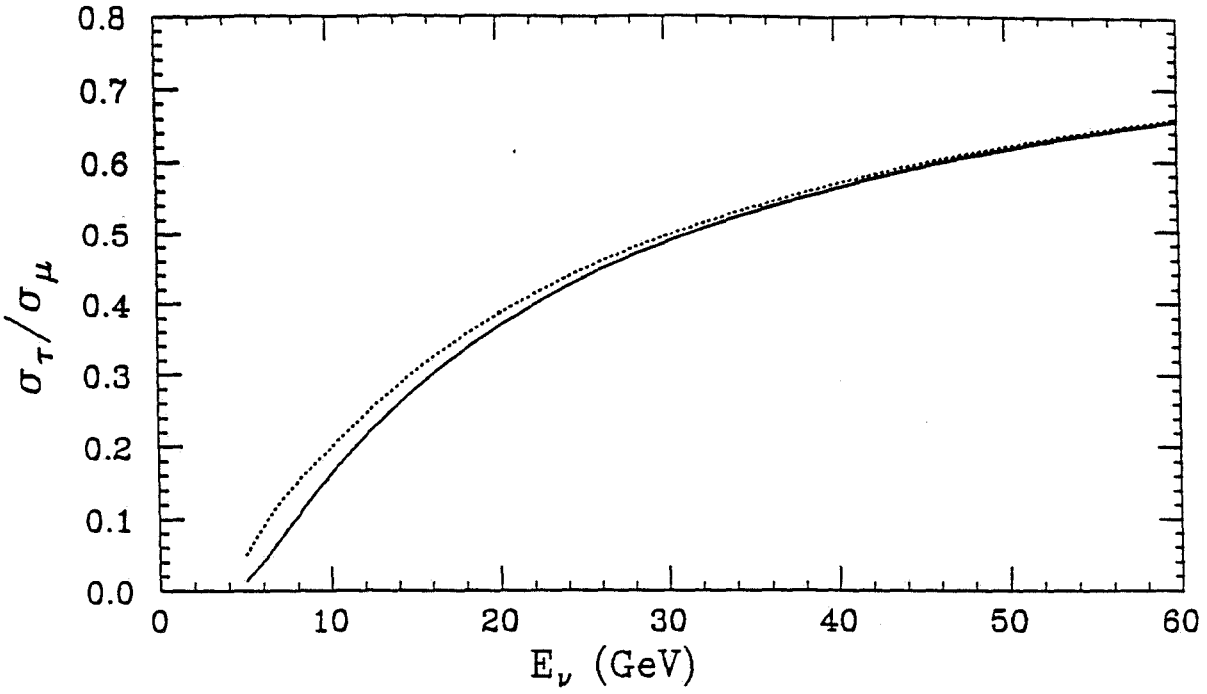

FIGURE 3a. The ratio of ν_τ/ν_μ cross-sections displayed as a function of incident neutrino energy. The solid curve shows the deep inelastic parton model contributions, while the dotted curve includes also quasi-elastic and Δ^{++} contributions to both ν_τ and ν_μ cross-sections.

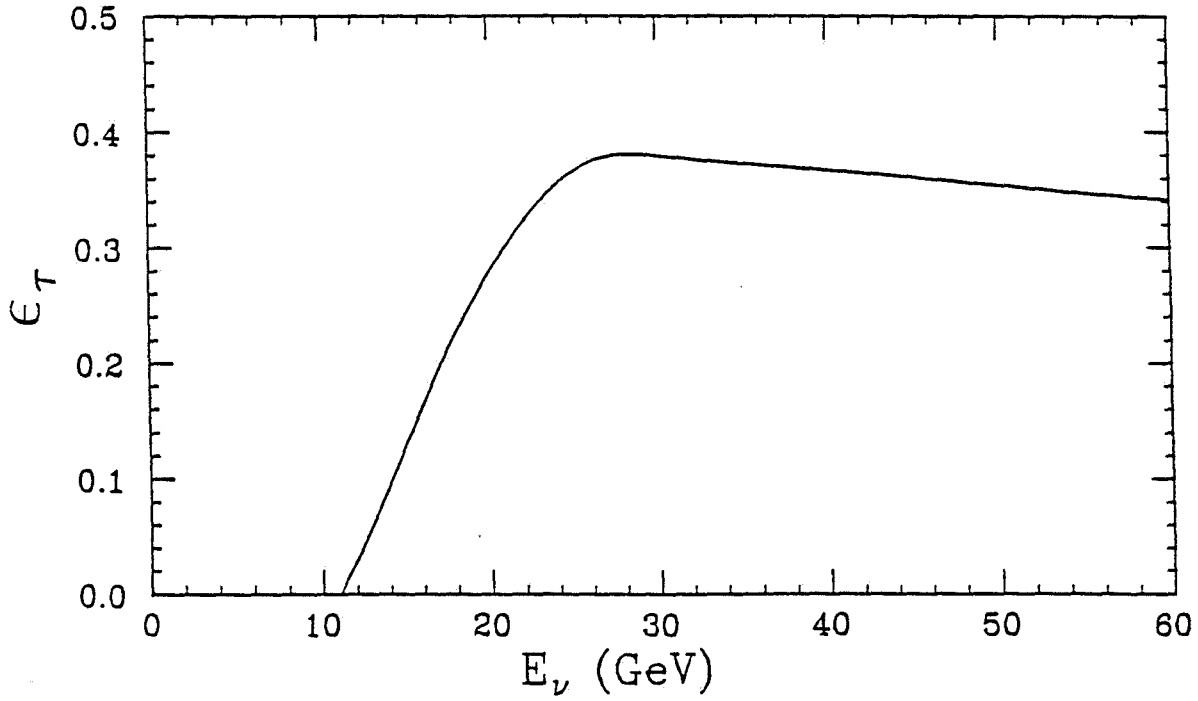

FIGURE 3b. Neutrino energy dependence of τ detection efficiency ϵ after event selection cuts have been applied. Energy-independent efficiency contributions have been suppressed.

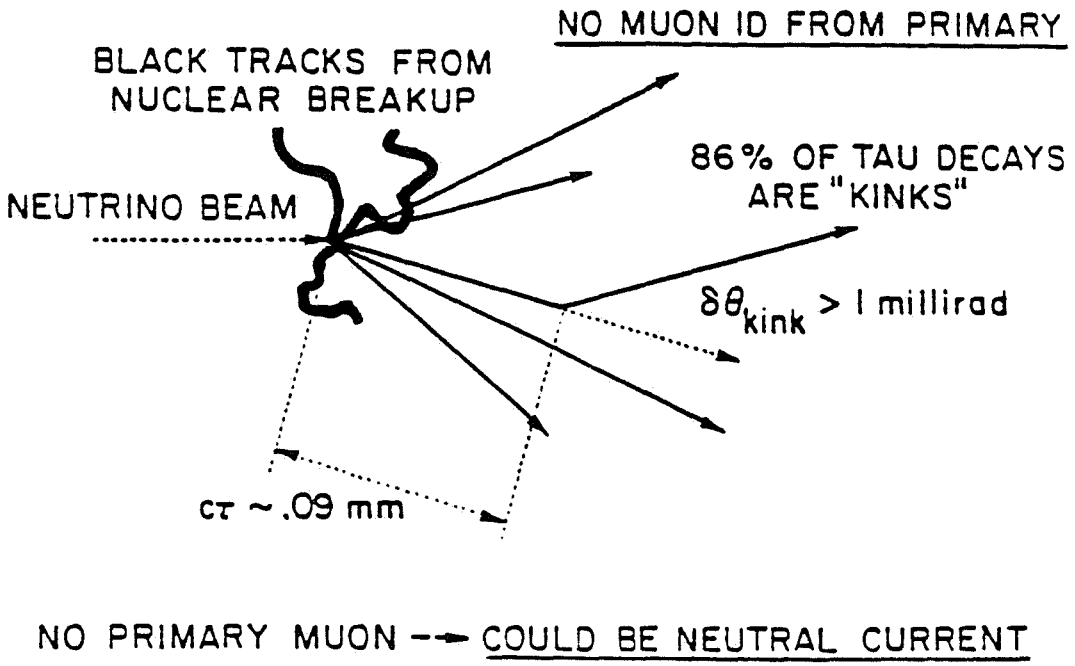

FIGURE 4. Schematic picture of a ν_τ interaction. Note the heavily-ionizing tracks from nuclear breakup, the absence of an identified muon from the interaction vertex and a short decay-length "kink" with a large P_T.

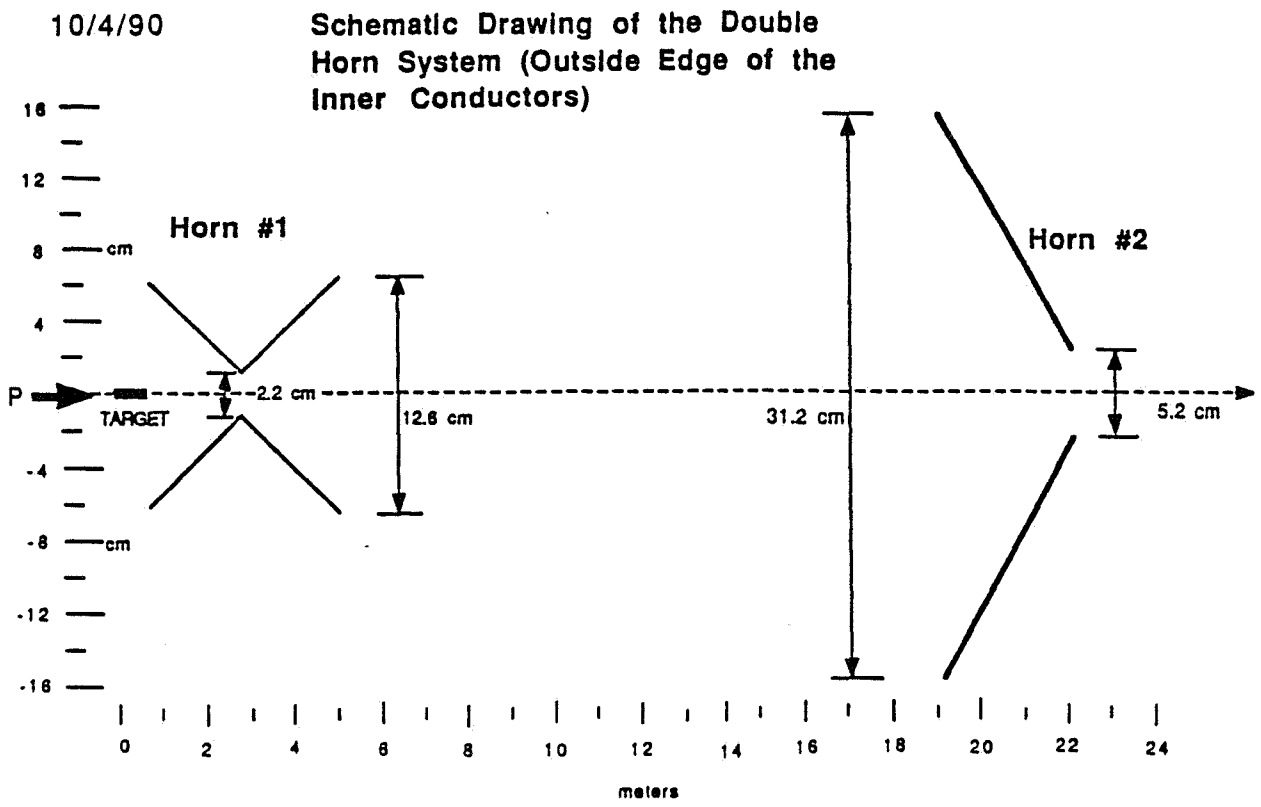

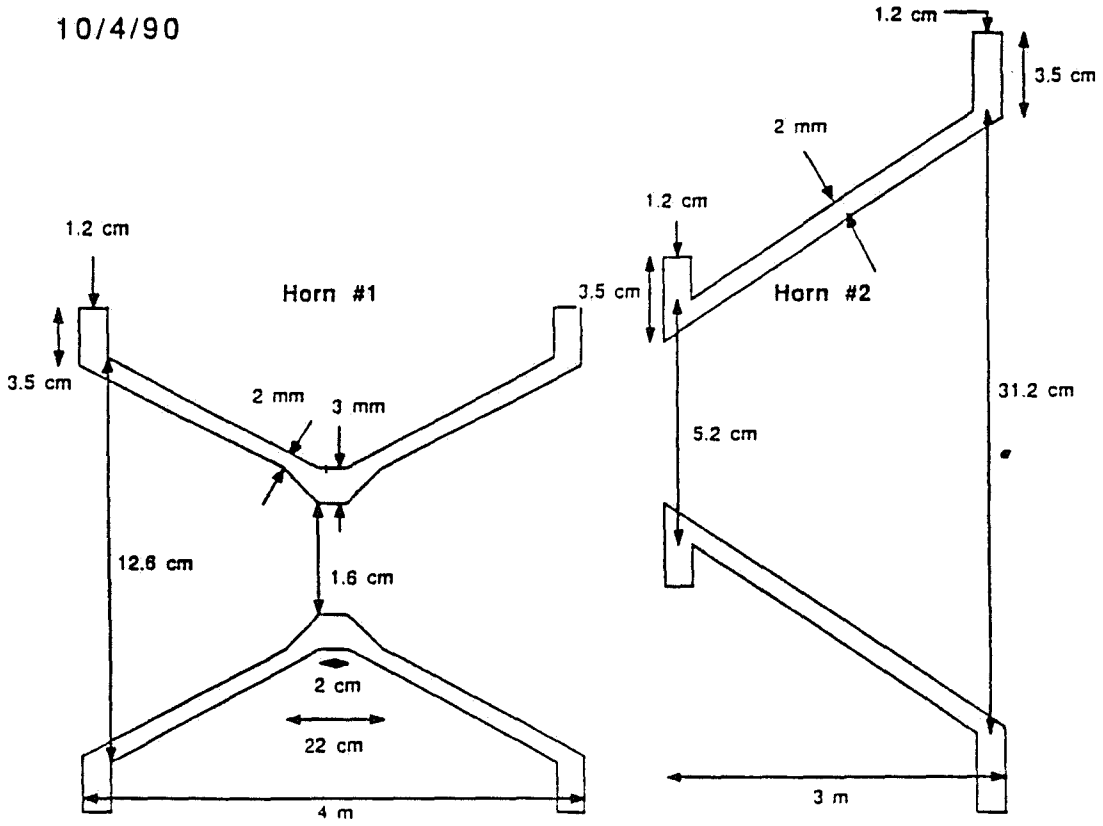

FIGURE 5. Double horn system for the neutrino beam. Upper: schematic drawing, showing placement of components. Lower: Detail, showing thickness of walls.

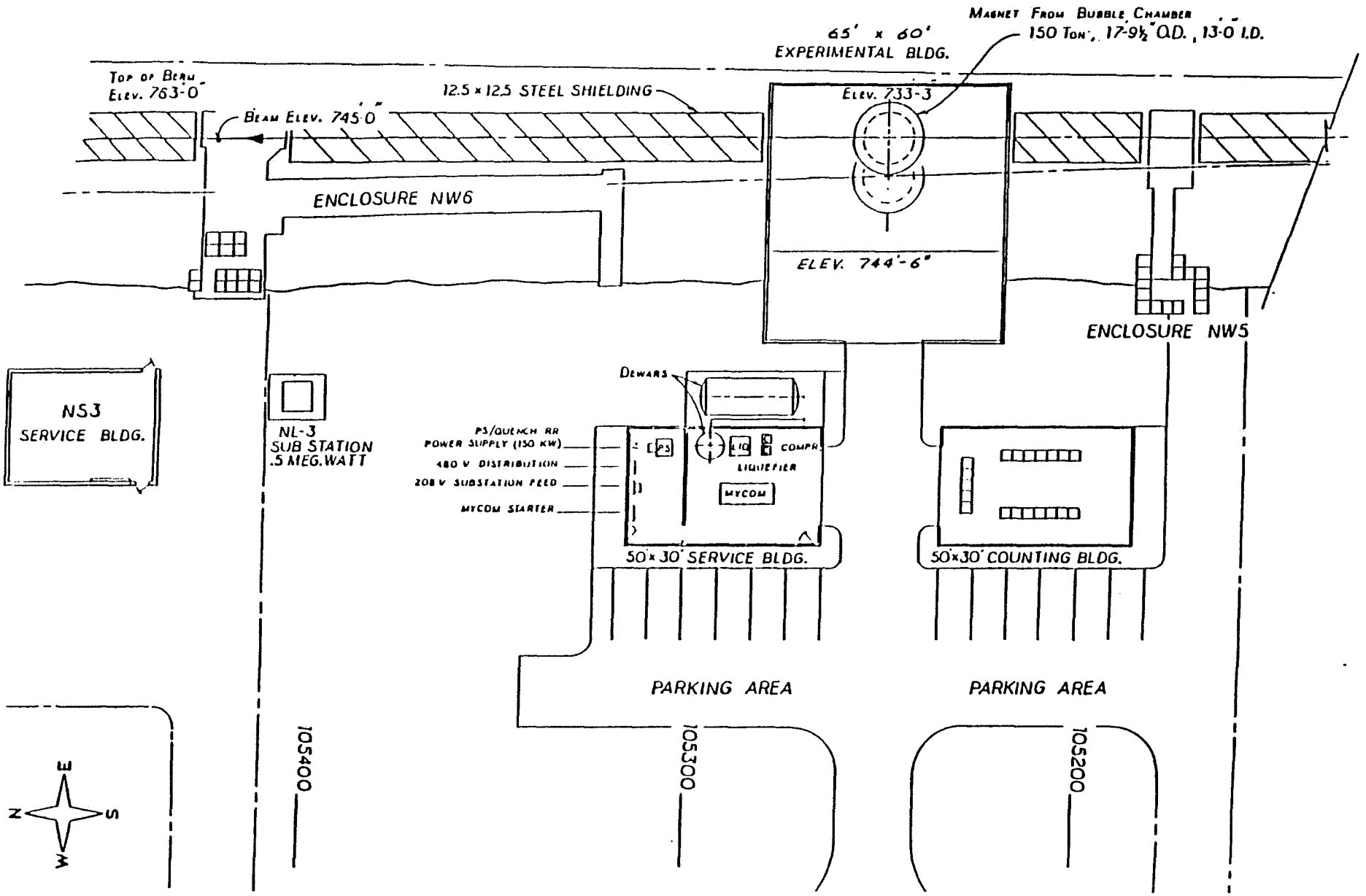

FIGURE 6. Layout of the proposed neutrino beam line showing the location of the oscillation experiment after the construction described in the text is completed.

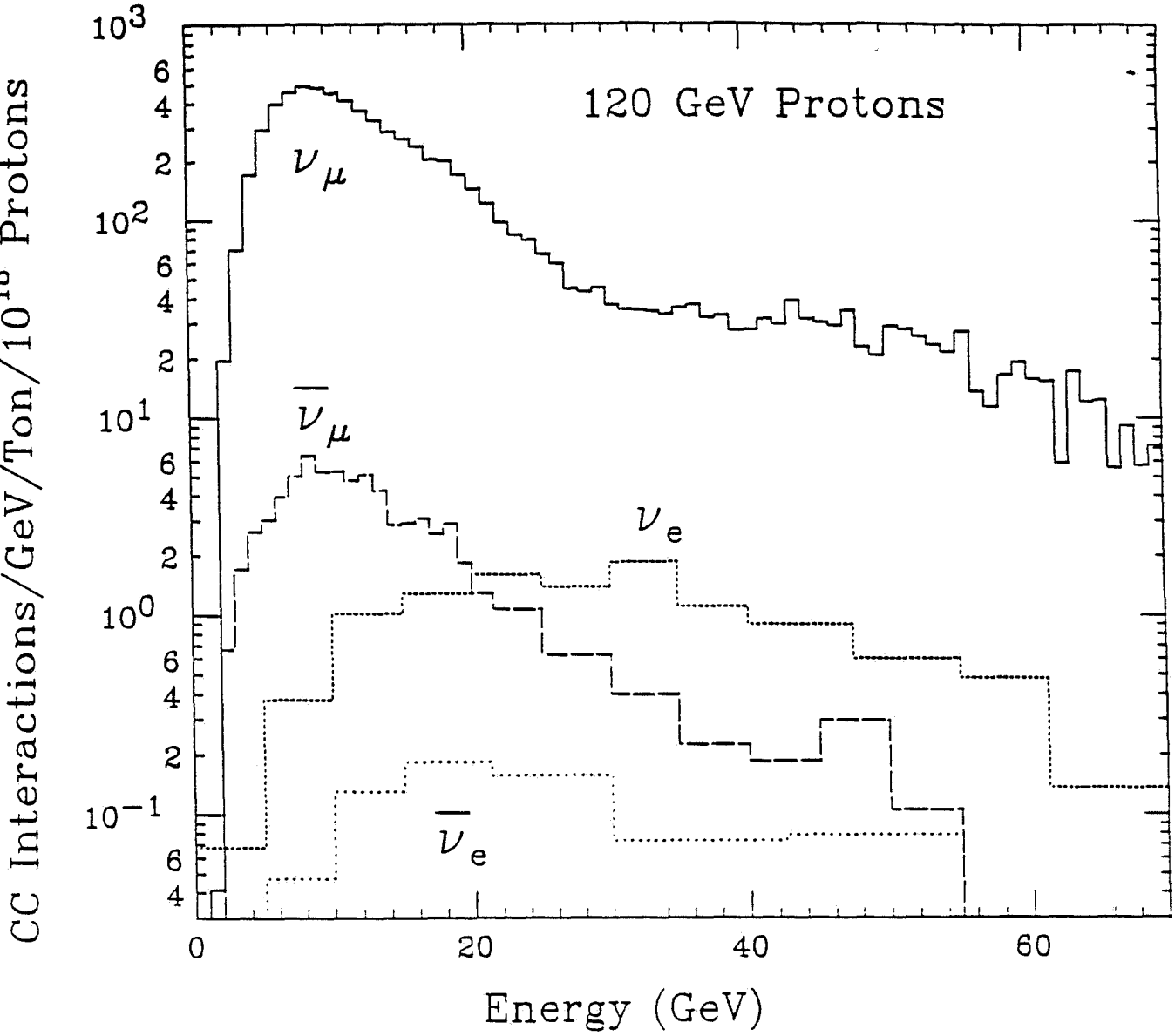

FIGURE 7. Results from a Monte Carlo simulation of the charged-current event rates for ν_μ and ν_e, and for background $\overline{\nu_\mu}$ and $\overline{\nu_e}$, at the P803 detector. The calculation assumes the target, horn and beamline shown in the previous figures and a 120 GeV proton beam with the horn set to focus positively-charged particles.

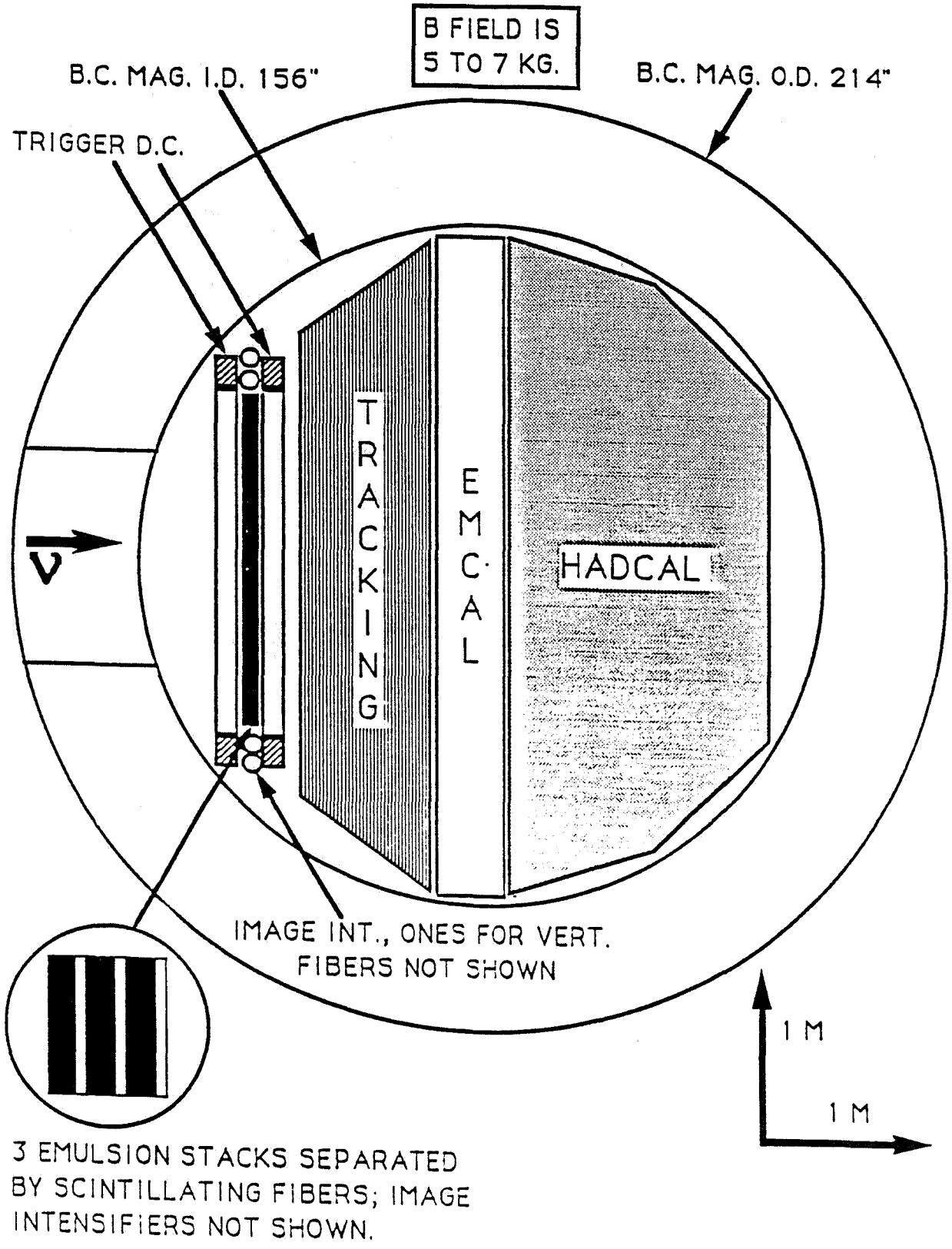

FIGURE 8a. Plan view of the experiment.

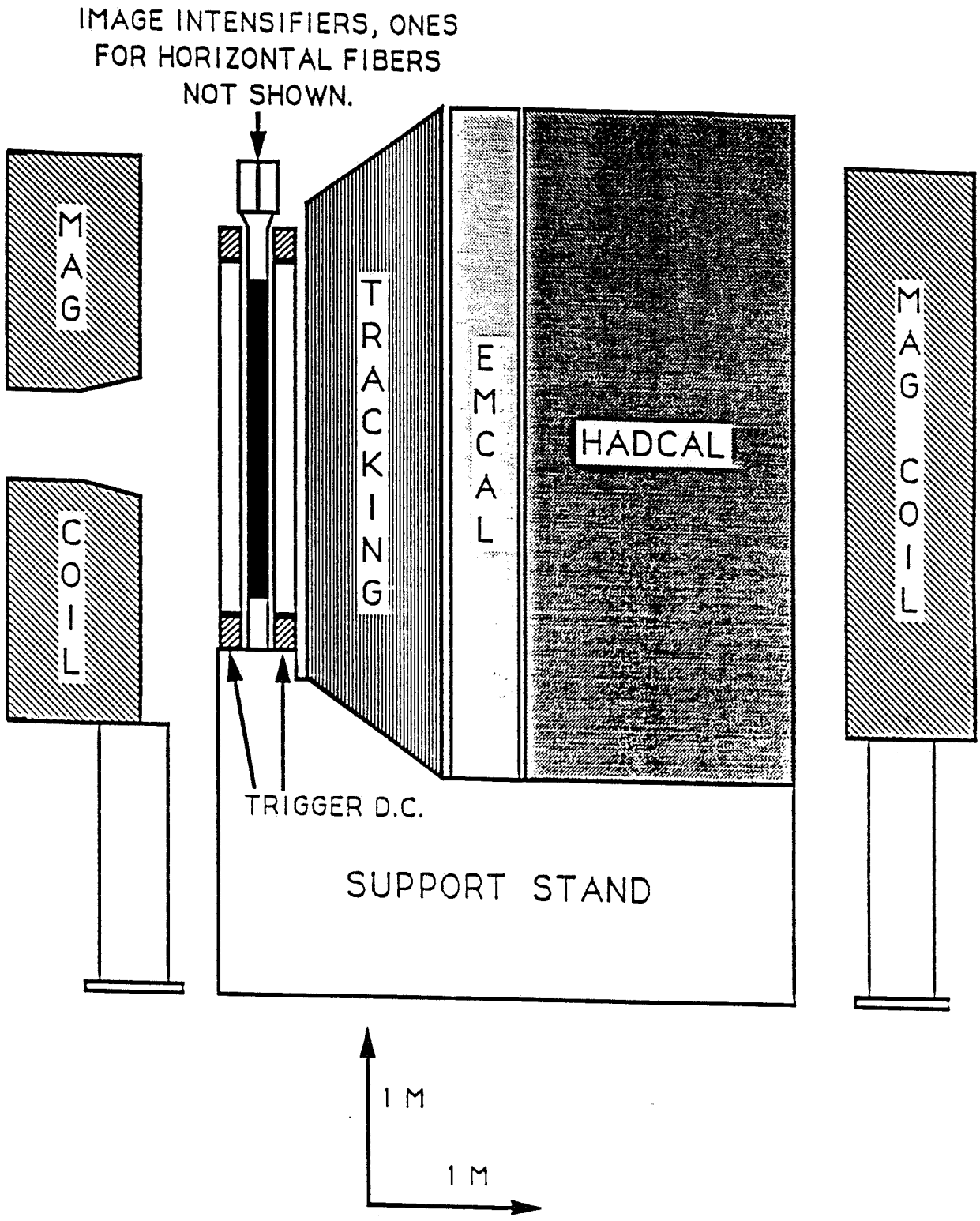

FIGURE 8b. Elevation view of the experiment.

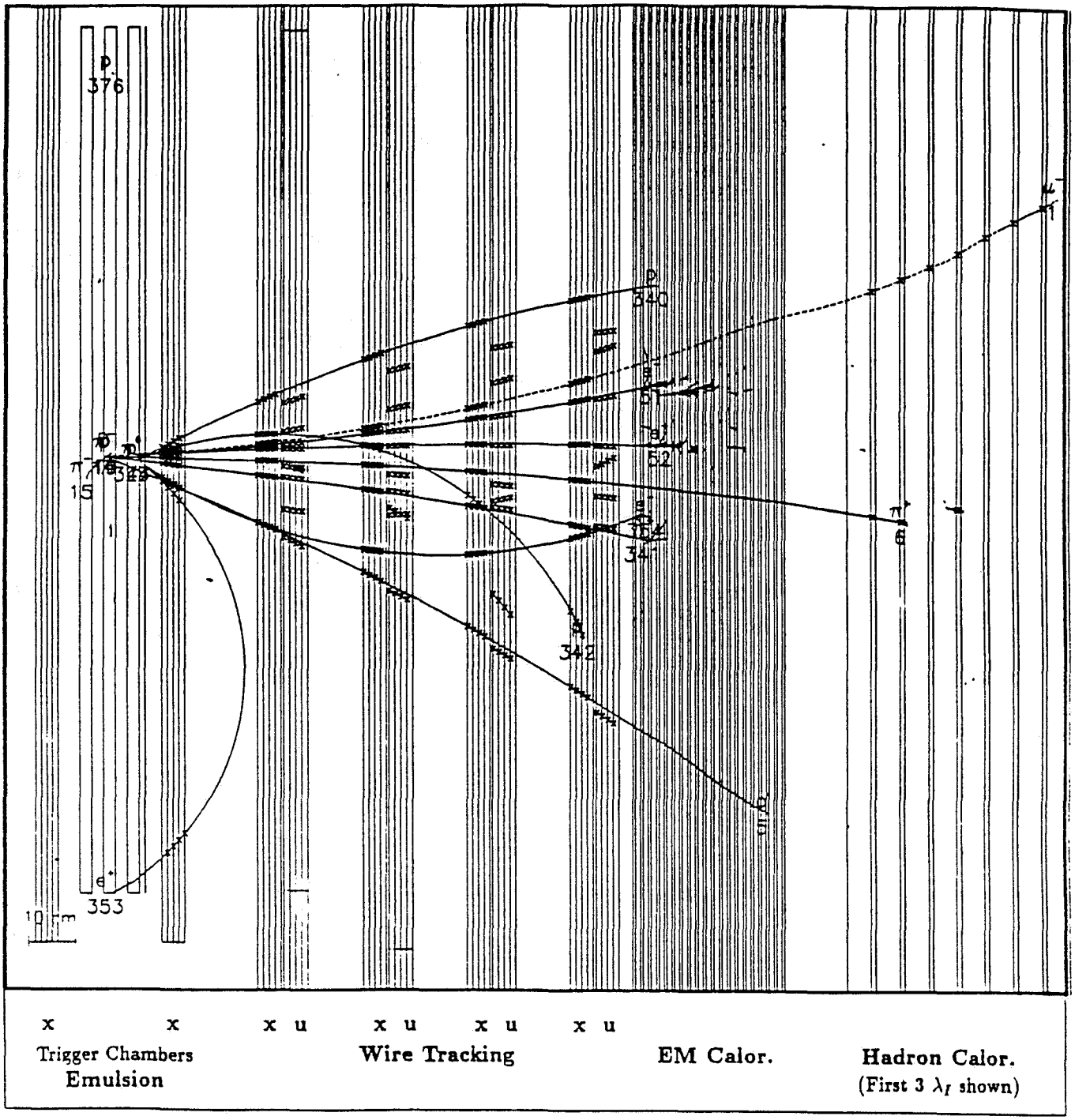

FIGURE 9a. LUND-GEANT simulation of a typical event, as seen in the bend plane of the magnet (x-view). This is a charged-current interaction; the muon is the dashed track.

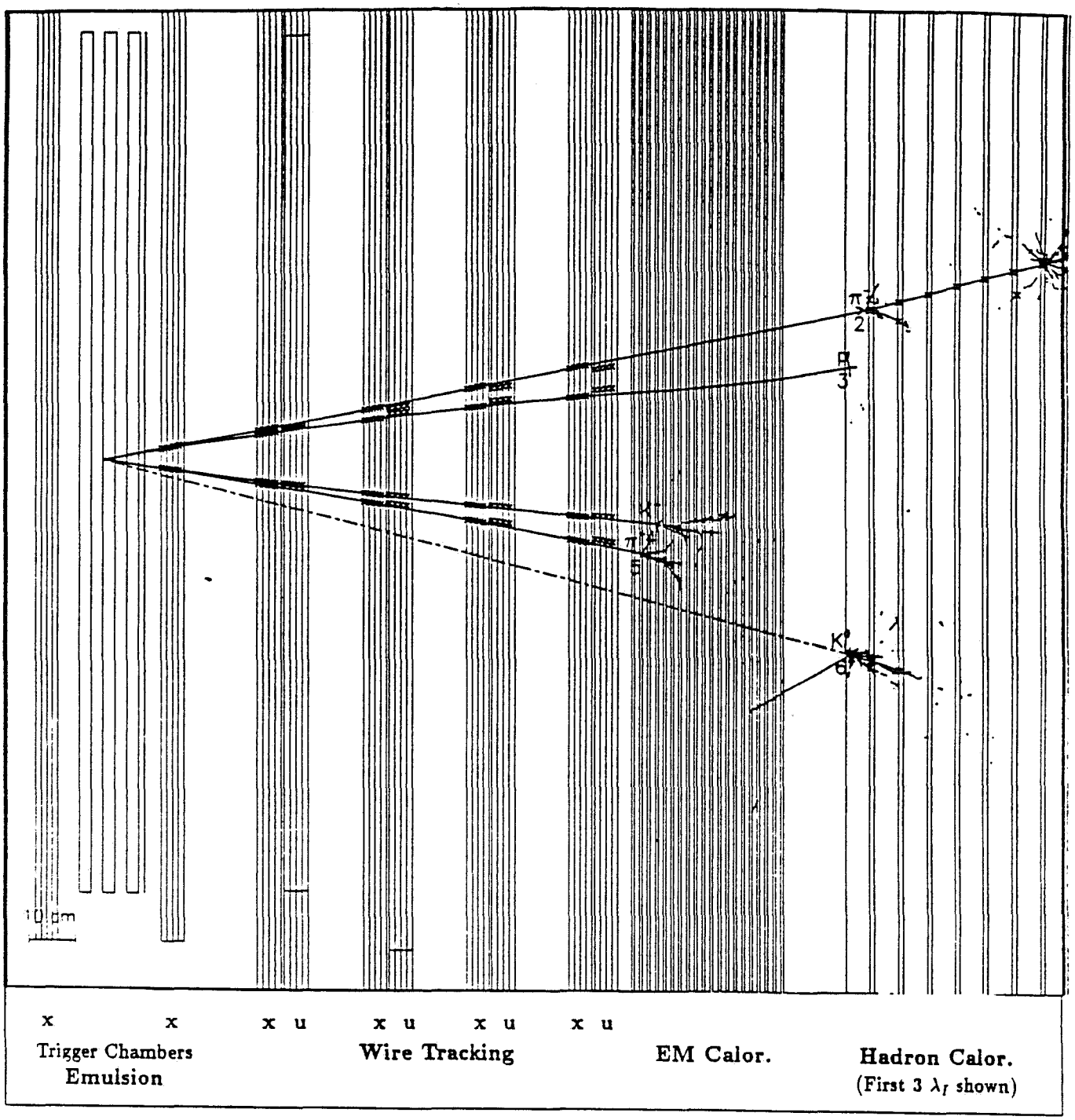

FIGURE 9b. LUND-GEANT simulation of a typical event, as seen in the bend plane of the magnet (x-view). This is a very clean ν_τ event, with $\tau \rightarrow \pi^- \nu_\tau$. Note the absence of a muon.

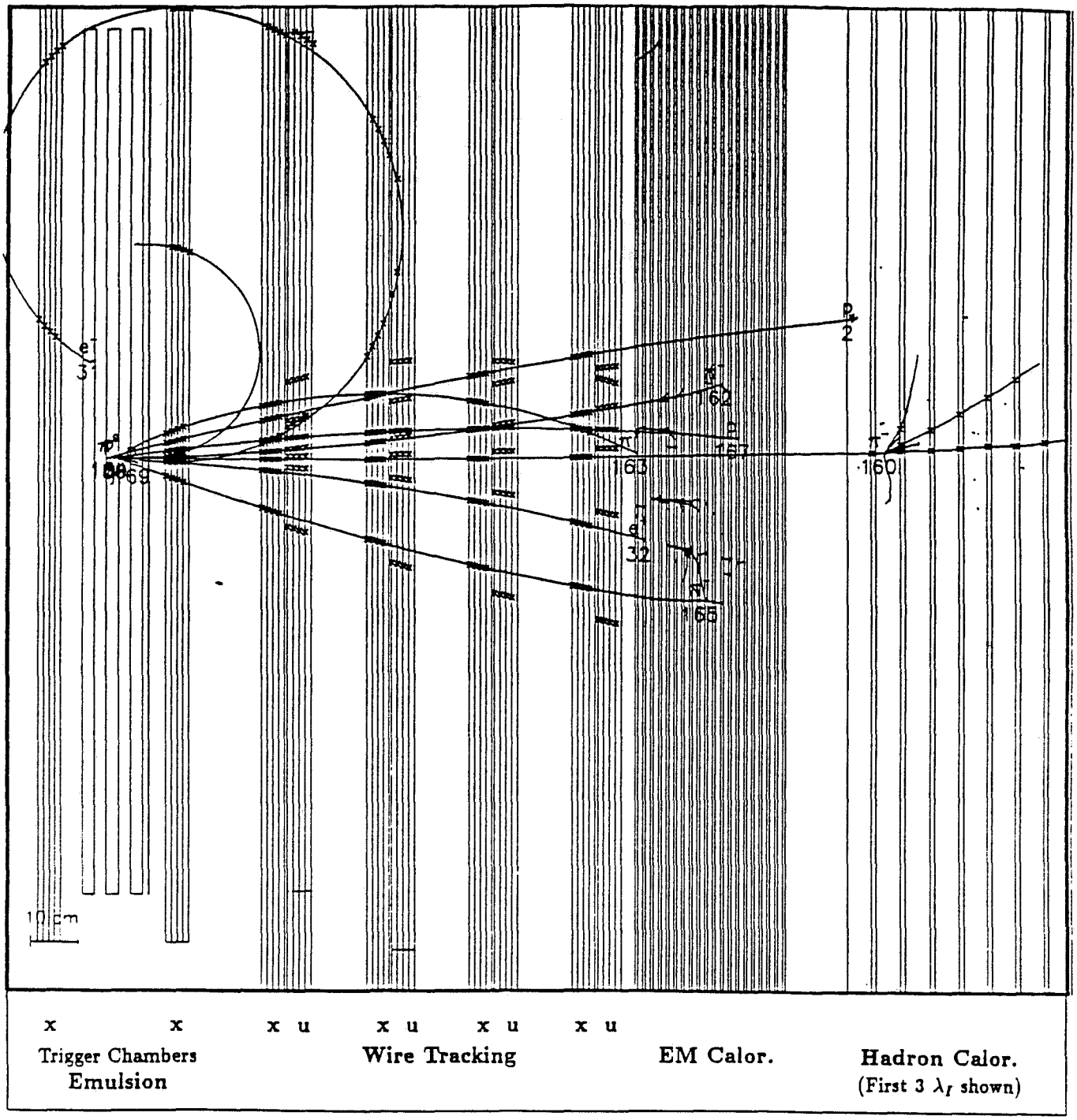

FIGURE 9c. LUND-GEANT simulation of a typical event, as seen in the bend plane of the magnet (x-view). This is a ν_τ event with $\tau \rightarrow \rho^- \nu_\tau$, and $\rho^- \rightarrow \pi^- \pi^0$. One γ shower from the π^0 has converted in the emulsion, and the wire tracking chambers act as a pair spectrometer.

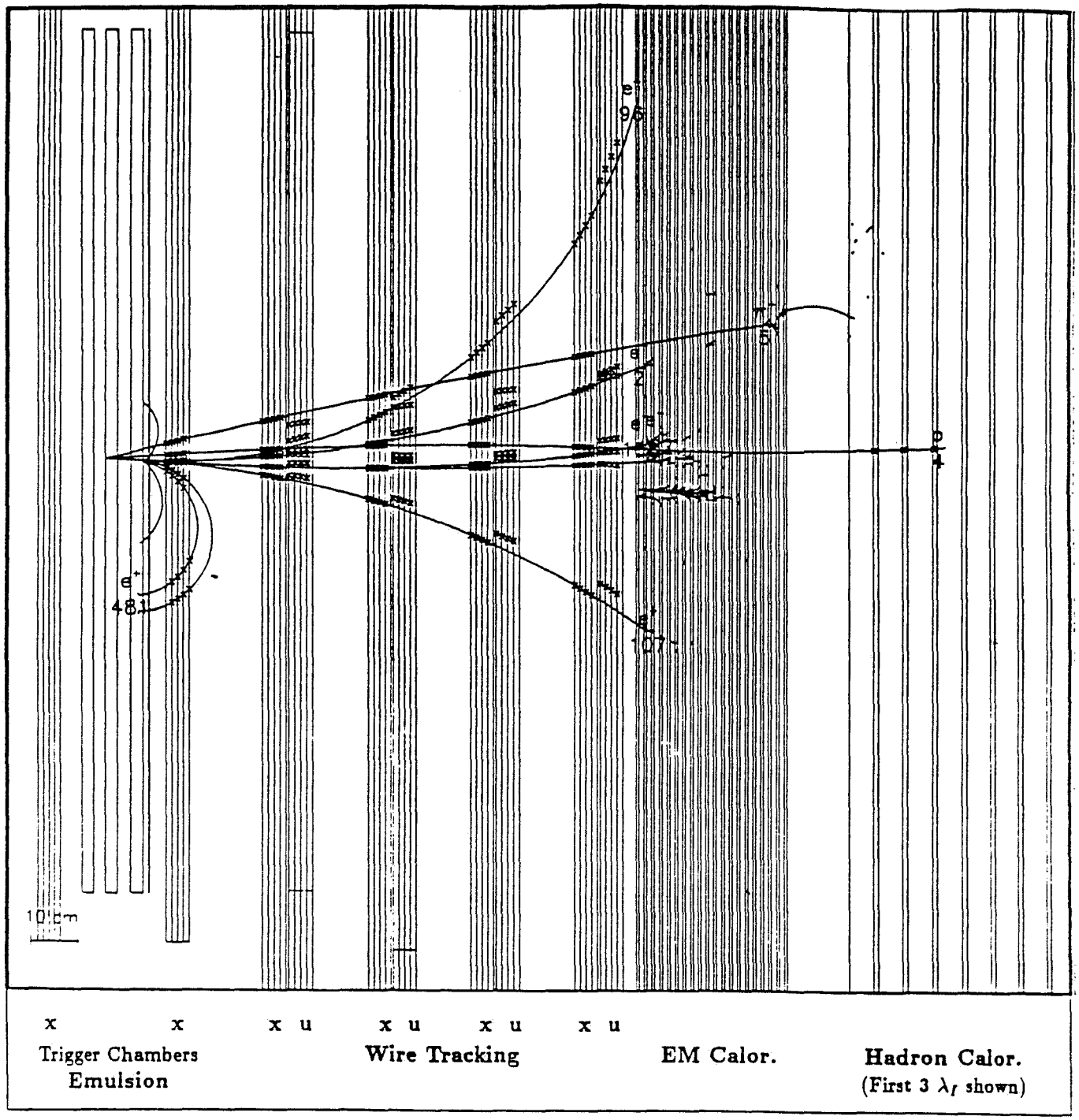

FIGURE 9d. LUND-GEANT simulation of a typical event, as seen in the bend plane of the magnet (x-view). In this ν_τ event $\tau \rightarrow e^- \overline{\nu_e} \nu_\tau$. The electron is identified by its accompanying electromagnetic shower with odd total charge.

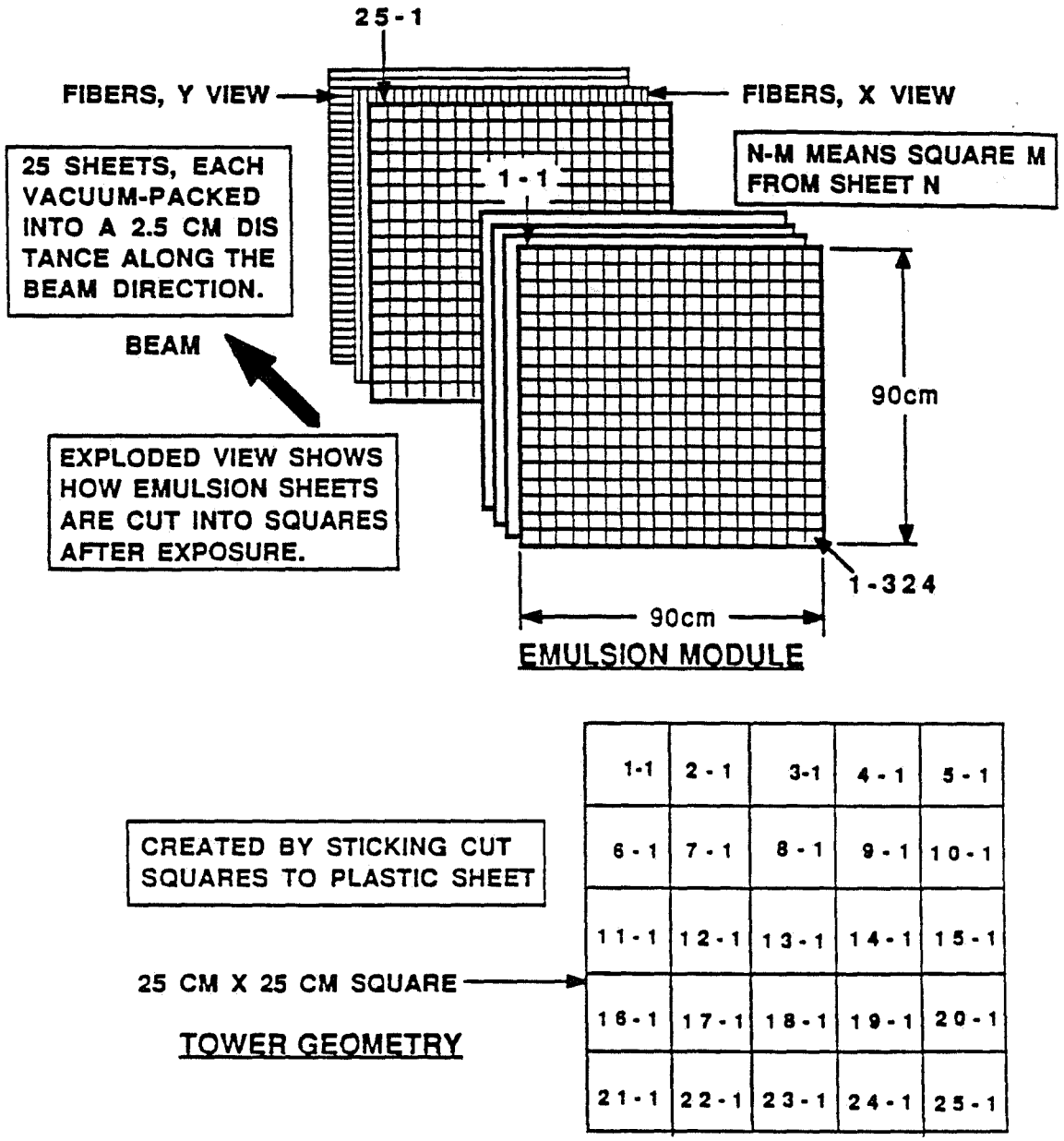

FIGURE 10. Detail of emulsion and scintillating fibers which indicates how a tower geometry will be created during the emulsion developing process in order to speed scanning.

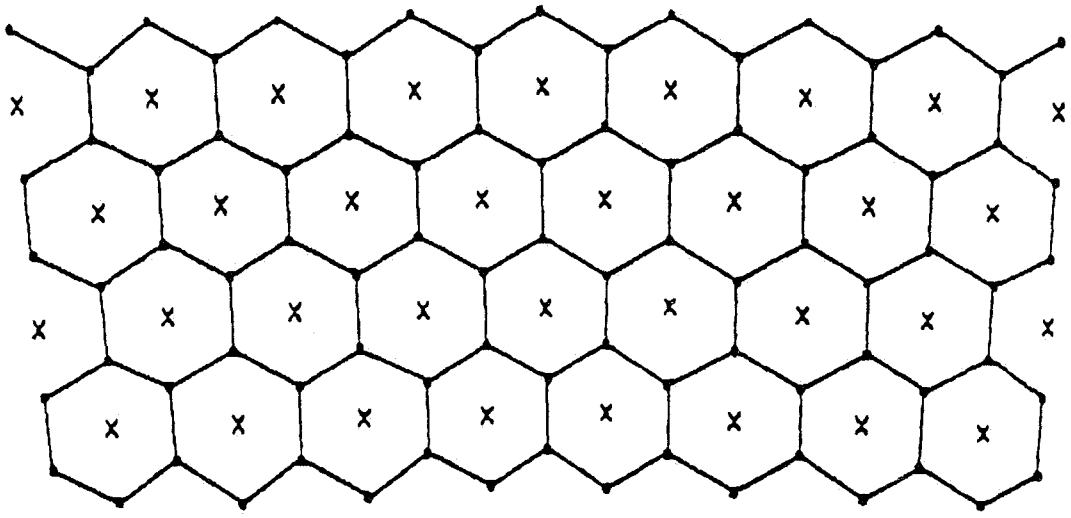

FIGURE 11. The hexagonal cell configuration of a wire chamber module. The spacing between sense wires is 1.2 cm.

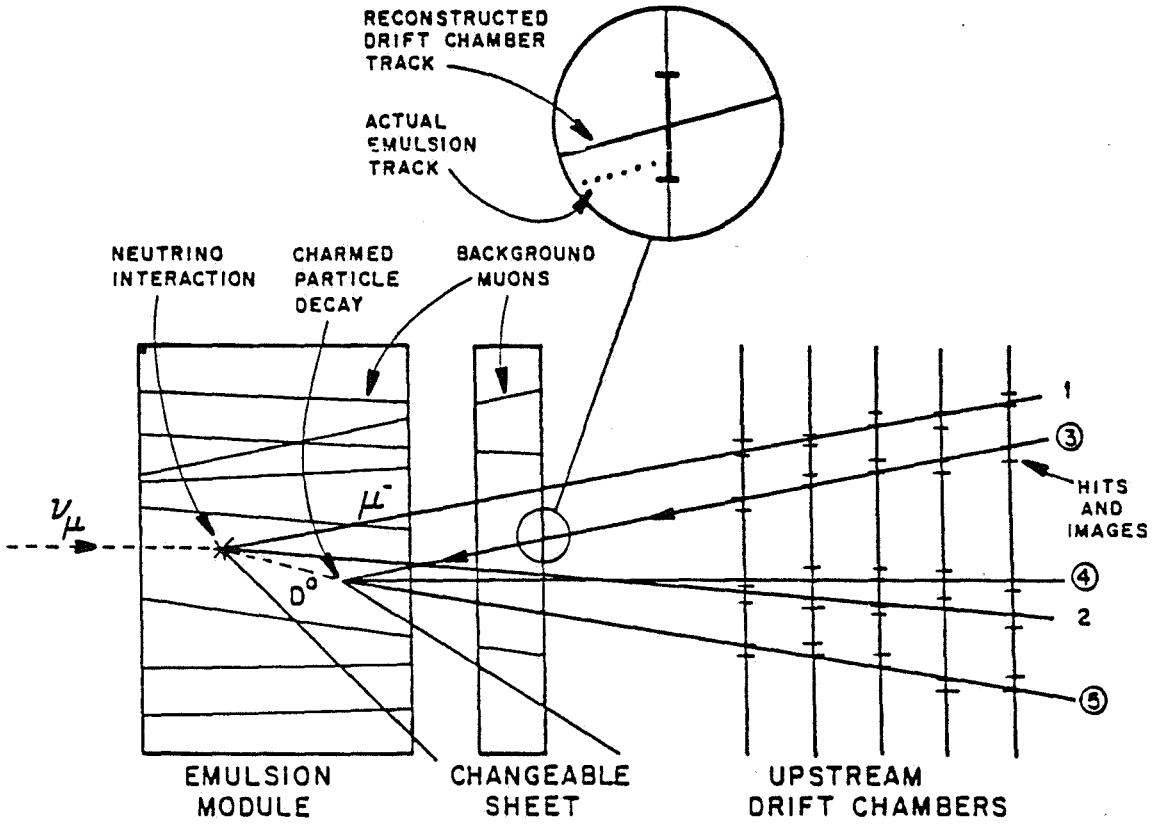

FIGURE 12. Schematic illustration of the use of a changeable interface sheet (emulsion-plastic-emulsion) in Fermilab experiment E531. The emulsion tracks on both sides of the plastic sheet form a precision vernier pointing into the emulsion.

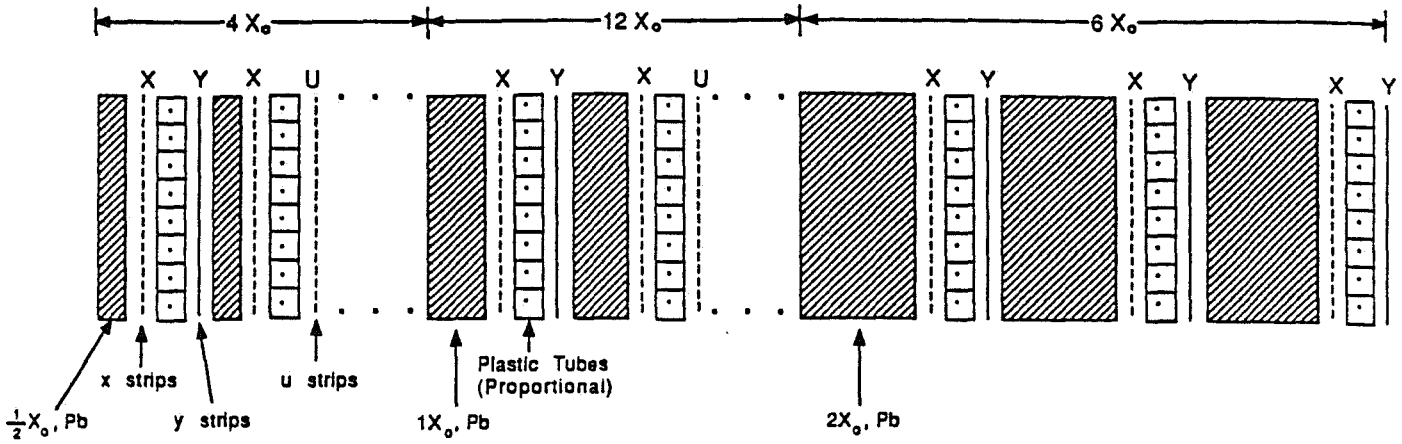

FIGURE 13. Layout of the electromagnetic calorimeter showing alternating layers of converter and proportional tubes.

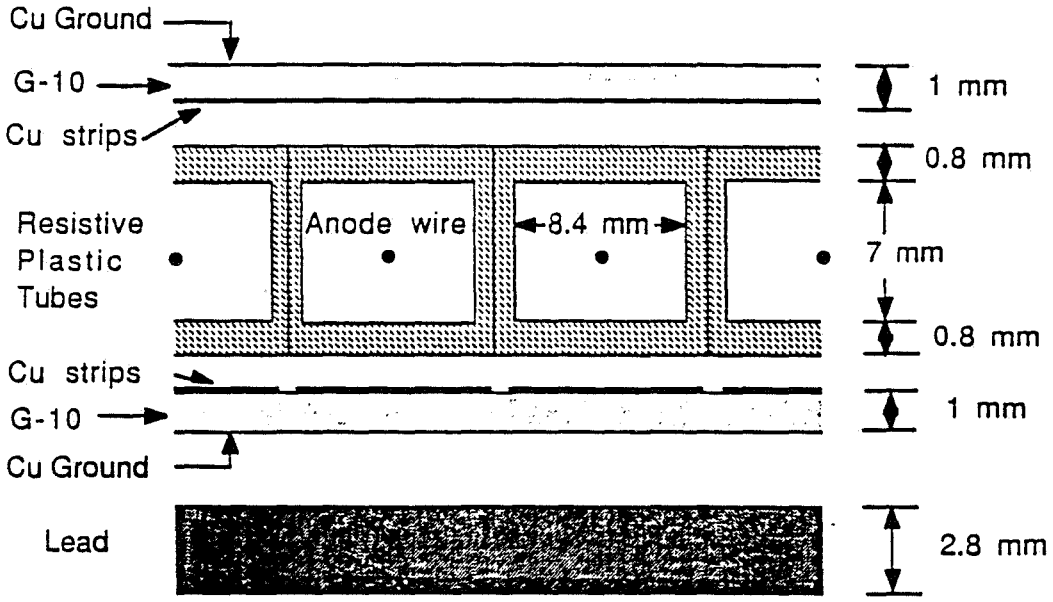

FIGURE 14. Detail of one EMCAL layer.

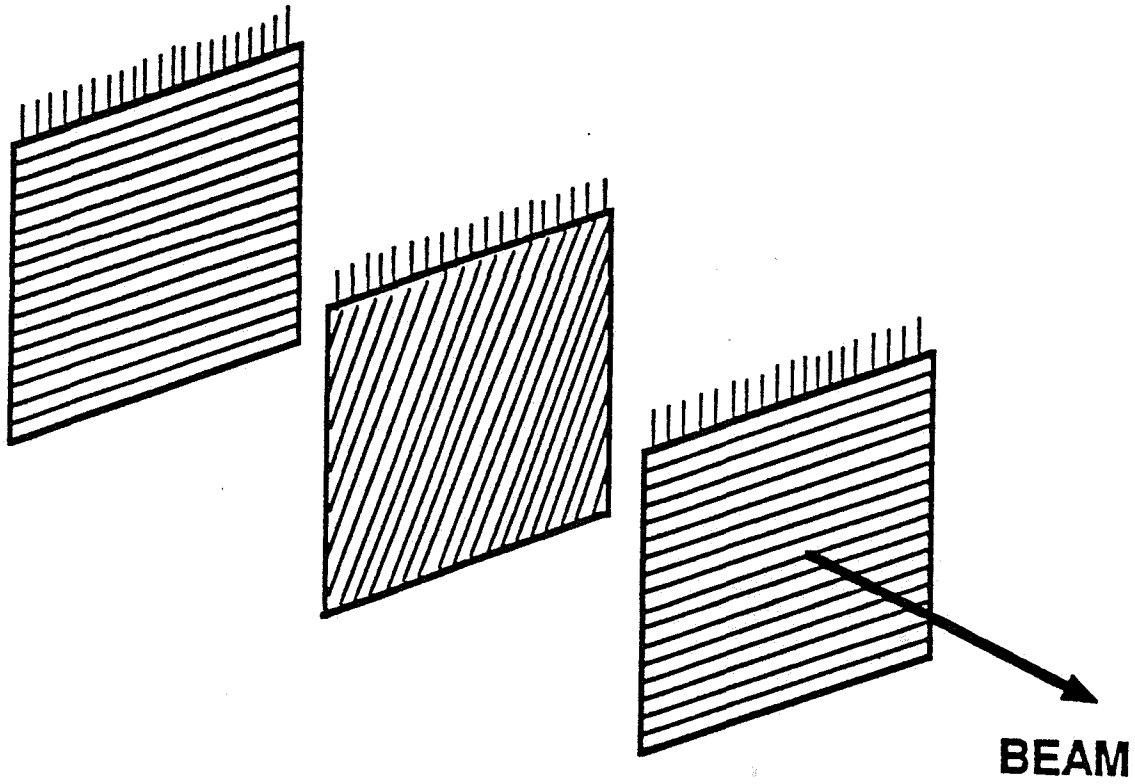

FIGURE 15. Exploded view of three successive layers of the electromagnetic calorimeter, showing the x-readouts and alternating y- and u-readouts.

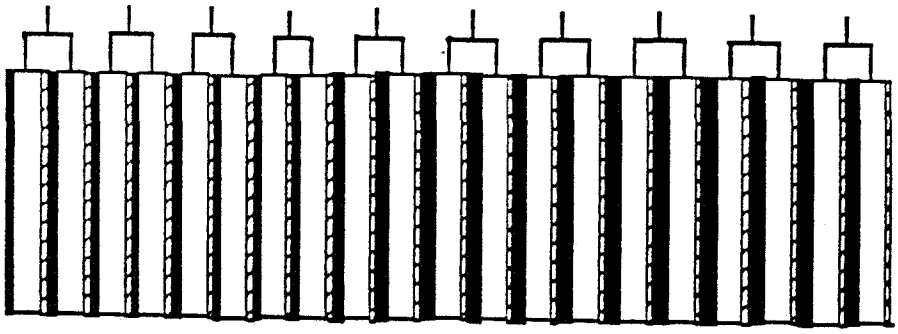

FIGURE 16. Schematic picture of the longitudinal ganging of the x-readouts of the electromagnetic calorimeter. Similar ganging in y and u gives half the number of samples in each of these projections.

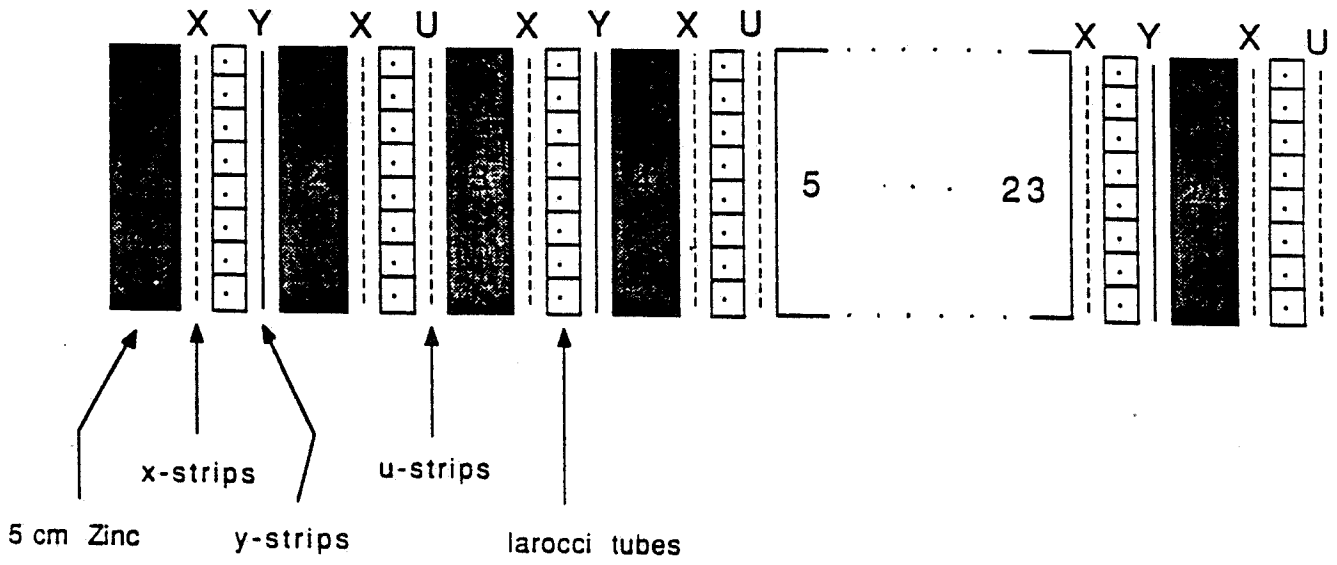

FIGURE 17. Schematic layout of the hadron calorimeter, showing alternating layers of zinc absorber and larocci tubes.

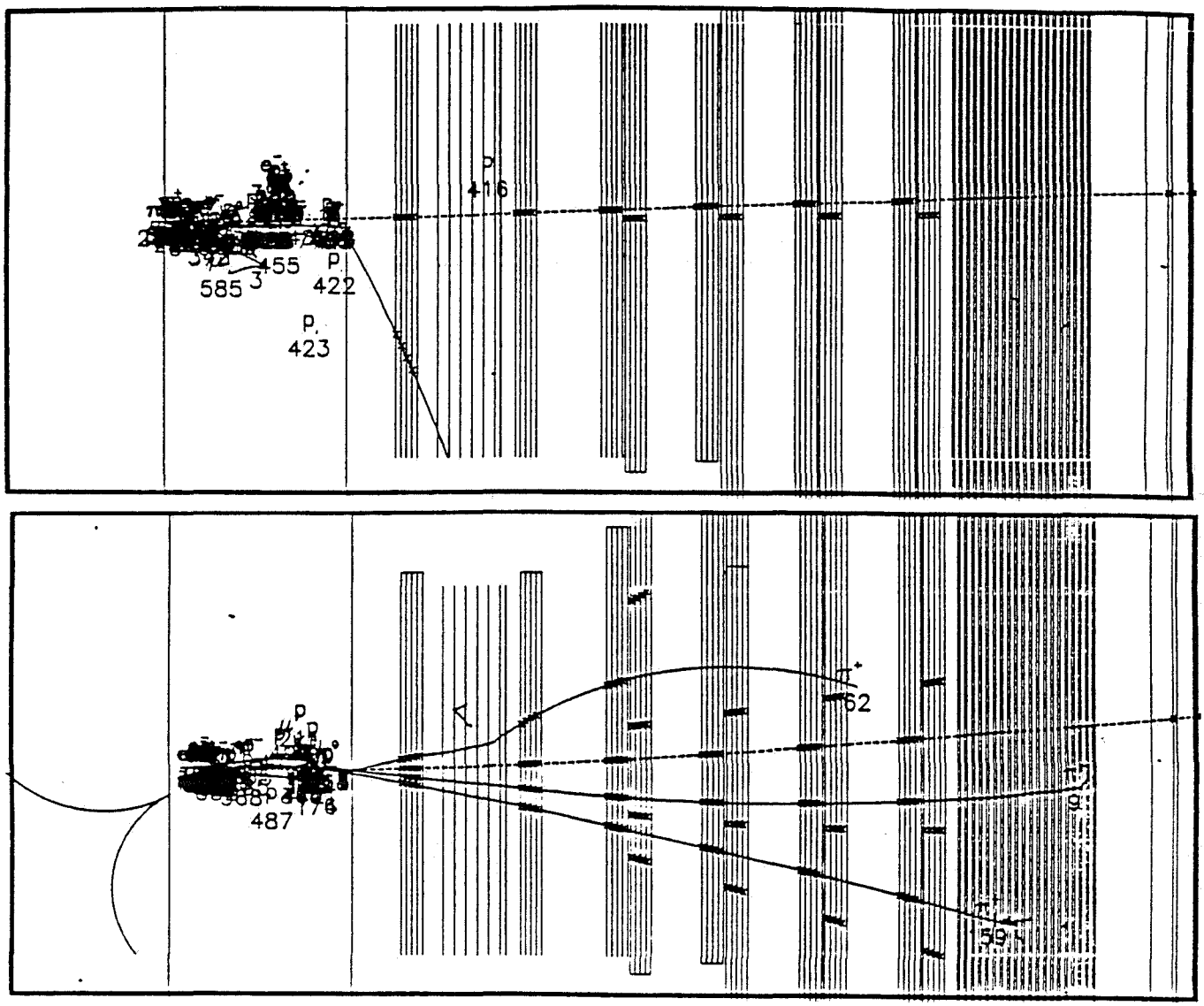

FIGURE 18. Typical examples (LUND-GEANT simulations) of neutrino interactions in the magnet coil upstream of the emulsion, which the event trigger must be designed to suppress.

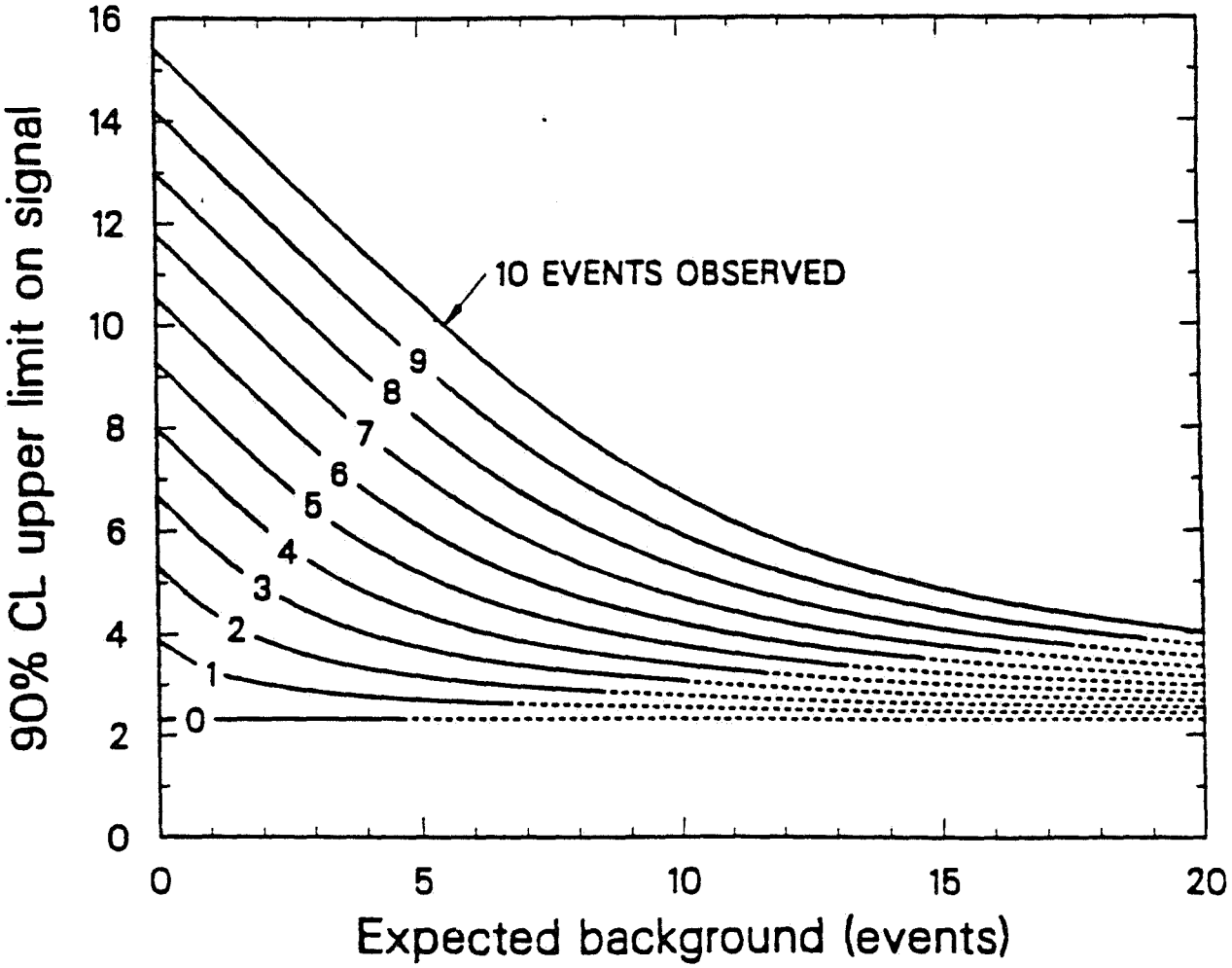

FIGURE 19. 90% confidence level limits as a function of expected background and number of observed events.

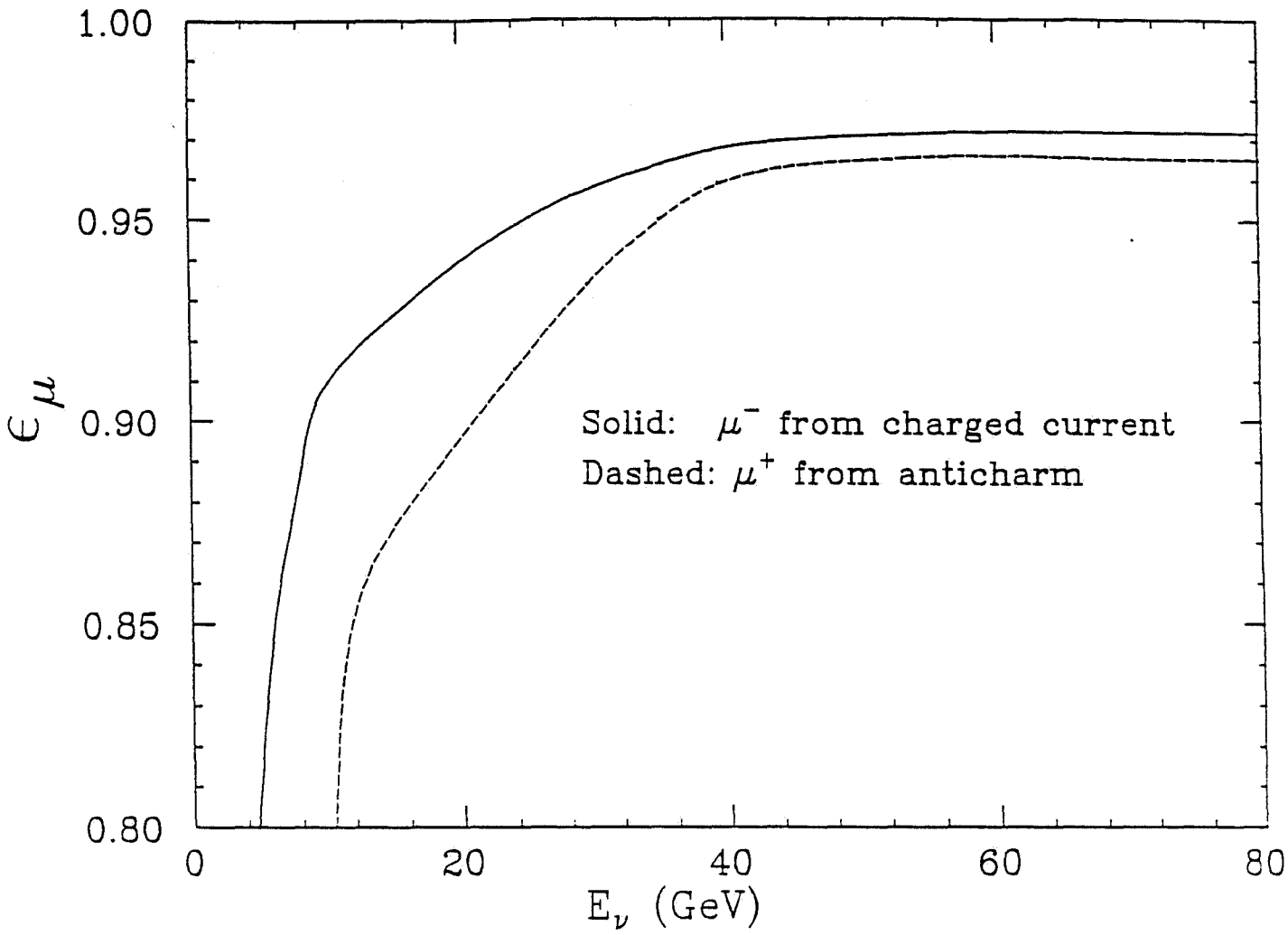

FIGURE 20. Average muon detection efficiency as a function of neutrino energy for μ^- from all charged current events (solid), and for μ^+ from anticharm production by antineutrinos (dashed); note the suppressed zero.

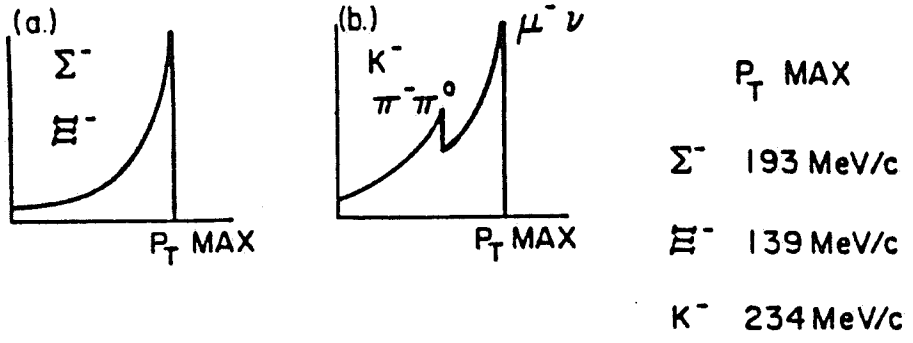

FIGURE 21. Distribution of decay p_T (transverse momentum relative to the parent direction) for (a) hyperon, (b) charged kaon decays. Note that all strange decays are eliminated with a cut of $p_T \geq 0.25 GeV/c$.

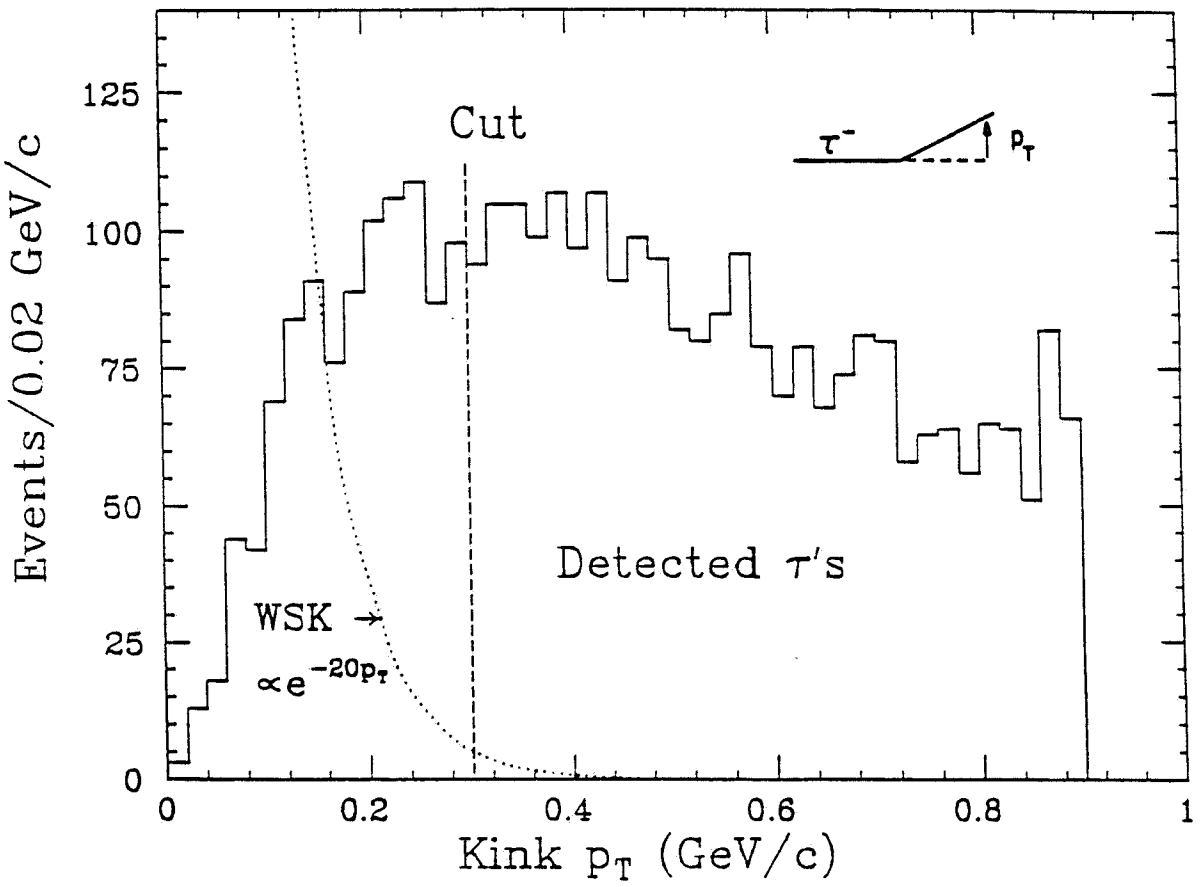

FIGURE 22. Distribution of decay p_T (histogram) for τ's passing the scan cuts and the kink cuts other than p_T. The measured $p_T$falloff for whitestar kinks is shown as a dotted curve. The p_T cut specified in this proposal (0.30 GeV/c) is also indicated.

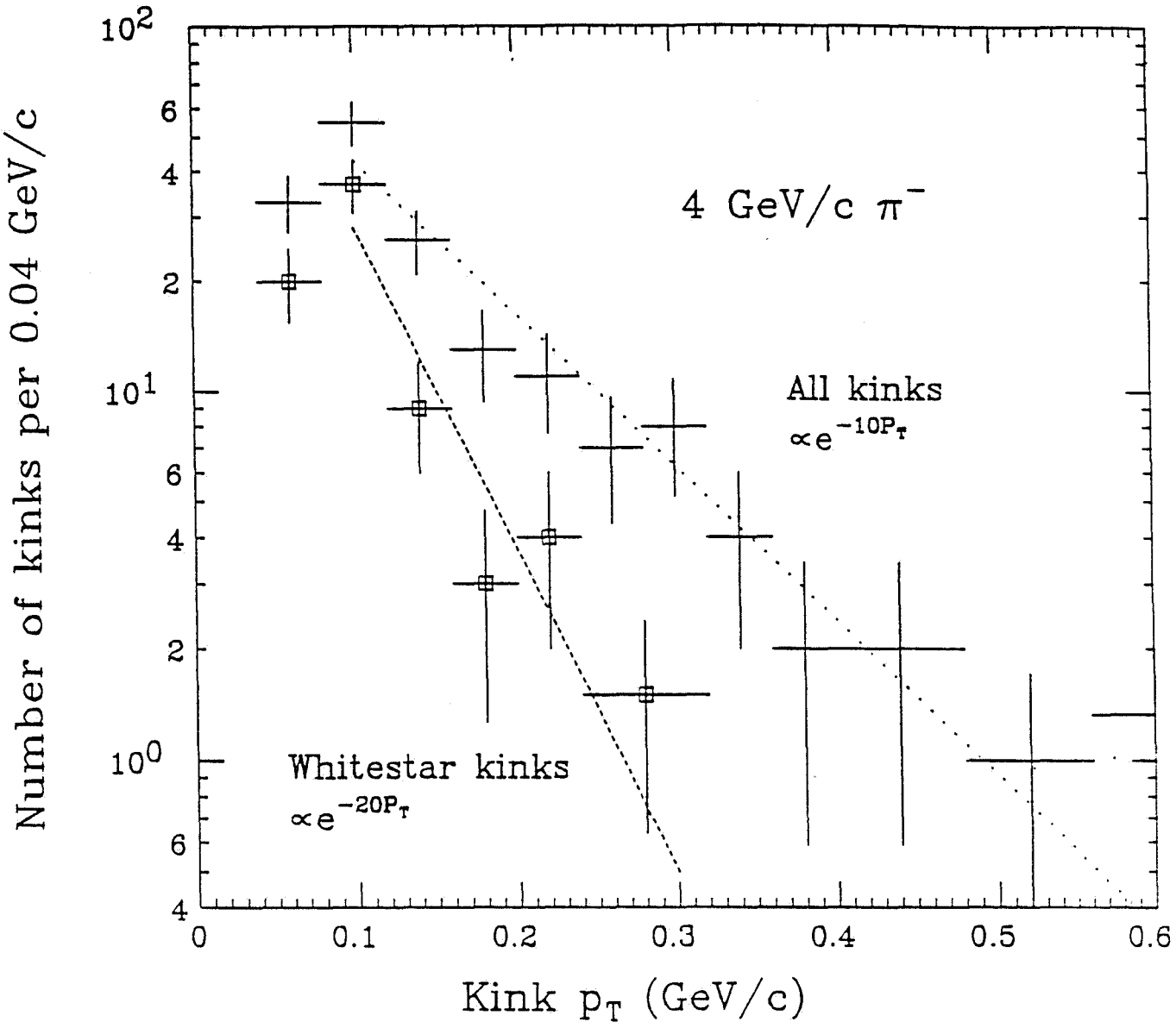

FIGURE 23. Preliminary results from the KEK measurement of whitestar kinks produced by 4.0 GeV/c π^-: number vs. p_T for all kinks (crosses), and for whitestar kinks (squares). There is one additional WSK event above 0.6 GeV/c. The p_T dependences for $p_T > 0.1$ GeV/c are indicated by the dotted and dashed lines.

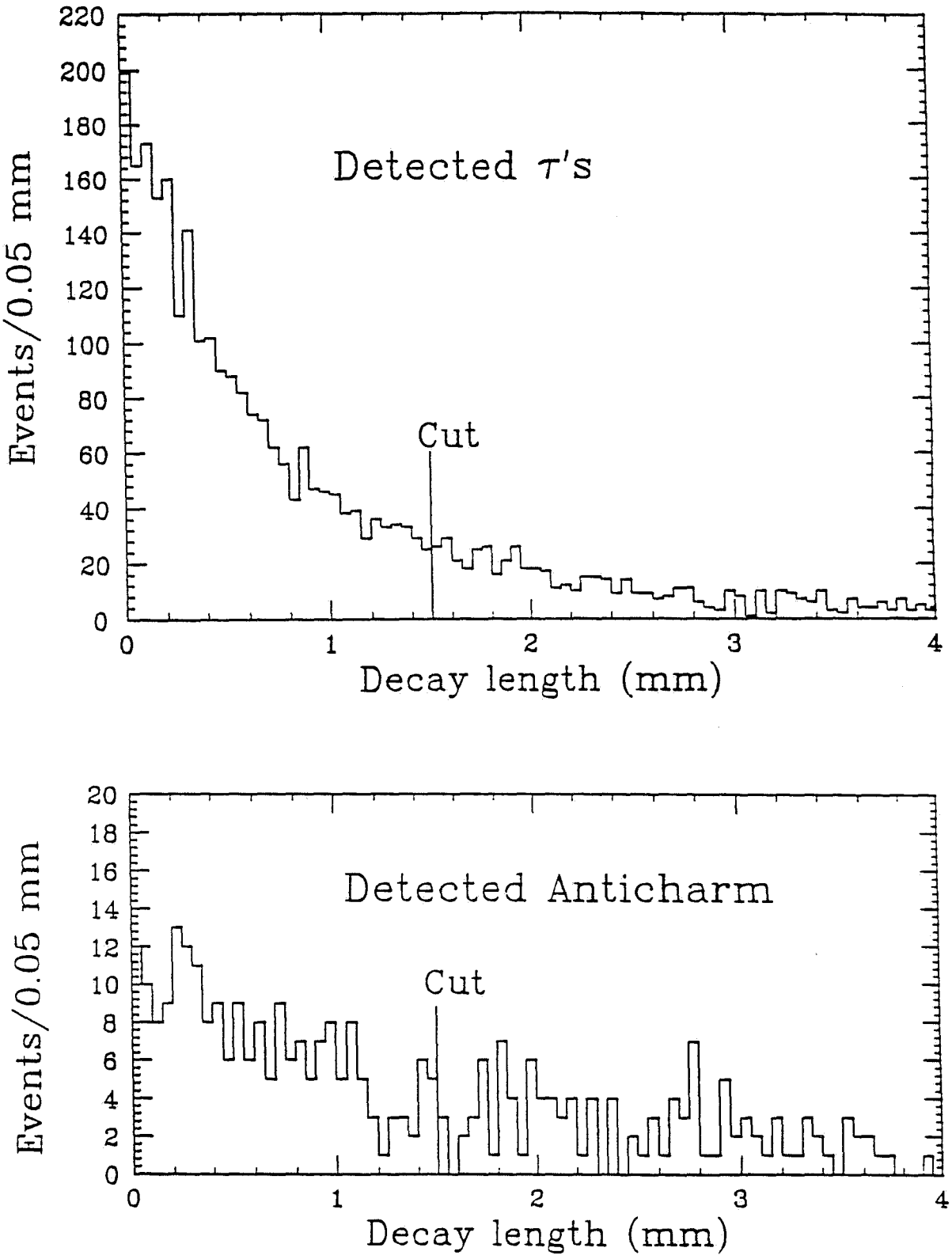

FIGURE 24. Monte Carlo distributions in decay length for a) τ events passing all cuts except decay length (top histogram); and for b) anticharm background events passing the same cuts. Whitestar kinks have a uniform decay length distribution. The cut used in this proposal is indicated.

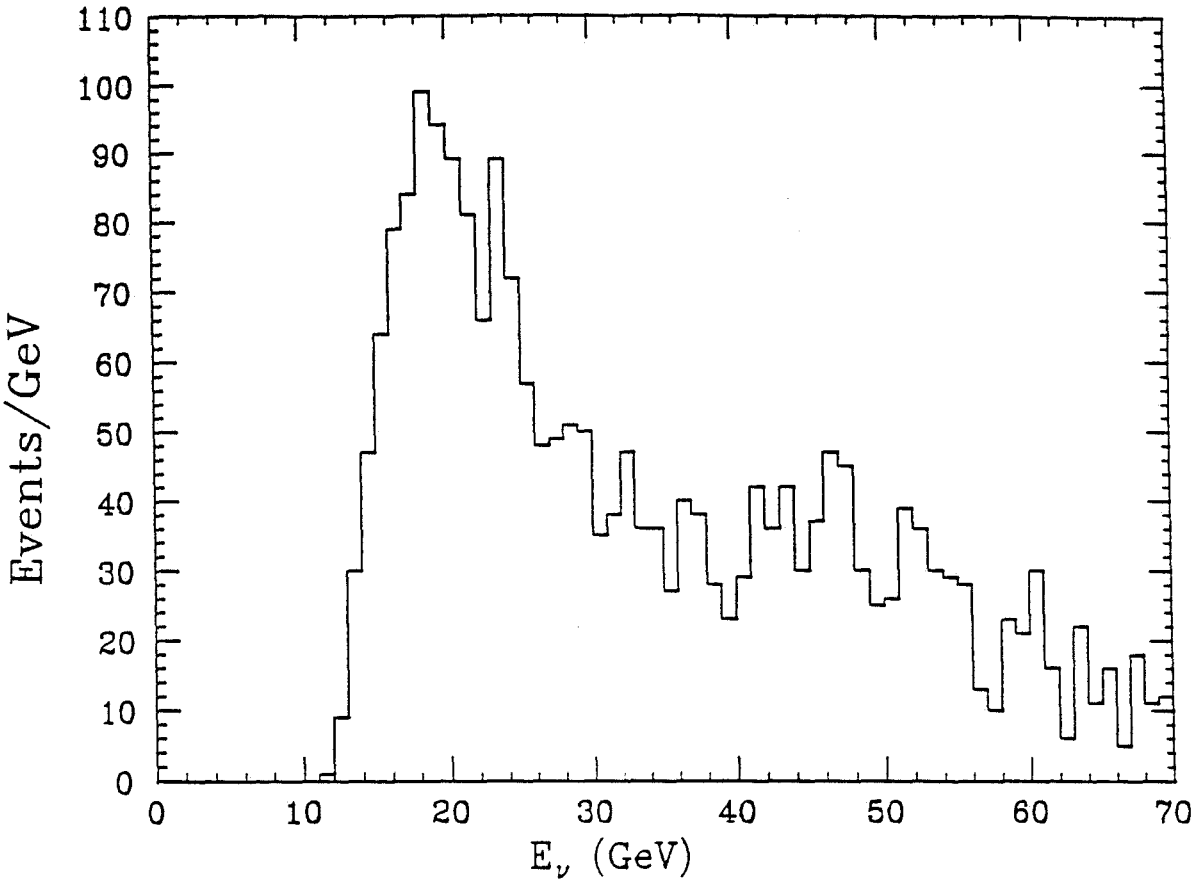

FIGURE 25. Neutrino energy distribution of all τ events passing the scan and kink cuts.

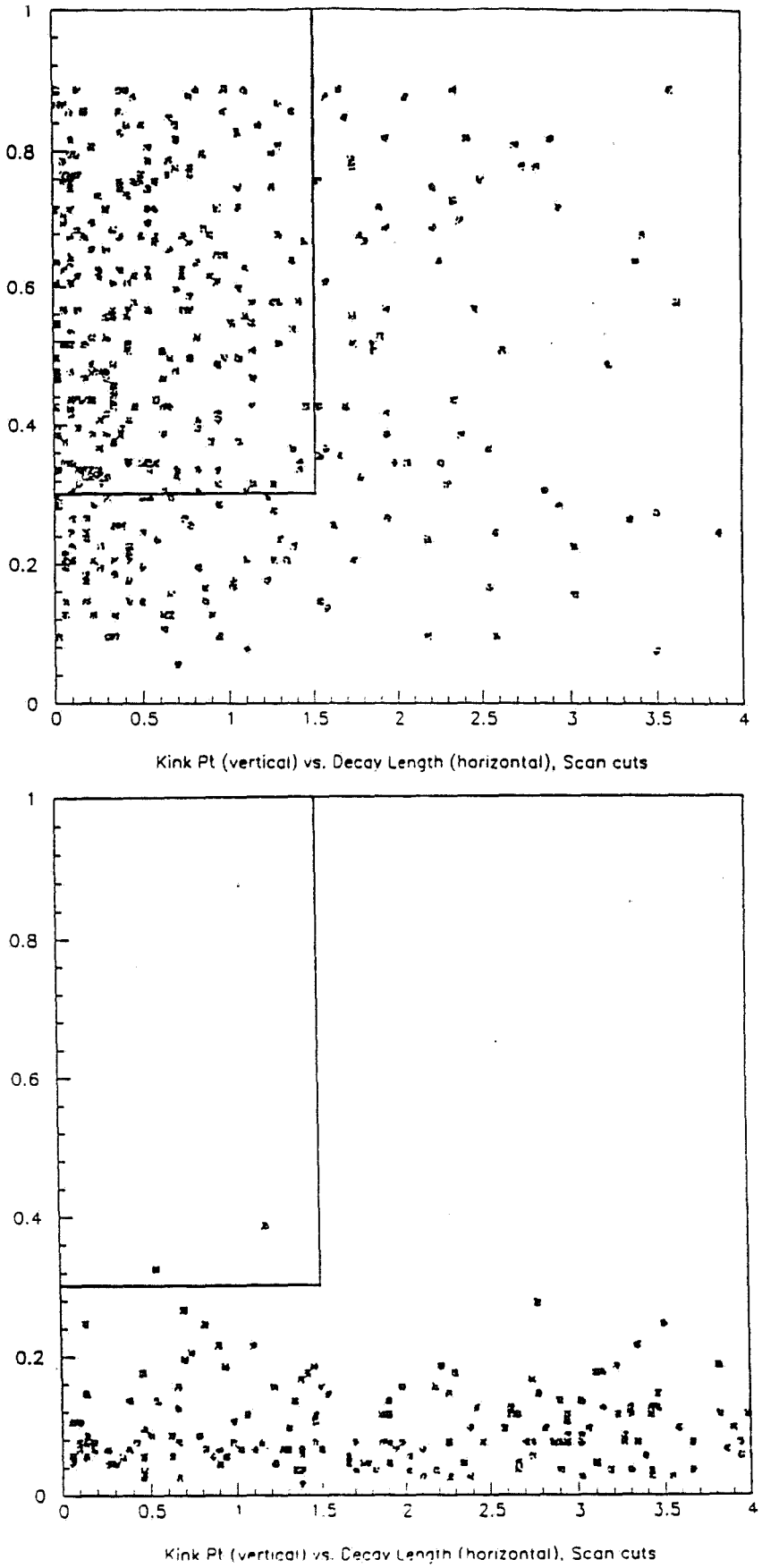

FIGURE 26. Monte Carlo scatterplots of kink p_T in GeV/c relative to the parent direction (vertical axis) vs. decay length in mm (horizontal axis). The upper scatterplot is for τ events passing the scan cuts, while the lower one (arbitrarily normalized) is for whitestar kinks passing the same cuts. The two distributions are very dissimilar. Events accepted by the kink cuts are inside the boxes.

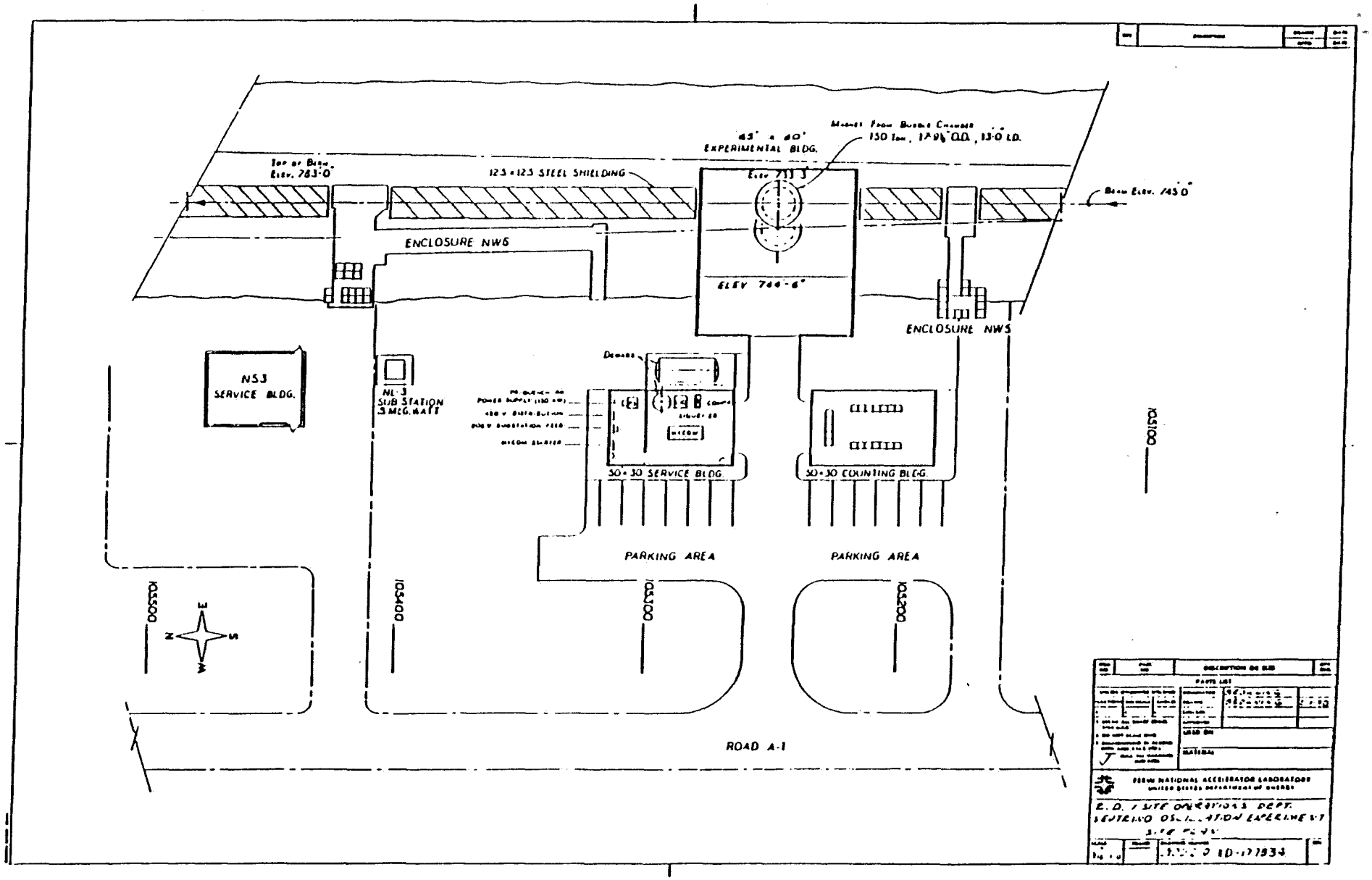

FIGURE 27. Layout of civil construction for the experimental area.

List of Appendices

Appendix A

STANDARD MODEL TESTS FROM CHARM PRODUCTION BY NEUTRINOS NEAR THRESHOLD

Data on charm production by neutrinos and antineutrinos permits in principle the determination of several quantities of great interest for testing the standard model: the absolute square of the K-M matrix element V_{cd}, the effective charm quark mass M_c, and the structure function for the strange sea. Because these quantities enter the data in a highly correlated way, extracting them with precision has been difficult. For example, preliminary dimuon results [1] from Fermilab E744 based on 1500 ν and 300 $\overline{\nu}$ events determines $|V_{cd}|$ to $\pm 8\%$ and M_c to ± 0.5 GeV, provided that statistical and systematic errors are added in quadrature. A more conservative treatment of systematic errors would make $|V_{cd}|$ uncertain to $\pm 13\%$.

Measurements of charm production near threshold which will be a byproduct of this proposed $\nu_\mu \leftrightarrow \nu_\tau$ oscillation experiment will allow determination of $|V_{cd}|$ to $\pm 3\%$, and of M_c to better than ± 0.05 GeV, if sources of systematic error are carefully handled.

In the P803 hybrid emulsion spectrometer, the decays of charm will be observed directly in the emulsion target; the acceptance in x and y is nearly 100%. High sensitivity to neutrino production of charm near threshold results in large part from the intense medium-energy ν and $\overline{\nu}$ beams available from the new Fermilab Main Injector. The spectrum shape is ideally matched to charm production and should provide a nearly constant yield of charm events between 8 and 40 GeV.

Neutrino production of charm in the parton model is described by

$$\frac{d^2\sigma}{dxdy} \propto [|V_{cd}|^2 \xi f_{val}(\xi, Q^2) + |V_{cd}|^2 \xi f_{dsea}(\xi, Q^2) + |V_{cs}|^2 \xi f_{ssea}(\xi, Q^2)] \qquad (1)$$

$$\cdot[1 - M_c^2/(2M_N E_\nu \xi)] \cdot \Theta(W^2 - (M_D + M_N)^2)$$

while for production of anticharm by antineutrinos

$$\frac{d^2\sigma}{dxdy} \propto [|V_{cd}|^2 \xi f_{\bar{d}sea}(\xi, Q^2) + |V_{cs}|^2 \xi f_{\bar{s}sea}(\xi, Q^2)] \qquad (2)$$

$$\cdot[1 - M_c^2/(2M_N E_\nu \xi)] \cdot \Theta(W^2 - (M_D + M_N)^2).$$

In these expressions the step function Θ ensures that the hadronic mass is sufficient for producing charm, and the slow-rescaling variable $\xi = x + M_c^2/(2M_N E_\nu y)$ replaces x in the structure functions f_i, suppressing the cross section most strongly at low y and E_ν. The additional suppression factor $[1 - M_c^2/(2M_N E_\nu \xi)]$ arises from the mixed helicity of a charm quark of finite mass. Antineutrino production of charm is predominantly off the strange sea, while ud valence and ssea make roughly equal

contributions to neutrino production at high energy. Slow rescaling causes a greater reduction in the ssea contribution relative to ud valence at low energy because of the much steeper ssea x-dependence.

To investigate the improved sensitivity to $|V_{cd}|$ and M_c from low-energy data, a simple calculation was performed evaluating (1) and (2) on an (x,y,E_ν) grid for several values of M_c. In this exercise the structure functions f_{val} and f_{dsea} were given by the parametrization of Reutens [2] from Fermilab E616 data, while for f_{ssea} three different parametrizations were tried, the default version being $\xi f_{ssea} = 0.133(1-\xi)^{10.8}$ as suggested by preliminary results [1] from E744.

The effects of slow rescaling are illustrated in Figs. A1a and A1b, which are Lego plots showing the ud valence and strange sea contributions to $d^2\sigma/dxdy$ for $\nu + N \rightarrow C + X$ at E_ν=15 GeV. (The single filled bin at lower right is a "ruler" of constant $d^2\sigma/dxdy$ to establish the relative scale of the two figures.) The W^2 threshold and the increasingly strong effects of slow rescaling at low y are apparent, as is the severe suppression of the ssea contribution from slow rescaling. The energy dependence of this suppression is illustrated in Fig. A2, which shows the relative sizes of the contributions to $\nu + N \rightarrow C + X$ together with the data from dimuon [1],[3] and hybrid emulsion [4] experiments.

Figures A3a, A3b (which appear also in the body of the proposal) illustrate the sensitivity of the $\nu, \overline{\nu}$ charm cross sections to the slow rescaling parameter M_c for a fixed parametrization of the strange sea. In addition to the data points from the existing experiments, these figures include simulated data from a very conservative estimate of the yield from P803: 500 ν and 200 $\overline{\nu}$ events with a binning in E_ν based on the beam spectra in the proposal. It is clear that if the size and shape of the strange sea is known, the low-energy $\overline{\nu}$ data pins down M_c with great precision, which then allows an excellent determination of $|V_{cd}|$ from the ν data.

The effects of incomplete knowledge of the strange sea were investigated using three different parametrizations, illustrated in Fig. A4, which probably more than span the present uncertainties.

1. $\xi f_{ssea} = 0.133(1-\xi)^{10.8}$;
2. $\xi f_{ssea} = 0.5 f_{udsea}$, with ξf_{udsea} as per Reutens [2];
3. $\xi f_{ssea} = 0.63(1-\xi)^5 \xi f_{udsea}$.

For each description of ssea a fit was performed to the E744 and (simulated) P803 $\nu, \overline{\nu}$ data to determine 3 parameters: $|V_{cd}|/sin(\theta_C)$; the amount of strange sea relative to the input; and M_c. The results gave errors of $\pm$2.4% to $\pm$2.7% on $|V_{cd}|$, and $\pm$0.031 to $\pm$0.037 on M_c for each fit. The maximum variation among parametrizations was $\pm$5% for $|V_{cd}|$, and $\pm$0.10 GeV on M_c. Extracting maximal physics from the data will require obtaining the best available parametrization of the strange sea

from existing high-energy data, and a careful measurement of the x,y dependence of $\overline{\nu}$-produced anticharm in P803 itself, to reduce this source of systematic error below the small statistical errors. At least one ambitious program to parametrize structure function is now well-advanced [5].

REFERENCES FOR APPENDIX A

1. C. Foudas et al., Phys. Rev. Lett. **64**, 1207 (1990); Michael Shaevitz, Notes from the 1989 SLAC Summer Institute; Heidi Schellman, talk presented at SLAC 1988 Summer Institute (FERMILAB-Conf-88/160-E).

2. Patrick G. Reutens, Ph.D. Thesis, University of Chicago (1986).

3. P. Abranowicz et al. (CDHS) Z. Phys. **15C**, 19 (1982).

4. N. Ushida et al. (E531), Phys. Lett. **B206**, 375 (1988).

5. W. K. Tung, Talks presented at the Breckenridge Summer Study (1989) and at Snowmass Summer Study (1990).

a.

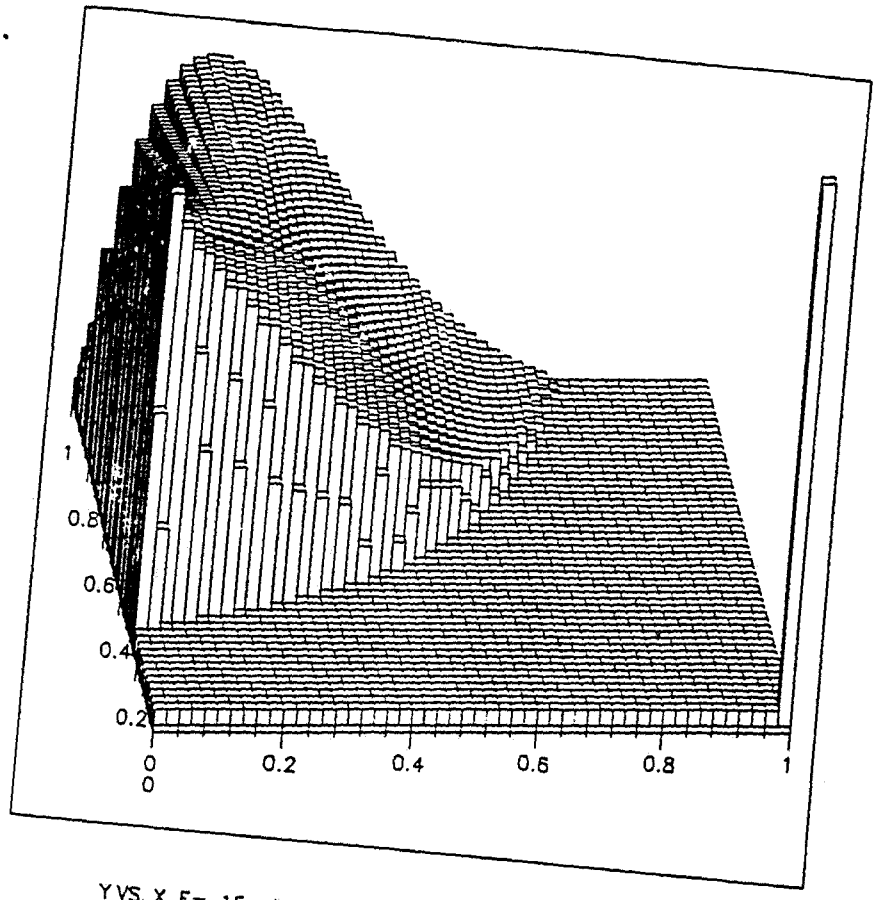

Y VS. X, E= 15. NU CHARM UD VAL KAPPA=.50 MC=1.50

b.

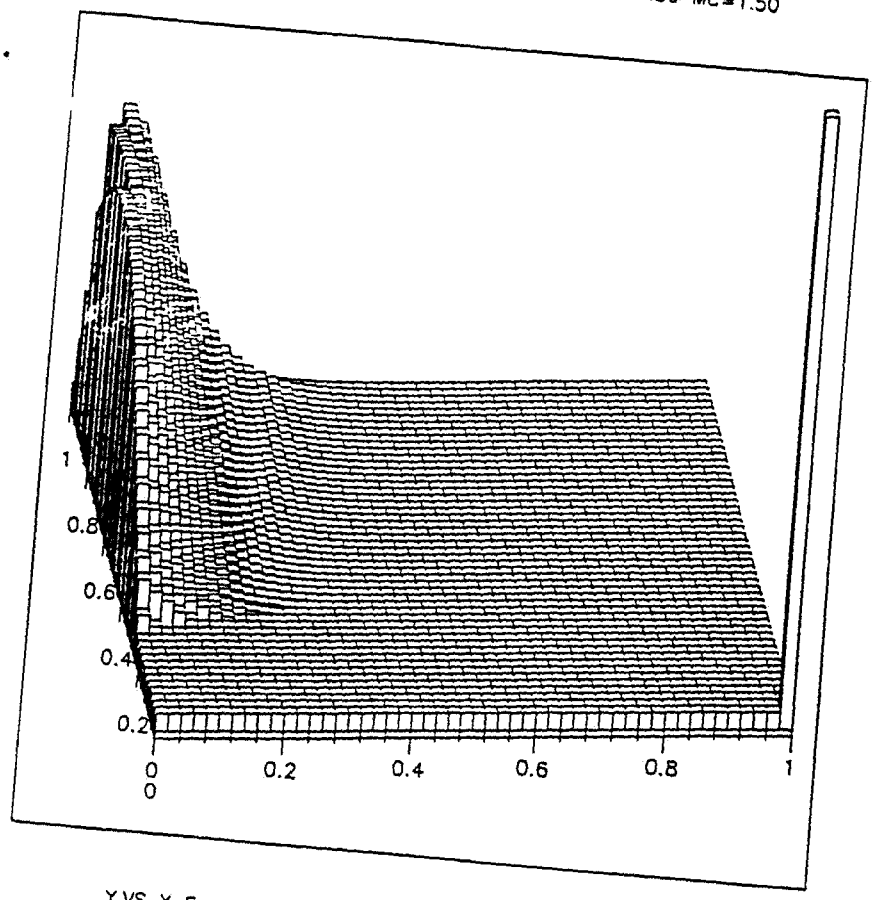

Y VS. X, E= 15. NU CHARM S SEA KAPPA=.50 MC=1.50

FIGURE A1. Lego plots showing the calculated ud valence (a) and strange sea (b) contributions to $d^2\sigma/dxdy$ for charm production by neutrinos at E_ν=15 GeV, with charm quark mass M_c=1.5 GeV. On these plots x is the nearly horizontal axis. The large single bin at (x,y)=(1,0) is a "ruler" for comparing the two plots.

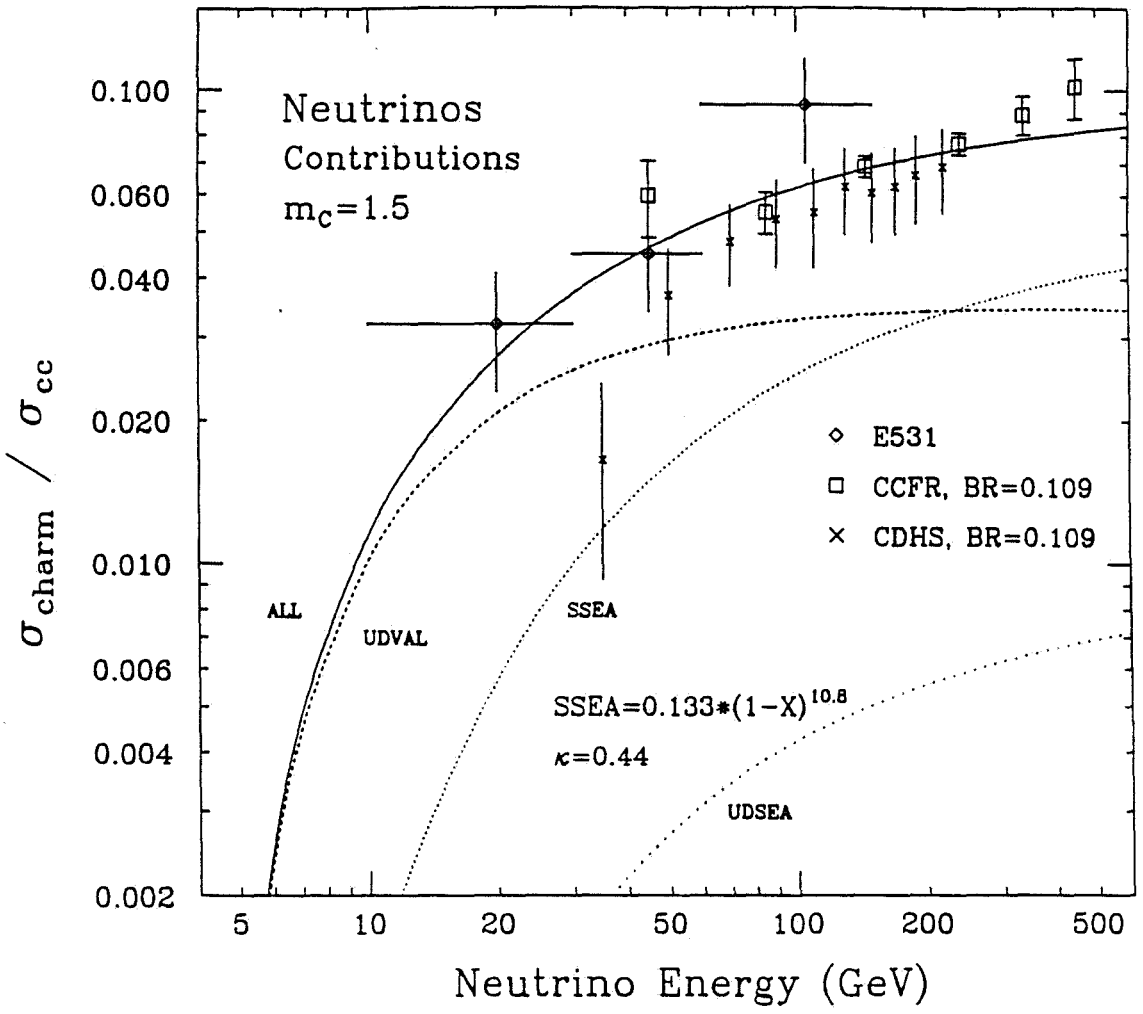

FIGURE A2. Calculated contributions to the cross section for $\nu + N \rightarrow C + X$ as a function of neutrino energy, using a charm quark mass M_C=1.5 GeV.

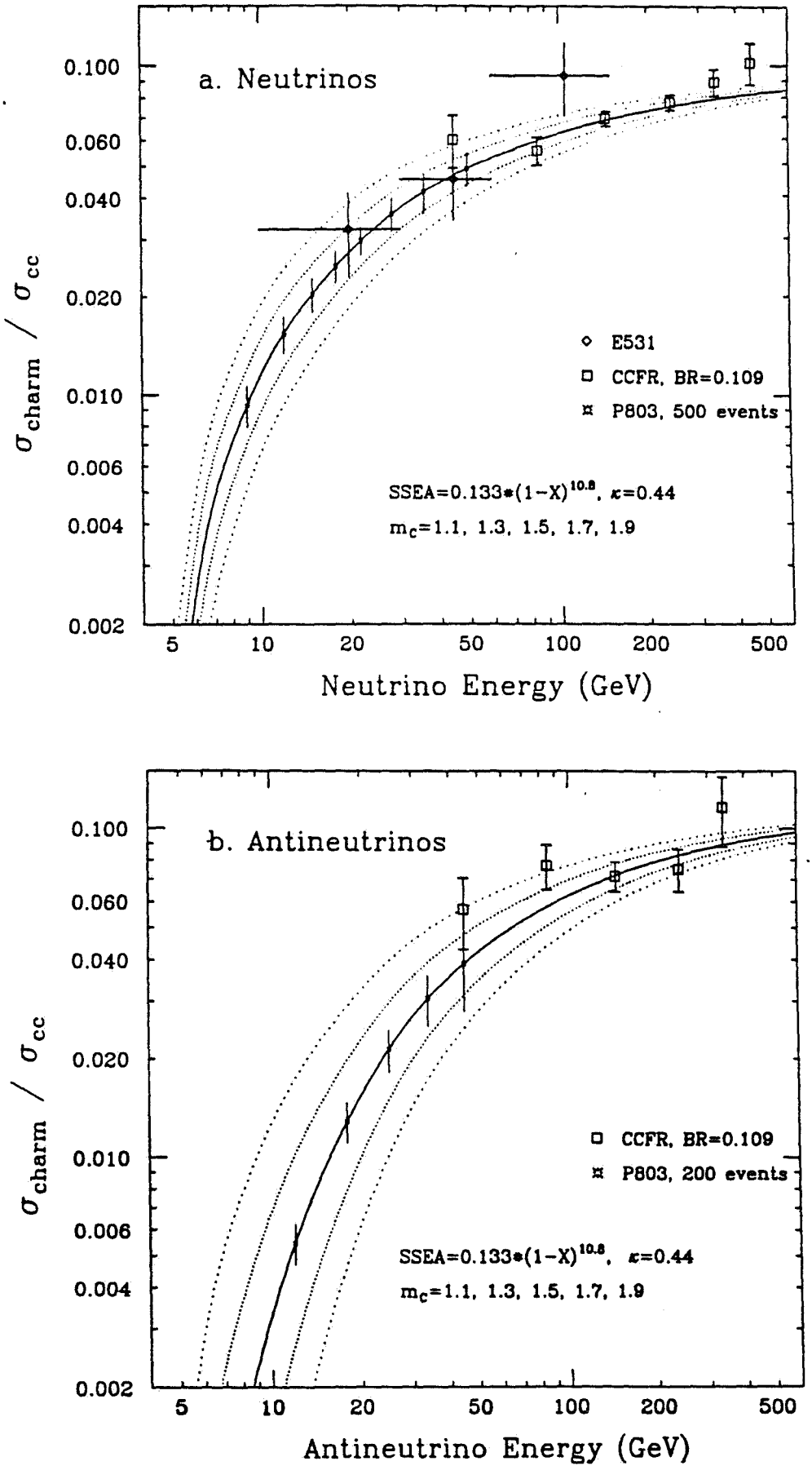

FIGURE A3. Sensitivity of ν (a) and $\overline{\nu}$ (b) production of charm to the charm quark mass parameter M_c. Data shown for P803 are simulated, based on a conservative estimate of the yield from the beams discussed in the proposal.

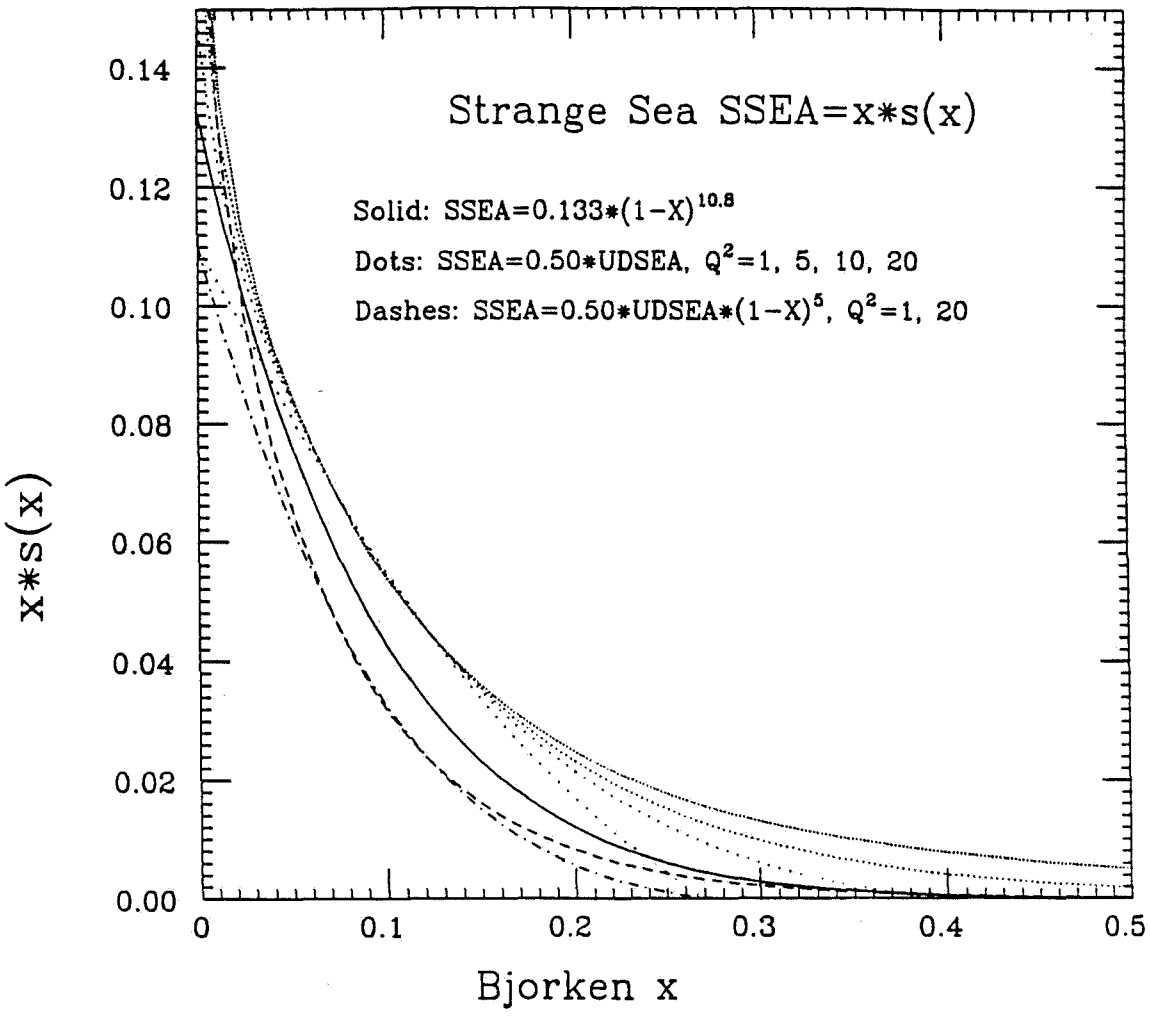

FIGURE A4. Parametrizations of the strange sea used in estimating systematic errors.

Appendix B

BACKGROUND FROM BEAM DUMP TAU NEUTRINOS

The source of the horn-focussed muon neutrinos for P803 is a 120 GeV proton beam passing through a 2.0 interaction length target 605 m upstream of the detector. The remaining protons are then stopped in an iron beam dump only 105 m from the emulsion. Real ν_τ's from the decay chain

$$\overline{D_s} \rightarrow \tau^- + \overline{\nu_{\tau 1}}, \qquad \tau^- \rightarrow \nu_{\tau 2} + X \tag{1}$$

are a potentially serious background to ν_τ's resulting from oscillation of ν_μ's.

In this Appendix we summarize a calculation of this direct ν_τ background which uses known production properties of charmed particles and Monte Carlo simulations of the decays (1) and

$$D \rightarrow \nu_\mu + X \tag{2}$$

to scale the results of the Fermilab E613 [1]. That experiment measured the yield of (2) from charm produced by dumping 400 GeV protons on a tungsten target. The calculation parametrizes charm production by

$$\sigma \propto (1 - x_F)^n e^{-1.0 p_T^2}, \tag{3}$$

and assumes that D_s and D production have the same x, p_T dependence at a given beam energy. The D semileptonic decay modes used in the simulation are $K\mu\nu$ (33%), $K^*\mu\nu$ (33%), $K\eta\mu\nu$ (17%), and $K\rho\mu\nu$ (17%), consistent with the most recent results [2],[3]. The τ decay modes are taken from PDG 1988 [4].

Simulation of ν_μ Charged-Current Yield from E613

The simulation program was checked by calculating the absolute yield of ν_μ charged-current events from E613 [1]. E613 used a Pb and liquid scintillator neutrino target with a fiducial mass of 75 tons and a fiducial frontal area of 264 cm × 111 cm (2.3×10^3 gm/cm^2) located 56 m from the proton dump. This detector was offset horizontally so that the beam passed 24 cm inside one edge. The measured yield of ν_μ charged-current events with $E_\nu \geq 20$ GeV was 43.6 ± 7.4 per 10^{16} protons, with an inferred $D\overline{D}$ production cross section from 400 GeV protons on tungsten of $57 \pm 2.9 \pm 8.5$ μb/nucleon, n=3.2 ($\pm$ approx. 1.0), and atomic weight dependence of $A^{0.75 \pm 0.05}$, essentially the same as $A^{0.72}$ for the absorption cross section of protons on nuclei. The experiment was insensitive to production at x_F below about 0.2.

For comparison, $D\overline{D}$ production data from LEBC for 400 GeV protons on hydrogen [5], sensitive to all positive x_F, finds a pair cross section of 30.2 ± 3.3 μb and

n=4.9±0.5; there are no events for $x_F > 6$. Since (3) is an empirical parametrization and no single experiment has good data over the full range of x_F, it is certainly possible that the effective n is actually somewhat different for small and large x_F. Note that P803 is sensitive to large-x_F production.

The yield from E613 was calculated using several values of n and a $D\overline{D}$ crossection of 57 μb. The experimental corrections (total factor 0.83) specified in [1] have been applied. The resulting simulated absolute yields are in excellent agreement with the measured rate of 44 per 10^{16} protons for n≈3.5; this gives us confidence that our simulation is valid.

Table 1. Calculated Yield of ν_μ Charged-Current Events from E613.

Assumed n-value	E613 Acceptance	$\overline{E_\nu}$ (GeV)	$\overline{x_F}$	E613 Yield per 10^{16} p
2.5	0.101	64.4	0.522	77.9
3.2	0.0824	55.3	0.464	54.3
4.0	0.0673	51.1	0.412	41.2
4.9	0.0552	32.5	0.367	21.5

In the estimates of direct ν_τ event yields for P803 in the next section which are scaled from E613, the E613 values of n and $D\overline{D}$ cross section, rather than those from LEBC, will be used, because a) the large-x_F data is more relevant; and b) if the A-dependence of high-x_F charm production is somewhat different than that of proton interactions, tungsten-target data will be a better approximation to an iron dump than hydrogen data.

Scaling to Direct ν_τ Event Yield for P803

A. Proton flux. This yields for this proposal are based on 2.4×10^{20} protons on a 2.0 interaction length, half-density 3 mm diameter target in which 80% of the protons interact, leaving 0.20 of these protons, or 4.8×10^{19}, to strike the dump. There should be no significant production of charm by secondaries from the production target because of the low energy of the beam.

B. Neutrino target mass/area. The emulsion target of P803 will have 0.259 tons/m^2, compared to 25.6 tons/m^2 in the fiducial volume of E613; the ratio is 0.0101.

C. Energy dependence of $D\overline{D}$ cross section. There is data from NA32 [6] on $D\overline{D}$ production on silicon by 200 GeV protons (9 events). The cross section (all x_F) is 3.0±1.4±0.2 μb, with n about 5.5. Production data by π^- from the same experi-

ment (with much better statistics) gives $5.1^{+0.6}_{-0.5} \pm 0.3$ μb for x_F>0 and n=2.5±0.3. Another approach is to use theoretical calculations to extrapolate downward in energy. Results of two such calculations [7],[8], are shown in Figs. B1a and B1b; a conservative value of the decrease between 400 GeV ($\sqrt{s} = 27.4$) and 120 GeV ($\sqrt{s} = 15.0$) is a factor of 6 (0.17).

D. Ratio of D_s to D production. A preliminary measurement [3] from E653 (800 Gev protons) is $D_s/D \approx 0.2$, which we take as an upper estimate at 120 GeV.

E. Semileptonic branching ratios. We assume a branching ratio for $D_s \rightarrow \tau\ \nu_\tau$ of 2%, and a production-averaged semimuonic branching ratio for D of 10%. There is an additional factor of approximately 0.5 which arises as follows: we detect only τ^-, and are almost completely insensitive to the low-energy ν_τ's from $\overline{D_s}$ decay. In production of D_s, it is much more likely that a $D_s$will be produced as $D_s\overline{D}$ than as $D_s\overline{D_s}$. On the other hand, when E613 detects ν_μ, either member of the $D\overline{D}$ pair could have produced the neutrino. The scaling factor is then (0.02)(0.5)/(0.10)=0.10.

F. Angle and energy acceptance. The P803 detector subtends an angle of 8.5 mr from the dump, and is inefficient for detecting ν_τ's below 10 GeV. Geometric acceptances are presented for several values of n in Table 2 below; the acceptance is quite sensitive to n. Since n is generally observed to increase with energy, one expects n to be less than 3.2 at 120 GeV. For the best-guess value of n=2.5, the acceptance is 0.022, compared to 0.0824 for E613, a ratio of 0.27.

G. Average neutrino energy, and energy dependence of $\sigma_{\nu_\tau}/\sigma_{\nu_\mu}$. The charged- current cross section is proportional to E_ν, which will be lower in the 120 GeV beam than its average value of 55 GeV for E613. In addition, ν_τ interactions are suppressed at low energy due to kinematic effects. The value of $\overline{E_\nu}$ for accepted events is a weak function of the assumed value of n. For n=2.5, $\overline{E_\nu}$=27 GeV, $\sigma_{\nu_\tau}/\sigma_{\nu_\mu}$=0.47; the ratio is (0.47)(27)/(55)=0.23.

H. Detection efficiency for ν_τ events. Beam dump ν_τ's are subject to the same event-finding losses and cuts as oscillation ν_τ's, a factor of approximately 0.15.

We now put these factors together for an assumed n=2.5. Results for other values of n are presented in Table 2.

Yield of beam dump ν_τ events = $(44/10^{16}\text{protons}) \cdot (4.8 \times 10^{19}\text{protons}) \cdot (0.0101)$

$\cdot (0.17) \cdot (0.2) \cdot (0.10) \cdot (0.27) \cdot (0.23) \cdot (0.15)$

= 0.067 detected events.

The uncertainty in this estimate is at least a factor of 2; however, direct ν_τ's do not appear to be a significant source of background.

Table 2. Calculated Yield of Direct ν_τ Events for P803.

Assumed n-value	P803 Acceptance	$\overline{E_\nu}$ (GeV)	$\sigma_{\nu_\tau}/\sigma_{\nu_\mu}$	$\overline{x_F}$	P803 Yield/ 2.4×10^{20} p
2.0	0.030	28	0.48	0.66	0.096 events
2.5	0.022	27	0.47	0.60	0.067 events
3.2	0.015	26	0.46	0.548	0.043 events

The energy-weighted spectrum of ν_τ's for n=2.5 is shown in Fig. B2. The low- and high-energy peaks from the two sources (1) of ν_τ are evident.

Effect of Deflecting Proton Beam before Dumping

A substantial reduction in the already low direct ν_τ event rate can be obtained by deflecting the proton beam before it strikes the dump. This has been simulated by displacing the P803 detector horizontally relative to the centerline of neutrino production. The results (for n=2.5) are summarized in Table 3 below. The deflection from one ring magnet (25 mrad) reduces the direct ν_τ rate by a factor of 3, while two such magnets reduce it by a factor 20.

Table 3. Effect of Deflecting Proton Beam.

Beam Deflection	P803 Acceptance	$\overline{E_\nu}$ (GeV)	$\sigma_{\nu_\tau}/\sigma_{\nu_\mu}$	Relative Yield
0 mr	0.022	27	0.47	1.0
25 mr	0.0098	24	0.44	0.37
50 mr	0.0022	17	0.34	0.046

REFERENCES FOR APPENDIX B

1. M. E. Duffy et al., Phys. Rev. **D38**, 2032 (1988).

2. J. C. Anjos et al., Phys. Rev. Lett. **61**,1587 (1989);
   J. C. Anjos et al., Phys. Rev. Lett. **62**,1587 (1989);
   J. Adler et al., Phys. Rev. Lett. **62**,1821 (1989).

3. Preliminary results from Fermilab E653, internal group communication.

4. Particle Data Group, Phys. Lett. **B204**, (1988).

5. M. Aguilar-Benitez et al., Z. Phys. **40C**, 321 (1988).

6. S. Barlag et al., Z. Phys. **39C**, 451 (1988).

7. R. K. Ellis, Preprint Fermilab-Conf-189/168-T (1989).

8. E. L. Berger, Proceedings of the Advanced Workshop on QCD Hadronic Processes, (B. Cox ed.), Plenum Press, p. 501 (1989).

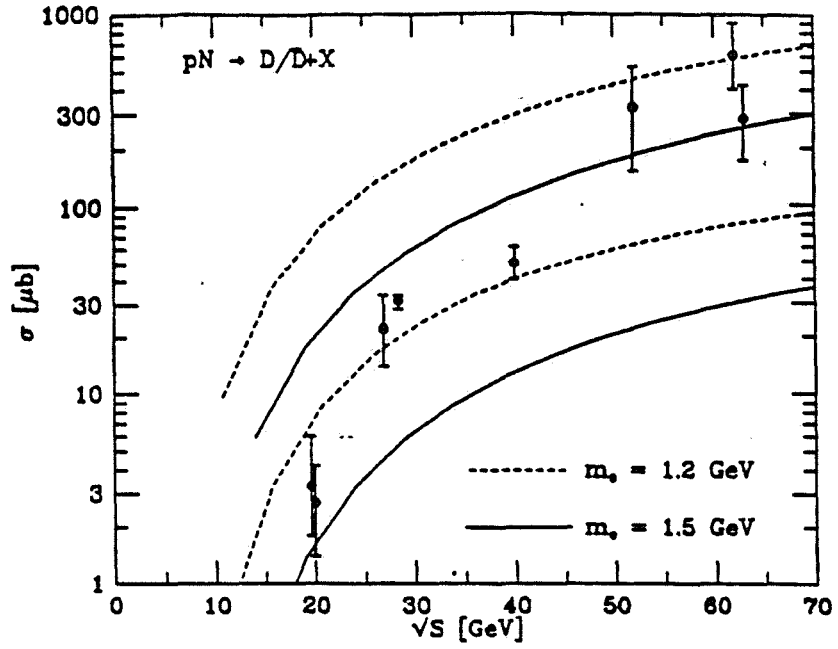

FIGURE B1a. Calculated energy dependence of charm production by protons from Ref. 7.

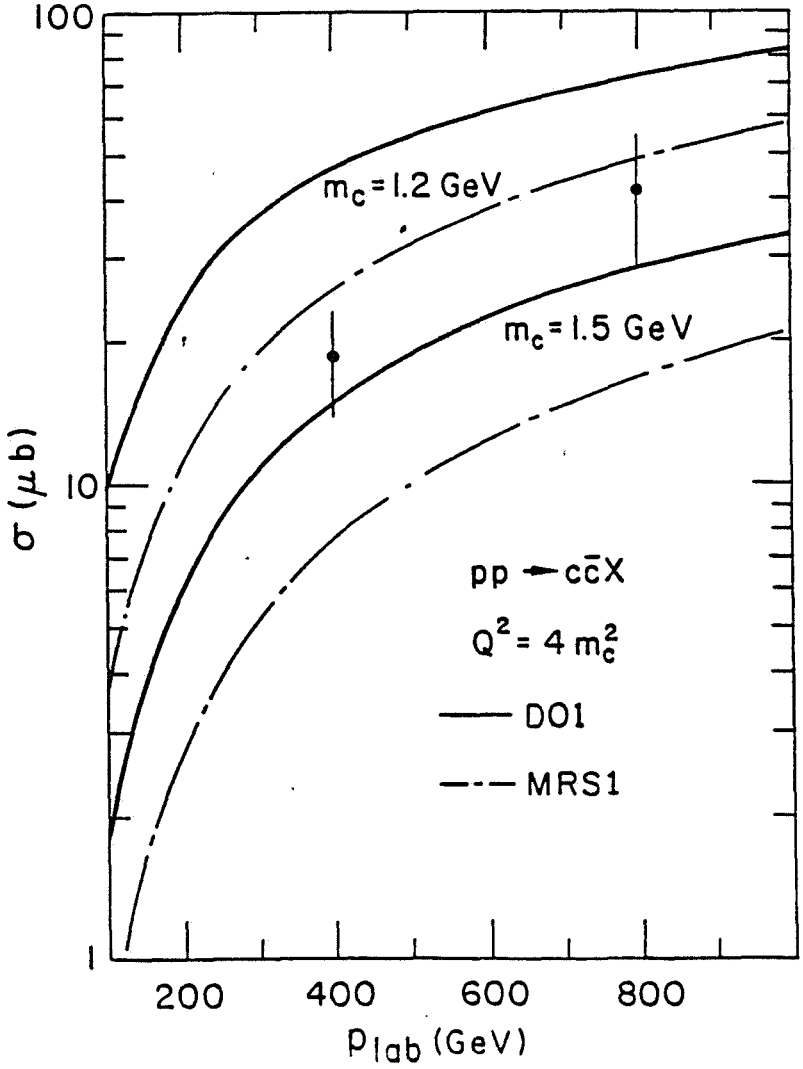

FIGURE B1b. Calculated energy dependence of charm production by protons from Ref. 8.

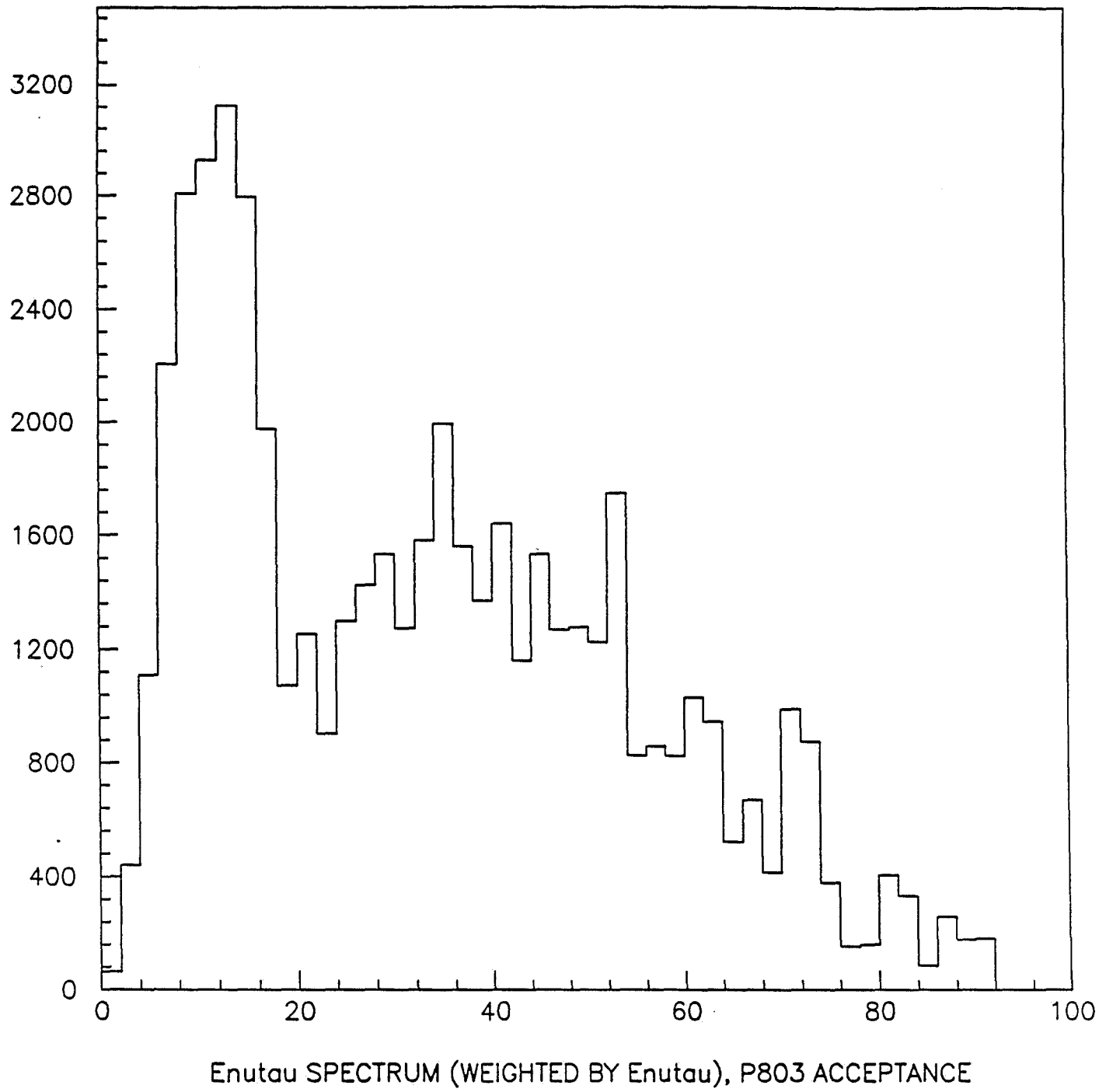

FIGURE B2. Calculated energy spectrum (weighted by E_ν) of direct ν_τ within the geometrical acceptance of P803. For this simulation the primary proton energy was 120 GeV, and the production of D_s was assumed $\propto (1 - x_F)^{2.5}$.

Appendix C

DETAILS OF EMULSION MOUNTING AND ANALYSIS

A. Mounting of Active Target Components

The emulsion target and decay analyzer for P803 has a volume of $180 \times 180 \times 7.5$ cm^3 and a mass of 0.84 tons. It is segmented in depth into 3 modules, each containing "bulk" emulsion 2.5 cm deep, a (changeable) interface sheet, and scintillating fibers. As discussed in the body of the proposal, the purpose of the fibers and interface sheet is to provide a high-precision vernier for matching drift chamber tracks to those in the emulsion. The arrangement of these components and a mechanical mounting scheme for them are shown in Figs. C1 and C2. The interface sheets have been designed to be changed several times during the experiment (as was done in Fermilab experiment E531 [1]) if the density of background muon tracks from the shielding is high enough to require this measure.

B. Scanning of Emulsion

1. Miniplate technique. The "bulk" emulsion in the active target is actually comprised of sheets 90×90 cm^2 in area and 1 mm thick; each sheet has two layers of emulsion coated on a thin plastic base to preserve dimensional stability, a well-proven [1],[2] technique. Before the bulk emulsion is scanned, the large sheets are cut up into 5 cm $\times$ 5 cm squares and mounted 25 at a time on a "miniplate" 25 cm $\times$ 25 cm square (Fig. C3). These 25 squares are chosen to be consecutive in depth, so that a miniplate contains all the emulsion information in a tower 5×5 cm^2 wide and 2.5 cm deep. Any position in any square in the miniplate can be accessed by computer control of the large-stroke microscope stage, allowing any track in the tower to be followed quickly from sheet to sheet through the depth of the tower.

This miniplate technique worked very well in Fermilab experiment E653 [2], resulting in a sheet-to-sheet traceback location time of 0.5 to 1 minute per plate, compared to 2 to 5 minutes per plate in the earlier E531 experiment in which this technique was not used. However, it requires careful calibration [2] of the coordinates on each mounted square. For the large volume of emulsion to be used in P803, it is estimated that 30 man-months will be needed after development of the emulsion for assembling the miniplates, and an additional 30 man-months for calibration. This effort proceeds in parallel with the calibration and software tuning of the electronic portions of the hybrid detector.

2. Time estimate for scanning and decay search. The key to rapid processing of a large number of scan candidates is the fully automatic scanning [3] in the interface sheet for the leading track which is to be followed back to the primary vertex. A flow chart for this fully automatic process is shown in Fig. C4. The interface sheet consists of thin layers of emulsion on both side of a plastic base 0.5 mm thick; the track coordinates in the separated layers form a 3-dimensional pointer with 2 milliradian accuracy. Once this high-precision pointer in the interface sheet is found, the leading track is located in the most downstream square of

the miniplate tower and followed back to the primary vertex. This step is done by a semiautomatic system in which a human scanner watching a TV monitor guides the computer control. When the vertex is found, all tracks within 15° of the beam direction are followed out for 2.5 mm under semiautomatic control looking for kinks, which are the candidate τ decays. The approximate time needed for each of these steps is shown below.

Time Estimate for Emulsion Analysis

Interface sheet scanning by automatic system	2–3 minutes/event
Traceback of leading track by semiautomatic system	15–20 minutes/event
Search for τ decay candidates by semiautomatic system	30–60 minutes/event

One fully automatic system can process 6×10^4 events per year. One scanner-operated semiautomatic system can handle 20 events per day. For the 15 such semiautomatic systems which will exist among the institutions collaborating in the emulsion analysis, a total of 300 events per day can be processed. Thus the emulsion analysis of the first 6×10^4 events will take about two years.

REFERENCES FOR APPENDIX C

1. N. Ushida et al., Nuc. Instr. and Meth. **224**, 50 (1984).
2. K. Kodama et al., Nuc. Instr. and Meth. **A289**, 146 (1990).
3. S. Aoki, Ph.D. thesis, Nagoya University (1990); S. Aoki et al., to be published in Nuclear Instruments and Methods.

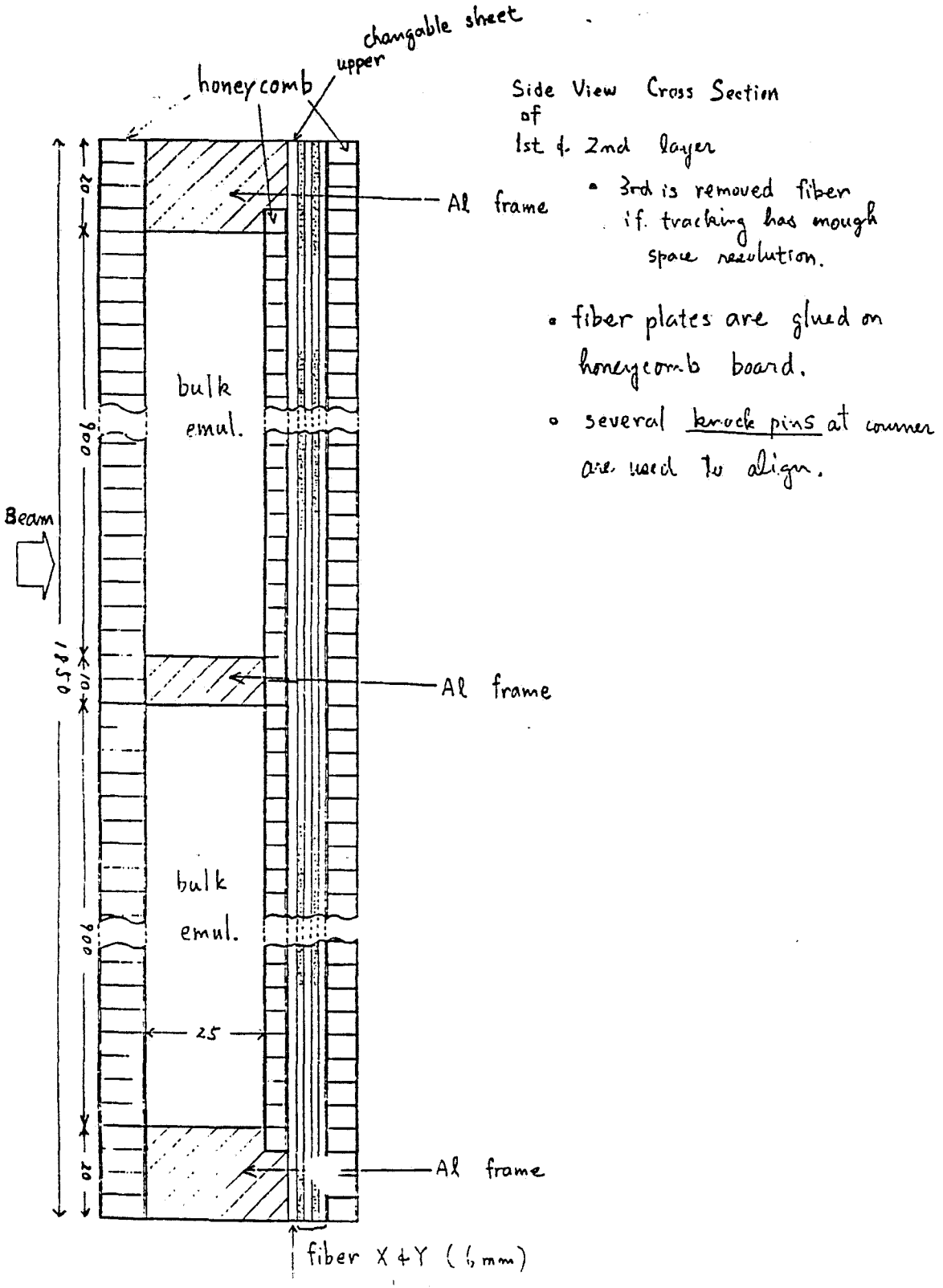

FIGURE C1. Schematic layout of an active target module, showing the mounting of bulk emulsion, (changeable) interface sheet, and optical fibers. The target consists of a stack of three of these modules along the beam direction.

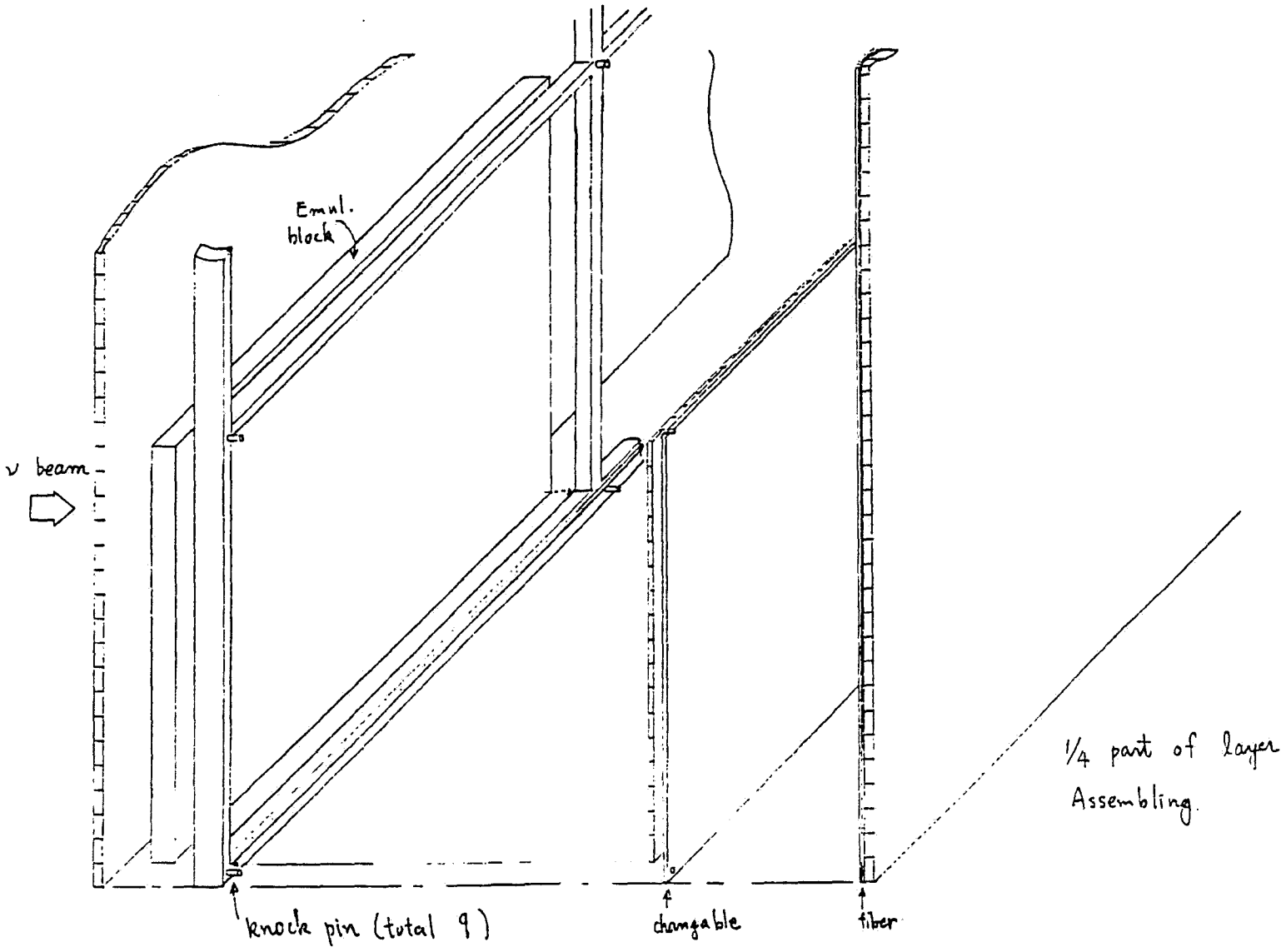

FIGURE C2. Exploded view showing assembly details of bulk emulsion, changeable sheet, and optical fibers.

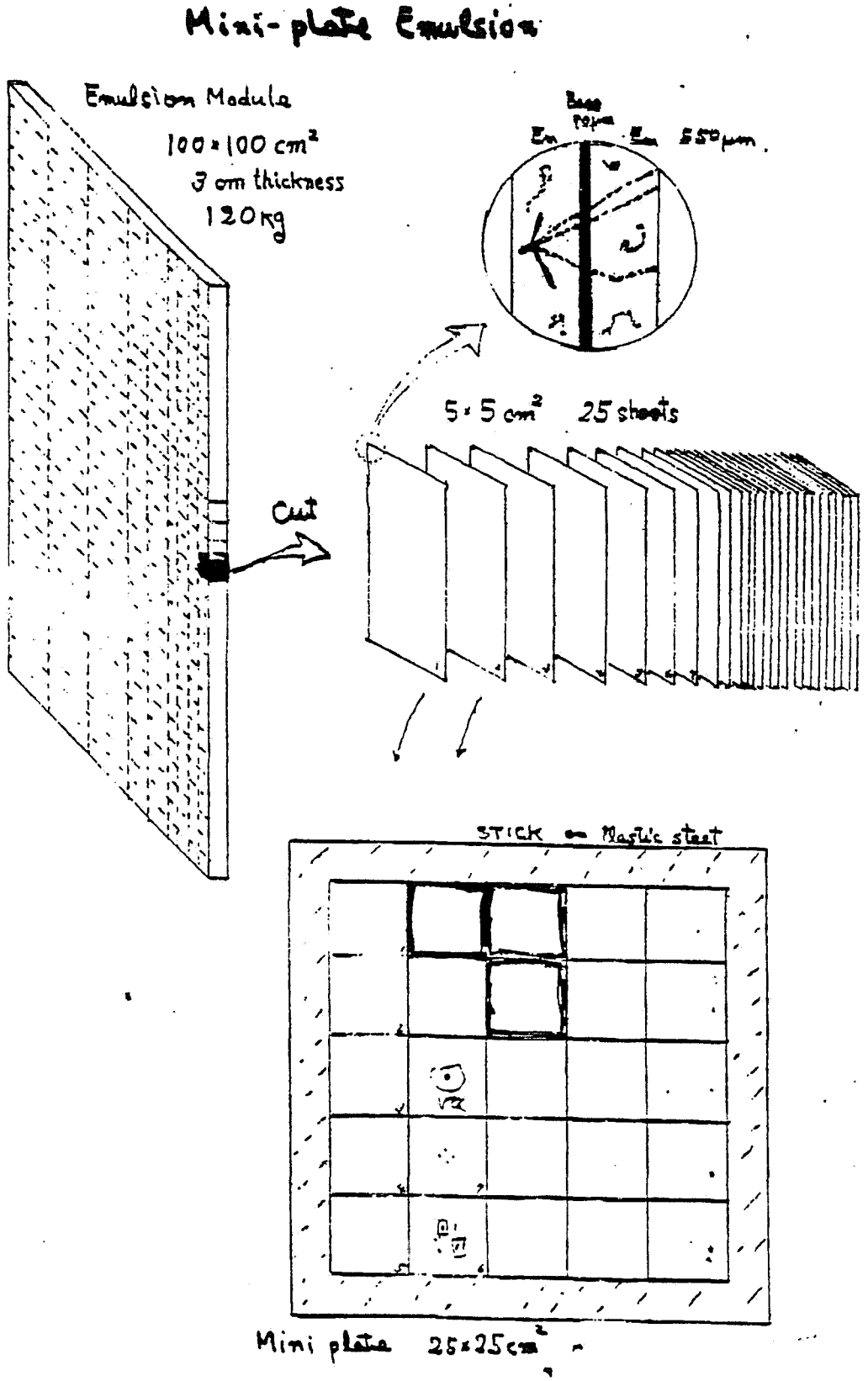

FIGURE C3. Schematic drawing illustrating the mounting of squares of emulsion on a miniplate containing information on an emulsion tower 5 × 5 cm^2 wide and 2.5 cm deep.

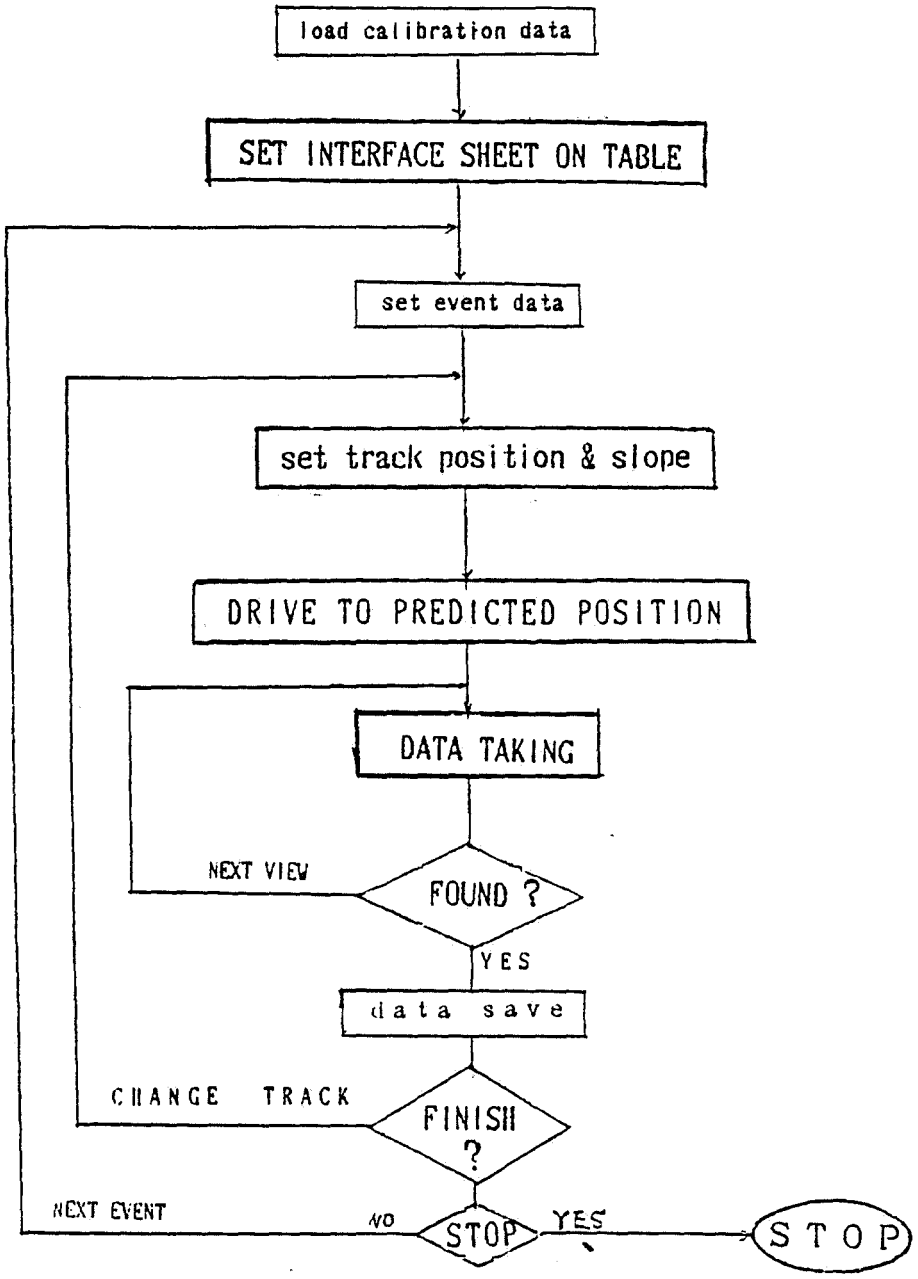

FIGURE C4. Flow chart for scanning of interface sheets by the fully automatic system.

Appendix D

MEASUREMENT OF THE MEAN FREE PATH AND TRANSVERSE MOMENTUM DEPENDENCE OF WHITESTAR KINKS

The dominant background to hadronic τ decays in this experiment is expected to be single-prong interactions of tracks from the primary vertex which show no evidence of nuclear breakup, called whitestar kinks (WSK's). As discussed in the main body of the proposal, knowledge of the mean free path (mfp) for WSK's as a function of the transverse momentum p_T relative to the parent direction is essential for understanding the achievable sensitivity. An experiment has been performed at KEK by members of this collaboration to measure this quantity with π^- beams of 2 and 4 GeV/c. Another measurement for momenta of 10 and 15 GeV/c is planned at Fermilab.

The setup for the KEK experiment is shown in Fig. D1; it was performed in a magnetic field of 1.2 Tesla. The emulsion was divided into a main block which acted as a target and kink analyzer, and sheets separated by low-density spacers in which the secondaries were detected. The π^- beam was 2×2 cm^2 in area, and contained a 3% contamination of electrons. The emulsion was exposed to a density of 10^5 to 10^6 tracks/cm^2.

At the present time about half of the 4 GeV/c sample has been scanned by both the beam-following and scan-back methods. The results presented here are based on a preliminary analysis which does not use the information on the momenta of the secondary tracks which is available from bending in the magnetic field; it is assumed that the p_T of the kink is the product of kink angle and the parent momentum. Therefore, WSK's due to bremsstrahlung by the electron contamination in the beam have not been removed. Since the interest for P803 is in kinks with p_T above about 0.2 GeV/c, the scan was allowed to be inefficient for kinks with angle less than about 0.03 radians.

A total of 727 multiprong interactions, and 145 kink interactions with angle $\geq$ 0.2 radians, were found. These include 58 WSK's and 87 kinks with evidence of nuclear breakup (dark evaporation tracks or blobs). The 817 interactions correspond to the known mean free path of 50 cm for π^- in emulsion.

The p_T spectra of all kinks, and for WSK's, are shown in Fig. D2; there are no WSK events between 0.3 and 0.6 GeV/c, and one additional WSK event (off scale) with a $p_T >$ 0.6 GeV/c. As shown in this figure, the total kink sample has a p_T dependence above 0.1 GeV/c of approximately e^{-10p_T}, while the WSK's have a much steeper dependence of about e^{-20p_T}. There are 8 WSK with $p_T \geq$ 0.2 GeV/c, corresponding to a mfp of (0.50 m)$\cdot$(817)/(8$\pm$2.8) = (50$\pm$18) m. The exponential p_T dependence then implies a mfp of (370 $\pm$ 130) m for p_T above 0.3 GeV/c.

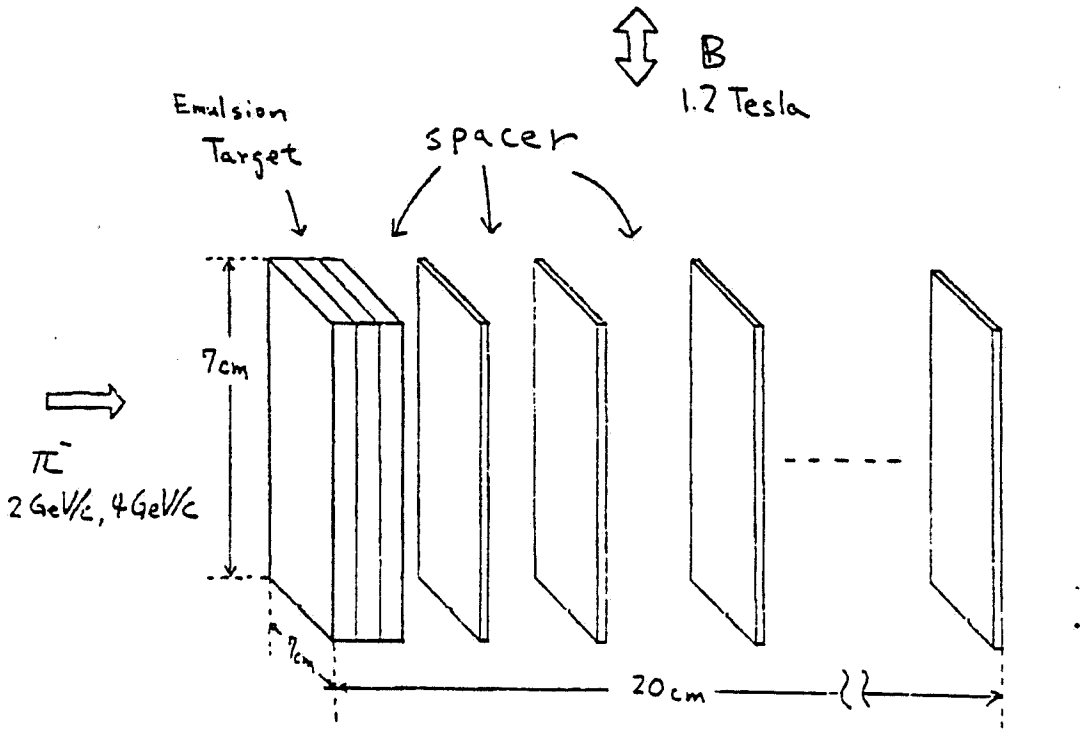

Fig 1.

FIGURE D1. Sketch of the experimental setup used in the KEK exposure.

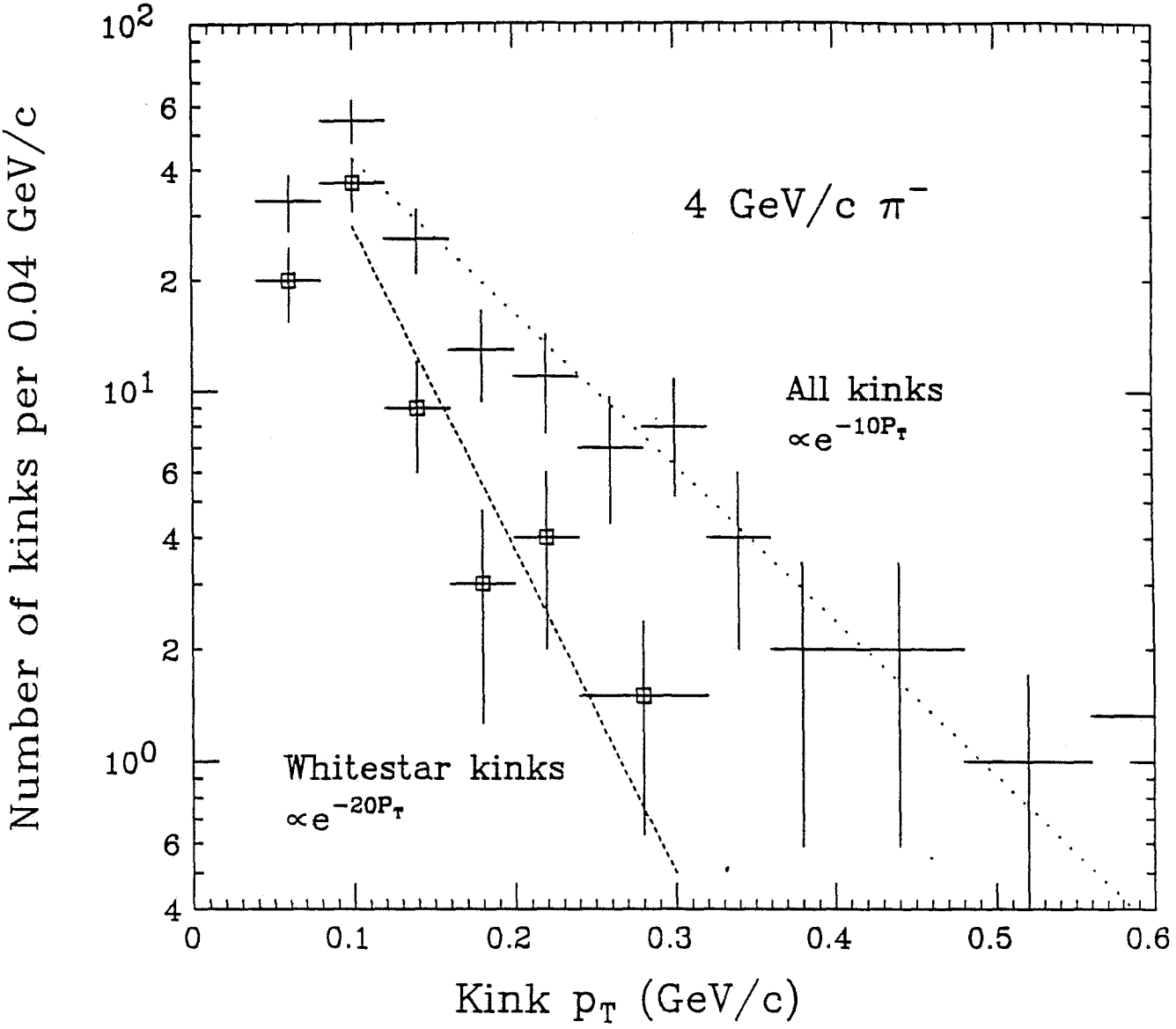

FIGURE D2. Preliminary results from the KEK exposure with 4.0 GeV/c π^-. Number vs. p_T for all kinks (crosses) and whitestar kinks (squares). There is one additional WSK event above 0.6 GeV/c. The p_T dependences for $p_T > 0.1$ GeV/c are indicated by the dotted and dashed lines.

Appendix E

IMAGE INTENSIFIERS FOR READOUT OF SCINTILLATING FIBERS

Use of scintillating fibers in P803 is made more difficult by the ubiquitous fringe field of the detection magnet. A promising solution to this problem is the detection system shown conceptually in Fig. E1, which is insensitive to magnetic fields. This design is based on a modification of an existing product from Hamamatsu, Inc. (Figs. E2, E3) to eliminate the electron lens and operate with a small distance between the cathode and the first microchannel plate. A phosphor screen provides a short-term memory of 1 μsec so that a later stage can be gated by the event trigger.

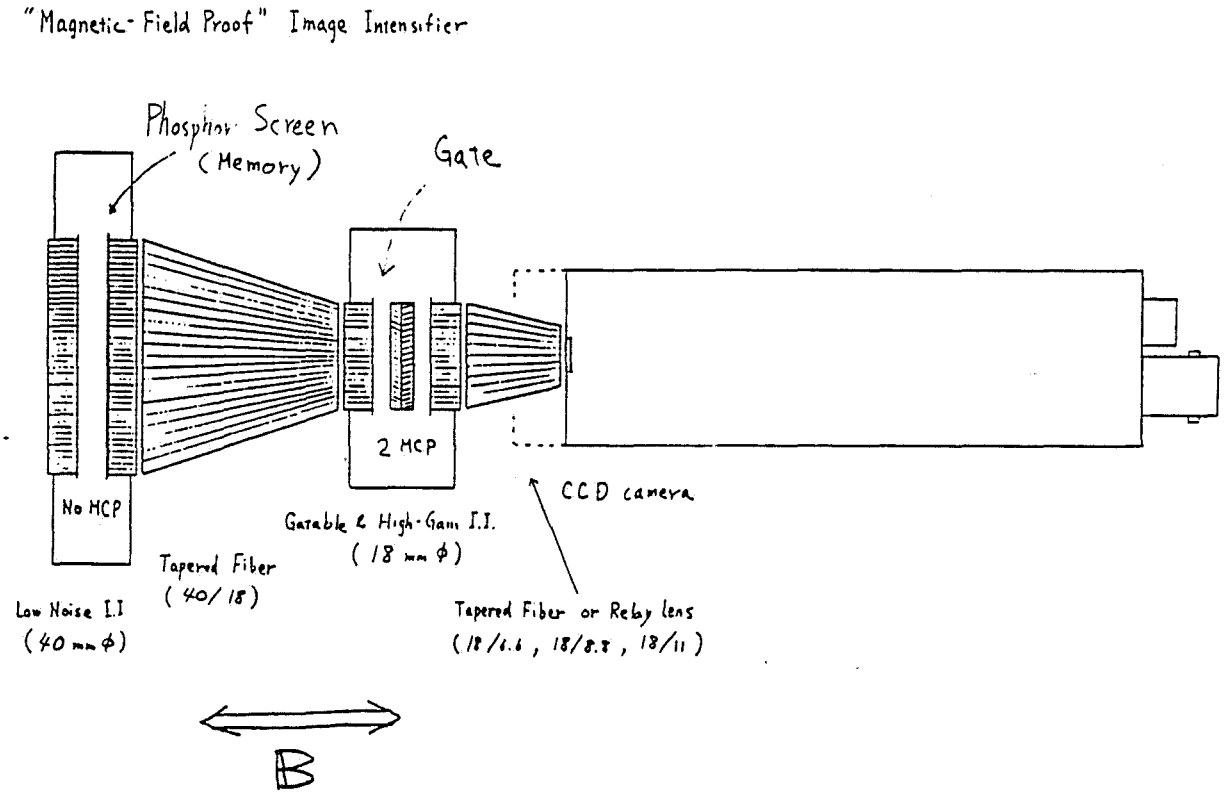

FIGURE E1. Conceptual design of the imaging system.

HAMAMATSU

Sep. 1989

4 INCH(100mm) DIAMETER
IMAGE INTENSIFIER/CASCADED I.I.
WITH CCD CAMERA

APPLICATIONS

- Scintillation Fiber Read Out
- X-ray Radiography
- Particle Physics

CONFIGURATION

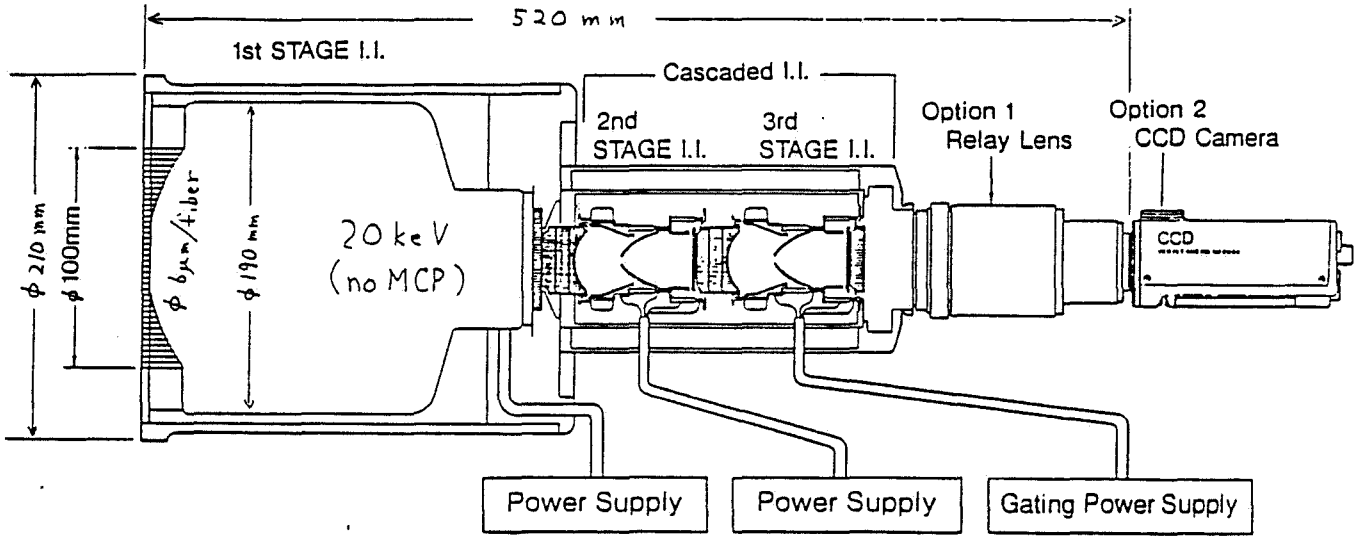

FIGURE E2. The unmodified Hamamatsu cascaded image intensifier.

図-1 (A) インバータ型イメージインテンシファイアの構造(V1366)

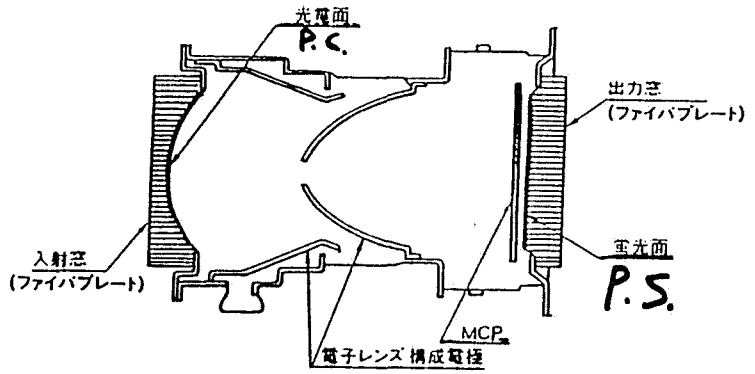

図-1 (B) 近接型イメージインテンシファイアの構造(V2697)

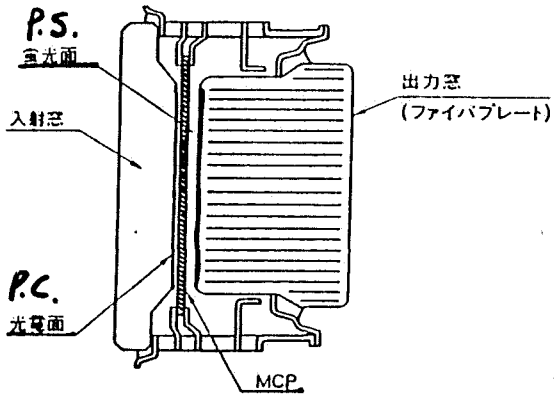

HAMAMATSU
T-2000

図-6 MCPの模式図

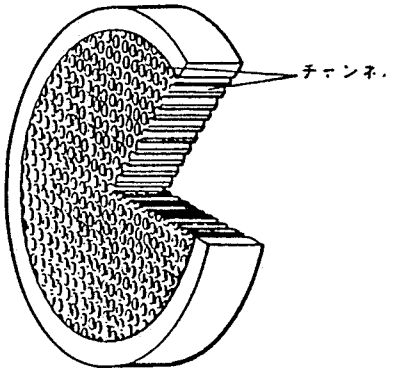

図-7 MCPの増倍原理

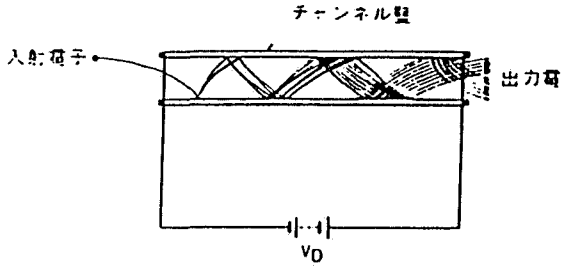

FIGURE E3. Modifications to first stage of the Hamamatsu cascaded image intensifier to eliminate the electron lens.

Appendix F

CONSTRUCTION OF THE ELECTROMAGNETIC CALORIMETER (EMCAL)

The EMCAL consists of 23 alternating layers of lead and proportional tubes, as shown in Fig. F1. Much of the design and many of the construction techniques have been borrowed from the AMY barrel calorimeter [1], which operates in a magnetic field in a similar energy regime. The proportional tubes (Fig. F2) are made of conductive plastic tubes extruded under controlled conditions to ensure that the conductivity of the tube walls does not vary excessively along the tube length and in different batches. The tube has inside dimensions 7 mm $\times$9.2 mm, and a wall thickness of 0.8 mm. The resistivity of the wall material will be about 50 KΩ/square. Gold plated wires of 50 microns diameter will be strung with a tension of 250 g. The wires will be passed through the tubes and attached at the two ends to plastic Y pieces which fit into the inside of the tube walls. The center of the Y pieces will contain metallic inserts to which the wire will be soldered, epoxied and covered with plastic tubing.

The readout will be done with 1 cm strips parallel to the wires (x-strips) on one side and strips perpendicular to the wires (y-strips) on the other side of the tube plane. Strips at a small angle with the wires (u-strips) will provide a stereo view for half of the tubes. The readout strips will be made from double sided copper plated G-10, with one side serving as ground plane.

The 23 alternate layers of lead absorber, conducting plastic tubes, and readout board will be epoxied together to form one right module and one left module, each of dimensions 189 cm $\times$377 cm, as shown in Fig. F3. The breaking up of the calorimeter into two modules is done in order to avoid the difficulty of obtaining and handling a heavy lead absorber of 377 cm x 377 cm. Each of the two modules will be enclosed in a container that holds the gas, provides for the mounting of gas fittings and feedthrus to the detector, and serves as mechanical support. Each module will be built by bonding the planes on top of each other on a specially-constructed flat table [1] to preserve the flatness of the layers. Again for flatness, the thickness of the thin lead absorber (2.8 mm) in the front will be the nominal thickness purchased, and the thicker absorber planes (5.6 mm and 11.2 mm) should be made of multiple layers. A partial-vacuum bagging layer-by-layer bonding technique is to be used, with careful inspection, measurement and correction to insure flatness. A front and rear support plate will bonded to the module to facilitate fastening of the container. Because of this type of support, special care will be taken to obtain lead with low creep rate characteristics under shear stress. With this scheme of construction the wires will be vertical, the x- and u-strips will be read out from the top, whereas the y-strips (horizontal) will be read out from both left and right sides of the detector.

Reference for Appendix F

1. A. Abashian et al., "The Amy Barrel Electromagnetic Calorimeter at TRISTAN", draft preprint (1990); A. Abashian, private communication.

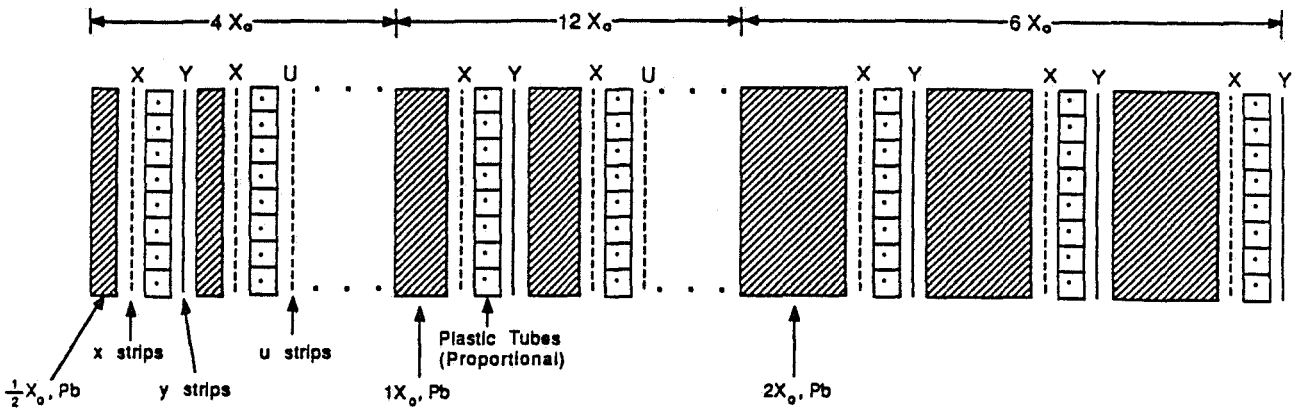

FIGURE F1. Layout of the electromagnetic calorimeter showing alternating layers of converter and proportional tubes.

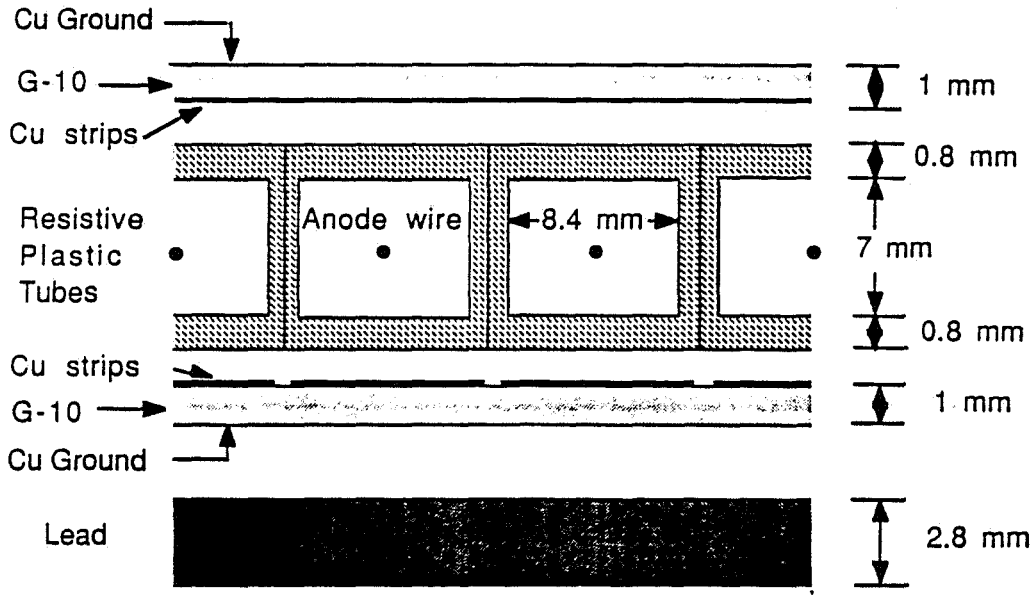

FIGURE F2. Detail of one EMCAL layer.

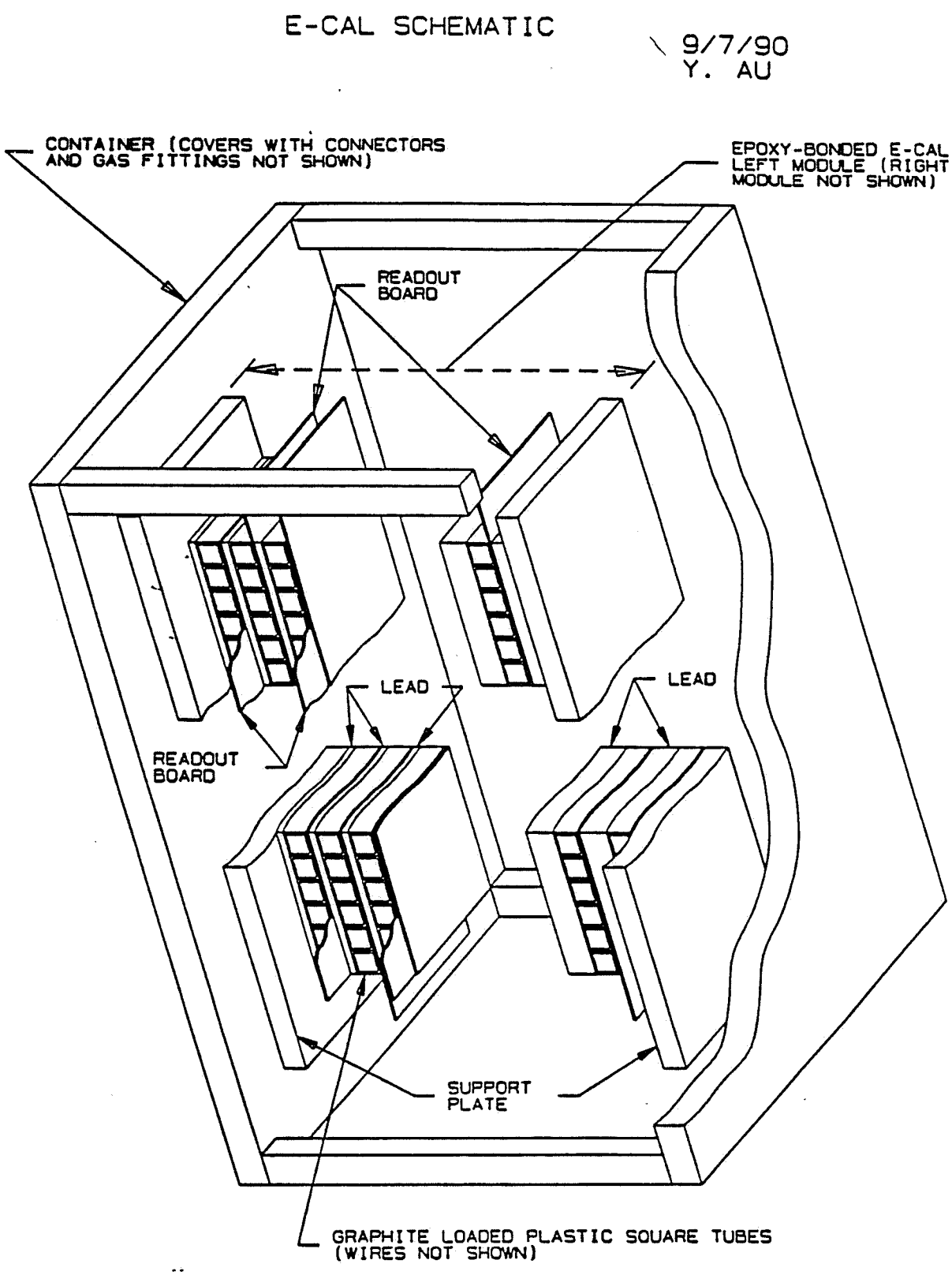

FIGURE F3. Schematic drawing of the mechanical mounting scheme for the EMCAL.

Appendix G

CONSTRUCTION OF THE HADRON CALORIMETER (HADCAL)

The main purpose of the P803 hadron calorimeter is to identify muons. This device consists of 24 alternating layers of nonmagnetic absorber (5 cm of zinc) and limited streamer chambers (Iarocci tubes), as shown in Fig. G1.

Iarocci tubes [1],[2] have been successfully used for long periods of time in several experiments (NUSEX, UA1, CHARM II); they are rugged and allow mass production techniques in large quantities at relatively low cost [3]. They would be constructed in sets of 8 tubes per module, each 4.2 meters long, as shown in Fig. G2. Modules would consist of PVC tubes with a square profile of 0.9×0.9 cm^2 and 0.1 cm walls coated on the inside with high-resistivity graphite paint (100 KΩ to 1 MΩ per square) to form the cathode surface. Cu/Be anode wires of 100 micron diameter would be strung down the middle of the cell at 250 grams tension, supported at intervals of approximately 50 cm by PVC spacers. Each strung profile will then be inserted inside a PVC sleeve which will form the gas volume. An arrangement with double sleeves will be used in order to retain the flexibility of replacing modules. Only the outer sleeves will be inaccessible, while their contents could slide in and out.

The cathodes are transparent to the chamber signal, allowing readout from strips, 2 cm in width, glued on both sides of the outer sleeve. One set of these strips reads out the bend plane coordinate (x) on all layers of tubes, while the set on the other side alternates between the nonbend coordinate (y) and a stereo view (u). These strips will then be ganged two layers deep, as discussed in the main body of the proposal.

These chambers would be operated in the streamer mode, probably with an argon-isobutane 1:3 mixture at a voltage of approximately 4.7 kV, though other mixtures are possible [4]. The resulting signals from the strips are comfortably large (about 10 picocoulombs per strip), avoiding signal-to-noise problems and permitting the use of inexpensive electronics.

The construction of the hadron calorimeter is shown conceptually in Fig. G3. The hadron calorimeter utilizes the mechanical strength of the zinc absorber plates to form a receiver structure with vertical slots to allow panels made of Iarocci tubes to slide in and be locked downed. The zinc panels will be mechanically fastened together with spacers at the two sides to create slots for the Iarocci panels. For the ease of handling, each zinc panel consists of 3 zinc plates. For the requirement of flatness, each plate is made with laminated thin zinc sheets using a flat table and partial-vacuum bagging technique. The Iarocci panels will be constructed by the conventional method. Each tube contains 8 wires with conductively painted partitions and end caps with gas fittings and feedthrus. A layer of tubes is covered with a readout board in front and a readout board in the back. Each readout board has 2 cm wide copper strips in the appropriate direction on one side and copper ground plane on the other side.

References for Appendix G

1. E. Iarocci, Nuc. Instr. and Meth. **217**, 30 (1983).
2. G. Batistoni, et al., Nuc. Instr. and Meth. **A245**, 277 (1986).
3. W. Busza, Nuc. Instr. and Meth. **A265**, 210 (1988).
4. G. Bagliesi, et al., Nuc. Instr. and Meth. **A268**, 144 (1988).

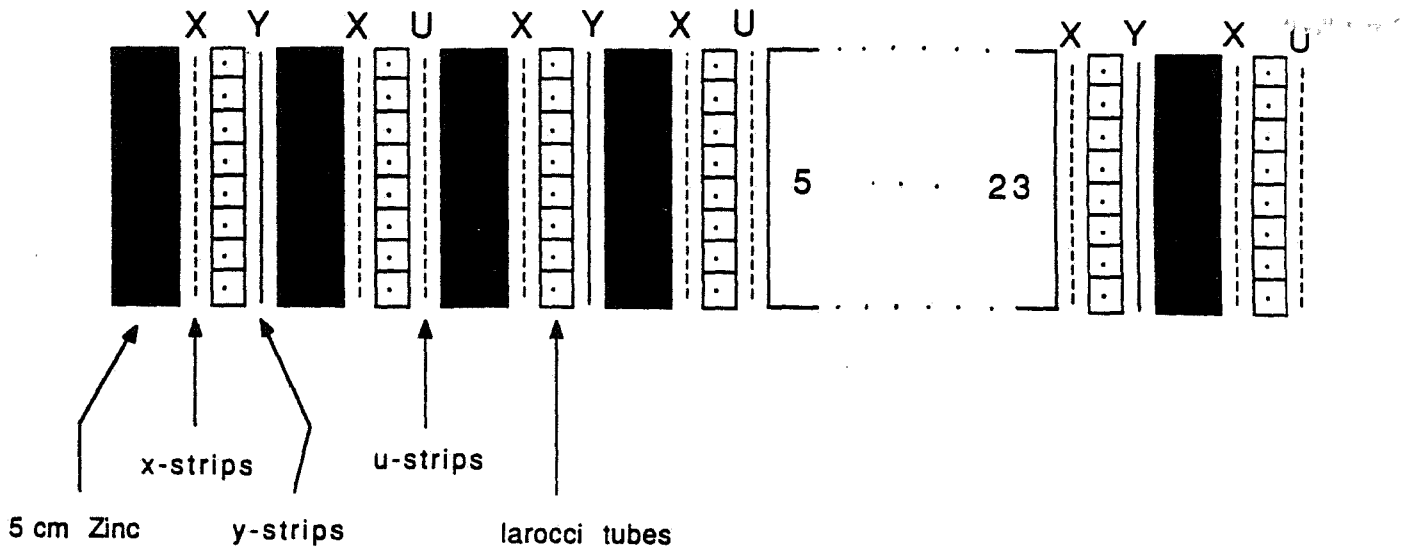

FIGURE G1. Schematic layout of the hadron calorimeter, showing alternating layers of absorber and Iarocci tubes.

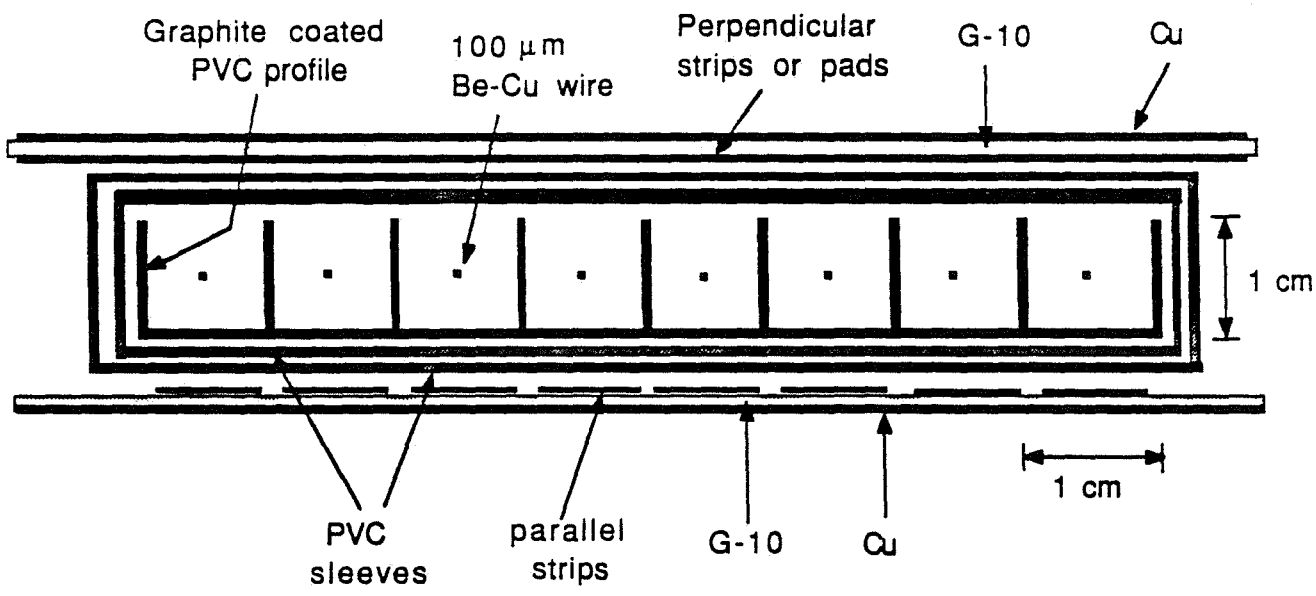

FIGURE G2. Details of the Iarocci tube design.

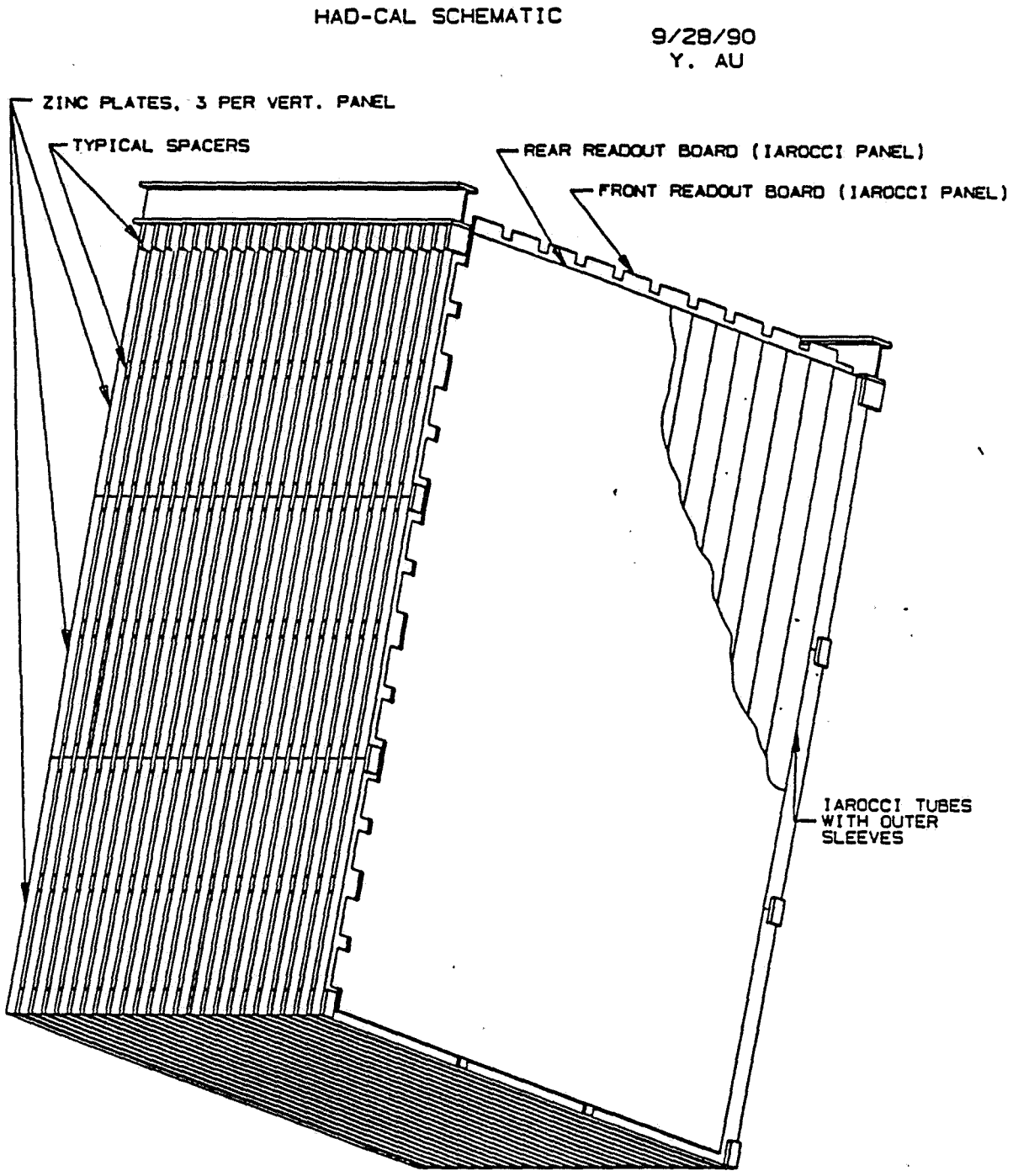

FIGURE G3. Mecanical construction of the hadron calorimeter.

Appendix H

CALORIMETER ELECTRONICS

Both EMCAL and HADCAL will measure energy deposited in the calorimeter and thus the electronics can be almost identical. The energy measurement in the EMCAL will result from from measurement of the total charge in a shower, by integrating the pulses from the proportional tubes. The energy measurement in the HADCAL will result from measurement of the total number of streamers produced by the hadronic shower particles in the limited streamer tubes, which in turn is proportional to the total charge measured by the device, despite the fact that the Iarocci tubes do not work in the proportional mode. Thus, the electronics can be the same with the exception of the front end, where different amplification and different impedance matching may be needed.

The design of the calorimeter electronics is shown in Figs. H1 and H2. The signal from each strip is amplified and integrated with a preamp hybrid, the output of which drives one of the inputs of a 4-channel S/H (sample-and-hold) circuit. A trigger from the detector system activates the HOLD. The analog output voltage drives one of the inputs of an 8-input multiplexer. A NIM signal generated by the trigger switches the S/H circuit from the TRACK to HOLD mode, and causes the sequential readout of 32 analog voltages from the S/H circuits by employing a controller that uses a programmable gate array. The controller generates control signals ENA1-4 and a 3-bit address to readout one by one the S/H outputs. The S/H signals are sent to the input of a 12-bit ADC for digitization and storage in a 1000-word deep FIFO memory, the output of which is connected to FASTBUS via a ribbon cable (which can be daisy chained). Between spills the FASTBUS initiates the readout of 32 channels, performs zero suppression and generates channel addresses and pulse heights to be sent to the computer.

This design emphasizes onboard digitization, local storage, all-digital readout, and storage of multiple events before readout. All circuit components starting from the preamp and including the FIFO memory will be mounted on a board residing on the detector. Thirty-two strips with 1 cm spacing can be instrumented on a 12" x 6" circuit board. This design should process an event in about 100 microseconds, which can be easily reduced if necessary by using a faster ADC. Many boards can be connected together on a common cable for readout and control. This will minimize cabling costs and complexity. Several events can be stored on the cards. Cards can be read out during the digitization of the event, or several events can be stored on the card and read out after the spill.

In the proposed scheme the energy of a shower is measured twice: once with the x-strips and once more with the y- or u-strips. One could consider the alternative of measuring the y- and u-strips digitally (yes/no) only. However, the redundancy in the energy measurement will be necessary in the analysis in order to correlate the orthogonal projections of the showers and tracks and associate them in three dimensions. Otherwise very small pads (instead of strips) would be necessary, a rather expensive option.

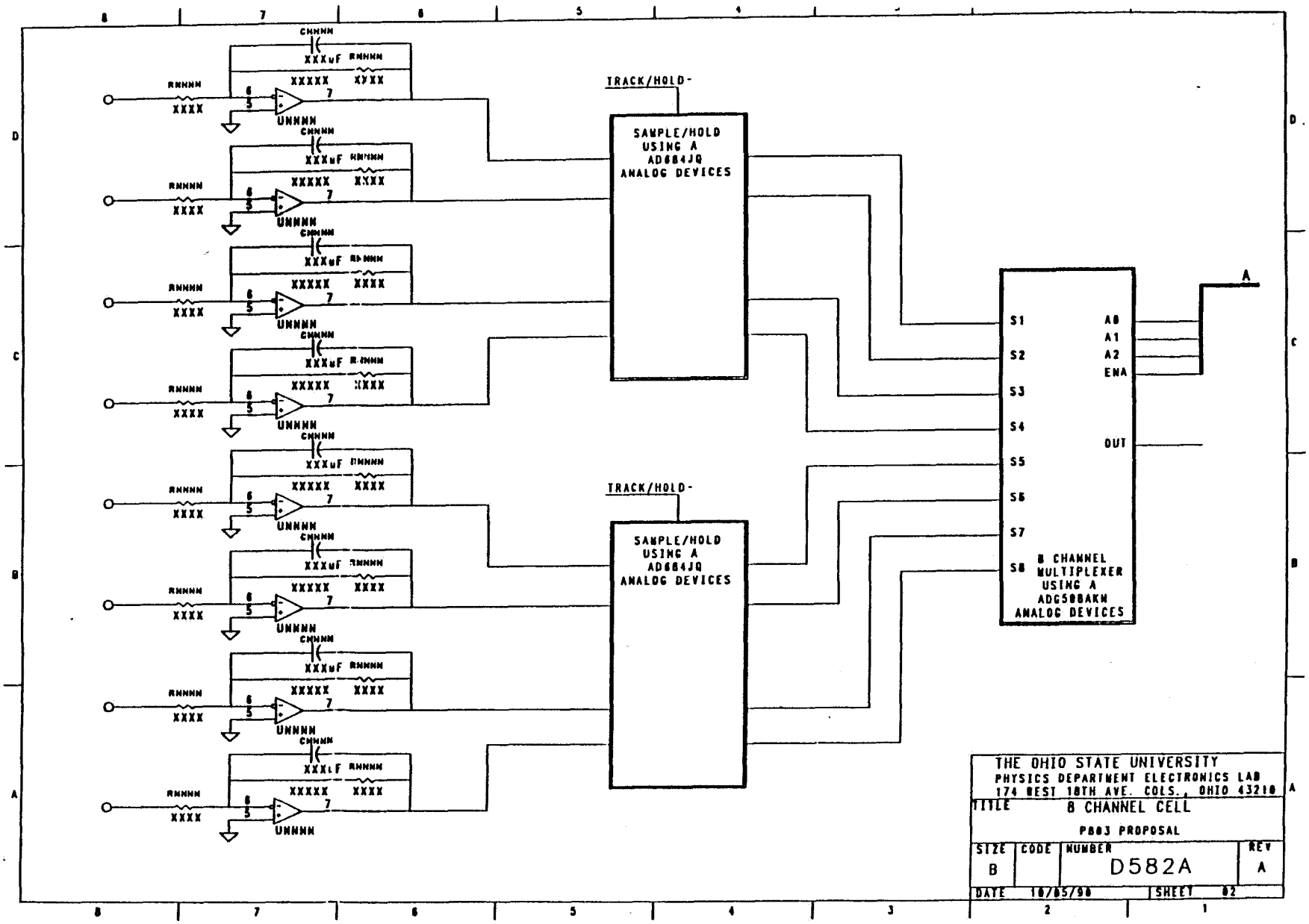

FIGURE H1. Schematic for the 8-channel cell.

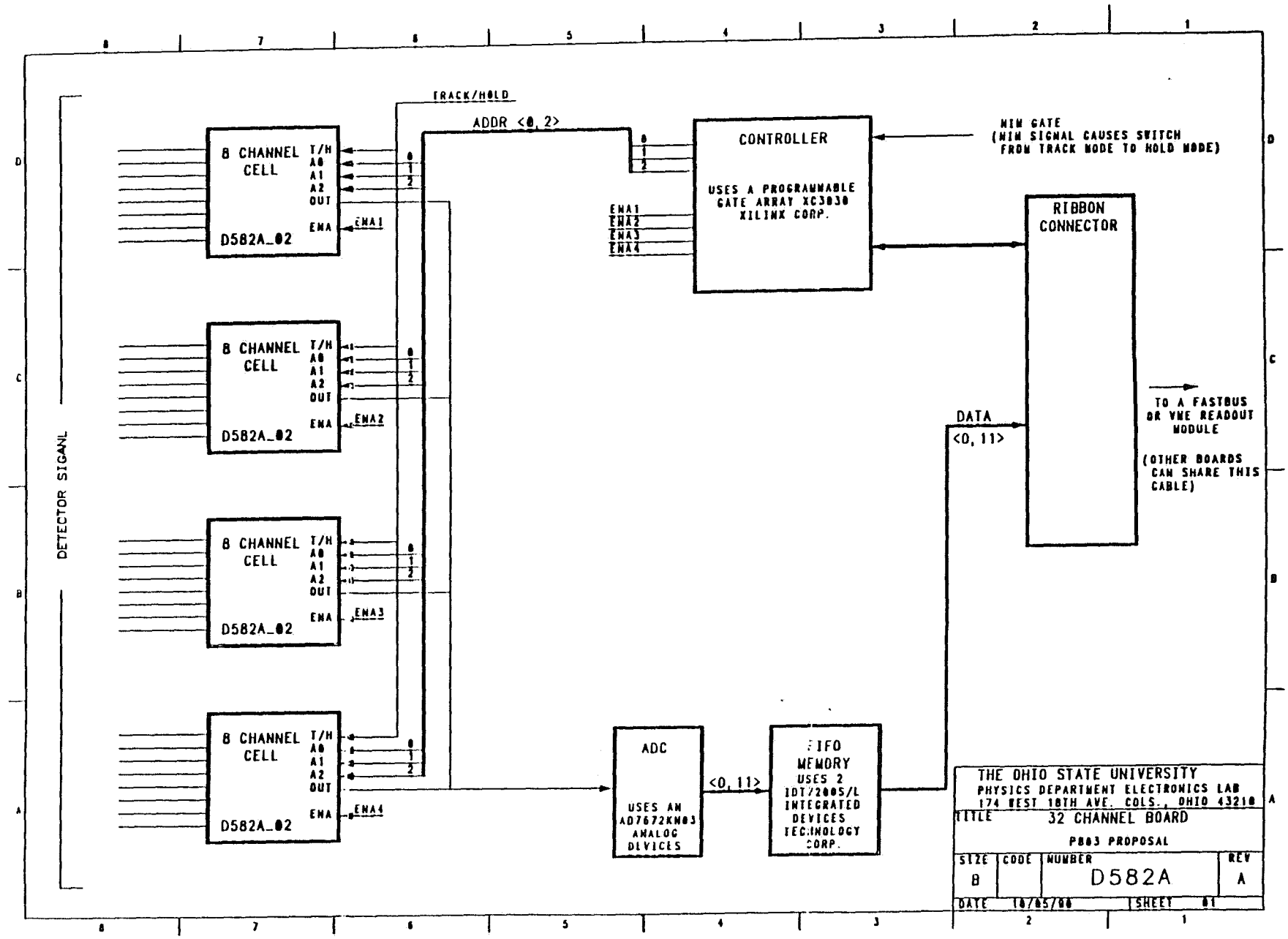

FIGURE H2. Schematic for the 32-channel board.

Appendix I

CALORIMETER CALIBRATION

Both EMCAL and HADCAL will be calibrated with electrons, pions, and muons in a test beam, where test modules identical in structure with the real calorimeters will be installed. In addition, the calorimeters will be continously calibrated on line with external electron, pion, and muon beams brought to the detector. The small window in the magnet coil (about 2'×1') poses a problem for calibrating the calorimeter above and below the central region, whereas in the horizontal direction one can use the magnet to deflect the beam somewhat left and right.

Using cosmic ray muons one can monitor the whole calorimeter and in addition calibrate the out of reach parts by proper scaling of the measured response. Scale factors are extracted by comparing the response of the central part of the calorimeter to cosmic ray muons on one side and to electrons, pions, and muons on the other. With these data one can determine response variations as a function of time (atmospheric pressure changes, etc) and extract the dependence of calorimeter response on energy. In addition, with these data one can determine the necessary criteria to allow for electron/pion/muon separation.

A different solution to the calibration problem is to design the calorimeters to move up and down vertically via hydraulic control, and thus reach and calibrate all parts of the calorimeter directly with external beams. The open structure of the magnet makes such a scheme possible.

FERMILAB P803 PROPOSAL

October, 1993

MUON NEUTRINO TO TAU NEUTRINO OSCILLATIONS

K. Kodama and N. Ushida
Aichi University of Education, Kariya 448, JAPAN

G. S. Tzanakos
University of Athens, Athens, GREECE

P. M. Yager and V. S. Paolone
University of California (Davis), Davis, CA 95616

C.H. Hahn
Changwon National University, KOREA

J.Y. Kim
Chonnam National University, Kwangju 500-757, KOREA

T. Bolton, J. Conrad and M. Shaevitz
Columbia University, New York, NY 10027

D. Bogert, G. Koizumi, B. Lundberg, A. J. Malensek, and R. Rameika
Fermilab, Batavia, IL 60510

J.S. Song and I.G. Park
Gyeonjsang National University, Jinju 660-300, KOREA

K. Nakazawa and S. Tasaka
Gifu University, Gifu 501-11, JAPAN

S. Kuramata
Hirosaki University, Hirosaki 036, JAPAN

N. W. Reay*, R. A. Sidwell, and N. R. Stanton
Kansas State University, Manhattan, KS 66506

K. Green, D. Levin, J. Matthews, D. Nitz, G. Tarle, R. Thun, and J. Van der Velde
University of Michigan, Ann Arbor, MI 48109

R. W. Rusack and V. Singh
University of Minnesota, Minneapolis, MN 55455

M. Chikawa
Kinki University, Higashi-Osaka 577, JAPAN

S. Aoki and T. Hara
Kobe University, Kobe 657, JAPAN

Jae Kwan Kim
Korea Advanced Institute of Science and Technology, KOREA

J. S. Kang and C. O. Kim
Korea University, Seoul, KOREA

Y. Isokane and Y. Tsuneoka
Nagoya Institue of Technology, Nagoya 466, JAPAN

K. Hoshino, H. Kitamura, M. Kobayashi, M. Miyanishi, M. Nakamura, Y. Nakamura, S. Nakanishi, K. Niu, K. Niwa, M. Nomura, K. Saito, H. Tajima, K. Teraoka and S.Yoshida
Nagoya University, Nagoya 464-01, JAPAN

K. Moriyama and H. Shibata
Okayama University, Okayama 700, JAPAN

T. Okusawa, M. Teranaka, T. Tominaga, T. Yoshida and T. Watanabe
Osaka City University, Osaka 558, JAPAN

G. Fujioka and Y. Takahashi
Osaka University of Commerce, Higashi-Osaka 577, JAPAN

H. Okabe and J. Yokota
Science Education Institute of Osaka Prefecture, Osaka 558, JAPAN

O. Kusumoto
Soai University, Osaka 559, JAPAN

Jewan Kim
Seoul National University, Seoul, KOREA

F.T. Avignone and C. Rosenfeld
University of South Carolina, Columbia, SC 29208

J. Goldberg
Technion - Israel Institute of Technology, Haifa 32000, ISRAEL

M. Adachi, M. Kazuno, Y. Kobayashi, E. Niu, S. Ono, H. Shibuya, and Y. Umezawa
Toho University, Funabashi 274, JAPAN

A. Napier, W. P. Oliver, T. Kafka and J. Schneps
Tufts University, Medford, MA 02155

Y. Maeda
Yokohama National University, Yokohama 240,JAPAN

Y. Sato and I. Tezuka
Utsunomiya University, Utsunomiya 350, JAPAN

*Contact person.

Summary

P803 is a ν_τ appearance experiment sensitive to very small neutrino mixing angles and to neutrino mass differences in the cosmologically interesting region. It focuses on the ability to demonstrate an unambiguous τ signal if oscillations exist within a factor of five of its 90% confidence level sensitivity, $\sin^2(2\alpha) \leq 2.8 \times 10^{-5}$. Ultimate results from P803 will come from the very intense neutrino beams possible with the Fermilab Main Injector. However, P803 can achieve discovery potential superior to competing experiments in a shakedown run using a beam from the existing Main Ring, and then remain at the same site for Main Injector beam when it becomes available. Alternatively, P803 could run in the same beamline with the long-baseline experiment P822 (Soudan 2 detector) during the Main Injector era.

The P803 apparatus is a hybrid emulsion-electronic spectrometer. Candidates for τ decays are directly observed in the emulsion target, and information from the electronic spectrometer is used both to select and locate events to be scanned, and to provide momentum, energy, and particle identification for kinematic analysis of the τ candidates. A possible one-prong τ decay appears in the emulsion as a 'kink', with no evidence of nuclear breakup, in an outgoing track from a neutrino interaction; the emulsion kink track must be matched to a spectrometer track of measured momentum and negative charge.

This proposal replaces the P803 proposal submitted in October, 1990, and the update report of June, 1993. There have been major increases in sensitivity, reductions in cost, and simplifications in design since 1990. The estimate of total neutrino interactions available to P803 from the Main Injector has increased by more than a factor of four. A revised apparatus based on an inexpensive conventional air-gap magnet instead of the obsolete 15-foot bubble chamber magnet has made the experimental design simpler and cheaper. The recently-realized option of early oscillation running with Main Ring beam before the Main Injector provides major savings in civil construction costs, more timely results, and increased opportunity to do other physics with the same detector.

TABLE OF CONTENTS

LIST OF APPENDICES

1. Introduction

P803 is a ν_τ appearance experiment sensitive to very small neutrino mixing angles and to neutrino mass differences in the cosmologically interesting region. It focuses on the ability to demonstrate an unambiguous τ signal if oscillations exist within a factor of five of its 90% confidence level sensitivity, $\sin^2(2\alpha) \leq 2.8 \times 10^{-5}$. Ultimate results from P803 will come from the very intense neutrino beams possible with the Fermilab Main Injector. However, P803 can achieve discovery potential superior to competing experiments in a shakedown run using a beam from the existing Main Ring, and then remain at the same site for Main Injector beam when it becomes available. Alternatively, P803 could run in the same beamline with the long-baseline experiment P822 (Soudan 2 detector) during the Main Injector era.

The P803 apparatus is a hybrid emulsion-electronic spectrometer. Candidates for τ decays are directly observed in the emulsion target, and information from the electronic spectrometer is used both to select and locate events to be scanned, and to provide momentum, energy, and particle identification for kinematic analysis of the τ candidates. A possible one-prong[1] τ decay appears in the emulsion as a 'kink', with no evidence of nuclear breakup, in an outgoing track from a neutrino interaction; the emulsion kink track must be matched to a spectrometer track of measured momentum and negative charge[2].

This proposal replaces the P803 proposal submitted in October, 1990, and the update report of June, 1993. There have been major increases in sensitivity, reductions in cost, and simplifications in design since 1990. The estimate of total neutrino interactions available to P803 from the Main Injector has increased by more than a factor of four. A revised apparatus based on an inexpensive conventional air-gap magnet instead of the obsolete 15-foot bubble chamber magnet has made the experimental design simpler and cheaper. The recently-realized option of early oscillation running with Main Ring beam before the Main Injector provides major savings in civil construction costs, more timely results, and increased opportunity to do other physics with the same detector.

New collaborators have joined P803: the E815 contingent from Columbia University, and groups from the University of Michigan and Technion - Israel Institute of Technology. The Fermilab component of the collaboration has more than doubled.

[1] One-prong modes are chosen to discriminate against 'white-star' interactions and anticharm decays, which have a larger three-prong component.

[2] The beam is predominantly ν_μ rather than $\bar{\nu}_\mu$, hence τ^- rather than τ^+ is expected.

2. Physics

2.1 Motivation for ν_τ oscillation search

Interest in neutrino oscillations is even higher now than it was in 1990 [1]. There is an apparent deficit both of ν_e coming from the sun [2], [3], [4] and of ν_μ coming from atmospheric cosmic-ray interactions [5], [6], [7]. The recent COBE observations [8] suggest that 30% of the matter needed to close the universe could reside in hot dark matter, e.g. neutrinos. Cosmological arguments [1] assert that there is a window for the mass of the heaviest neutrino between 7 and 28 eV, and general arguments based on see-saw mechanisms [9] predict that ν_τ is by far the heaviest of the three neutrino species.

Accelerator searches are also being actively pursued. The CHORUS [10, 11] and NOMAD [12] experiments at CERN are now being staged; each claims an eventual sensitivity for $\nu_\mu \rightarrow \nu_\tau$ an order of magnitude better than that obtained [13] by E531 a decade ago. Within the past year, an ambitious long-baseline experiment (E889) to look for $\nu_\mu \rightarrow \nu_x$ has been approved at Brookhaven.

The probability for two-component neutrino oscillations is given by

$$PROB(\nu_a \rightarrow \nu_b) = \sin^2(2\alpha) \int \sin^2\left(1.27\,\delta m^2 \frac{L}{E_\nu}\right) d\left(\frac{L}{E_\nu}\right)$$

with $\delta m^2 = m_a^2 - m_b^2$ in eV^2, the source-to-detector distance L in meters and the neutrino energy E_ν in MeV. P803 short-baseline measurements made close to the source have the advantage of high statistics for investigating small mixing angles α for δm^2 above 5 eV^2, just the range which is cosmologically interesting.

2.2 Standard Model physics

The combination of 6×10^6 charged current interactions, an intermediate energy neutrino beam, high precision charged particle tracking, and emulsion-quality vertex resolution permits several high quality standard model measurements in the P803 experiment. These include the determination of the CKM matrix element V_{cd} to an accuracy approaching the unitarity limit; a 5% determination of the charm quark mass; a unique exploration of charm production dynamics in neutrino scattering; and the first precision extractions of the structure functions $F_2(x, Q^2)$ and $xF_3(x, Q^2)$ using neutrino data in an (x, Q^2) regime which overlaps comparable electroproduction data from SLAC.

This Standard Model physics is described in Appendix A. An alternate method (from the 1990 proposal) for determining V_{cd} to $\pm 3\%$, but with more model dependence, is presented in Appendix B.

2.3 Observation of directly-produced ν_τ's: P872

Another option for additional physics with the P803 detector which would result from a possible a Proton West location (see Section 5.2) for the P803 spectrometer, would be the capability of observing ν_τ's produced directly in an 800 GeV proton beam dump, as suggested in Letter of Intent P872. The physics of P872 is complimentary to the oscillation physics of P803: P872 is a probe for measuring properties of ν_τ interactions in their own right, and is not sensitive to oscillations at the expected level. Tests for conventional, Standard Model properties can be done as well as searches for more exotic processes.

P872 could use most of the same detector elements proposed for P803: an emulsion target with scintillation fiber tracking and a magnetic spectrometer. However, instead of targeting 120 GeV protons for a neutrino horn, P872 would dump 800 GeV protons 35 m from the emulsion target, and observe ν_τ's from decays of D_s produced in the dump.

3. The focus of P803: seeing τ's

When all proposed running is complete, the improved P803 will have a 90% confidence level sensitivity an order of magnitude better than that aimed for by CHORUS or NOMAD, and more than two orders of magnitude better than that obtained by E531. However, we believe that discovery potential is even more valuable than a greatly improved null limit. In contrast to the CERN experiments which emphasize the $\mu\nu\bar{\nu}$ and $e\nu\bar{\nu}$ modes, P803 concentrates on the ability to identify τ decays in the two-body and quasi-two-body modes $\pi^-\nu$ and $\rho^-\nu$ (with $\rho^- \rightarrow \pi^-\pi^0$), which have distinctive kinematic signatures and measurable proper decay times, in addition to the $e\nu\bar{\nu}$ mode.

The essential quantity in seeing a signal is the transverse momentum p_T of the measured decay products relative to the parent direction, which can be measured to better than 1 mr in the emulsion. A decay mode with only a neutrino unmeasured, such as $\tau \rightarrow \pi\nu$, has a pronounced Jacobian cusp at the maximum allowed p_T (Fig. 1a). As shown in Figs. 1b-1d, it is essential that momentum as well as direction be well-measured, since the cusp signature rapidly degrades as momentum resolution worsens. Of competing experiments worldwide, only P803 will have the apparatus to deliver a sharp edge. For example, CHORUS [10, 11] is designed[3] for a typical hadron momentum resolution of typically $\pm 18\%$ (Fig. 1d) while P803 will maintain a resolution of typically $\pm 3\%$ (Fig. 1c). NOMAD, which has no emulsion, does not measure the direction of the τ candidate and thus cannot see

any edge at all.

The p_T cusp technique has been proven to work on one-prong decays in emulsion, as shown by the preliminary result from E653[4] in Fig. 2. This plot is a histogram of p_T from one-prong muonic kinks found in the E653 emulsion. The clean cusp at the endpoint of the spectrum contains 23 events (of an eventual 70) of the purely leptonic decay $D_S \to \mu\nu$, which kinematically closely resembles $\tau \to \pi\nu$. The events at lower p_T in Fig. 2 come largely from $D^+ \to \bar{K}^0\mu\nu$, which has two missing neutrals. The lack of background events above the D_S mass shows the power of combining emulsion and electronic techniques. It should be noted that the product of cross section and branching ratio for $D_S \to \mu\nu$ is 10^{-3} of all produced charm, or roughly 10^{-6} of all 600 GeV π^- interactions in emulsion.

The ability to obtain proper decay times and correct lifetimes from one-prong decays in emulsion has also been demonstrated by E653; a momentum estimator developed for measuring lifetimes of unconstrained beauty decays [14] works well also for one-prong charm semileptonic decays. Fig. 3, unpublished data from E653, shows proper decay time distributions for 103 two-prong neutral charm decays, and for 101 one-prong charged charm decays with a muon; these events were found in the emulsion scan for beauty [14]. The resulting lifetimes are (0.40 ± 0.04) ps (neutral) and (0.81 ± 0.08) ps (charged); the former agrees well with the world average D^0 lifetime, and the latter is consistent with the average lifetime of the expected mix of D^+ and D_S decays. These momentum and lifetime estimation techniques are directly applicable to one-prong τ decays.

The quasi-two-body decay $\tau \to \rho^-\nu$ can be treated in a manner similar to $\tau \to \pi^-\nu$ by identifying the electromagnetic decay products from the ρ^- and adding their 4-vectors to that of the π^-. Since at least one gamma usually converts in the emulsion target, π^0's often must be assembled from several pieces. Fortunately, the π^0 multiplicity at our energies is small, and the π^0 from the τ decay is usually the most energetic one in the event.

In terms of a null limit, P803 will still have high efficiency for the $e\nu\bar{\nu}$ mode, although the larger flux of ν_μ charged current (CC) events and the consequent increase in scan load now preclude attempting to see $\tau \to \mu\nu\bar{\nu}$.

[3]In the July, 1993 reworking of the CHORUS proposal [11], the estimated momentum resolution is a factor 2 better than in the December, 1991 version [10].

[4]Fermilab E653 is a hybrid emulsion experiment in a 600 GeV π^- beam. Most of the emulsion participants, and many of the counter participants, of P803 are also in the E653 collaboration.

4. How the experiment is done

4.1 General considerations

P803 will operate in a double-horn, wideband neutrino beam which is predominately ν_μ, with an average energy of ν_μ charged-current (CC) interactions of 16 GeV. The ν_τ interaction cross section is suppressed at low energy by kinematic and helicity effects (Fig. 4), so that the average energy of a ν_τ interaction is significantly higher: if the ν_μ beam were to oscillate completely to ν_τ's, the average energy of a ν_τ CC interaction would be 26 GeV. Simulated momentum distributions for τ's from ν_τ CC interactions, and for μ's from ν_μ CC interactions, are compared in Fig. 5. Distributions of expected momenta and energies from τ decay modes of interest, and from ν_μ charged-current events, are given in Fig. 6. The decay products of produced τ's are on average considerably stiffer than particles in background events. For example, the average momentum of the π^- from $\tau \rightarrow \pi^-\nu$ is 4.2 times that of a negative hadron from the background, and the average energy of a γ from $\tau \rightarrow \rho^-\nu$ is 2.7 times that of a CC or NC γ. This feature is important in selecting events for scanning, and in kinematic reconstruction of τ candidates.

Because of the large number of neutrino interactions expected in P803, approximately 8×10^6, it is not possible to scan the emulsion for every neutrino interaction (as was done in E531) even though the event-handling capacity of the emulsion groups has increased by more than an order of magnitude since that experiment was done. A potentially τ-rich subset containing a few percent of the interactions must be selected from the spectrometer data for emulsion scanning, implying some detection efficiency losses from the necessary cuts. The spectrometer and the selection procedure must be designed to perform these cuts efficiently. Fig. 7 shows the resulting τ efficiency as a function of neutrino energy after selection.

The large number of neutrino interactions in P803 makes it imperative that the rate of background events be small and measurable. Since most interactions and charm decays are multiprong, a major reduction in background results from limiting the search to single-prong decay modes of τ^- (Table 1 [15]), in events in which there is no detected muon or electron from the primary vertex.

4.2 Beam and target parameters

Beam and target parameters for P803 are given in Table 2 for Main Injector running. The emulsion target is smaller in area and thickness than in the 1990 proposal, to eliminate regions with marginal beam flux and reconstruction efficiency. Predictions of Main Injector performance have become more optimistic since 1990, and the stated 6×10^{13} protons per 1.9 sec is a conservative estimate

TABLE 1.
Single-Prong Decay Modes of τ^-

Label	Decay Mode	Branching Ratio
1	$\mu^-\nu_\tau\overline{\nu_\mu}$	17.6%
2	$e^-\nu_\tau\overline{\nu_e}$	17.9%
3	$\pi^-\nu_\tau$, $K^-\nu_\tau$	12.7%
4	$\pi^-\pi^0\nu_\tau$	24.4%
5	$\pi^-\nu_\tau$ multi-γ	13.2%
	Total one-prongs	85.8%

(10^{14} protons and 1.5 sec are perhaps possible from the mature machine). One 8-month run is not a sensible return on the investment in building the beam and spectrometer, and does not realize the full physics potential of the experiment. We assume here that there will be four 8-month runs spread out over several years, and that the total number of protons will be 6.3 times that in the 1990 proposal: 13×10^{20}. The resulting number of interactions in the target is 4.2 times greater than in the 1990 P803 proposal. Sensitivity equal to that anticipated by either of the CERN experiments will be achieved in only a few months of running.

4.3 Summary of procedure

Virtually every neutrino interaction in the emulsion target will be recorded on tape. Analysis then proceeds as follows: First, events recorded on tape are reconstructed. A subset is then selected for scanning in the emulsion. The primary neutrino interaction vertex is found by linking one track (the "leading track") from the spectrometer tracking to the downstream face of the emulsion, and following it back to the primary.

The features of a tau decay candidate in the emulsion are indicated schematically in Fig. 8. Because of the relatively large mass of the τ, it is produced at relatively small laboratory angles: 98% of real τtracks will be at angles less than 15°. One-prong decay candidates are located by following down all primary tracks within a cone of 15° from the beam direction for a distance of 1.5 mm, searching for a kink of more than 10 mrad. (Note that $c\tau$ for τ's is 0.091 mm, and γ's are of the order of 5, so that 1.5 mm is more than adequate.)

For events in which a kink is found, the kink secondary must be followed all the way to the exit of the emulsion and linked to the spectrometer so that its charge and momentum can be determined. Positively-charged kinks are rejected

TABLE 2.
Beam and Target Parameters of P803

(Main Injector Running)

Item	**P803**
Volume of emulsion	150 liters
Mass of emulsion	0.52 ton
Area of emulsion	1.8 m×1.4 m
Thickness of emulsion	6.0 cm
Primary proton energy	120 GeV
Protons per pulse	6×10^{13}
Cycle time	1.9 sec
Number of pulses†	2.2×10^{7}
Total protons on target	13×10^{20}
Average CC interaction energy	16 GeV
CC interactions in target (all E_ν)	6.3×10^{6}
NC interactions in target (all E_ν)	1.8×10^{6}

† Assumes four 8-month run at 100 useful hours/week.

at this stage, as are those which are too soft (momentum $p < 1.0$ GeV/c) or have insufficient transverse momentum ($p_T < 0.30$ GeV/c) relative to the candidate τ direction. For events meeting these criteria, it must be established that none of the tracks from the primary vertex are identified as muons (ν_μ CC event) or electrons (ν_e CC event). Many such tracks can be matched between emulsion and spectrometer without followdown, but ambiguous matches must followed out.

The small number of events in this kink sample are then studied intensively by physicists, as was done in E531. Neutral pions are reconstructed by combining information from the electromagnetic calorimeter, the spectrometer, and the emulsion. In addition to gamma conversions in the calorimeter, gamma conversions in the emulsion are located, and the conversion electrons (even those too soft to traverse the magnet) are reconstructed interactively. Finally, the τ decay modes consistent with the event must be identified, and the event must pass the particle identification and kinematic cuts for at least one of these modes.

Backgrounds to τ decays are discussed in detail in Section 8. We mention the most serious of them here, because the experimental design described in Section 6

is motivated in part by the need to reduce them. They turn out to be one-prong decays of anticharm produced by the $\overline{\nu_\mu}$ contamination of the beam, and one-prong interactions with no indication of nuclear breakup ("white star kinks").

5. Beam issues

5.1 Main Injector beam

Considerable progress has been made by the Neutrino Areas Working Group in understanding and optimizing the high intensity neutrino beam from the 120 GeV Main Injector [16]. The beam described here has been optimized for useful high energy ($\geq$ 15 GeV) flux. Equally important for this experiment, the background fluxes of $\overline{\nu_\mu}$ and $\overline{\nu_e}$, which give rise to anticharm background to τ's, are much smaller than those in previous Fermilab beams. These design results have been confirmed by agreement among four independent simulation programs. Effects such as interactions in the horn material have been studied and understood. Particle production data for two of these programs have been parametrized using data from the Fermilab Single Arm Spectrometer (SAS) [17], [18] for 100 and 175 GeV protons. Agreement with the older 400 GeV parametrization formerly used, extrapolated to 120 GeV, is good to 10%-15% in most kinematic regions of interest.

The production target (inspired by a CERN design) is a series of thin graphite cylinders 3.0 mm in radius, totalling 2.0 interaction lengths, and separated by gaps to give an average density half the normal value. Heat load studies by A. Malensek indicate that this design is indeed practical. Most of the secondary flux from this target escapes out the sides of the cylinder rather than being reabsorbed; it gains more than a factor 2 in flux per proton over the 1.1 interaction length Be targets employed in past Fermilab neutrino experiments. If the proton beam has a Gaussian area density of standard deviation 1.3 mm, 80% of the primary beam interacts in the target, and only 24% of the useful secondaries are absorbed.

The horn for the new beam (Fig. 9), designed by A. Malensek, is significantly more efficient than previous double-horn implementations, achieving nearly 50% of the flux from a "perfect" horn (one which puts all particles on-axis) for neutrinos above 15 GeV. It will run at a current of 140 to 160 kA.

The beam used for rate calculations in this proposal has a decay pipe 320 m long, followed by a muon shielding berm 150 m in length[5]. The energy spectra for ν_μ, $\overline{\nu_\mu}$, ν_e, and $\overline{\nu_e}$ expected from this beam (weighted by E_ν and expressed as charged current interactions/ton/GeV) are shown in Fig. 10. The yields come from a Monte Carlo program which uses the SAS particle production data, and

includes absorption of secondaries in the target and horn but does not simulate the additional flux from tertiaries. This buildup effect has been studied using another (GEANT-based) Monte Carlo; it shows an enhancement by 30-50% of the ν_μ flux below 10 GeV, which is below our effective anticharm threshold and therefore harmless.

The ν_μ spectrum peaks around 8 GeV, slightly below the effective threshold for ν_τ interactions; the huge flux per unit real time available from this beam (Table 2) more than compensates for its low energy. The total ν_μ charged current (CC) interaction rate in the P803 detector is 5.0×10^3 per 10^{18} protons. The ν_e CC rate is 0.8% of that for ν_μ but peaks at higher energy since it comes predominantly from K^- decays. This flux will be measured and used to set a limit for $\nu_e \leftrightarrow \nu_\tau$ oscillations.

The background $\overline{\nu_\mu}$ CC rate is only 0.7% of that for ν_μ CC; above 10 GeV it is dominated by decays of π^- and K^- which pass through the horn apertures undeflected. Estimating this rate correctly requires knowledge of the small p_T dependence of production cross sections, which is helped greatly by the newer data [17],[18]. The excellent efficiency of the horn for ν_μ's also reduces the relative contamination of $\overline{\nu_\mu}$, which are not focussed. The $\overline{\nu_e}$ CC rate is shown by the Monte Carlos to be dominated by K^0_L decays; the CC rate for this background component relative to ν_μ is only 6×10^{-4}, which means that the anticharm background from $\overline{\nu_e}$ is negligible compared to the already small background from $\overline{\nu_\mu}$.

Most of the running for P803 would require neutrinos rather than antineutrinos. The antineutrino running is important, however, for both the standard model physics (production of anticharm from the sea by antineutrinos), and for understanding the cuts necessary to remove the anticharm background to τ decays. The $\overline{\nu_\mu}$ charged current interaction rate, with the horn set for negatives, is somewhat less than half of the ν_μ rate given above.

5.2 Main Ring beam

At this time, there are two possible locations for P803 in the Main Injector era:

- Sharing a beam with the long-baseline oscillation experiment P822. This beam must incline downwards at a 3.3° angle to aim at the Soudan detector in Minnesota. This location would put the P803 detector about 200 feet underground, and would delay the start of P803 until both the Main Injector and the slant beam are built.

[5] Recent simulation studies have shown that the high-energy flux useful for P803 is not a strong function of the decay pipe length.

- A surface or near-surface beam. This option becomes very attractive if the beam could be fed by 150 GeV protons from the Main Ring, and then later by 120 GeV protons from the Main Injector.

One possible location for P803, currently being investigated, is the PW8 experimental hall, located at the end of the Proton West beamline. Though the full feasability and cost effectiveness of using this location have not been determined, this location has the advantage that the experimental hall, major beamline enclosures and supporting utilities exist. The PW6 enclosure contains a high intensity target station, including groundwater protection and adequate space to install a neutrino beam target/horn system and to begin the decay tube. The PW7 enclosure is 123 m long and wide enough to contain the remainder of the decay tube and the beginning of a 60-70 meter steel shield. The PW8 enclosure is a large experimental hall which would contain the remainder of the steel shield and the P803 hybrid emulsion spectrometer.

The feasibility of this location will depend on developing a cost-effective plan for extracting and transporting through the switchyard 150 GeV protons from the Main Ring and studying the PWest beamline in much more detail than has been done to date. In particular, the plan's success will depend on the ability to target and focus the beam using elements in the PW5 enclosure, which is 100 feet upstream of PW6. Additionally, the parameters which determine the neutrino flux and oscillation length, namely, the length and diameter of the decay tube, and the length of the muon shield, will have to be optimized to fit in the existing enclosures. We believe these studies can be accomplished within three months.

6. Detector design

P803 was originally designed to fit inside the surplus superconducting Helmholtz coils of the old 15-foot bubble chamber magnet. In the intervening time, cost estimates for moving, refurbishing and operating this obsolete magnet have steadily escalated. A revised P803 detector is presented here, based on an inexpensive conventional air-gap magnet. The new open design (Fig. 11) is cleaner, simpler, and cheaper; it resembles a scaled-up version of the E531 spectrometer. The essential elements are the emulsion target and interface sheets, the scintillating-fiber upstream tracking, the magnet, the drift-chamber downstream tracking, the electromagnetic calorimeter, and the muon identifier. Event simulations which illustrate features of the design are shown in Figs. 12-15.

6.1 Emulsion target

The emulsion target is comprised of two stacks of 'bulk' emulsion, each 1.8 m wide, 1.4 m high and 3.0 cm ($\approx$ 1.0 radiation length) thick, with a total volume of 150 liters and a mass of 0.52 tons. High-quality Fuji emulsion, used in E531 and E653, will again be obtained. Each stack consists of four 90×70 cm modules of the "vertical" type [20] in which particle track directions are nearly perpendicular to the emulsion sheets; this configuration is well-suited to rapid semiautomatic and fully automatic scanning techniques [21] developed at Nagoya University. Each module is composed of 25 emulsion sheets, vacuum-packed into a stack 3.0 cm deep in the beam direction. The sheets are constructed of two 600 micron emulsion layers bonded on opposite sides of a 90 micron acetate rayon base, which increases rigidity and minimizes emulsion warpage due to shrinking during the development process. Two such $180\times140\times3.0$ cm^3 bulk targets are separated by layers of scintillating fibers and interface sheets to expedite event location (see below).

The radial distribution of high-energy neutrinos falls off rapidly beyond a radius of 1 meter, so that a larger area for the emulsion is not cost-effective, and also requires increased size of the downstream spectrometer components. The depth of the stack is a more complex issue. The radiation length of emulsion is only 2.89 cm, so that many neutrino interactions in the upstream portion of the target produce well-developed electromagnetic showers in the emulsion, which the tracking system must be able to deal with (see simulations, Figs. 13-15). In E531, which used drift-chamber upstream tracking, and which had no tracking between emulsion stacks, events more than 5 cm deep in the emulsion were located less efficiently, and complete kinematic reconstruction of charm decays was more difficult. However, improved tracking may well allow a thicker target. The CHORUS collaboration is planning [11] to use a target 12 cm deep in conjunction with fiber tracking similar to that planned for P803. While we believe that a target this thick is truly challenging, the effectiveness of increasing the P803 target thickness

beyond 6 cm is being investigated.

6.2 Linking tracks into the bulk emulsion

Timely analysis of the experiment depends in large measure on the speed and efficiency of finding, and linking to the bulk emulsion, a 'leading track' which can be followed back to the primary vertex. For quick followback this track should have a small polar angle ($< 15°$ mrad) and not be too soft ($p \geq 1$ GeV/c).

There is an inherent bad match between electronic tracking devices and bulk emulsion resulting from the small field of view of the scanning microscope, about 150 microns on a side; this is a scale similar to the rms error in good wire chambers. When reconstructed wire chamber tracks are projected back to the emulsion, high efficiency demands making a search window which is 3 or 4 times the rms error (including that from multiple scattering) in the extrapolation. This search window can easily encompass 30 fields of view, which slows down the linking procedure and increases the chance of an accidental match to an unrelated track, leading to a large waste of time while a false trail is followed and rejected.

In past hybrid experiments by members of this collaboration special devices have been used to solve this problem: the "changeable emulsion sheet" [20] in E531, and silicon microstrips, an emulsion sheet, and a moving emulsion tape [21] in E653. The proposed solution here is small-diameter scintillating fibers which are interspersed with the emulsion layers, together with changeable interface sheets similar to those used in both E531 and E653, and by CHORUS.

6.3 Interface sheets

Interface sheets consisting of thin layers ($\approx 70\,\mu$) of emulsion, on opposite sides of a thicker sheet of plastic ($\approx 800\,\mu$), were used in both E531 and E653; the concept is illustrated in Fig. 16. These interface sheets act as a precision vernier on spectrometer tracks, allowing tracks to be extrapolated into the emulsion with high precision. They will be changed frequently to lower the track density, and can be scanned with high efficiency for near-normal tracks ($\theta \leq 15°$) with the fully automatic system developed by Nagoya University [19].

One interface sheet (I) will be located immediately downstream of each bulk emulsion stack (E), for extrapolating into the bulk emulsion. A few cm downstream of each such sheet is another pair of sheets (II), which may be changeable, followed immediately by a fiber tracking module (F); as shown in Fig. 17, the full target configuration is thus (EI IIF) (EI IIF). Track extrapolation proceeds from F to II, from II to I, and I to E.

6.4 Upstream tracking: scintillating fiber modules

Tracking on the upstream side of the bending magnet must be able to reconstruct all tracks coming out of the emulsion with high efficiency, including soft electrons which do not get through the magnet. Successful pattern recognition close to the thick P803 target requires many samples and good two-track resolution; this must be accomplished in only 50 cm of depth between target and magnet.

It was originally proposed to use a combination of scintillating fibers close to the target, and multisampling drift chambers farther away. However, the Nagoya members of this collaboration have made great progress in scintillating fiber technology. Their proven fiber modules, which are now being mass-produced for the CHORUS experiment at CERN, are ideally suited for the upstream tracking in P803, and we now plan to depend solely[6] on fibers for pattern recognition in this tracking region.

The present Nagoya fiber modules are built of ribbons 43 cm wide and 7 fibers deep (Fig. 18), of 0.5 mm diameter clad plastic fibers. Bundles of fibers (Fig. 19) are read out by assemblies (Fig. 20) each consisting of a high-efficiency, low-gain electrostatic image intensifier, a gated high-gain microchannel plate, and a demagnifying stage coupled to a CCD. The measured combined efficiency of fibers and readout is better than 1.0 detected photoelectron per fiber for a normal minimum ionizing track, or about 4.4 hits from a ribbon 7 fibers deep. Fiber modules consist of ribbons oriented in four directions, separated by a 1.0 cm spacer of low-density plastic honeycomb: x y (spacer) x' y', where the x' and y' fiber ribbons are rotated 10° from x and y. Each module thus typically delivers 4.4 hits per track in each of four projections. The present design calls for one such fiber module after each of the two emulsion stacks as described above, and two more at 20 cm intervals in the remaining space upstream of the magnet. This design will allow rough determination of the momenta of soft tracks by their curvature in the fringe field, and will also allow topological identification of e^+e^- pairs and showers emerging from the emulsion, since there will be enough samples to discriminate doubly-ionizing from singly-ionizing tracks (Fig. 15).

The Nagoya fiber system has two relatively minor drawbacks. First, the image intensifier assemblies must be mounted in regions well-shielded from magnetic fields. Second, although the microchannel plates in these assemblies are gated by a trigger, to minimize deadtime it is intended to read out the CCD's at the end of each 1 ms spill. A typical spill readout may thus contain more than one event.

Although the present Nagoya fiber modules are an existence proof of fiber

[6] Because of the limited time resolution of the fiber readout, it may be desirable to put a pair of drift chambers immediately upstream of the magnet for time-tagging of tracks.

tracking technology, improvements to this system will likely occur before P803 is built. The Nagoya group is experimenting with plastic fibers of 300 micron diameter, and the Tufts and Technion groups are testing cerium-loaded glass fibers which show promise of good photon yield at even smaller diameters. Kansas State and the University of Minnesota are testing avalanche photodiodes as an alternative to the image intensifier package; this readout solution has excellent quantum efficiency and time resolution, and is not bothered by magnetic fields.

6.5 Magnet

The bending magnet must have a large aperture to accomodate relatively low-energy events originating in the large-area target. It must have a useful p_T kick greater than 0.1 GeV/c to provide the $< 5\%$ momentum resolution needed to preserve the characteristic cusp signature of 2-body τ decay modes. A uniform field is not required if the field is well-mapped, since the number of candidates for which this resolution is required is small.

A preliminary computer-based design which meets these specifications has been prepared by R. Fast and B. Wands of Fermilab. The magnet (Fig. 21) has a vertical aperture of 2.3 m and a pole width of 2.7 m, and is only 1.2 m thick. It has an average useful field integral of 0.5 T-m (Fig. 22), giving a p_T kick of 0.15 GeV/c. The momentum resolution for tracks measured on both sides of the magnet will be $\Delta p/p = 0.0031p \oplus 0.028$, while for tracks measured only in the upstream fringe field $\Delta p/p = 0.071p \oplus 0.33$ ($\oplus$ means quadrature addition).

6.6 Downstream tracking

For best efficiency, the tracking downstream of the magnet should be able to reconstruct track segments independently of the upstream tracking, as was done in E531 and E653. In order not to contribute significantly to momentum error, it should have direction resolution somewhat better than that of the upstream tracking. These considerations lead to drift chambers with about 1 m of lever arm, with at least three projections, (e.g. x, $x \pm 15°$) and at least four samples per projection. Larger versions of the simple single-gap E531 chambers now appear to suffice. The chambers will be 3.1×3.1 m^2 in size, with a sense wire spacing of 2.5 cm. The LeCroy timing chip we are planning to use (Section 6.9) will record multiple hits per cell, and both leading and trailing edges of the shaped pulses, for good two-hit resolution.

6.7 Electromagnetic calorimeter

Information from the electromagnetic calorimeter will be used in selecting the sample of events to be scanned (offline analysis of a large number of events), and in reconstructing in detail the small number of events with a candidate kink

(interactive work by physicists). The initial vector momenta of photons and electrons will be reconstructed from both calorimeter information and from the measured trajectories of secondary electrons which traverse the magnet or penetrate its fringe field. Our simulations indicate that such secondary electrons can be identified quite well as charged tracks with nearly the same initial direction as an identified photon or another charged track, within a few degrees. The kinematic reconstruction used in selecting events (Section 7) requires knowledge of the vector transverse momentum $\vec{p}_T$ of photons and charged particles in order to distinguish candidate τ decay tracks from the rest of the event. The calorimeter must therefore measure the directions of photons to about a degree, and resolve showers coming from different parent γ's or hadrons. The required energy resolution is still being studied; the performance assumed thus far for simulations, $\Delta E/E = 0.1 \oplus 0.3/\sqrt{E}$, appears to be adequate. Due to the low mean energy of γ's expected from NC and CC interactions (Fig. 6), and to the high probability of pair production and bremsstrahlung in the emulsion target, it is desirable for the emcal to detect photons with energy as low as 100 MeV.

In the 1990 P803 proposal, a gas calorimeter with cathode readout of Iarocci tubes was discussed. This choice of calorimeter technology was based on its good position resolution and low cost. However, detecting shower energies between 100 MeV and 20 GeV may prove difficult with a calorimeter based on gas amplification. Our preferred choice is now an uncompensated lead-scintillating fiber calorimeter with lateral readout. This type of calorimeter was first discussed in 1984 [22], and since then there have been many versions of this type of calorimeter and much theoretical work on their operation [23]. The principal advantage of this type of calorimeter is its demonstrated very high light yield [24]. If the ratio of the volume of lead to fiber is close to unity, the photon yield is of the order of 5000 photo-electrons per GeV of deposited energy. This high light yield will allow identification of low energy showers and matching of stereo views of the shower with using energy deposition information.

The disadvantage of this type of calorimeter is the difficulty of doing in-situ calibration. Since there are no convenient calibration sources in the beam, we will have to rely on muons from charged current interactions, stabilization of the photo-detector response using light pulse injection, and fitting of π^0 peaks from CC data. However, since our requirement on the constant term for the calorimeter resolution is estimated to be $\sim$ 10%, this can be achieved without the use of embedded sources and current measurements.

The design of the calorimeter has still to be worked out in detail; nevertheless it is clear to us that this is the best type of calorimeter for P803. A schematic of our current design for the calorimeter is shown in Fig. 23. The overall dimensions of 3.1×3.1 m^2 are determined by acceptance requirements. Scintillating fibers are laid perpendicular to the beam direction and are arranged in three views (x,y, and

u), with the stereo view (u) set at an angle of 15° to the horizontal plane. The full 21 X_o is made up of three identical modules each 7 X_o thick, with the back two modules ganged together. Each module has 3 layers of fibers in each stereo view, with each layer consisting of a pair of staggered fiber planes. We plan to use 1 mm diameter fibers with a center-to-center spacing of 1.3 mm in the plane to maintain a uniform response across the surface. Strips of fibers 20 mm wide will be ganged together from the three layers of the same stereo view. These strips would be ganged together at the photodetector to give two depth samplings, one from the first module and second from a combination of the second and third modules. Ganging together the fibers in this way leads to a photodetector count of 2000, with an allowance for 5% spares. This ganging scheme is being considered since most of the signal from the low energy electromagnetic showers will be in first module alone, further reducing the confusion matrix, and, in addition, the front to back ratio will supplement the electron identification.

The fibers will run the full width and height of the calorimeter and will be read out at both ends. In this way the location of the shower in a single view can be obtained from the ratio of the pulse-heights. It would also be possible to use time differences between the two readout ends for the same function. It has recently been reported that time resolutions of 70 psec can be achieved for electromagnetic showers with this type of calorimeter. At present it is not clear that the redundancy obtained with timing will be required and has accordingly not been included in our cost estimates for the calorimeter.

Detailed Monte Carlo simulations are needed to further define the calorimeter requirements and to optimize the calorimeter design. Similarly, the construction method remains to be fully defined. This will be included in the technical design report which will be submitted after Phase I approval. At present, we believe that the best way to build the calorimeter would be to stack layers of lead with fiber layers supported in a frame sandwiched between layers. Another possibility would be to use grooved lead to provide both the absorber and the fiber support; however, it is not clear that it will be possible to place grooves in large area plates of lead while maintaining the required tolerances. Although the weight of each calorimeter module will be greater than 4 metric tons and the number of fibers will be 85000, it is clear to us that it will be possible to build a calorimeter with these dimensions without encountering significant technical problems.

The readout of the calorimeter will be with phototubes. Due to the presence of the fringe field from the spectrometer magnet, stable operation of the phototubes will require either tubes that are relatively insensitive to magnet fields, or else conventional tubes with good shielding. For the first option we are considering the new miniature tube R5600 from Hamamatsu, a compact 8 stage tube with a canister diameter of only a 15 mm diameter and a length of 10 mm. Because of their small structure these tubes are relatively insensitive to magnetic fields. An

additional advantage is that of their small size allows them to be mounted on a printed circuit board several to a board, opening up some interesting possibilities for an economic readout scheme with local signal processing. We have received a quote from the manufacturer for these tubes of $200 each in the quantity that we require. Alternatively we could use conventional phototubes with good shielding made of one or possibly two layers. The cost of a good 1" tube, including base, from Burle (S83062E) would be $265 each in quantity, to this would have to be added the cost of the magnetic shielding.

Since the operation of phototubes in a large fringe field is always problematic, an interesting possible alternative is the use of avalanche photodiodes to readout the calorimeter. These are insensitive to magnetic fields of the expected magnitude. The smaller gain ($\sim$ 500 as opposed to 5×10^5) is in part compensated by an increase in the quantum efficiency (80% as opposed to 20%). This response is high in the green, allowing for the use of green scintillation fibers which have much longer attenuation length than those which use blue light. Assuming 5000 photo-electrons per GeV with a phototube, the signal at 100 Mev would have a 2000 photoelectons or a signal of 100 fC, which would require some amplification. The cost in quantity of these APD's is $100 and would allow for better segmentation if required, or significant cost savings. We are exploring some operational issues with these devices. The first is catastrophic damage which has been observed when operated in a beam line. This is understood to be caused by second breakdown initiated by a nuclear interaction in the device and can be avoided by operating them in constant current mode, which should be simple to implement in this low rate environment. The second is the use of muons to set the calibration scale: this may be too close to the noise level for these APD's.

In summary we believe that an uncompensated lead-fiber calorimeter is the best choice for this application where we need to identify showers with energies between 100 MeV and 20 GeV. The cost estimate for this calorimeter (Section 12) is approximately $1.1, including 15% EDIA and 25% contingency factors. Since this is a well developed technology it is not necessary to follow a lengthy or expensive development path.

6.8 Muon identifier

The purpose of the muon identifier is to allow offline rejection of most ν_μ charged-current interactions so that the emulsion scanning load is manageable. Good muon identification is also needed for the proposed Standard Model physics.

One of the most constraining features of the 1990 design was the limited depth (about 1.5 m) available for muon identification inside the 15-foot bubble chamber magnet. Identifying muons then required a highly instrumented detector only 6.3 interaction lengths (IL) thick with frequent samplings of pulse height and track

direction. The new muon identifier, although larger, is a conventional device based on range of penetration. It is 6 m wide, 5.7 m high, and 2.3 m (12 IL) deep. The detector will be instrumented after each 38 cm of absorber with crossed 3 cm proportional tubes (measuring x', x" views, at $\pm 7.5°$ from the horizontal), and 15 cm scintillator paddles measuring the y (vertical) coordinate; see Fig. 24. Thus both the positions and the approximate directions of penetrating particles will be measured in order to match them to momentum-analyzed tracks in the spectrometer.

An unresolved issue is the absorber material. The 2.3 m magnet aperture may well preclude the use of iron; cost estimates in Section 12 are based on zinc. Further study in this area is needed.

6.9 Trigger and data acquisition strategy

In the 1990 design, triggering and readout were a major problem because the massive coils of the 15-foot magnet were just upstream of the emulsion target. The estimated neutrino interaction rate in these coils was twenty times that in the emulsion, and inability to reject most of these coil interactions would have led to loss of efficiency from readout deadtime.

The revised design has no massive objects upstream of the emulsion. Muons from the berm will be vetoed by an upstream scintillator wall, and the trigger will require only that one or more tracks originate in the emulsion and traverse the magnet to a counter hodoscope. The real charged- and neutral- current interaction rate in the emulsion is 0.3 events per 1 ms spill.

The readout problem has been considerably simplied by 'triggerless' buffered electronics from Lecroy. Timing signals will be entered directly into LeCroy timing chips, while pulse areas will first be converted into pulse widths. Analogue signals then correspond to the difference between leading and trailing edge timing from the LeCroy device. A satisfactory pulse area-to-width converter has been developed in SPICE simulations, and a discrete device is being evaluated before proceeding with custom design. It is now planned that all devices except the scintillating fibers will be stored quickly and continuously in time-stamped buffered form, thus incurring neglibible deadtime; readout and recording to tape will occur only between spills. The scintillating fiber information is also buffered, as follows: The microchannel plate of each fiber readout assembly is gated by the tigger. Signals are stored by the phosphor of the image intensifier (decay time of ≈ 10 μsec) until the simple trigger is formed. Gated signals are then stored in the CCD until the end of the spill. More than one event per spill may then appear in the CCD's, but such multiple events will almost always be widely separated in space because of the large area of the beam and target.

7. Analysis

7.1 Selection of oscillation events for scanning

It is impossible to scan all 8×10^6 neutrino interactions which will be recorded by P803, and a τ-rich subsample containing only a few percent of these interactions must be selected on the basis of kinematic variables available from spectrometer reconstruction alone. To avoid the very large potential scan load from CC events, it will be first be necessary to reject offline all events with a detected muon. The discriminant analysis technique described below will then be used to choose the scan sample.

The idea is to use the discriminating ability from several kinematic variables to form a relative probability P_{NC} that an event is a specific τ decay rather than a neutral current interaction, and another relative probability P_{CC} for τ decay rather than a ν_μ charged current event with an undetected muon. One then selects events by imposing cuts on P_{NC} and P_{CC} rather than on the kinematic variables themselves.

The method was tested and tuned with simulations produced by LUND and GEANT. Electromagnetic and hadronic interactions in the emulsion and fibers, bending in the magnet, muon penetration, and apertures of detection devices were faithfully simulated, while detectors were treated phenomenologically using the resolution estimates given in Section 6.

The three tau decay modes targeted for discrimination were $\pi^-\nu$, $\pi^-(n\pi^0)\nu$ (including $\rho^-\nu$), and $e^-\nu\nu$. Examples of distributions of discriminant variables for $\pi^-\nu$ and $\rho^-\nu$ selection are shown in Fig. 25. At P803 energies, the τ decay products tend to have high total momentum p_{lead} and total transverse momentum p_{Tlead} relative to the beam direction, and $\vec{p}_{Tlead}$ tends to be 180° in azimuth ϕ away from the $\vec{p}_T$ of the rest of the event. In addition, the $\pi^-(n\pi^0)\nu$ and $e^-\nu\nu$ modes tend to have large electromagnetic energy fractions. The algorithm first chooses the most likely τ decay products for each event by maximizing p_{lead}, p_{Tlead}, and $\Delta\phi$, and then evaluates P_{NC} and P_{CC} from distributions similar to those in the figure.

Minimal cuts were applied to events before discriminant analysis: at least one charged particle with $p > 1$ GeV/c and $\theta < 15°$ for event location; a negatively-charged assigned τ decay track with $p > 1$ Gev/c, the existence of a "rest" of the event against which to measure $\Delta\phi$, and at least 0.5 GeV (2.0 GeV) of electromagnetic energy assigned to the τ decay for the $\pi^-(n\pi^0)\nu$ ($e^-\nu\nu$) modes. A conservative γ-detection threshold of 0.35 GeV was imposed for this selection process.

The performance of this discriminant analysis is summarized in Fig. 26, which plots the number of remaining τ's in each mode, and the resulting scan load,

against the discriminant[7] P_{NC}. Satisfactory τ efficiencies, comparable to or better than those in the 1990 P803 proposal, can be achieved for a scan load of less than 150K events[8] from all of the P803 running.

Furthermore, a much richer selection of events in any of the three modes can be made for early scanning: for example, scanning only 10K events will find half of the $\pi^-\nu$ candidates; or, scanning half of the 150K events will lose only 25% of the total τ sample.

7.2 Selection of other samples

Additional scanning of a smaller number of neutrino and antineutrino charged-current events will be required both to investigate backgrounds and to study Standard Model physics (Section 2). The scan load for this portion of the experiment has not yet been determined, but can be bounded from above: if no special kinematic selection criteria are used, about 2.5×10^4 events must be scanned for charm. Kinematic selection appears to reduce this number by about a factor of 2, but more study in this area is needed.

In scanning for charm, the follow-down distance will be increased to 6 mm, and a scanback technique similar to that in E531 will also be incorporated. In this latter method, electronic detector tracks whose slopes do not match emulsion track slopes measured near the production vertex will be located in the downstream face of the emulsion block, then followed upstream in an attempt to locate neutral charm decays.

7.3 Emulsion scanning

7.3a Miniplate technique

The "bulk" emulsion in the active target is actually comprised of sheets 91 × 70 cm^2 in area and 1.2 mm thick; each sheet has two layers of emulsion coated on a thin plastic base to preserve dimensional stability, a well-proven [20, 21] technique. Before the bulk emulsion is scanned, the large sheets are cut up into 7 cm × 7 cm squares and mounted 25 at a time on a "miniplate" 35 cm × 35 cm square (Fig. 27). These 25 squares are chosen to be consecutive in depth, so that a miniplate contains all the emulsion information in a tower 7 × 7 cm^2 wide and 3.0 cm deep. Any position in any square in the miniplate can be accessed by computer control of the large-stroke microscope stage, allowing any track in the tower to be followed quickly from sheet to sheet through the depth of the tower.

This miniplate technique worked very well in Fermilab experiment E653 [21],

[7] A cut on the complementary variable P_{CC} has already been applied.

[8] There is $\approx$ 10% overlap between the three selections.

resulting in a sheet-to-sheet traceback location time of 0.5 to 1 minute per plate, compared to 2 to 5 minutes per plate in the earlier E531 experiment in which this technique was not used. However, it requires careful calibration [21] of the coordinates on each mounted square. For the large volume of emulsion to be used in P803, it is estimated that 6 to 9 months will be needed after development of the emulsion for assembling the miniplates and for calibration. These efforts will be done in parallel with the calibration and software tuning of the electronic portions of the hybrid detector.

7.3b Time estimate for scanning and decay search

The key to rapid processing of a large number of scan candidates is the fully automatic scanning [19] system developed at Nagoya University. This system presently is used for finding a particular track in low-track-density changable interface sheets and following it back into bulk emulsion. A semi-automatic system involving a human scanner is then used in the high-track-density bulk environment for continuing the followback to the primary vertex. Once the primary vertex is found, all tracks within 15° of the beam direction are followed out for 2.5 mm under semiautomatic (human) control looking for kinks, which are the candidate τ decays. The approximate time needed for each of these steps is shown below.

Time Estimate for Emulsion Analysis

Interface sheet scanning by automatic system	2–3 minutes/sheet/event ($\times$6 sheets)
Followback of leading track by semiautomatic system ($\approx$ 30% of events)	15–20 minutes/event
Followback of leading track by automatic system ($\approx$ 70% of events)	5–15 minutes/event
Search for τ decay candidates by semiautomatic system	5–10 minutes/event

7.3c Expanding the emulsion scanning capability

P803 emulsion physicists believe that expanding the semiautomatic scanning capability beyond the existing stations in Japan, with their trained personnel, would be logistically difficult, and that expanding this capability to the U.S. would be even more difficult.

However, a collaboration of Kobe and Nagoya scientists is working to improve the automatic scanning devices so that they can also be used in the high-track density environment of bulk emulsion. This R&D project should be completed by Spring, 1994. Once complete, expanding the automatic scanning capability is a matter of duplicating working devices, rather than training additional skilled

people. The emulsion physicists now envision "farms" of automatic scanners, analogous to the computer workstation farms now being used for analysis of electronic experiments, which could be located both in Japan and at Fermilab. Scanning capabilities would be increased by an additional 50% due to the Fermilab contribution. Good candidates for "farm managers", persons with experience in both emulsion and counter work and who are presently working on U.S.-based counter experiments, have been identified.

The present capability, using semiautomatic scanning, is 2×10^4 events per year in Japan. However, with the new automatic scanning technology implemented both in Japan and at Fermilab, a capacity of 6×10^4 events/year should be an achievable goal.

8. Estimate of backgrounds

Candidates for charged current interactions of tau neutrinos consist of events with no primary muon or electron, and which have a negative kink track with a production angle less than 15 degrees. Possible sources of background include tau neutrinos from the primary proton beam dump, charged hyperon and kaon decays, single-prong decays of charm antiparticles, and ordinary interacting tracks which scatter without leaving evidence for nuclear breakup in the emulsion.

It is important to note that all sources of background except direct ν_τ are inherently measurable, and will be measured in this experiment. For example, one can scan a subset of non-muon tracks for several centimeters in emulsion. The number of kink interactions and strange decays per unit length will be roughly uniform over this distance, while all real τ decays would occur in the first few millimeters of path. The number of anti-charm particles produced in $\overline{\nu}$ interactions can be determined by searching for their decays in events with an identified primary μ^+.

Good muon rejection efficiency is important for reducing the number of events to be scanned, and is essential for reducing the background of kinks from anticharm decays found in the emulsion. Muon efficiency is presented as a function of neutrino energy in Fig. 28 both for μ^- from all charged-current neutrino events, and also for μ^+ from antineutrino-produced anticharm.

In the sections below, we discuss individual sources of background in increasing order of severity. The kink-selection criteria are listed in Table 3. As will be shown below, they reduce the estimated background to approximately one event.

TABLE 3.

Kink Selection Criteria

Kink Attribute	Requirement
Maximum track angle	$< 15°$
Minimum kink angle	> 10 mrad
Minimum momentum of secondary	> 1.0 GeV/c
Minimum p_T relative to parent direction	> 0.30 GeV/c
Maximum decay length	< 1.5 mm

8.1 Decays of strange particles

Background from one-prong hadronic decays of negatively-charged strange particles was studied with LUND-generated neutral current interactions. (Muonic decays are suppressed by at least an order of magnitude by identification of the μ from the kink). Candidate decays were required to occur in events meeting the scan selection criteria, and in addition, the secondary track from the kink was required to meet the kink selection criteria of Table 3 with the exception of the p_T cut. The background under these conditions would be about 1 event. The distributions in the transverse momentum p_T relative to the measured parent direction for strange and τ decays are shown in Figs. 29 and 30. The ability to measure the direction of a short-lived parent to obtain a good measurement of p_T is a major strength of emulsion experiments. The p_T cut actually used, 0.3 GeV/c, is 30% greater than the maximum p_T available in any strange decay. This cut should suppress the strange background by at least a factor of 100, giving < 0.04 event.

8.2 Tau neutrinos from the proton dump

Only 20% of the primary proton beam fails to interact in the long production target for the neutrino horn. Those protons which do not interact are stopped in a beam dump 150 m from the emulsion. Real ν_τ's from the decay chain

$$\overline{D_s} \rightarrow \tau + \overline{\nu_{\tau 1}}, \qquad \tau \rightarrow \nu_{\tau 2} + X$$

are a potential background to ν_τ's resulting from oscillation of ν_μ's.

This source of background has been carefully simulated with a Monte Carlo program; details of the calculation are described in Appendix C. Known production properties of charmed particles and Monte Carlo simulations of charm and τ decays are used to scale the results of the Fermilab beam dump experiment

TABLE 4.

Calculated Yield of Direct ν_τ Events

Assumed n-value	P803 Acceptance	$\overline{E_\nu}$ (GeV)	$\sigma_{\nu_\tau}/\sigma_{\nu_\mu}$	$\overline{x_F}$	P803 Yield/ 2.4×10^{20} p
2.0	0.0065	28	0.48	0.66	0.17 events
2.5	0.0051	27	0.47	0.60	0.13 events
3.2	0.0039	26	0.46	0.55	0.10 events

E613 [25] from 400 to 120 GeV protons. The calculation is certified by reproducing the absolute yield of charged current interactions from prompt neutrinos in E613.

The major uncertainties in the calculation are in the unmeasured charm cross section at 120 GeV, and in the assumed x_F dependence of D_s production at that energy, parametrized as $(1 - x_F)^n$. The results are summarized below, assuming the beam flux from Table 2. Even within the limits of uncertainty in production, direct ν_τ's are not a serious source of background, due in large part to the low energy of the proton beam.

Using the best-guess value of $n = 2.5$, we obtain 0.13 background events from the beam dump.

8.3 Backgrounds from charm production

There are three types of charm background events: single and associated charm coming from neutrino interactions and anti-charm coming from interactions of anti-neutrinos.

Single charged charm generated by neutrinos is positive; a τ lepton coming from a charged-current interaction would be negatively charged. For an average neutrino energy of 16 GeV, the expected yield of charm per event (Fig. B3, Appendix B) is 2%. The primary muon will be found in 95% of the ν_μ interactions producing charm, and, most important, any single charged charm produced will have the wrong sign of charge. The background from single charm can thus be made arbitrarily small by rejecting kinks with an ambiguously-determined charge sign.

Associated production of charm is extremely small compared to single charm

production at these low neutrino energies. However, all events containing tau candidates would be scanned for a second vertex with an efficiency experimentally determined to be greater than of 80%.

The most serious source of charm decay background comes from anticharm production by antineutrino interactions in which a negative single-prong anticharm decay occurs, and in addition the primary charged-current muon or electron is missed. In the estimates below, we use the background $\overline{\nu_\mu}$ and $\overline{\nu_e}$ fluxes discussed in Section 5 and shown in Fig. 10. The $\overline{\nu_\mu}$ anticharm decay background may then be calculated as a product of the following factors:

a. Number of charged-current interactions in the target	6.3×10^6
b. Fraction of interactions from $\overline{\nu}_\mu$	0.0070
c. Efficiencies affecting both signal and background	0.64
d. Beam-weighted average of anticharm cross section to $\overline{\nu}_\mu$ cross section	0.010
e. Probability of missed μ^+ and passing scan selection	0.022
f. Ratio of charged anticharm to total anticharm	0.40
g. Branching ratio for charged charm to 1-prongs	0.43
h. Fraction passing kink criteria	0.46
Number of $\overline{\nu_\mu}$ anticharm events	0.49

Note that there is negligible anti-Λ_c production in a low-energy antineutrino beam. The decay length cut of 1.5 mm is effective in reducing the background of long-lived D^- relative to τ's. Decay length distributions for τ^- and D^- passing the other cuts are compared in Fig. 31.

A similar calculation may be done of the anticharm production by the $\overline{\nu_e}$ contamination in the beam, which from Section 5 is suppressed by an another order of magnitude below $\overline{\nu_\mu}$. If the identification inefficiency for electrons from the primary vertex is about the same as that for muons, this source of background adds only 0.05 events, bringing the total anticharm decay background to 0.54 events.

Further ways of discriminating anticharm decays from τ decays are under investigation. For example, at these low energies the anticharm is produced nearly back-to-back in azimuth with the μ^+, which is unidentified in the background events. For real tau decays, the chances of having a track from the rest of the event very near $\Delta\phi = 180°$ in azimuth is significantly smaller. A simple $\Delta\phi$ cut will thus be very effective against this background.

8.4 Background from interactions

The most serious source of background to hadronic τ decays will be single-prong interactions of tracks from the primary vertex which show no evidence of nuclear breakup, called white star kinks (WSK's). The important issues here are both the mean free path (mfp) and the p_T dependence of these interactions. For example, if they occur mostly through coherent scattering off the nucleus as a whole, they will have a very steep falloff in p_T, and a modest kink p_T cut can virtually eliminate them. If, on the other hand, WSK events are scattering off individual nucleons with a typical dependence of $e^{-8t} \approx e^{-8p_T^2}$, any reasonable p_T cut will have little effect.

Published quantitative information on WSK's is rather sketchy [26], indicating a mfp of about 30 m with an unknown p_T cutoff. This 30 m mfp is now known to be much too pessimistic. Members of this collaboration have exposed emulsion modules at KEK to π^- beams of 2.0 and 4.0 GeV/c, and have performed an efficient scan for kinks; this experiment is described in Appendix D.

The 4 GeV/c data are summarized in Fig. 32, which shows the p_T distribution both for all kinks, which includes those with breakup tracks or short "blobs" at the vertex, and for the WSK component. The p_T for each event is inferred from the kink angle under the assumption that the momentum of the kink secondary is the same as that of the beam; a WSK background from bremsstrahlung of the 3% electron contamination of the beam has not been subtracted in this data.

From the figure it is clear that white star kinks do have a significantly steeper p_T dependence than the total sample. The falloff of the WSK sample is approximately e^{-20p_T} (dashed line in the figure) for $p_T \geq$ 0.1 GeV/c. There are 8 WSK events with $p_T \geq$ 0.2 GeV/c, which corresponds (Appendix D to a mfp of (50 ± 18) m; the exponential falloff in p_T then gives a (370 ± 130) m mfp for $p_T \geq$ 0.3 GeV/c. The fractional mfp per scanned track with a 0.3 GeV/c p_T cut is then 1.5×10^{-3} m/370 m $= 4 \times 10^{-6}$.

The rapid falloff in p_T is very important; the WSK backgound decreases by about $1/e$ for each 0.05 GeV/c increase of the p_T cut in this region, while the corresponding signal losses in all detected modes are about 10%. This is illustrated in Fig. 30.

The background from white star kinks depends on the number of negatively-charged tracks from the primary vertex in the sample of events selected for scanning, discussed in Section 7. Note that this background scales with the number of events scanned, so that efficient scan selection criteria reduce it. WSK background is estimated from multiplying the following factors:

a. Number of hadronic τ decay candidates scanned	1.22×10^5
b. Negative tracks to scan per selected event	1.1
c. Scan distance per track	1.5 mm
d. Mean free path for WSK, $p_T > 0.3$ GeV/c	370 m
Number of WSK events	0.54

There is a good possibility of reducing this WSK background even further, based on a promising approach now under study in Japan. WSK events are studied under very high magnification, looking for evidence of very short tracks from nuclear breakup or Auger electrons. This minute scrutiny will be possible in P803 because of the very small number of final candidates. Preliminary studies indicate that an additional reduction factor of as much as 7 in WSK background may be obtained in this manner.

8.5 Summed backgrounds

The estimated backgrounds from all sources with the specified set of cuts are summarized in Table 5. The total estimated background is 1.2 events.

TABLE 5.

Estimated Background Contributions

Source of Background	# Events
Strange particle decays	< 0.04
Direct ν_τ	0.13
Anticharm decays	0.54
White star kinks	0.54
TOTAL	1.2

9. Null-limit sensitivity to oscillations

9.1 General sensitivity issues

The sensitivity of the experiment to the probability of $\nu_\mu \leftrightarrow \nu_\tau$ oscillations depends both on the estimated background and on the number of τ's which would be detected if the ν_μ beam were to be entirely converted to ν_τ. The latter number is most conveniently expressed relative to the equivalent ideal yield of charged-current interactions in the target, i.e. the integrated spectrum of Fig. 10 multiplied by the target mass:

$$N_{CC} = \int dE_\nu \, [dN_{cc}/dE_\nu] \, ,$$

where dN_{cc}/dE_ν = Number of ν_μ interactions per GeV in the target. From Table 2, $N_{CC} = 6.3 \times 10^6$.

Now suppose the same beam has oscillated with 100% probability to ν_τ. The yield of τ's would be

$$N_\tau(100\%) = \int dE_\nu \, [dN_{cc}/dE_\nu] \cdot \sigma_{\nu_\tau}/\sigma_{\nu_\mu} \cdot \epsilon(E_\nu)$$

where

$\sigma_{\nu_\tau}/\sigma_{\nu_\mu}$ = Energy-dependent cross-section ratio (Fig. 4);

$\epsilon(E_\nu)$ = Energy-dependent τ detection efficiency. $\epsilon(E_\nu)$ includes the efficiency factors listed in Section 9.2 below, and also the branching ratios and energy-dependent acceptances of all detected τ modes, given in Section 9.3.

There is thus a correction factor C for the sensitivity which is the weighted average of the σ and ϵ factors over the charged-current interaction spectrum, $C = N_\tau(100\%)/N_{CC}$. If no τ signal is seen, but rather an upper limit N_τ at 90% confidence level is set, the corresponding limit on oscillation probability (integrated over all energies) is

$$P(\nu_\mu \rightarrow \nu_\tau) \leq \frac{N_\tau}{C \cdot N_{CC}}.$$

If no candidates are observed, the 90% confidence level N_τ is 2.3 events. If however the expected background is not zero and events are observed, the situation is more complicated; it is summarized in Fig. 33 (reproduced from Ref. [15]).

Above an estimated background of about 2-3 events, the sensitivity decreases quite slowly with expected number of background events for fixed $C \cdot N_{CC}$. For estimated background levels well below 1 event, the sensitivity is nearly linear in $C \cdot N_{CC}$. These considerations are important in deciding whether to make cuts to remove background, since this almost always reduces the τ detection efficiency,

TABLE 6.
Efficiency for Detected τ^- Decay Modes

Decay Mode	Branching Ratio	Efficiency	BR×Effic.
$\mu^-\nu_\tau\overline{\nu_\mu}$	0.176	0.0	0.0
$e^-\nu_\tau\overline{\nu_e}$	0.179	0.245	0.0439
$\pi^-\nu_\tau$, $K^-\nu_\tau$	0.127	0.369	0.0468
$\pi^-\pi^0\nu_\tau$	0.244	0.307	0.0749
$\pi^-\nu_\tau$ multi-γ	0.132	0.347	0.0458
Total			0.21

and therefore C, as well.

9.2 Efficiency factors affecting both signal and background

Event losses due to detection efficiencies ϵ which affect signal and background in the same way are estimated below. These factors must be applied to all background estimates. (An event is not backgound if it is never found.) No efficiencies due to event selection or kinematic cuts are included here, since they affect signal and background differently.

1. Trigger efficiency (deadtime and veto overkill)	0.85
2. Emulsion fiducial volume	0.90
3. Efficiency in scanning back to the primary vertex	0.93
4. Efficiency for seeing kink (some occur in plastic backing)	0.90
Product of efficiencies	0.64

9.3 Oscillation limits

The detection efficiency ϵ for τ decay events which meet the scan and kink selection criteria depends on the decay mode. Multiprong modes are rejected completely; the efficiencies for the remaining kink modes, averaged over the energy spectrum of produced τ's, are given in Table 6. These efficiencies result from the scan selection cut described in Section 7, and the kink cuts in Table 3; the constant efficiency factor is not included here.

The factor C in Section 9.1 is the product of the common constant efficiency factors (0.64) and the beam-averaged product of relative τ production cross section

(0.29) and detection efficiency (0.21), giving $C = 0.039$, $C \cdot N_{CC} = (0.039) \cdot (6.3 \times 10^6) = 2.5 \times 10^5$.

Using the estimated 1.2 background events from Section 8 and the curves in Fig. 33, we find that if 1.2 events are actually observed, the 90% confidence level limit on the oscillation signal is 3.4 events. Then

$$P(\nu_\mu \rightarrow \nu_\tau) \leq \frac{N_\tau}{C \cdot N_{CC}} = \frac{3.4}{(0.039)(6.3 \times 10^6)} = 1.4 \times 10^{-5}.$$

This is a factor of 140 more sensitive than the E531 limit [13] of 2×10^{-3}.

A similar calculation can be done for $\nu_e \leftrightarrow \nu_\tau$ oscillations, using the beam-simulation estimate of 0.82% ν_e in the beam; in the actual experiment, the ν_e flux will be measured. Because the average energy of ν_e's is higher than that of ν_μ, we obtain a larger C, $C_{\nu_e} = 0.097$, and

$$P(\nu_e \rightarrow \nu_\tau) \leq \frac{3.4}{(0.097) \cdot (0.0082) \cdot (6.3 \times 10^6)} = 6.8 \times 10^{-4}.$$

This is 100 times as sensitive as the corresponding E531 limit.

$P(\nu_\mu \rightarrow \nu_\tau)$ may be interpreted in terms of a two-component representation of neutrino oscillations:

$$P(\nu_\mu \rightarrow \nu_\tau) = \sin^2(2\alpha) \int \rho(\frac{L}{E}) \sin^2(1.27 \delta M^2 \frac{L}{E}) d\frac{L}{E}$$

where ρ gives the normalized flux of neutrinos in terms of the variable (L/E), L is the neutrino flight path in meters, E the neutrino energy in MeV and δM^2 the neutrino mass difference squared in $(eV)^2$. For large δM^2 the oscillation length is small compared to the variation in neutrino flight length, and the (L/E) integral has an approximate value of 0.5; the P803 mixing angle sensitivity for $\nu_\mu \leftrightarrow \nu_\tau$ in the large-mass limit is then 2.8×10^{-5} at 90% CL.

Plots of P803 $\sin^2(2\alpha)$ sensitivity versus δM^2 for both ν_μ and ν_e are shown in Fig. 34, along with existing and expected ν_μ limits from other experiments.

10. Discovery potential

10.1 P803 discovery potential

An estimated 58% of the P803 τ sensitivity comes from the two-body $\pi^-\nu$ and $\rho^-\nu$ modes which have distinctive kinematic signatures and reduced backgrounds. The anticharm background for these modes is reduced because only a small fraction of one-prong hadronic decays have a single missing neutral and thus give a high-p_T cusp[9]. The white-star kink background for the $\pi\nu$ mode is also reduced because of the smaller number of stiff negative tracks to be scanned for kinks.

We believe that a total τ signal of 10 events in these two modes would stand out convincingly above background in a two-dimensional plot of p_T vs. proper decay time. The discovery potential sensitivity is estimated as follows: 10 events is 2.9 times the 90% CL background of 3.4 events, and comes from modes with 58% of the null-limit τ detection efficiency. The P803 discovery potential level is then about $2.9/0.58 = 5$ times the null limit. A similar calculation for E531, in which there were no background events and 37% of the sensitivity was in the two-body modes, gives a discovery potential 12 times the null limit.

10.2 Comparison with NOMAD and CHORUS

As the CERN experiments will run earlier, P803 must be shown to have greater physics reach. In terms of oscillations to ν_τ, P803 ultimately can access an order-of-magnitude smaller mixing because of higher beam intensity and reduced backgrounds at lower energies. Because P803 has both the benefit of precision vertex information and superior magnetic analysis, this experiment will be more powerful in verifying a positive signal should one exist. P803 also has an advantage for ancillary physics which relies heavily on identifying and mass-fitting decays, such as obtaining V_{cd} from a precision study of charm production near threshhold.

NOMAD [12] is an all-electronic experiment which concentrates on electromagnetic decay modes such as $\tau \to e\nu\nu$. A strong magnetic field and solid electromagnetic calorimetry give this experiment excellent ability to make kinematic selections. However, there is no ability to directly observe short-lived decays. Being all-electronic, data analysis will proceed quickly, but there will be little additional evidence to support any claim that tau-decay candidates indeed come from tau decays.

CHORUS [10, 11], as shown in Fig. 35, is an experiment which is similar to P803. It has an overlap in collaborators, and similar emulsion expertise. The submicron resolution of emulsion renders visible the entire geometry of tau decay

[9]For example, the branching ratios for $D^- \to \pi^- K^0$ and $D^- \to \rho^- K^0$ are 2.6% and 6.6%, respectively; $D^- \to \pi^-\pi^0$ and $D^- \to K^-\pi^0$ are singly- and doubly-Cabibbo-suppressed.

candidates, and permits determination of the parent tau direction in most cases to better than 2 milliradians.

However, the p_T kick of their magnet for hadrons is only 0.022 GeV/c, and it places a significant quantity of material in the path of analyzed particles. As a result, particle momenta typically are determined to 20% or worse. CHORUS plans to preferentially select events with muons, and will attempt to reduce emulsion scanning load using kinematic cuts on the muon and total hadronic momentum vectors. The latter comes from energy-flow calorimetry with twice the precision any previous neutrino experiment.

CHORUS will observe the geometry of tau decays, but both because of limited momentum resolution and concentration on multi-body decay modes will have difficulty in determining visible mass and proper decay times. Lack of momentum resolution also presents difficulties for a variety of ancillary physics. Previous Fermilab E531 experience indicates that achieving information about charm production near threshhold is hampered by severe backgrounds for candidates which are not fully mass-fit.

P803 has the advantage of using emulsion coupled with typically 3% determination of charged-track momenta and good electromagnetic calorimetry. A design which combines CHORUS and NOMAD strengths permits concentration on two-body decay modes. Masses and proper decay times will be determined for most found decays.

A shakedown run of P803 can be performed with a 150 GeV beam from the existing main ring. At a later date, the intense beam provided by the main injector upgrade permits several additional advantages. First, its low energy reduces backgrounds such as dicharm production. Secondly, its intensity permits making a design which sacrifices flux in favor of achieving higher quality per-event information. For example, using a thinner emulsion target minimizes multiple scattering and reduces confusion from secondary interactions. The increased intensity means that CERN sensitivities can be achieved in a couple of months of running, and ultimately surpassed by at least an order-of-magnitude.

11. Resources

A preliminary estimate of costs is given in the next section. We comment on some items here.

11.1 Fiber development

Although no item is included in the cost estimates, a program in optical fiber development complementary to that in Japan would be most useful both for this experiment and for others. This program was begun in 1993.

11.2 Computing

Online data acquisition is rather trivial; present computing and acquisition techniques are more than adequate to log two events per spill. Offline requirements are similarly modest by present-day standards. The recorded data from emulsion target interactions, and from other sources, will certainly be less than 10^8 events.

Most non-data triggers can be deleted quickly, leaving perhaps a few $\times 10^7$ which will require detailed processing. Typically, these events will have far fewer tracks than in E653, a previous hybrid emulsion-electronic experiment, or than the 2×10^{10} events from E791, which some of us are now analyzing. Workstation farms with a total capacity of 2700 MIPS, obtained for E791 analysis, will be available for P803, and the time to crunch the data will almost negligible compared to the normal time for calibrating and tuning the programs. However, computing would be labor intensive. Developing offline software would require at least 5 man-years over a two year period of calendar time. Most of this can be done prior to running.

11.3 Emulsion processing

It will be important to reconstitute the Fermilab Emulsion Pouring and Processing Laboratory used during E653. Some fraction of the emulsion must be analyzed during exposure in order to monitor emulsion quality, track backgrounds, etc., as a function of time.

11.4 Automatic scanning farm

As discussed in Section 7, scanning time for P803 can be substantially reduced by farms of fully automatic scanning both at Fermilab and in Japan. A cost estimate for the Fermilab system is included.

11.5 Civil construction

Careful design must follow physics approval. Estimates at the level of 40% are presently being carried out by Fermilab for several possible configurations.

12. Preliminary cost estimates

A. FERMILAB COSTS

1. Costs for Neutrino Beam and Experimental Area	
2. Data acquisition and PREP costs	$ 300K
3. Upgrading emulsion pouring facility	$ 100K
4. Ten automatic emulsion scanning systems	$ 500K
5. Spectrometer magnet	$ 850K
20% Contingency	$ 350K
15% EDIA (items 3,5 only)	$ 143K
TOTAL FERMILAB COSTS (not including beam)	**$ 2243K**

B. EXPERIMENTAL APPARATUS COSTS:

1. Emulsion; one hundred ninety liters @1M yen/liter, incl. processing and developing.	$ 1900K
2. Scintillating fibers tracking 900,000 fibers	$ 700K
3. Drift chambers, 18 @$25K each 3.1m square, 2.5cm cell size.	$ 450K
4. Drift chamber electronics Preamp, shaping 2400 channels @ $30ea ($72K) Readout 2400 channels @ $50ea ($120K)	$ 192K

5. Emcal chamber construction $ 792K

Lead ($57K)
Stand ($50K)
1410 PM tubes and bases ($324K)
1410 PM tubes readout ($56K)
Sci fibers, 508k m @ $.60/m ($305K)

6. Muon range calorimeter $ 2319K

Zinc, 1,230,000lb @ $1.1/lb. ($1350K)
Mechanical construction ($100K)
Scintillator ($320K)
456 PM tubes w bases and shields($182K)
PM tube electronics ($50K)
Prop tubes and electronics($317K)

7. Veto hodoscope, 24 scintillator counters $ 47K

(Each 6 in $\times$ 12 ft with tubes at each end,
plus $5K for stand)

8. First timing, trigger hodoscope plane 20 counters $ 50K
(Each 6 in $\times$ 10ft with tubes at each end and
Winston cone lightpipes, plus stand)

9. Second hodoscope plane 24 counters $ 60K

(Each 6 in $\times$ 12 ft with tubes at each end and
Winston cone lightpipes, plus stand)

10. Trigger and data acquisition $ 100K

11.	On-line computing, mostly existing	$ 35K
	(Four workstations with 32 MB memory, 2 gb of disk and two 8mm tape units, 2 printers, 4 X terminals)	
12.	Off-line computing	$ 50K
	Existing KSU DEC 5000/50 farms.	($ 500K)
	SUBTOTAL, NEW COSTS, excl emulsion	$ 4795K
	25% Contingency, exclude zinc & lead	$ 847K
	15% EDIA	$ 719K
	TOTAL NEW EXPT'L APPARATUS COSTS (excluding emulsion cost)	**$ 6361K**

Note on funding: We request that Fermilab play a substantial role in the funding for experimental apparatus costs. Use of Fe in the muon range calorimeter would reduce the experimental cost by nearly $1M.

The $2.6M cost of emulsion and the scintillating fiber tracking system will be funded by Japanese collaborators. We have assumed an exchange rate of 100 yen to the US dollar.

References

[1] See, e.g., Carlo Rubbia, 'The Renaissance of Experimental Neutrino Physics,' presented at the Conversaciones de Madrid, preprint CERN-PPE/93-08 (January, 1993).

[2] R. Davis, Jr., Proc. of the 19th Int. Conf. on Neutrino Phys. and Astrophys., 518 (1989).

[3] K.S. Hirata, *et al.*, Phys. Rev. Lett. 65, 2233 (1990).

[4] K. Lande, private conversation with N.W. Reay at Singapore '90.

[5] K.S. Hirata, *et al.*, Phys. Lett. B205 416 (1988). T. Kajita, talk at Singapore '90.

[6] D. Casper *et al.*, Boston University Preprint 90-23 (1990).

[7] Ch. Berger, *et al.*, Phys. Lett. B227, 489 (1989).

[8] G.F. Smoot *et al.*, Astrophys. J. 396 3, 155-B5 (1992); G.F. Smoot *et al.*, Astrophys. J. 396 L1, 160-B1 (1992); G.F. Smoot *et al.*, COBE preprint (1992); E.L. Wright *et al.*, COBE preprint (1992).

[9] See, e.g., H. Harari, Phys. Lett. B216, 413 (1989).

[10] N. Armenise *et al.*, 'A New Search for $\nu_\mu - \nu_\tau$ Oscillations', CERN-SPSC/90-42 (15 December 1990).

[11] M. deJong *et al.*, 'A New Search for $\nu_\mu - \nu_\tau$ Oscillations', CERN-PPE/93 (19 July 1993).

[12] P. Astier *et al.*, , 'Search for the Oscillation $\nu_\mu - \nu_\tau$', CERN-SPSLC/91-21 (11 March 1991).

[13] N. Ushida *et al.*, Phys. Rev. Lett. **57**, 2897 (1986).

[14] K. Kodama *et al.*, 'Measurement of the Lifetimes of Charged and Neutral Beauty Hadrons', preprint OHSTPY-HEP-E-92-019 (September, 1992), and Prog. Theo. Phys. 89, 679 (1993).

[15] K. Hikasa *et al.*, 'Review of Particle Properties', Phys. Rev. D 45, S1 (1992).

[16] R. Bernstein *et al.*, 'Conceptual Design Report: Neutrino Physics after the Main Injector Upgrade', Fermilab (June, 1991).

[17] A. E. Brenner, *et al.*, Phys. Rev. D26, 1497 (1982).

[18] D. S. Barton, *et al.*, Phys. Rev. D27, 2580 (1983).

[19] S. Aoki, Ph.D. Thesis, Nagoya University (1990).

[20] N. Ushida *et al.*, Nuc. Instr. and Meth. 224, 50 (1984).

[21] K. Kodama, *et al.*, Nuc. Instr. and Meth. A289, 146 (1990).

[22] H. Burmeister *et al.*, Nucl. Instr. and Meth. 225 530 (1984); P. Sonderegger, Nucl. Instr. and Meth. 523 523 (1987); D. Hertzog *et al.*, Nucl. Instr. and Meth. A294 446 (1990).

[23] 'On the Energy Resolution of Uranium and Other Hadron Calorimeters,' R .Wigmans, Nucl. Instr. and Meth. A259 389 (1987).

[24] 'High-Resolution Electromagnetic Pb-SCIFI Calorimetry: An Investigation on Fibers and Tests with Low-Energy Photons' S. Bianco *et al.*, Nucl. Instr. and Meth. A315 322 (1992).

[25] M. Duffy, *et al.*, Phys. Rev. D38, 2032 (1988).

[26] S. Hasegawa, *et al.*, Prog. Theor. Phys. Suppl. 47, 126 (1971).

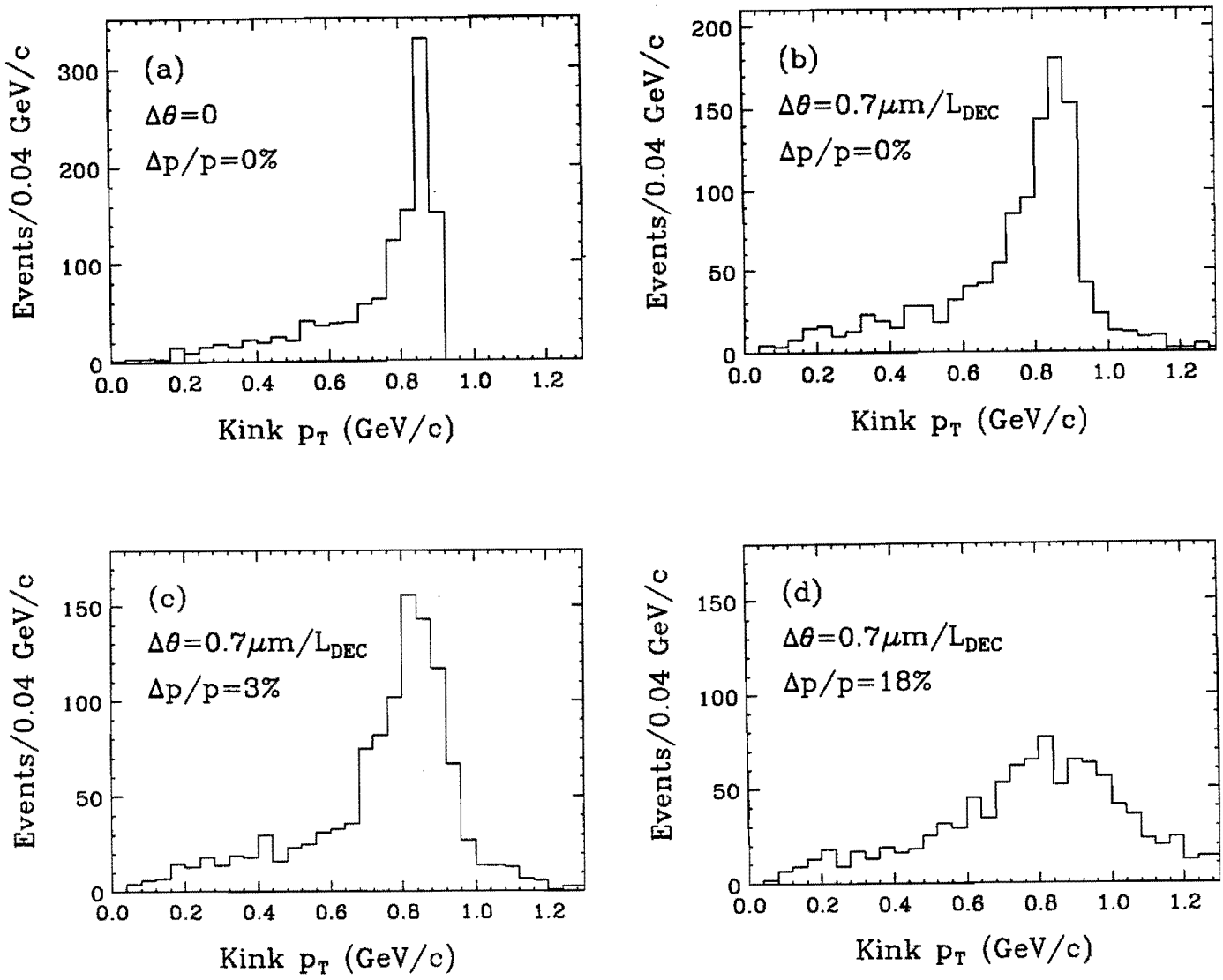

FIG. 1. Monte Carlo decay p_T distributions for $\tau \rightarrow \pi\nu$, showing the effects of resolution broadening on the Jacobian peak. (a) perfect resolution in angle and momentum; emulsion angle resolution of (0.7 micron)/(decay length) and momentum resolutions $\Delta p/p$ of: (b) 0%; (c) 3% (P803); (d) 18% (CHORUS).

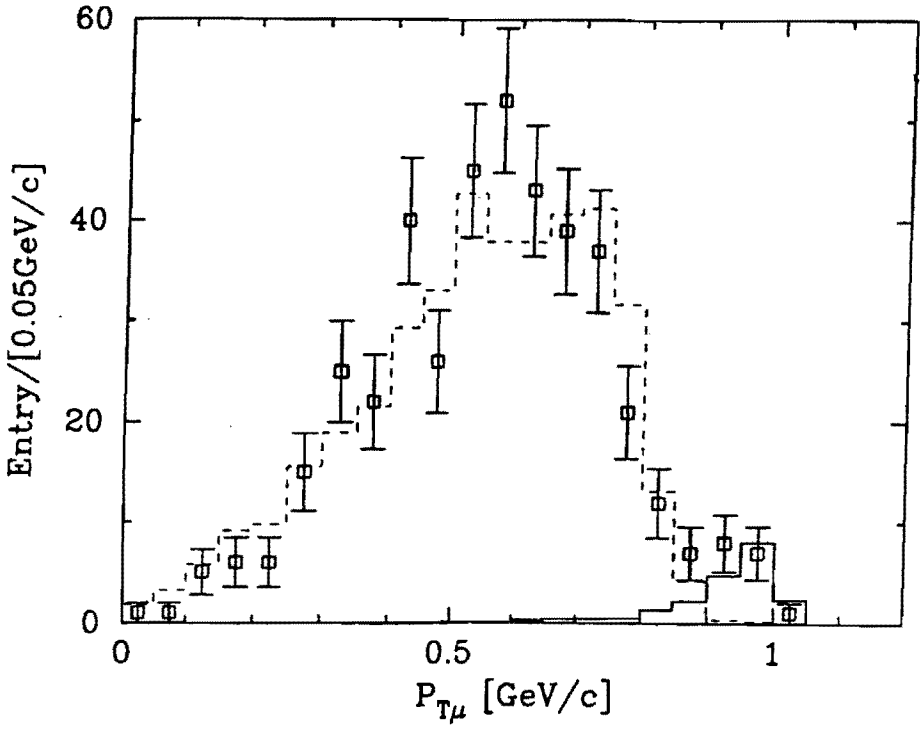

FIG. 2. Demonstration of the p_T cusp technique to find a small signal in hybrid emulsion spectrometer data: leptonic decays $D_S \to \mu\nu$ from E653. Data points (with error flags) are the measured distribution of the muon p_T relative to the decay direction, for one-prong decays to a muon for events found so far in a partial scan of E653 emulsion. The solid histogram is a simulation of the expected distribution from $D_S \to \mu\nu$, while the dashed histogram is a simulation of $D^+ \to \bar{K}^0\mu^+\nu$.

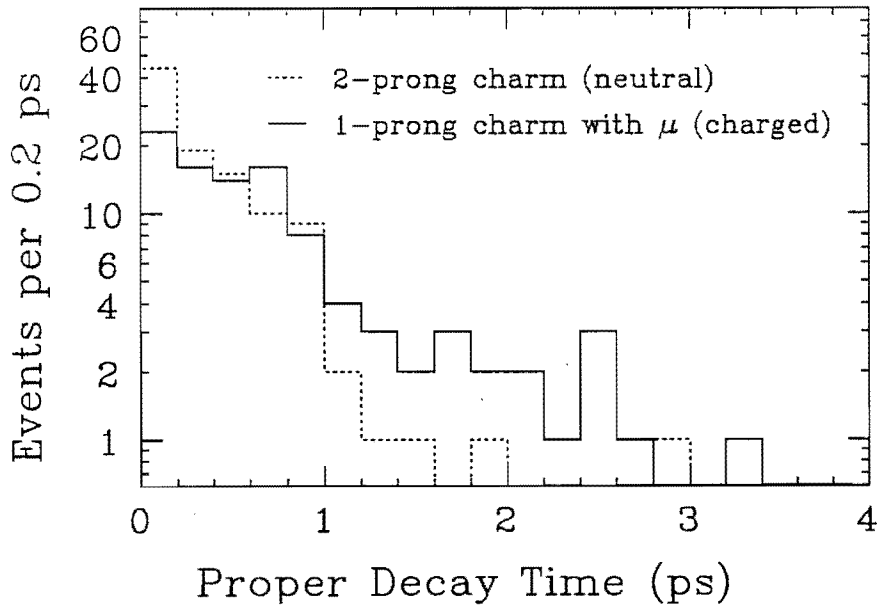

FIG. 3. Demonstration of the ability to measure lifetime for unconstrained one-prong charm decays in a hybrid emulsion spectrometer; events are from the E653 scan for beauty. The dotted histogram is for 103 two-prong neutral charm, and the solid one for 101 one-prong charged decays to a muon. The data is uncorrected for acceptance or detection efficiency. The momentum of each unconstrained decay was estimated using techniques developed for E653.

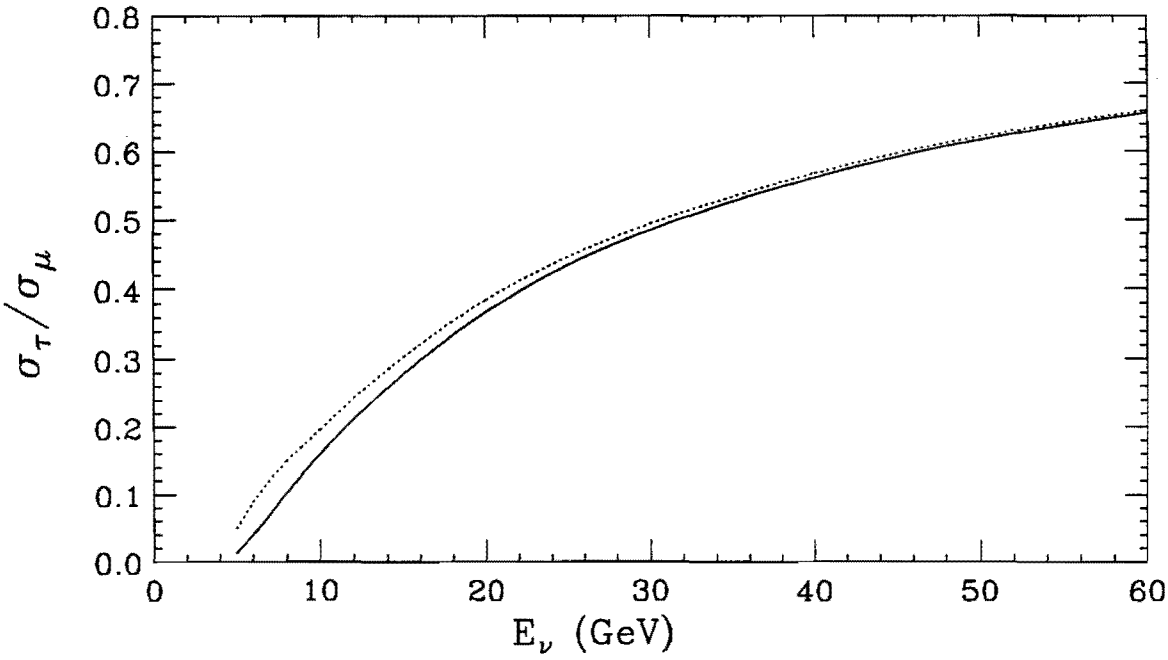

FIG. 4. Ratio of ν_τ to ν_μ cross section as a function of energy. The solid curve is the deep-inelastic parton model contribution, while the dotted curve also includes quasi-elastic and Δ^{++} contributions to both processes.

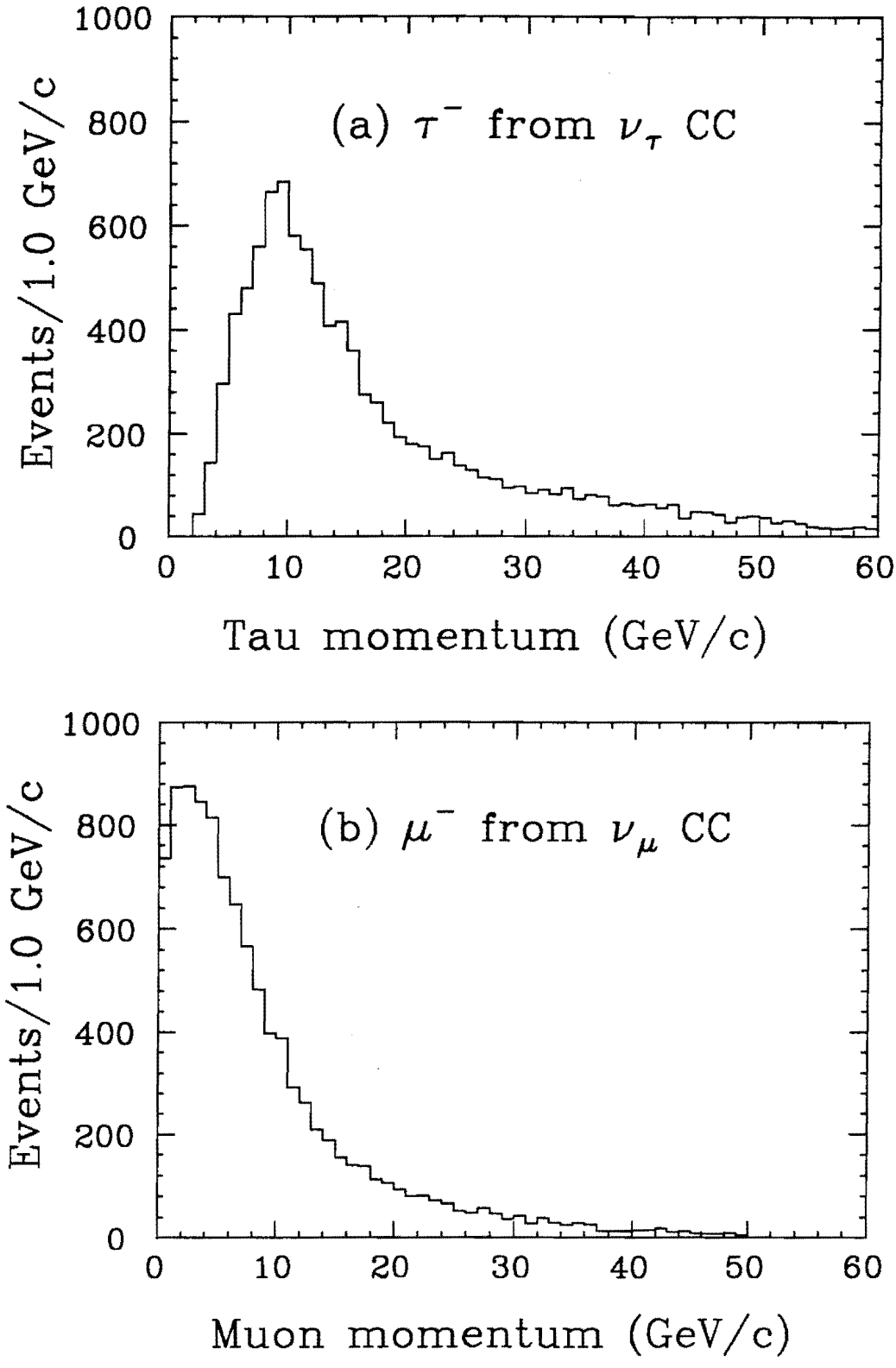

FIG. 5. Comparison of LUND Monte Carlo simulations of the momentum distributions of (a) τ from ν_τ interactions; (b) μ from ν_μ interactions.

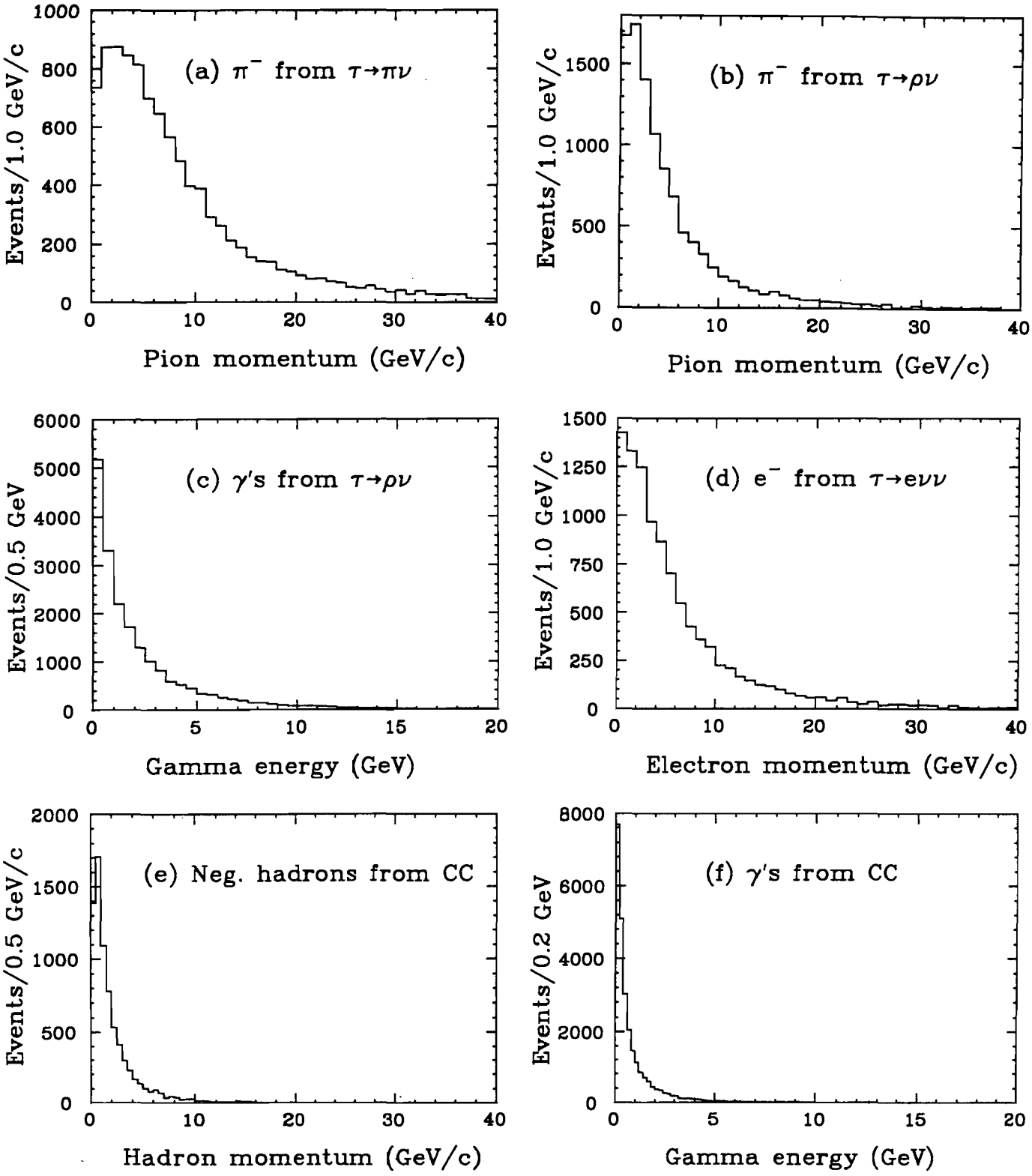

FIG. 6. Comparison of momentum distributions of τ decay products with those of particles from charged-current (CC) ν_μ interactions. (a)-(d) Negatively charged particles and gammas from τ decay. (e)-(f) Negatively charged particles and gammas from ν_μ CC; those from neutral current interactions are similar. These LUND spectra are not corrected for experimental acceptance and resolution, or for secondary interactions.

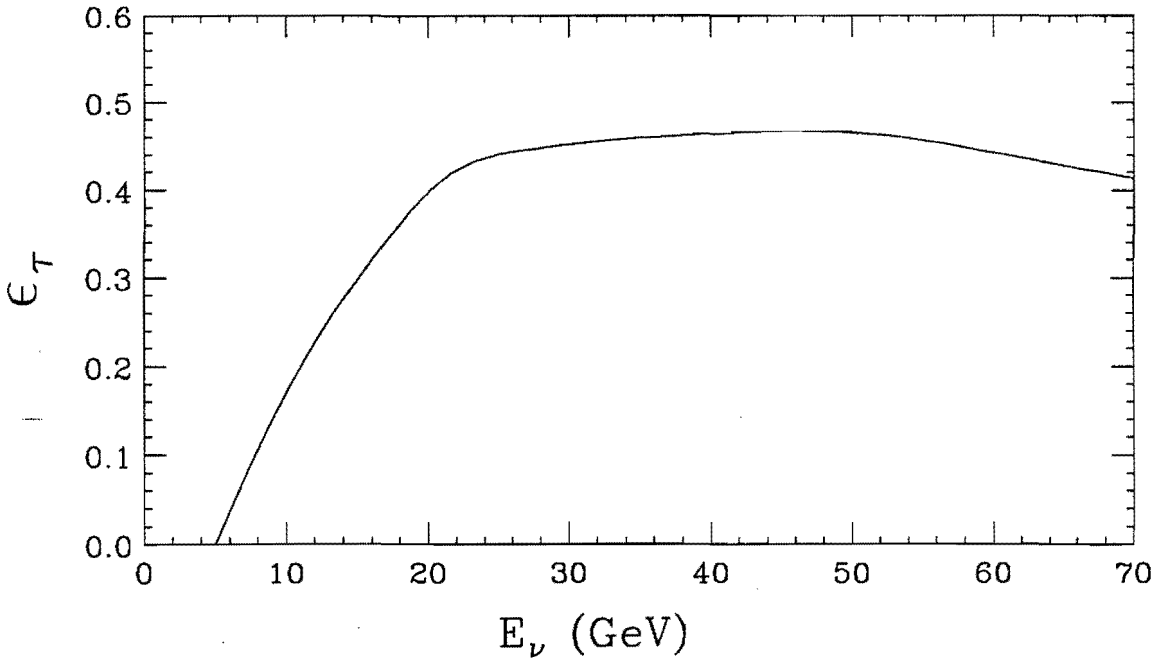

FIG. 7. Neutrino energy dependence of τ detection efficiency after scan selection and kink cuts have been applied. Energy-independent efficiency contributions are not included.

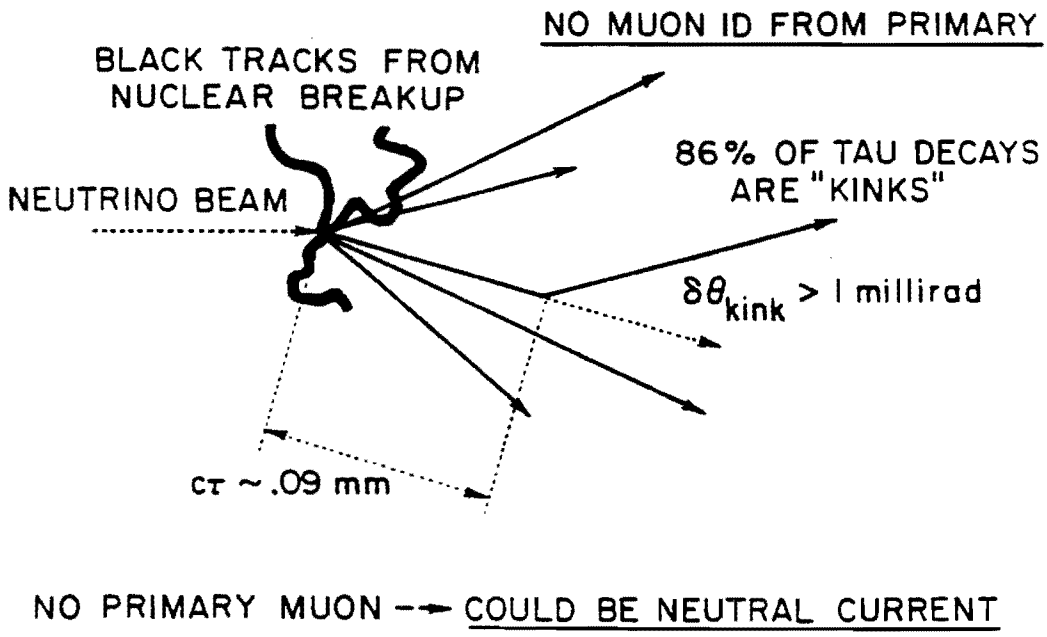

FIG. 8. Schematic sketch of a ν_τ interaction in emulsion. Note the heavily-ionizing tracks from nuclear breakup, the absence of an identified muon from the primary vertex, and a short 'kink' track with large decay p_T.

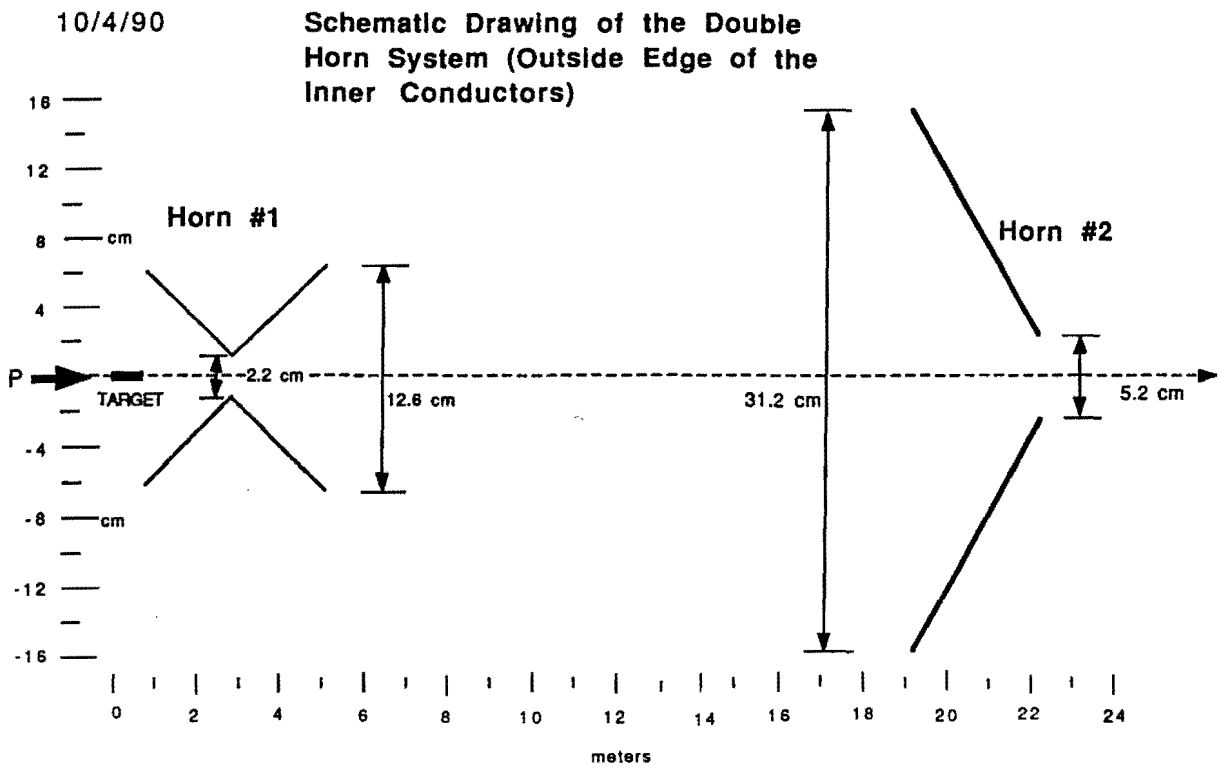

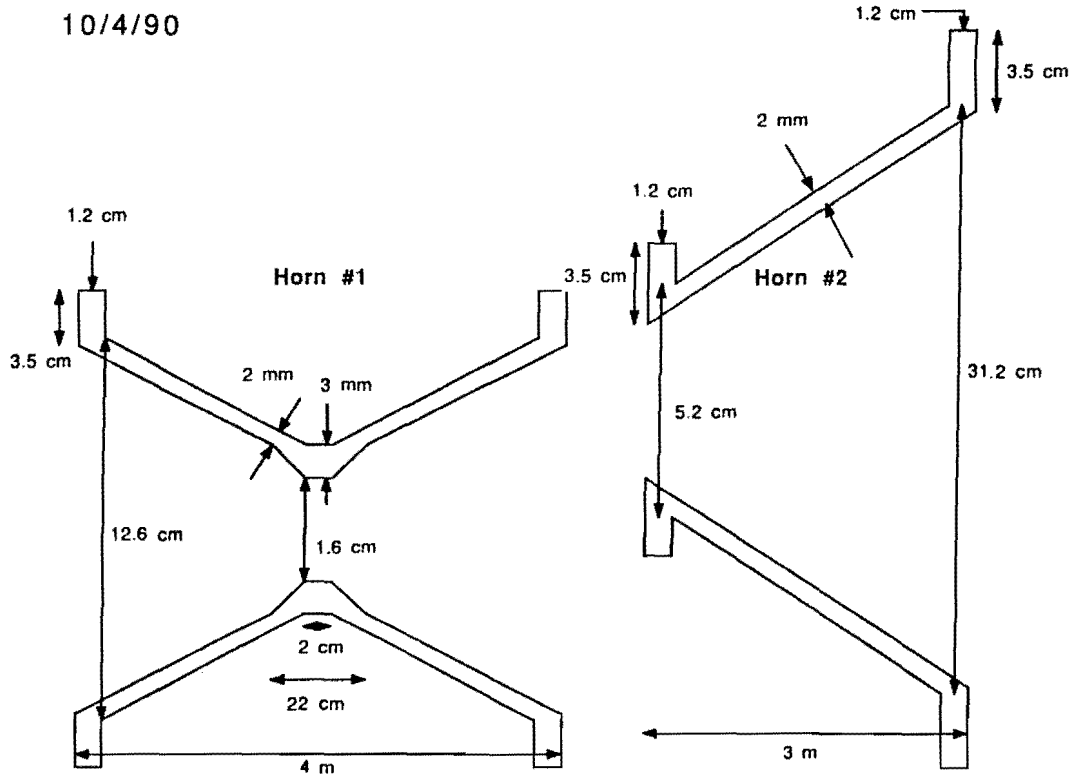

FIG. 9. Double-horn system for the neutrino beam.
Upper: schematic sketch, showing placement of components.
Lower: Detail, showing thickness of walls.

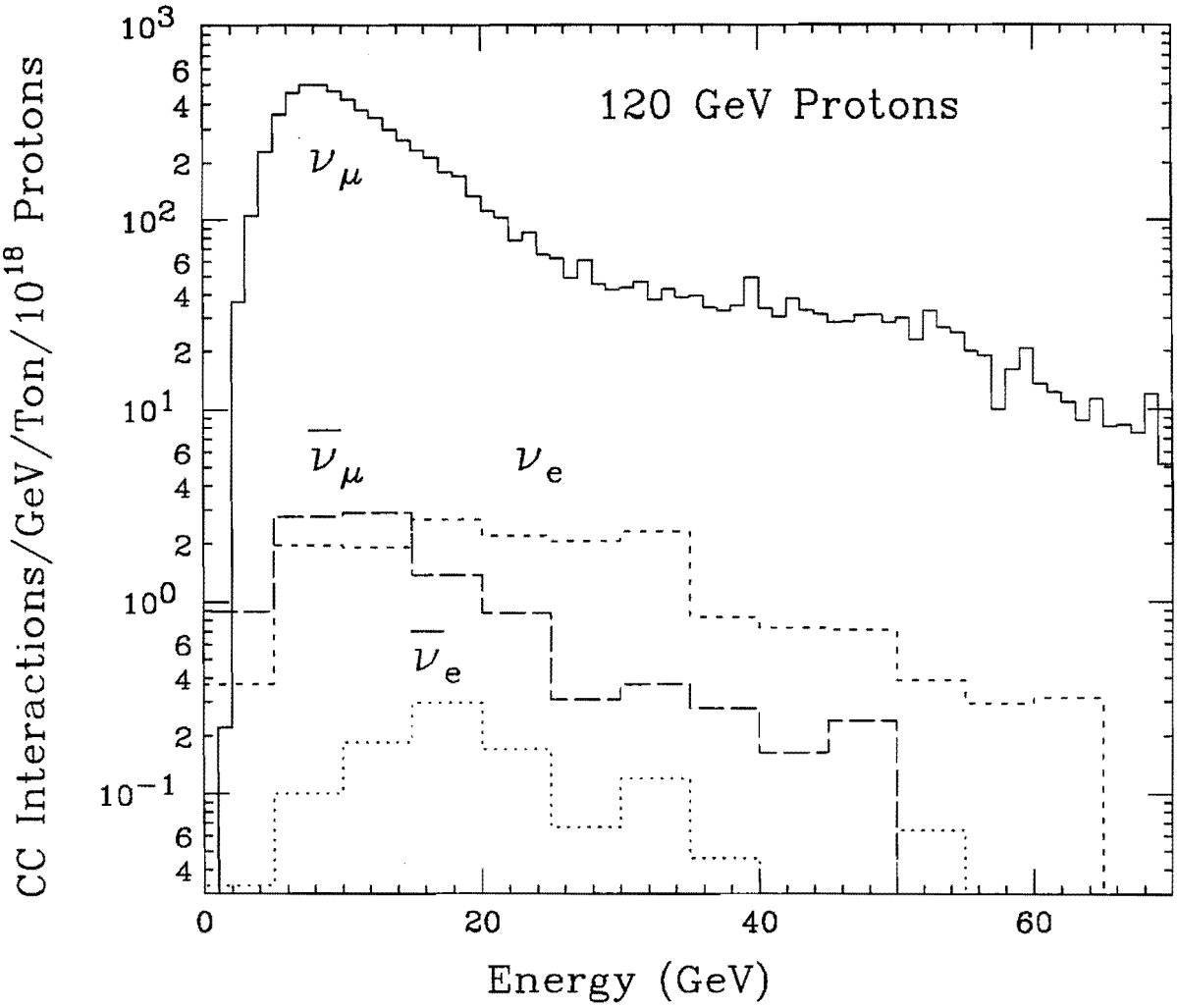

FIG. 10. Results of a Monte Carlo simulation of the charged-current event rates from the Main Injector beam assumed in this proposal, with a 320 m decay pipe followed by 150 m of shielding berm. The detector area is 1.8 m x 1.4 m.

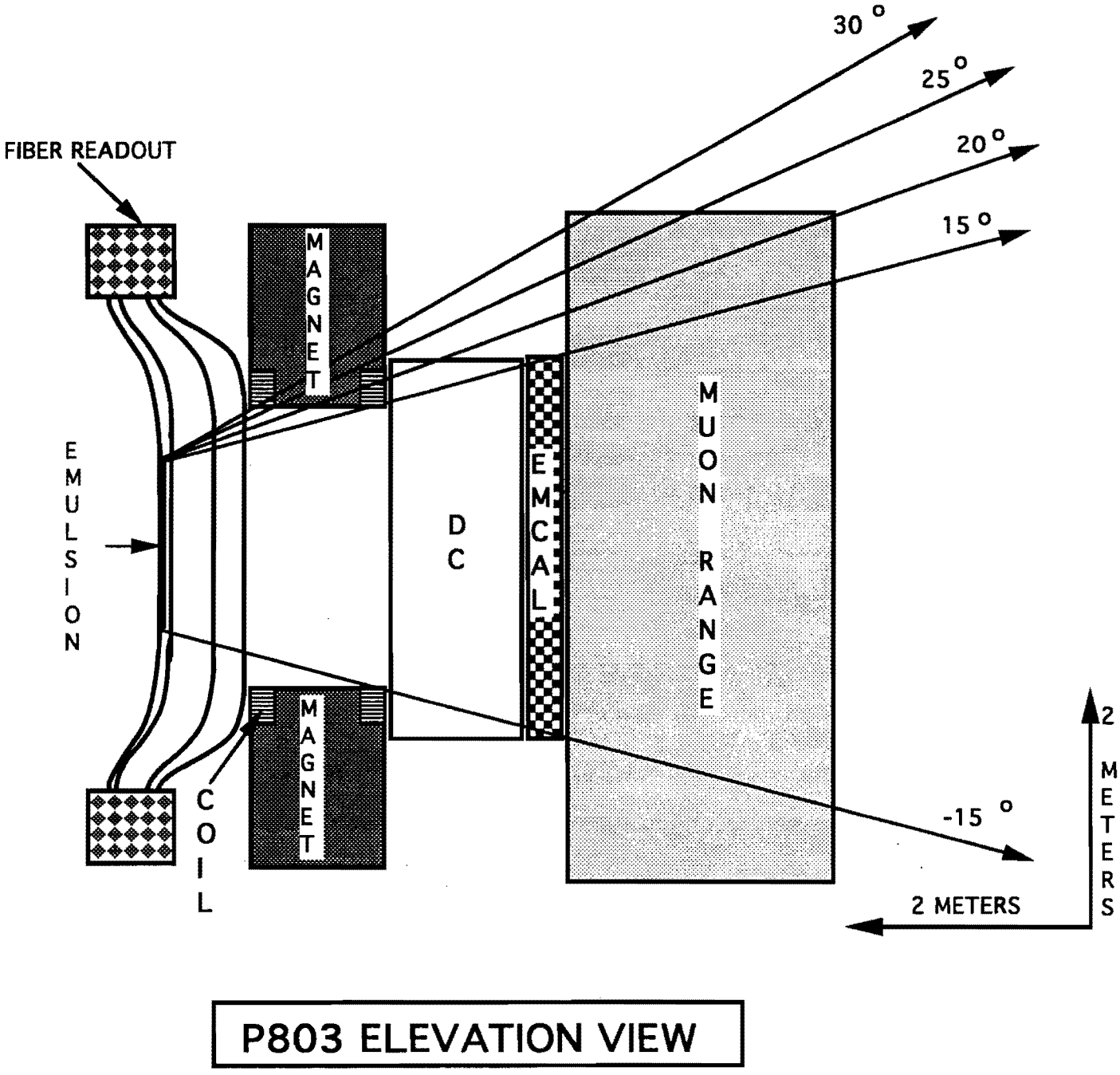

FIG. 11. Schematic elevation view of the P803 spectrometer.

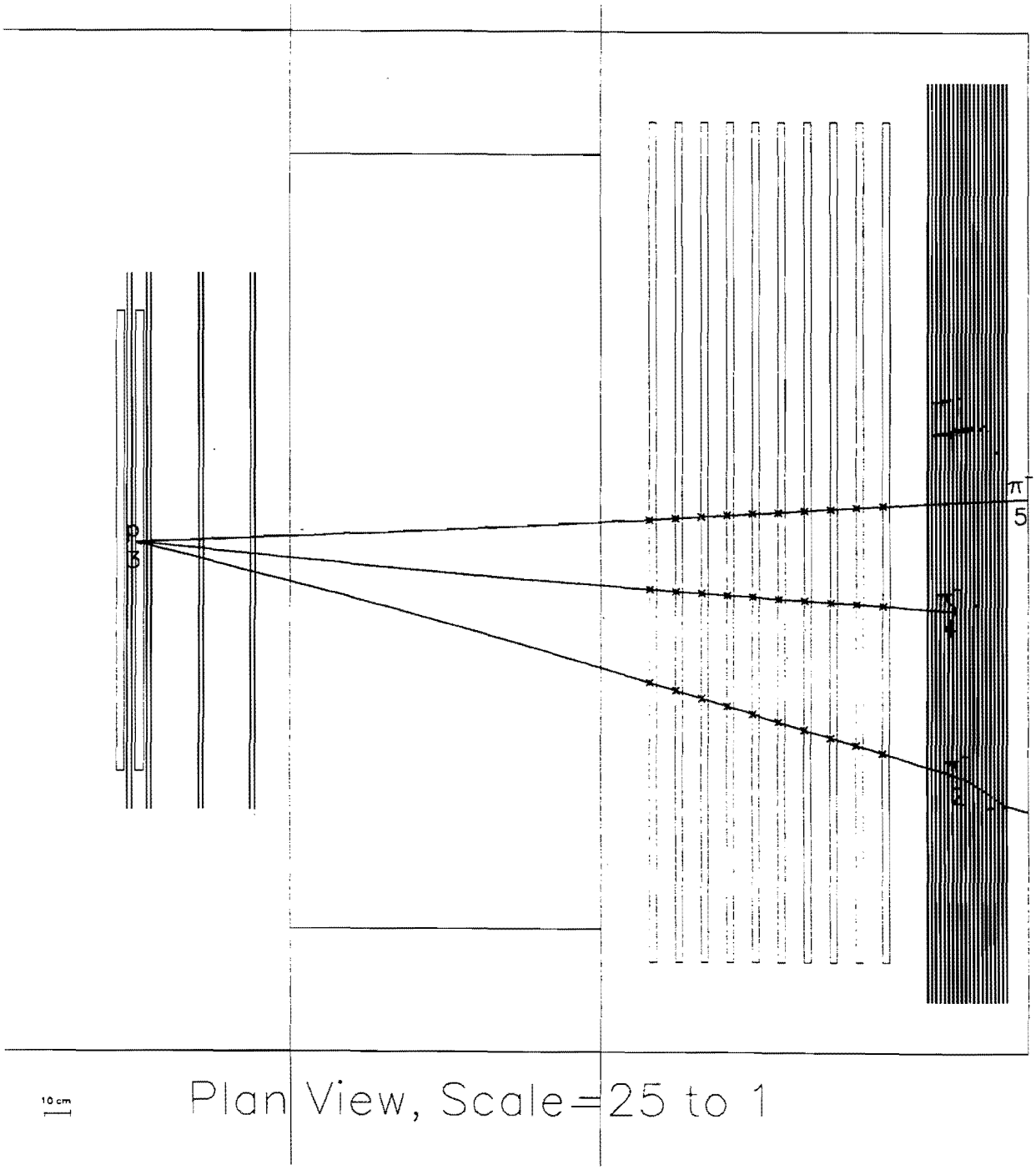

FIG. 12. LUND-GEANT simulation of a simple $\tau^- \rightarrow \rho^- \nu$ event, seen in the x (bend plane) view. The two emulsion targets and the four scintillating fiber modules are at the left, the bending magnet is at center, and the downstream tracking and electromagnetic calorimeter are at the right (the muon identifier is not shown).

A 22 GeV ν_τ interacts in the downstream target to produce a a 17 GeV/c τ, which decays into a 4 Gev/c π^- and γ's of energies 6 and 0.7 GeV. Both γ's convert in the electromagnetic calorimeter.

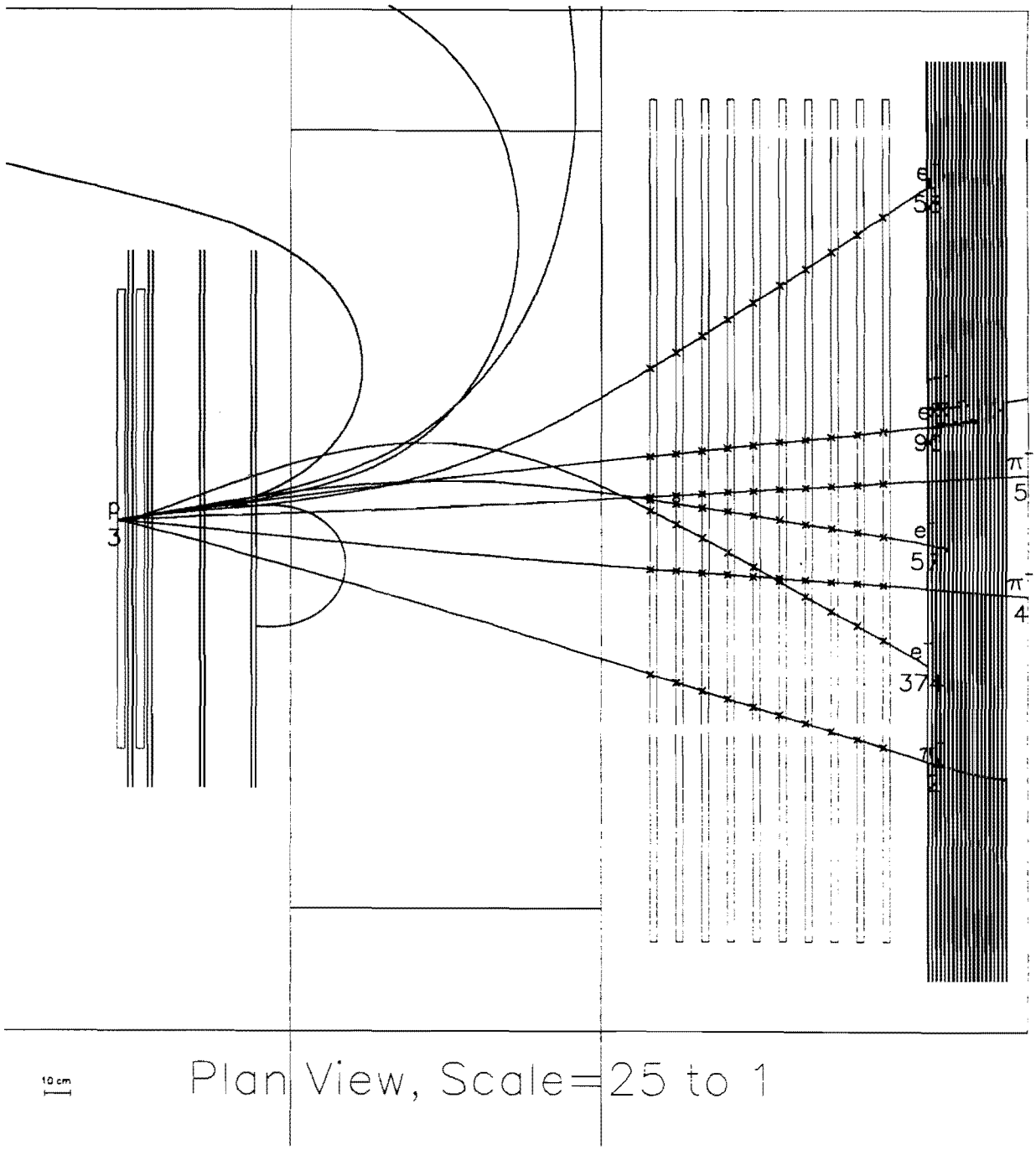

Fig. 13. The same simulated event as in the preceding figure, except that the neutrino interaction occurred near the upstream face of the first target. The 6 GeV γ has converted and showered in the emulsion.

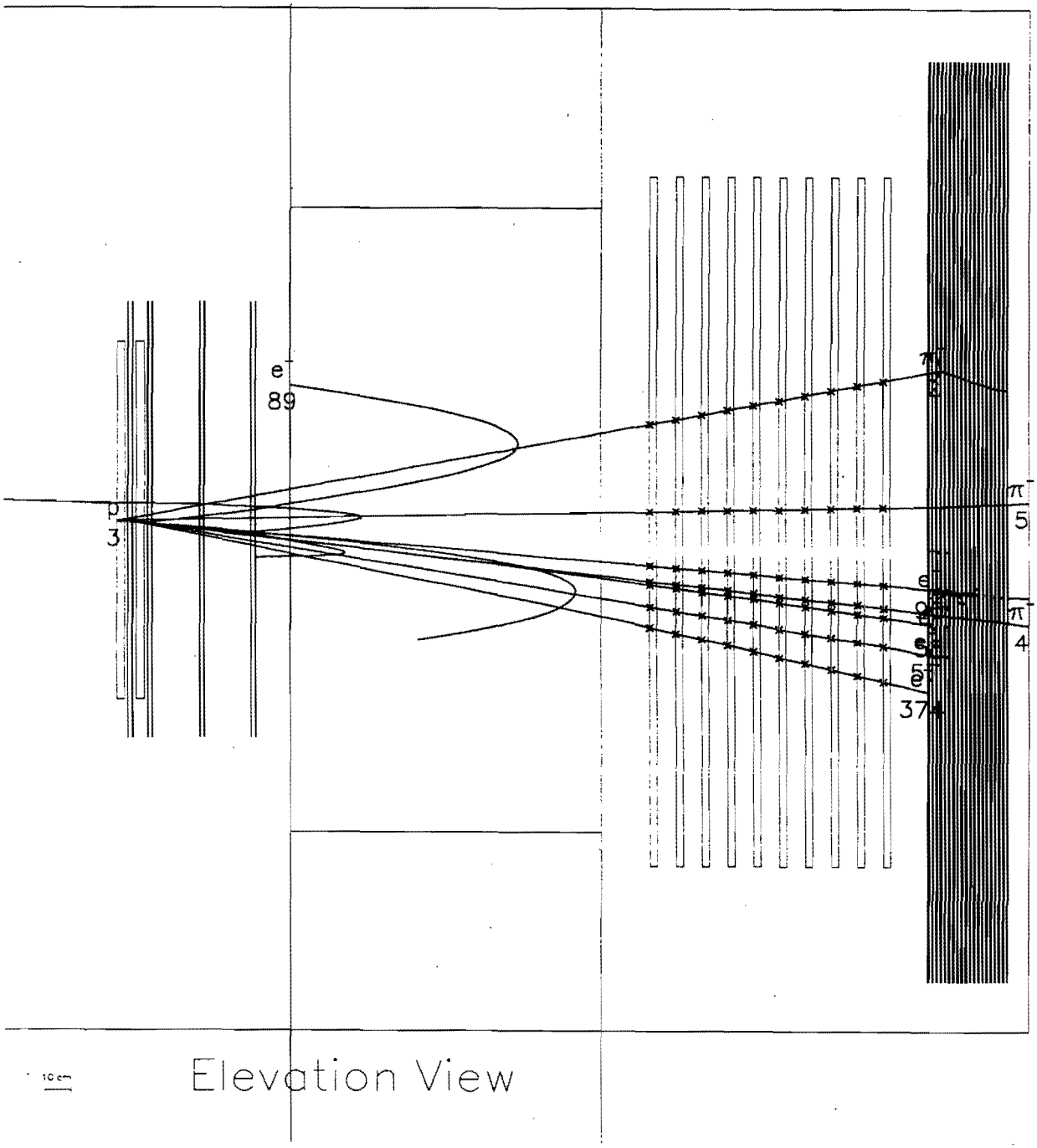

Fig. 14. The same event, as seen in the orthogonal y view.

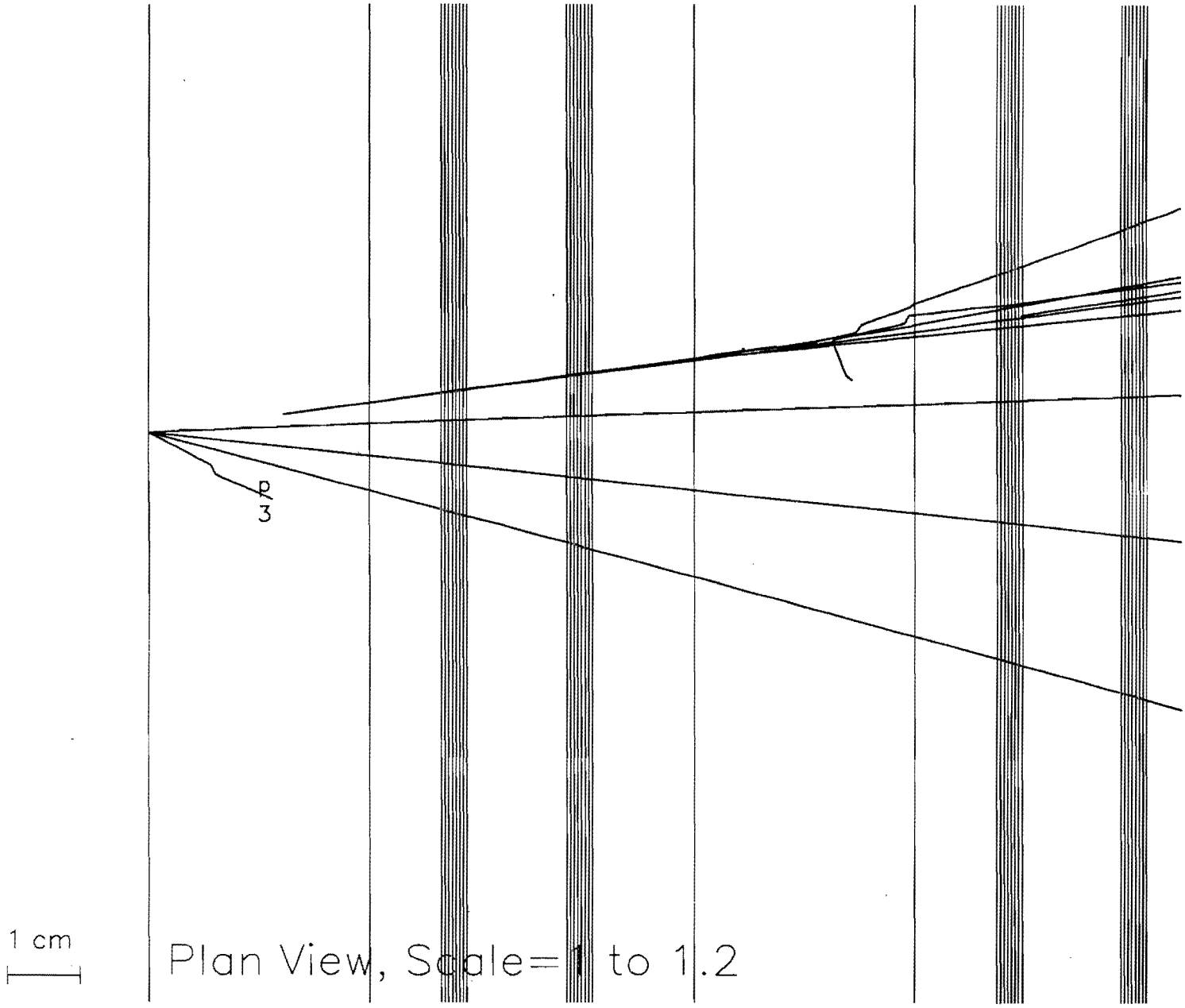

Fig. 15. Enlargement of the x view of same event, approximately lifesize. Pictured is the region of the two emulsion targets and the two post-target fiber modules; the interface sheets are not shown, and only the x, x' ribbons of the two fiber modules are drawn. Each ribbon will have 4-5 hits from a minimum ionizing track. The ν_τ interaction occurs near the upstream edge of the first target, and one γ converts in the emulsion and showers further in the second emulsion target.

The left fiber module will locate the event by pointing a track into interface sheets, and thence into the emulsion. It will also be used to find the γ conversion after the τ kink is found. The right fiber module is the first station in track momentum measurement, and also tags the electromagnetic shower topologically.

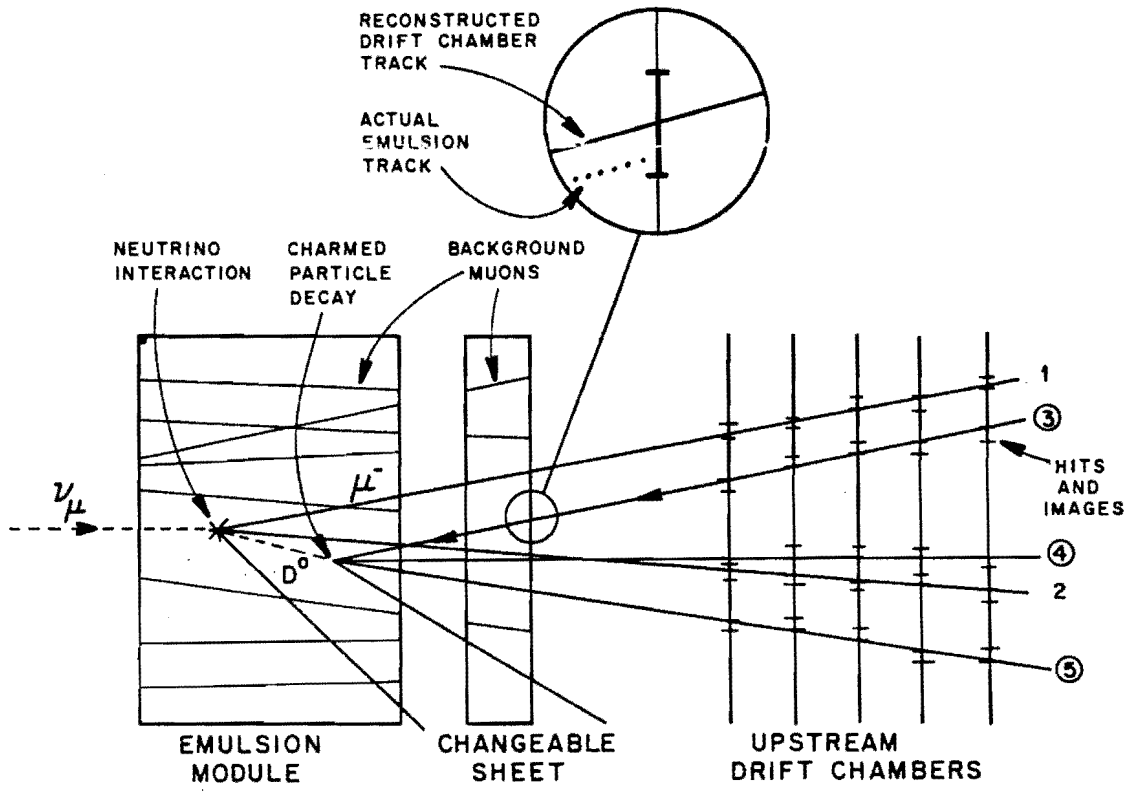

FIG. 16. Schematic illustration of the use of a changeable interface sheet (emulsion-plastic-emulsion) in Fermilab experiment E531. The emulsion tracks on opposite sides of the plastic sheet form a precision vernier pointing into the emulsion.

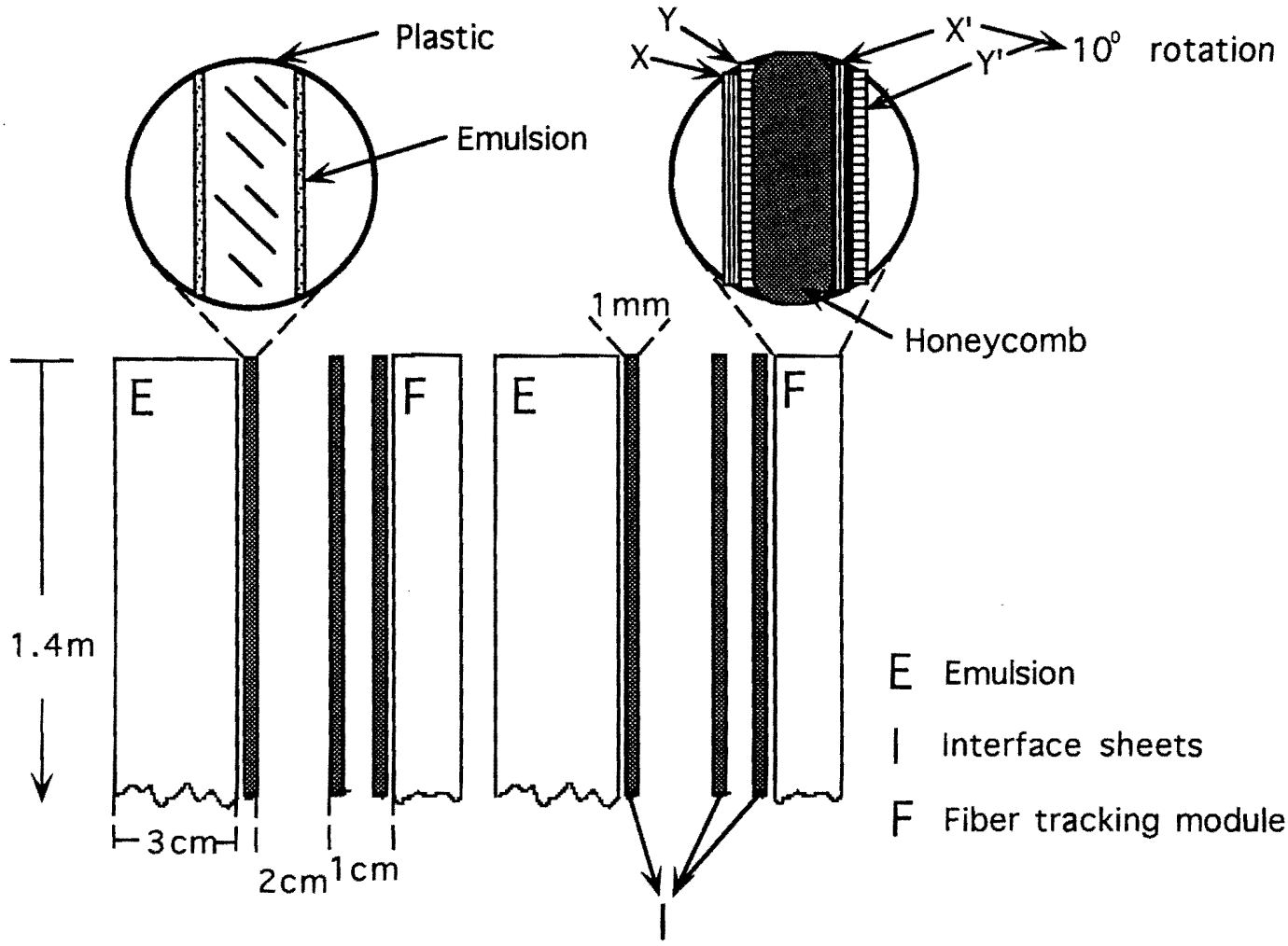

FIG. 17. Schematic layout of the P803 target region, showing placement of bulk emulsion targets (E), interface sheets (I), and scintillating fiber modules (F).

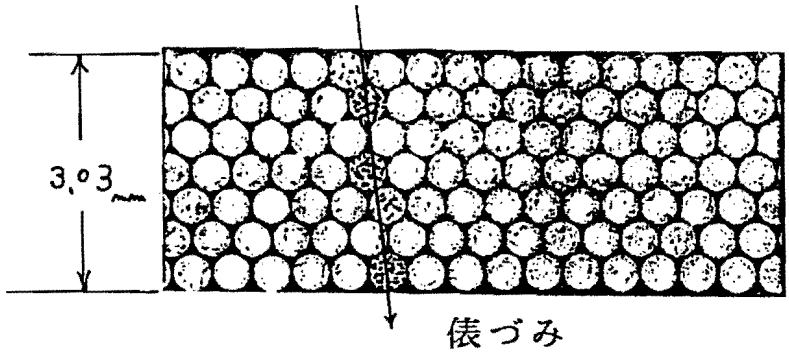

FIG. 18. Schematic illustration of a track in a 7-layer ribbon of 0.5 mm diameter scintillating fibers.

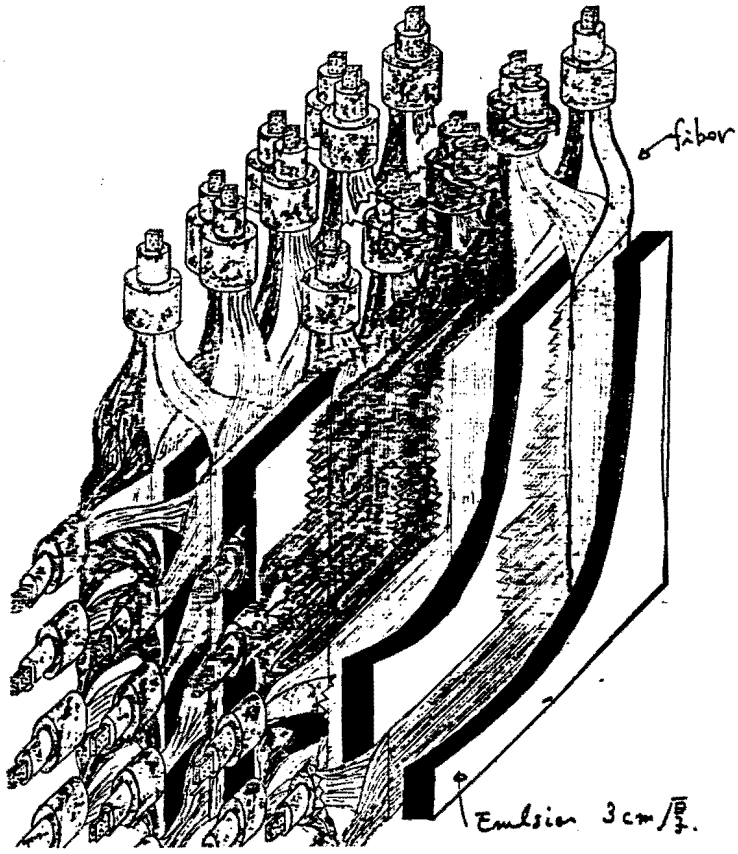

FIG. 19. Sketch of the arrangement of Nagoya scintillating fiber ribbons and readouts for the CHORUS experiment.

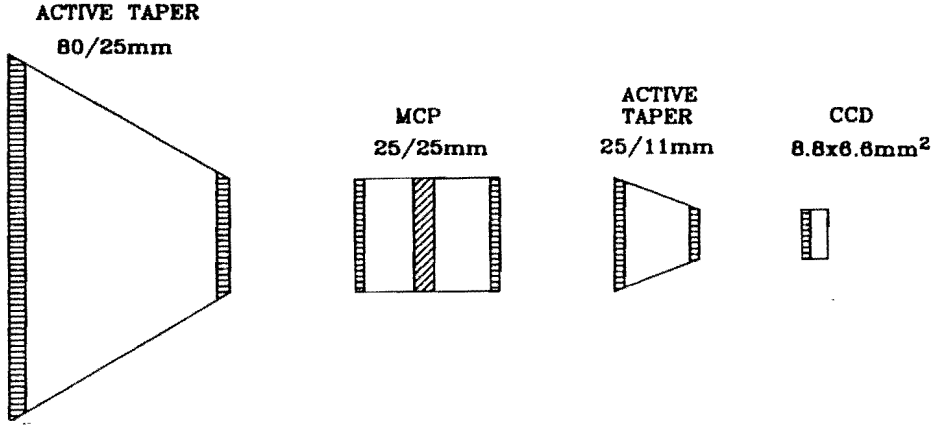

FIG. 20. Schematic diagram of one of the Nagoya fiber readout assemblies used in the Chorus experiment. The active tapers are image intensifiers, and the MCP is a gated high-gain microchannel plate.

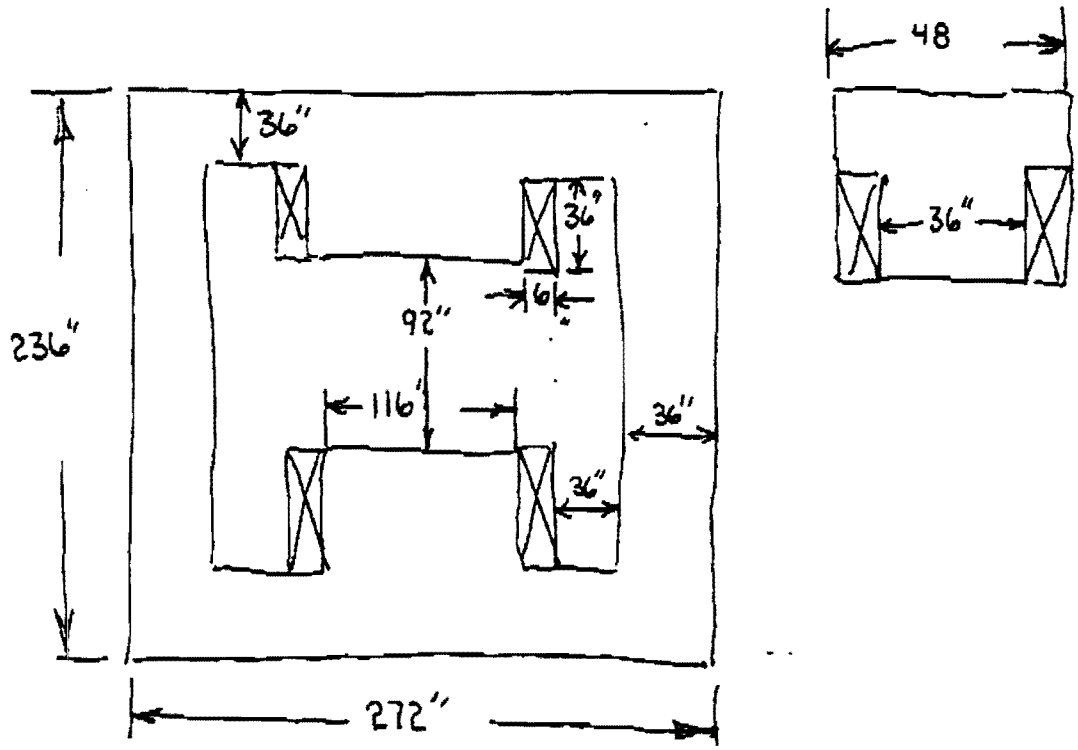

FIG. 21. Sketch of a preliminary magnet design.

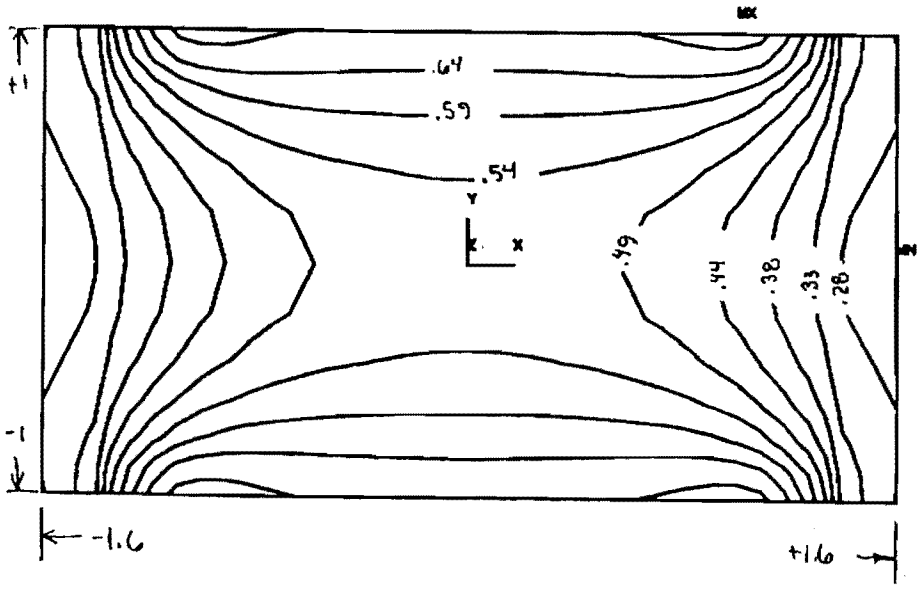

FIG. 22. Contour plot of the useful field integral (T-m) as a function of the coordinates perpendicular to the beam direction.

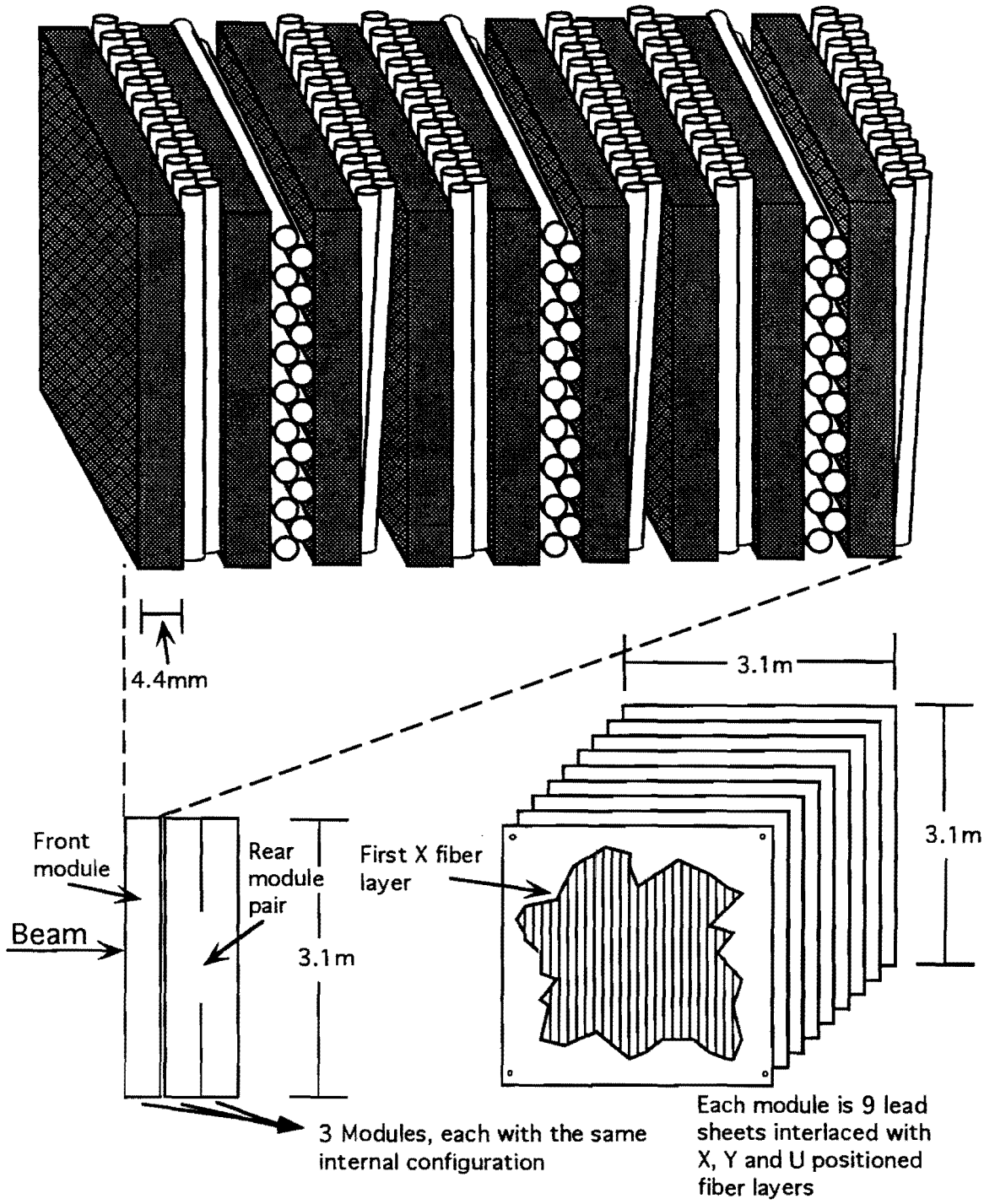

FIG. 23. Sketch of the electromagnetic calorimeter, showing the layers of lead and ribbons of scintillating fibers which provide 3 stereo views of readout (x, y, u). Each lead sheet is 7/9 X_0 thick, and the fiber ribbons are 2 cm wide. Fibers from the same view in the upstream in the upstream third of the calorimeter are ganged together, as are those from the same view in the second two-thirds.

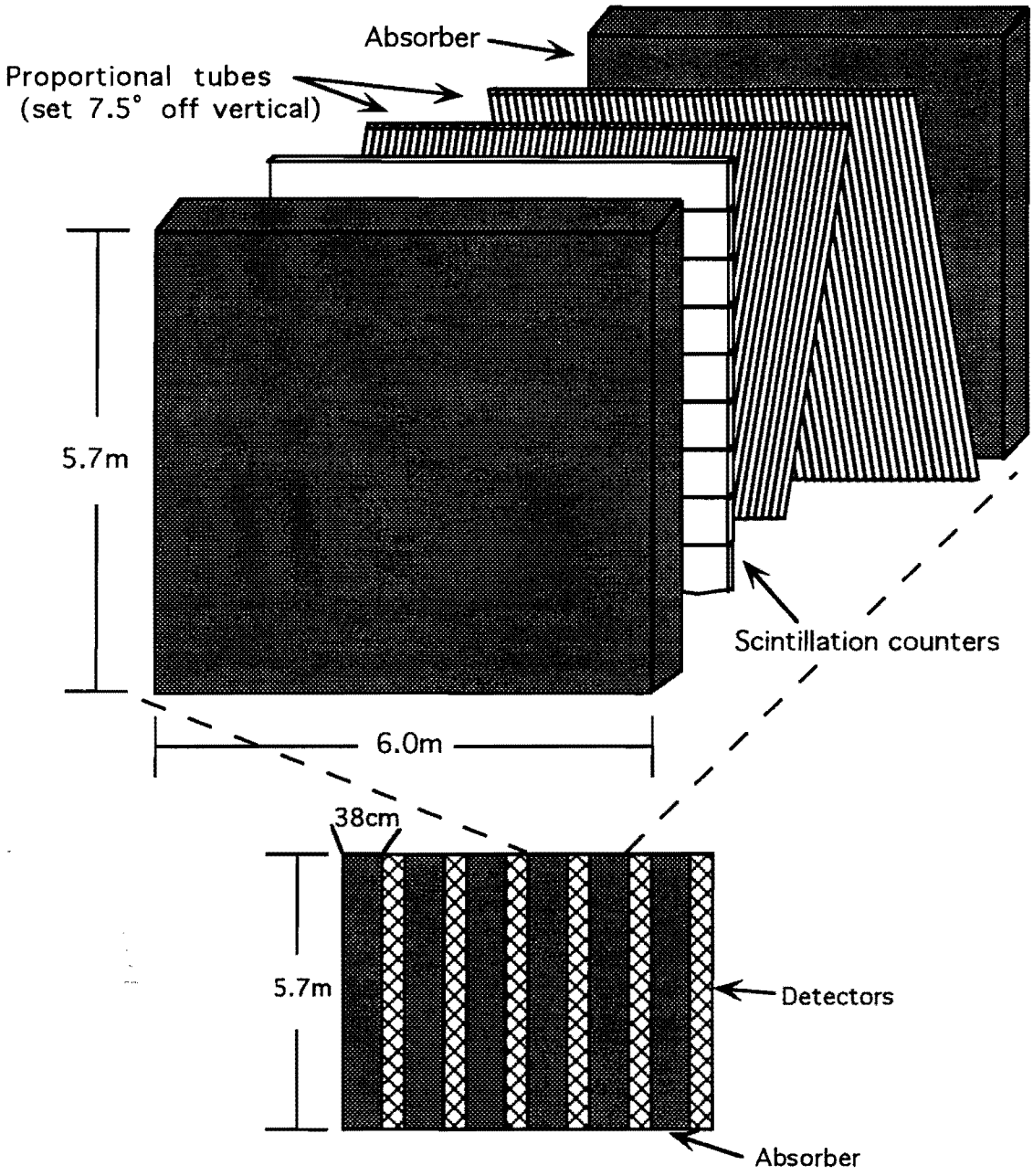

FIG. 24. Sketch of the muon identifier, showing the crossed planes of proportional tubes and scintillators.

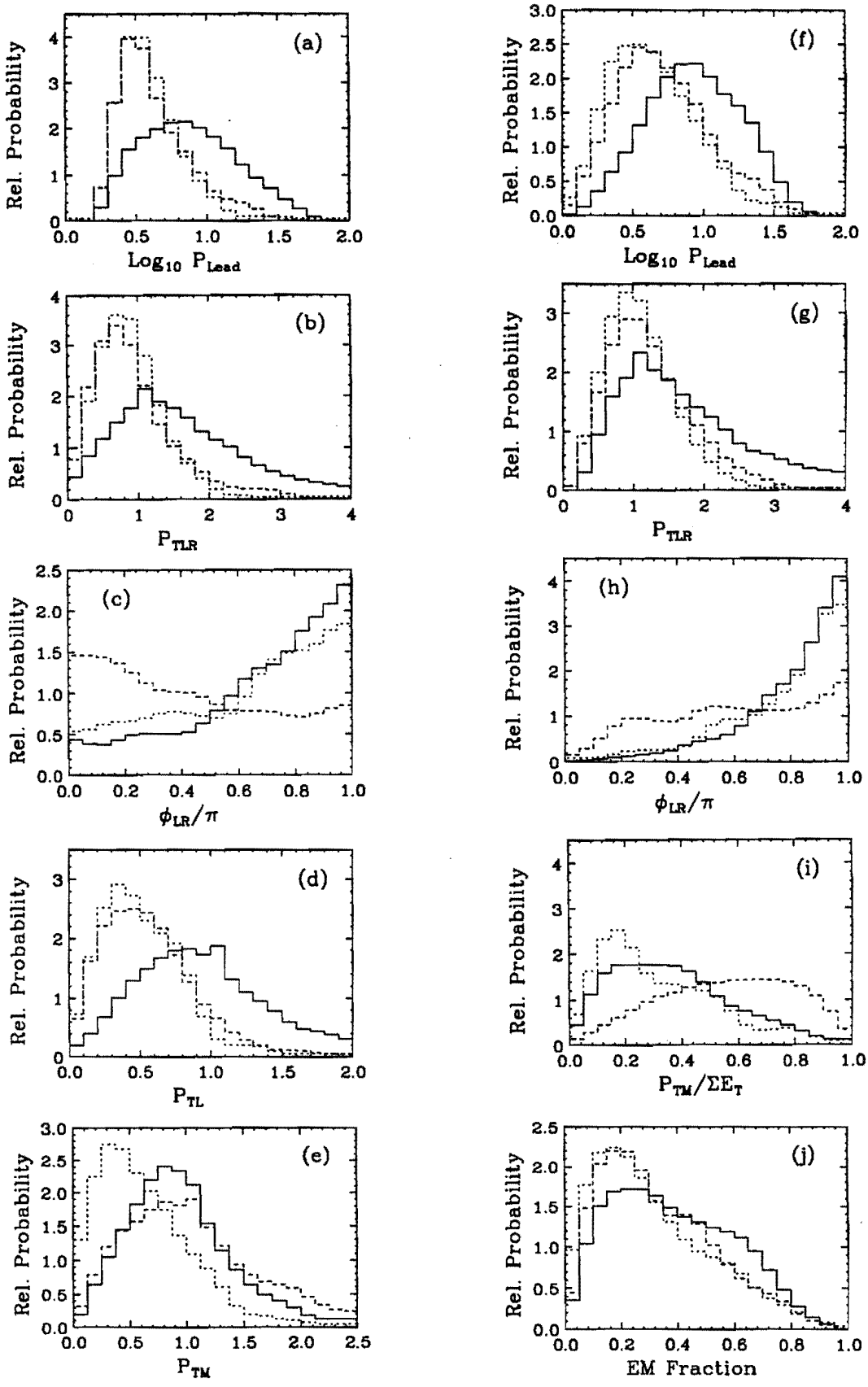

FIG. 25. Examples of distributions of variables used for discriminating τ decay candidates (solid histograms) from ordinary NC (dashed) and CC (dotted) interactions. (a)-(e): distributions for selecting $\tau \to \pi^- \nu$; (f)-(j): distributions for selecting $\tau \to \rho^- \nu$.

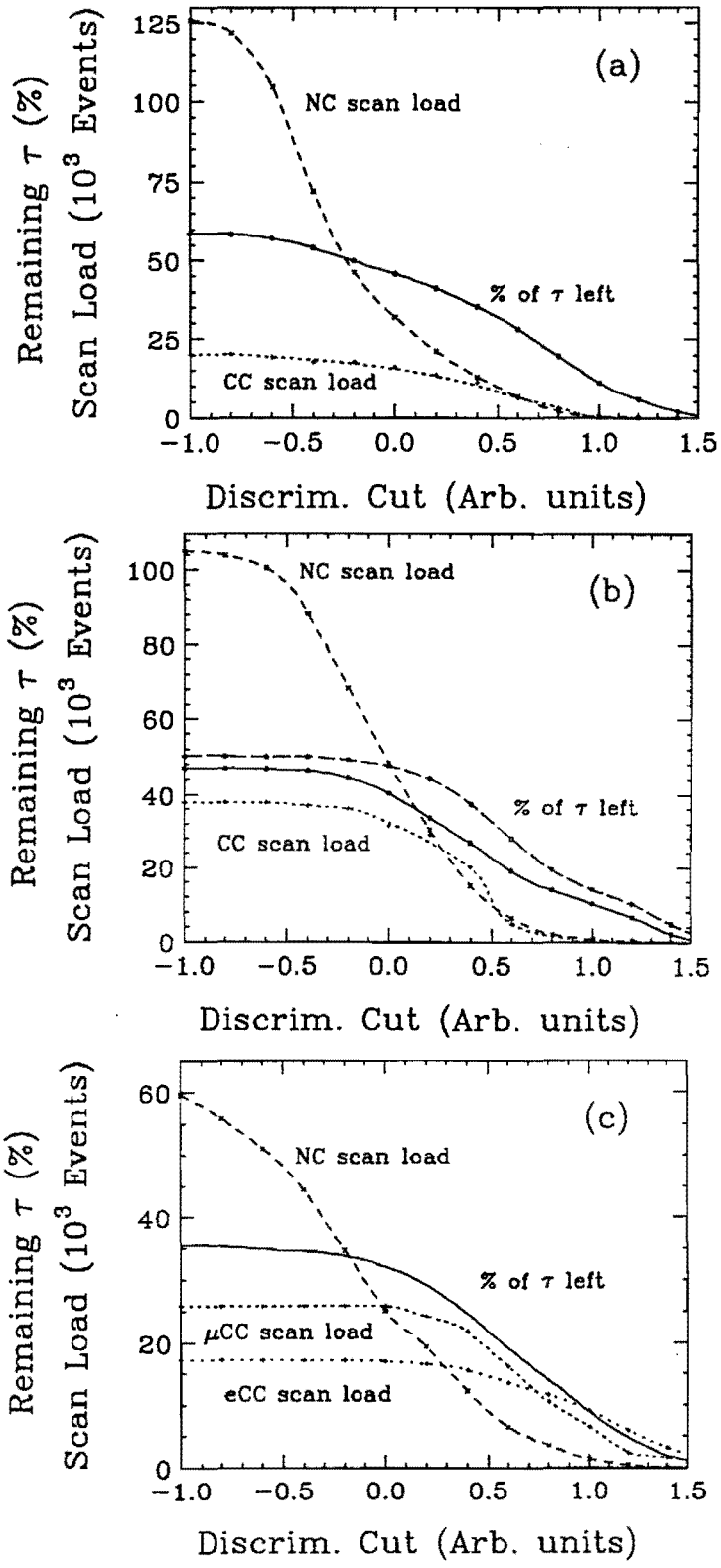

FIG. 26. Effectiveness of discriminant analysis for selecting scan samples for the (a) $\pi^-\nu$; (b) $\rho^-\nu$ and $\pi^-(n\pi^0)\nu$; and (c) $e\nu\bar{\nu}$ decay modes of the τ. In each plot, the abcsissa is the discriminant variable F_{NC}. The fraction of τ decays surviving an F_{NC} cut are shown as solid curves, while the NC and CC scan loads resulting from this cut are shown as dashed and dotted curves.

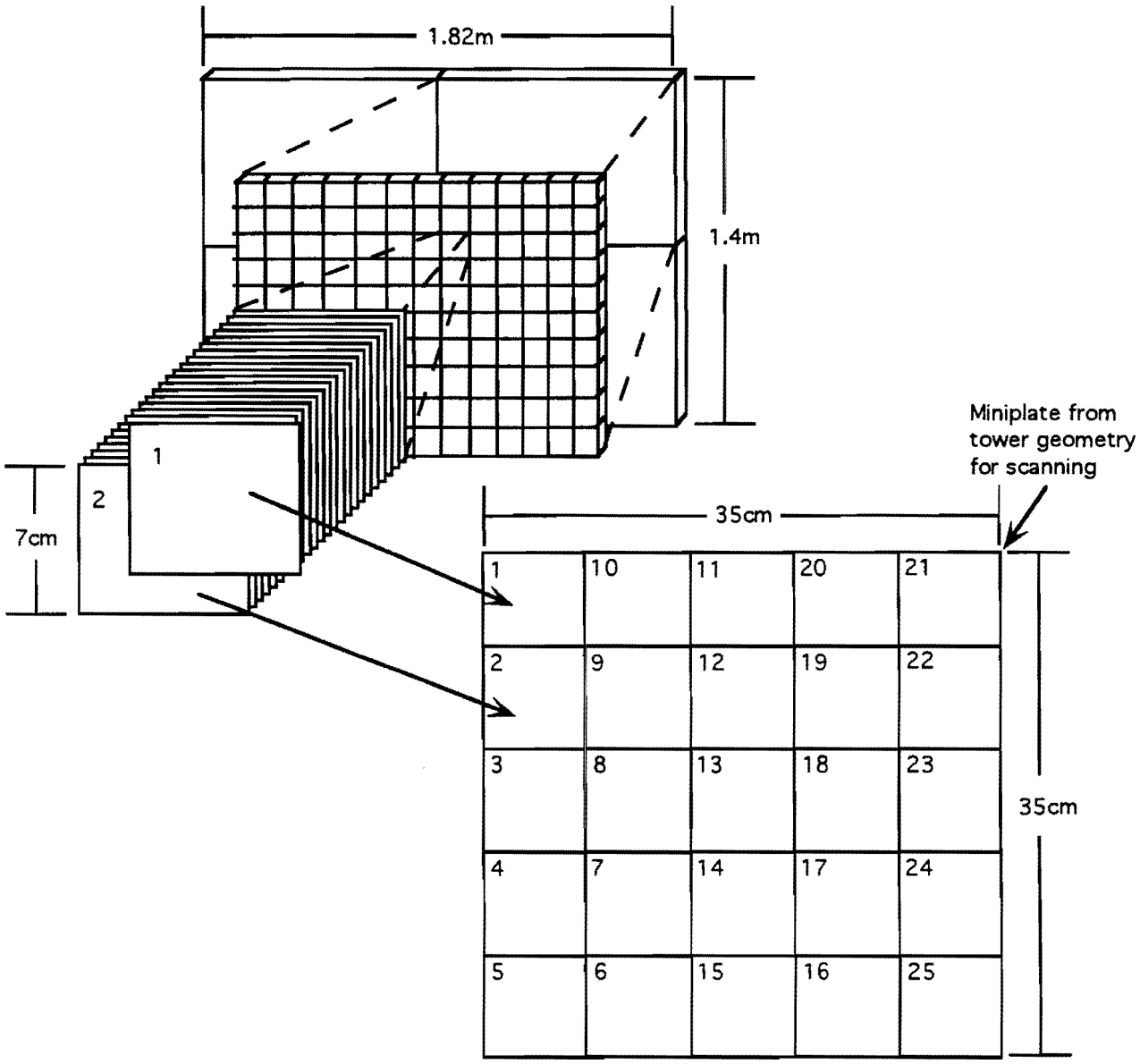

FIG. 27. Illustration of the miniplate technique: squares of emulsion containing information from a tower 7×7 cm^2 wide by 3.0 cm deep are mounted side by side for scanning.

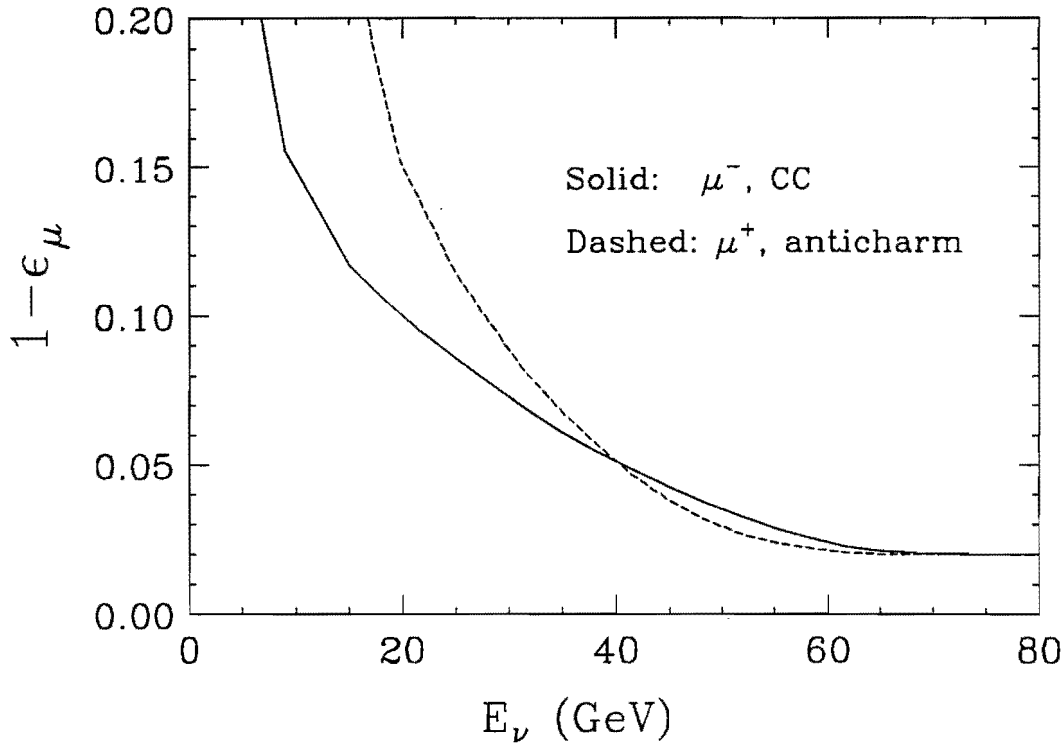

FIG. 28. Average muon rejection inefficiency $1 - \epsilon$ as a function of neutrino energy for μ^- from all charged current events (solid), and for μ^+ from anticharm production by antineutrinos (dashed).

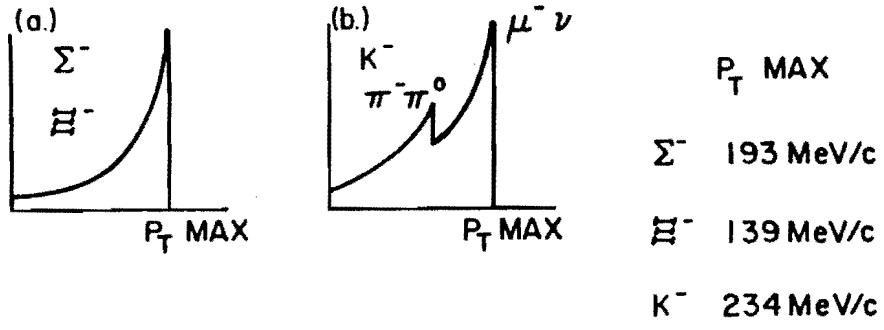

FIG. 29. Distribution of decay p_T (transverse momentum relative to the parent direction) for (a) hyperon, (b) charged kaon decays. Note that all strange decays are eliminated with a cut of $p_T \geq 0.25$ GeV/c.

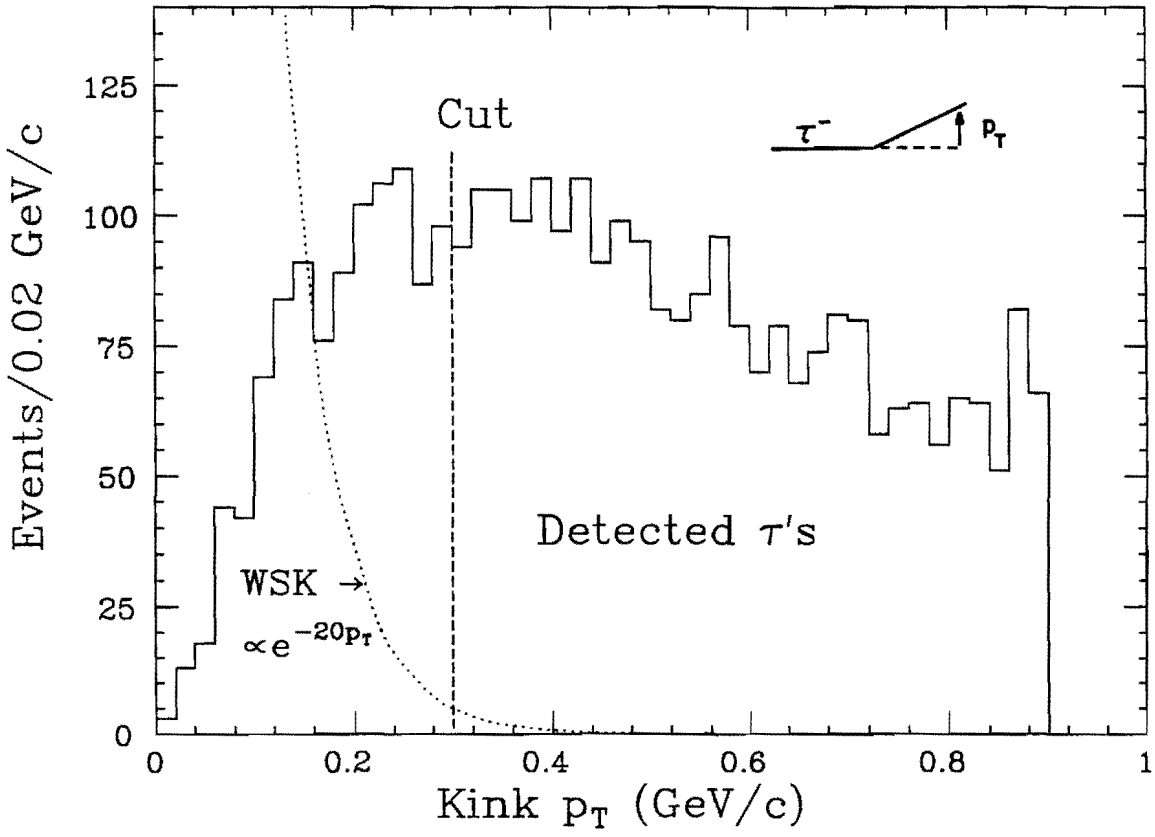

FIG. 30. Distribution of decay p_T (histogram), for all decay modes, for τ's passing the scan cuts and the kink cuts other than p_T. The measured p_T falloff for whitestar kinks is shown as a dotted curve. The p_T cut specified in this proposal (0.30 GeV/c) is also indicated.

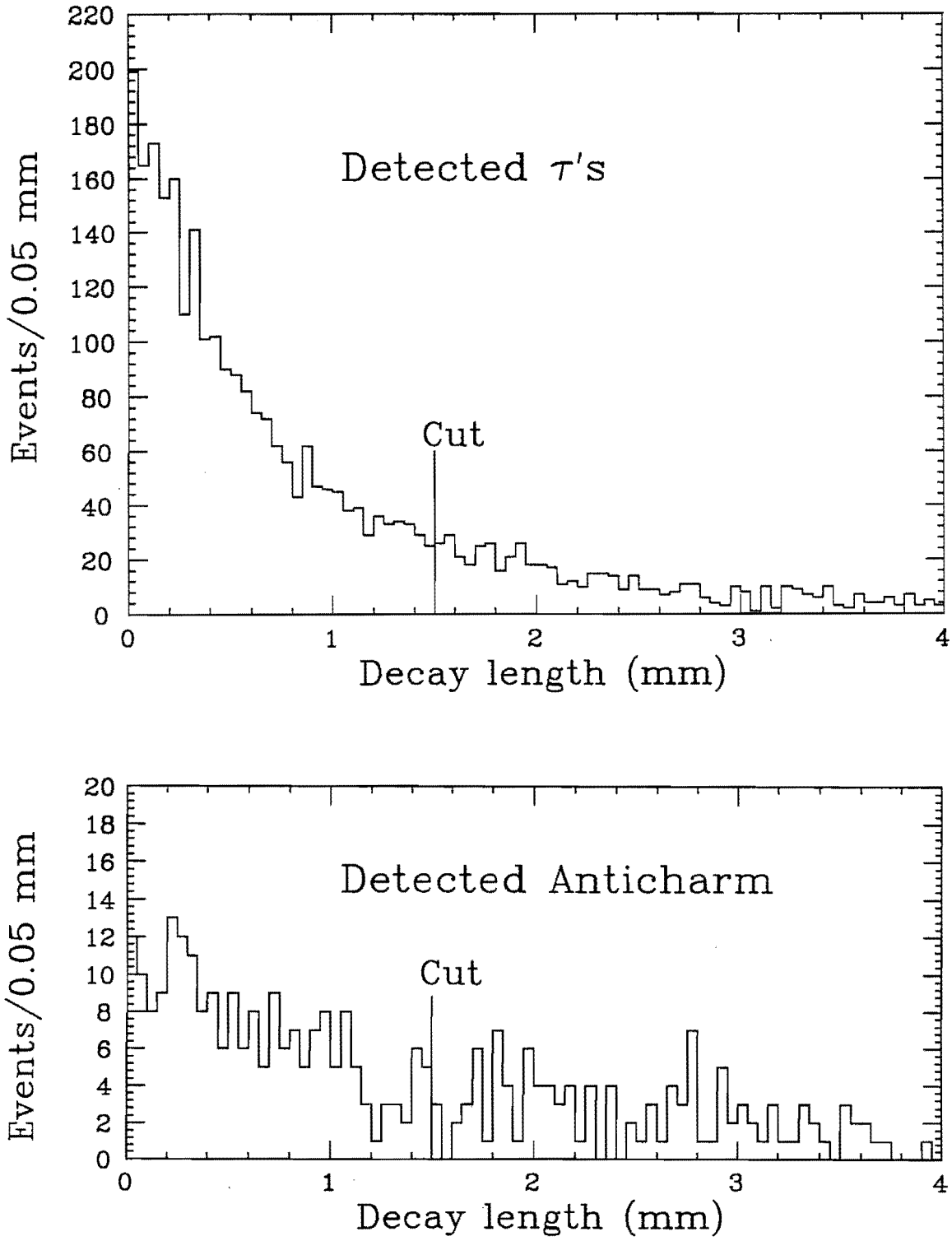

FIG. 31. Monte Carlo distributions in decay length for a) τ events passing all cuts except decay length (top histogram); and for b) anticharm background events passing the same cuts. Whitestar kinks have a uniform decay length distribution. The cut used in this proposal is indicated.

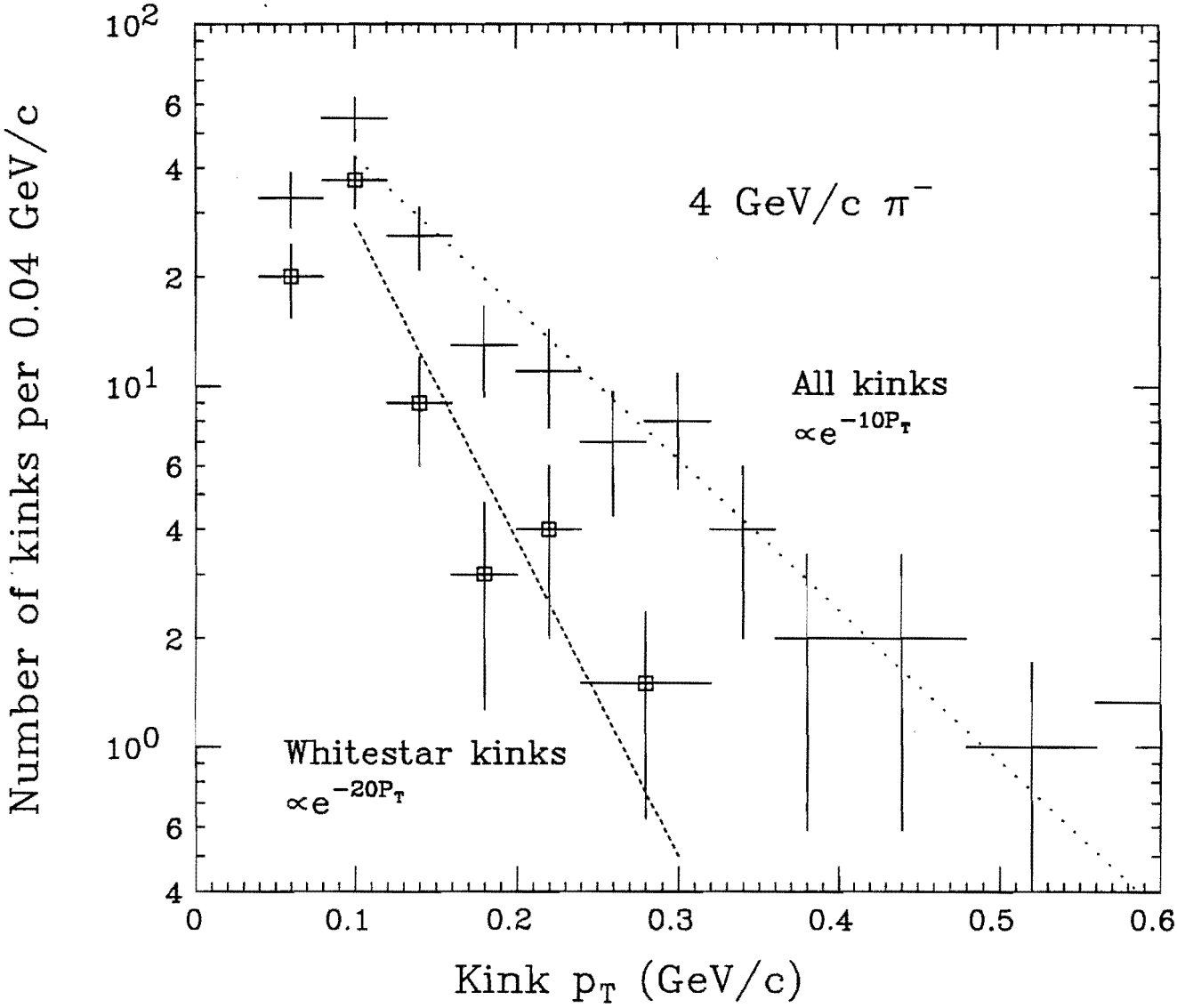

FIG. 32. Results from the KEK measurement of whitestar kinks produced by 4.0 GeV/c π^-: number vs. p_T for all kinks (crosses), and for whitestar kinks (squares). There is one additional WSK event above 0.6 GeV/c. The p_T dependences for $p_T > 0.1$ GeV/c are indicated by the dotted and dashed lines.

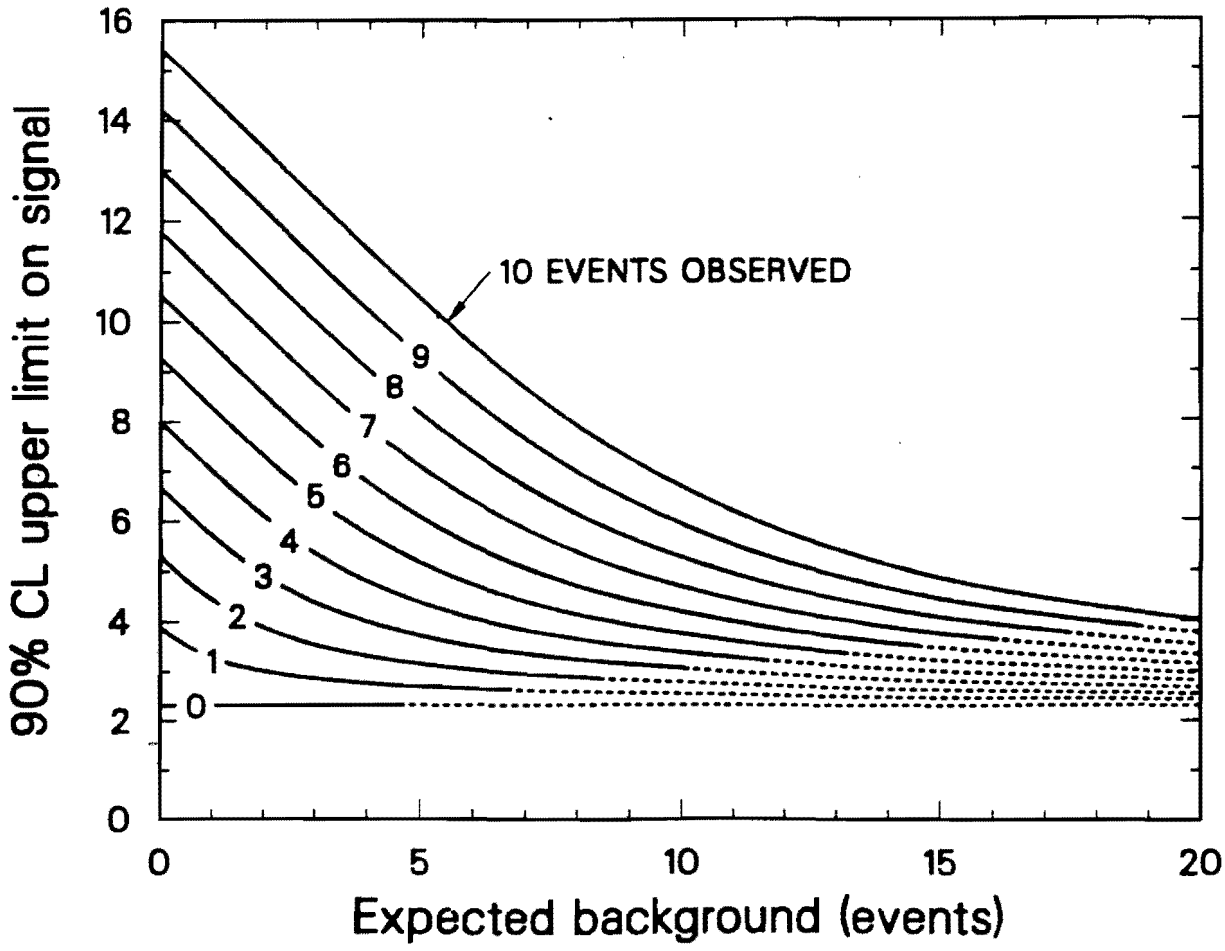

FIG. 33. 90% confidence level limits as a function of expected background and number of observed events.

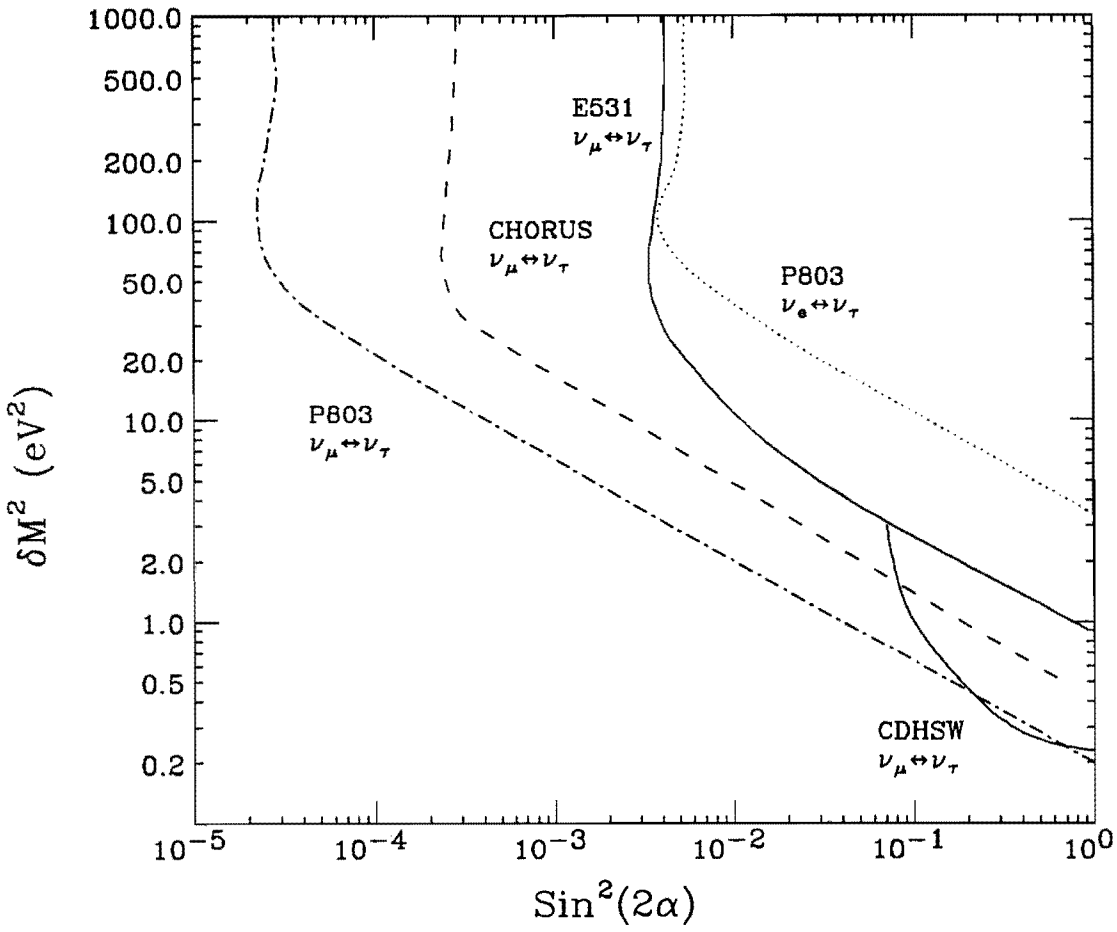

FIG. 34. Oscillation limits for $\nu_\mu \leftrightarrow \nu_\tau$ and $\nu_e \leftrightarrow \nu_\tau$ short-baseline experiments. Existing limits are given by the solid curves, and the anticipated CHORUS limit by long dashes. The P803 $\nu_\mu \leftrightarrow \nu_\tau$ projected limit is given by the dash-dot curve.

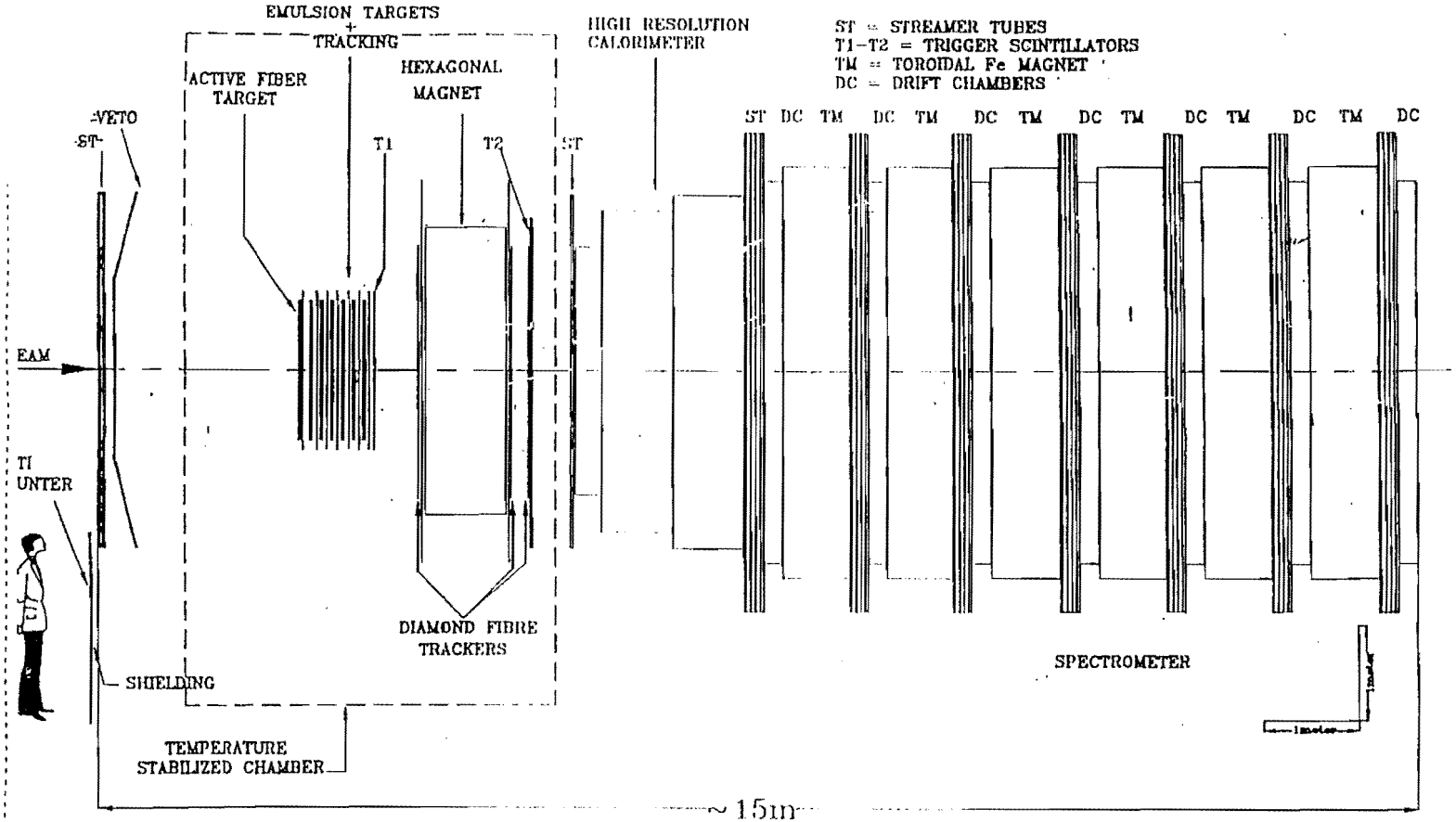

FIG. 35. Layout of the CHORUS experiment at CERN.

Appendix A

STANDARD MODEL PHYSICS IN P803

The combination of 6×10^6 charged current interactions, an intermediate energy neutrino beam, high precision charged particle tracking, and emulsion-quality vertex resolution permits several high quality standard model measurements in the P803 experiment. These include the determination of the CKM matrix element V_{cd} to an accuracy approaching the unitarity limit; a 5% determination of the charm quark mass; a unique exploration of charm production dynamics in neutrino scattering; and the first precision extractions of the structure functions $F_2(x, Q^2)$ and $xF_3(x, Q^2)$ using neutrino data in an x, Q^2 regime which overlaps comparable electroproduction data from SLAC.

Charm physics

The charm-to-down CKM transition element can only be measured using the neutrino production of charm. Except for FNAL E531 and a few low statistics bubble chamber experiments, all information currently known about charm production in neutrino physics comes from studies of di-lepton production. Such measurements have reached high statistics, but they are plagued by theoretical and experimental model dependences. Examples of such sources of systematic error include charm quark fragmentation, relative species population of charmed hadrons in the final state, charmed hadron branching ratios, charm-anticharm misidentification, and large dilepton backgrounds from π and K decays. At a fundamental level, dilepton experiments cannot measure the charm production kinematics due to the missing neutrino from the semi-leptonic decay.

The current best measurement of V_{cd} has a precision of 8%, with the error split roughly equally between statistical and systematic contributions. The charm mass m_c is measured to an accuracy of 240 MeV.

P803 can make a major advance in neutrino charmed physics. The ability to topologically identify charm allows for the nearly complete elimination of branching ratio, species production, and fragmentation related errors. Furthermore, by removing semi-leptonic decays from the charm sample, one can measure, for the first time at high statistics, the Bjorken x, inelasticity y, and fragmentation parameter z distributions. About 140,000 charmed particles are expected to be produced for the six million charged current events. The experimental challenge is the identify the charm with minimal reliance on scanning.

V_{cd} and m_c

The sensitivity to V_{cd} can be understood by considering the following first

order cross sections for neutrino production of charm off an isoscalar target:

$$\frac{d\sigma(\nu_\mu N \to \mu^- cX)}{dxdy} = \frac{G_F^2 ME}{\pi}(1-\frac{m_c^2}{2ME\xi})(|V_{cd}|^2\cdot(V(\xi,Q^2)+\bar{Q}(\xi,Q^2))+|V_{cs}|^2\cdot 2S(\xi,Q^2)).$$

In this expression, m_c is the effective charm mass; V_{cd} and V_{cs} are CKM matrix elements; x and y are the usual scaling varaiables; $\xi \simeq x(1+\frac{m_c^2}{Q^2})$ is the momentum fraction of the proton carried by the struck quark; and $V(\xi,Q^2)$, $\bar{Q}(\xi,Q^2)$, and $S(\xi,Q^2)$ are the valence, non-strange sea, and strange sea parton distribution functions, respectively. At first sight it would appear that there are too many parameters in the cross section to have sensitivity to V_{cd}. However, if one places the restriction that $x > 0.4$, the sea quark contributions essentially vanish, and the remaining dependence is on the theoretically better understood valence quark distributions (which P803 can measure), the desired CKM parameter, and m_c. Even the m_c dependence is fairly weak since the charm threshold suppression is strongest at small x. One approach to extract V_{cd} is thus to cut on x, which is possible in principle for topologically identified charm events.

A second approach would be to combine the P803 charm cross section measurement with neutrino dimuon data from FNAL E744/770. The older experiments effectively determine the strange sea, while the new experiment is highly sensitive to m_c owing to the lower energy beam. As discussed in Appendix B of this proposal, such a combined fit can determine, albeit in a model dependent way, m_c to a precision of 30 MeV and V_{cd} to $\pm 3\%$.

The model dependence of the two methods sketched above can largely be eliminated if one can also measure the anti-neutrino rate as a function of energy. To leading order again:

$$\frac{d\sigma(\bar{\nu}N \to \mu^+ \bar{c}X)}{dxdy} = \frac{G_F^2 ME}{\pi}(1-\frac{m_c^2}{2ME\xi})(|V_{cd}|^2\cdot\bar{Q}(\xi,Q^2)+|V_{cs}|^2\cdot 2S(\xi)).$$

The difference between neutrino and anti-neutrino cross sections depends only on V_{cd}, m_c, and the valence quark distribution. Higher order QCD corrections which depend on the gluon distribution function also cancel in the difference. If the difference in integrated charm production cross sections, $\sigma^\nu(c) - \sigma^{\bar{\nu}}(c)$, is normalized to the difference in the total neutrino cross sections, $\sigma^\nu(X) - \sigma^{\bar{\nu}}(X)$, one obtains, again to first approximation:

$$R_C^- = \frac{R_c - r\cdot R_{\bar{c}}}{1-r},$$

where $R_C = \sigma^\nu(c)/\sigma^\nu(X)$ and $R_{\bar{C}} = \sigma^{\bar{\nu}}(c)/\sigma^{\bar{\nu}}(X)$ are measured in P803; and $r = \sigma^{\bar{\nu}}(X)/\sigma^\nu(X) = 0.518 \pm 0.006$ from previous measurements. With 2000 reconstructed neutrino charm events and 500 reconstructed antineutrino charm events, it is estimated that P803 can measure V_{cd} to $\pm 4\%$ and m_c to ± 0.03 GeV.

This is consistent with the estimate in Appendix B, and the technique is much less model dependent. The drawback is that 2500 charm events must be topologically reconstructed; however, this number is not inconsistent with the maximum scan load of the experiment.

Charm production dynamics

At low energies, higher order QCD production mechanisms for charm via W boson-gluon fusion are comparable to the leading order processes. This can be qualitatively understood by considering the relative probability for producing charm from a d quark vs an s quark vs a gluon. The d quark is more plentiful in the nucleon than s, but the cross section is CKM suppressed. The s quark is less plentiful than the d quark, but the cross section is CKM allowed. The gluon cross section is suppressed by α_S, but gluons are the most plentiful of all the partons in the nucleon. There is considerable controversy currently concerning the relative importance of the production mechanisms and their influence on quantities such as the magnitude of the strange sea. Another interesting topic will be that of neutral current production of charm, which proceeds only through gluon initiated digrams. Using standard PDFLIB parton distributions, one estimates 100-300 $c\bar{c}$ pairs for the full data sample.

P803 offers a unique opportunity to study these questions concerning charm production dynamics. The major advantages are the ability to fully reconstruct the event kinematics, since reliance on semi-leptonic decays is not necessary, and the potentially high statistics available in the kinematic regime where the relative strength of gluon-initiated vs quark-initiated cross sections should be changing rapidly.

The challenge in doing detailed charm production physics will be to acquire the necessary statistics while keeping the scan loads low. Since one will want to study differential cross sections as opposed to total rates, one would like to have on the order of 20,000 charm events vs the 2500 for V_{cd} and m_c. To make this practical requires using spectrometer information to try to produce a sufficiently enriched charm sample. Areas under study include the tagging of exclusive final states and the partial reconstruction of final states in conjunction with kaon identification.

Structure functions

The P803 neutrino energy spectrum is roughly comparable to beam energies used by SLAC electroproduction experiments. SLAC data dominates measurements of $F_2(x, Q^2)$ for $Q^2 < 10$ and $x > 0.1$. There are no precise neutrino measurements of $F_2(x, Q^2)$ in this kinematic range; and there are virtually no

measurements at all of the parity violating structure function $xF_3(x, Q^2)$, which can only be measured using neutrino beams. P803 could thus contribute substantially to the understanding of nucleon structure at moderate Q^2. It should be noted that structure function measurements require no scanning of the emulsion.

The most interesting physics is that governing the transition from the non-perturbative description of the nucleon to the simple QCD corrected quark parton model. Higher twist contributions to the structure functions could be 50% or more at $x > 0.5$. These contributions cannot currently be calculated; thus it is important to provide theorists with good data for guidance in building models.

Standard Model competiton from NOMAD and CHORUS

NOMAD offers no direct competiton in charmed physics because the experiment cannot topologically identify charm. They will be able to perform di-lepton based analyses; and perhaps they can reconstruct a sample of exclusive final states. No matter what, they are still stuck with significant model dependences. In particular, they must understand very well the missing energy distribution inherent in di-lepton events; this has proven difficult in previous horn beam experiments, e.g. CDHS, due to the rapidly falling neutrino energy spectrum. Indeed, CDHS was unable to understand their charm data in the context of the standard slow rescaling model.

CHORUS can essentially do what P803 can do with charm, but with $20\times$ less statistics and an inferior spectrometer. They will have difficulty improving on current measurements due to statistical considerations alone.

NOMAD should do well with conventional structure function measurements; although they will have $6\times$ fewer events. History has shown that several precision measurements of structure functions are needed to sort the physics from the systematics; so the availability of results from P803 and NOMAD will be valuable.

Appendix B

AN ALTERNATIVE METHOD OF EXTRACTING V_cd AND M_c FROM CHARM PRODUCTION BY NEUTRINOS NEAR THRESHOLD[1]

Data on charm production by neutrinos and antineutrinos permits in principle the determination of several quantities of great interest for testing the standard model: the absolute square of the K-M matrix element V_{cd}, the effective charm quark mass M_c, and the structure function for the strange sea. Because these quantities enter the data in a highly correlated way, extracting them with precision has been difficult. For example, preliminary dimuon results [1] from Fermilab E744 based on 1500 ν and 300 $\overline{\nu}$ events determines $|V_{cd}|$ to $\pm 8\%$ and M_c to ± 0.5 GeV, provided that statistical and systematic errors are added in quadrature. A more conservative treatment of systematic errors would make $|V_{cd}|$ uncertain to $\pm 13\%$.

Measurements of charm production near threshold which will be a byproduct of this proposed $\nu_\mu \leftrightarrow \nu_\tau$ oscillation experiment will allow determination of $|V_{cd}|$ to $\pm 3\%$, and of M_c to better than ± 0.05 GeV, if sources of systematic error are carefully handled.

In the P803 hybrid emulsion spectrometer, the decays of charm will be observed directly in the emulsion target; the acceptance in x and y is nearly 100%. High sensitivity to neutrino production of charm near threshold results in large part from the intense medium-energy ν and $\overline{\nu}$ beams available from the new Fermilab Main Injector. The spectrum shape is ideally matched to charm production and should provide a nearly constant yield of charm events between 8 and 40 GeV.

Neutrino production of charm in the parton model is described by

$$\frac{d^2\sigma}{dxdy} \propto [|V_{cd}|^2 \xi f_{val}(\xi, Q^2) + |V_{cd}|^2 \xi f_{dsea}(\xi, Q^2) + |V_{cs}|^2 \xi f_{ssea}(\xi, Q^2)] \qquad (1)$$

$$\cdot[1 - M_c^2/(2M_N E_\nu \xi)] \cdot \Theta(W^2 - (M_D + M_N)^2)$$

while for production of anticharm by antineutrinos

$$\frac{d^2\sigma}{dxdy} \propto [|V_{cd}|^2 \xi f_{\bar{d}sea}(\xi, Q^2) + |V_{cs}|^2 \xi f_{\bar{s}sea}(\xi, Q^2)] \qquad (2)$$

$$\cdot[1 - M_c^2/(2M_N E_\nu \xi)] \cdot \Theta(W^2 - (M_D + M_N)^2).$$

In these expressions the step function Θ ensures that the hadronic mass is sufficient for producing charm, and the slow-rescaling variable $\xi = x + M_c^2/(2M_N E_\nu y)$

[1]This section is reproduced from the 1990 version of the P803 proposal.

replaces x in the structure functions f_i, suppressing the cross section most strongly at low y and E_ν. The additional suppression factor $[1 - M_c^2/(2M_N E_\nu \xi)]$ arises from the mixed helicity of a charm quark of finite mass. Antineutrino production of charm is predominantly off the strange sea, while ud valence and ssea make roughly equal contributions to neutrino production at high energy. Slow rescaling causes a greater reduction in the ssea contribution relative to ud valence at low energy because of the much steeper ssea x-dependence.

To investigate the improved sensitivity to $|V_{cd}|$ and M_c from low-energy data, a simple calculation was performed evaluating (1) and (2) on an (x,y,E_ν) grid for several values of M_c. In this exercise the structure functions f_{val} and f_{dsea} were given by the parametrization of Reutens [2] from Fermilab E616 data, while for f_{ssea} three different parametrizations were tried, the default version being $\xi f_{ssea} = 0.133(1-\xi)^{10.8}$ as suggested by preliminary results [1] from E744.

The effects of slow rescaling are illustrated in Figs. B1a and B1b, which are Lego plots showing the ud valence and strange sea contributions to $d^2\sigma/dxdy$ for $\nu + N \to C + X$ at E_ν=15 GeV. (The single filled bin at lower right is a "ruler" of constant $d^2\sigma/dxdy$ to establish the relative scale of the two figures.) The W^2 threshold and the increasingly strong effects of slow rescaling at low y are apparent, as is the severe suppression of the ssea contribution from slow rescaling. The energy dependence of this suppression is illustrated in Fig. B2, which shows the relative sizes of the contributions to $\nu + N \to C + X$ together with the data from dimuon [1],[3] and hybrid emulsion [4] experiments.

Figures B3a and B3b illustrate the sensitivity of the $\nu, \overline{\nu}$ charm cross sections to the slow rescaling parameter M_c for a fixed parametrization of the strange sea. In addition to the data points from the existing experiments, these figures include simulated data from a very conservative estimate of the yield from P803: 500 ν and 200 $\overline{\nu}$ events with a binning in E_ν based on the beam spectra in the proposal. It is clear that if the size and shape of the strange sea is known, the low-energy $\overline{\nu}$ data pins down M_c with great precision, which then allows an excellent determination of $|V_{cd}|$ from the ν data.

The effects of incomplete knowledge of the strange sea were investigated using three different parametrizations, illustrated in Fig. B4, which probably more than span the present uncertainties.

1. $\xi f_{ssea} = 0.133(1-\xi)^{10.8}$;
2. $\xi f_{ssea} = 0.5 f_{udsea}$, with ξf_{udsea} as per Reutens [2];
3. $\xi f_{ssea} = 0.63(1-\xi)^5 \xi f_{udsea}$.

For each description of ssea a fit was performed to the E744 and (simulated) P803

$\nu, \overline{\nu}$ data to determine 3 parameters: $|V_{cd}|/sin(\theta_C)$; the amount of strange sea relative to the input; and M_c. The results gave errors of $\pm 2.4\%$ to $\pm 2.7\%$ on $|V_{cd}|$, and ± 0.031 to ± 0.037 on M_c for each fit. The maximum variation among parametrizations was $\pm 5\%$ for $|V_{cd}|$, and ± 0.10 GeV on M_c. Extracting maximal physics from the data will require obtaining the best available parametrization of the strange sea from existing high-energy data, and a careful measurement of the x,y dependence of $\overline{\nu}$-produced anticharm in P803 itself, to reduce this source of systematic error below the small statistical errors. At least one ambitious program to parametrize structure function is now well-advanced [5].

REFERENCES FOR APPENDIX B

1. C. Foudas et al., Phys. Rev. Lett. **64**, 1207 (1990); Michael Shaevitz, Notes from the 1989 SLAC Summer Institute; Heidi Schellman, talk presented at SLAC 1988 Summer Institute (FERMILAB-Conf-88/160-E).

2. Patrick G. Reutens, Ph.D. Thesis, University of Chicago (1986).

3. P. Abranowicz et al. (CDHS) Z. Phys. **15C**, 19 (1982).

4. N. Ushida et al. (E531), Phys. Lett. **B206**, 375 (1988).

5. W. K. Tung, Talks presented at the Breckenridge Summer Study (1989) and at Snowmass Summer Study (1990).

a.

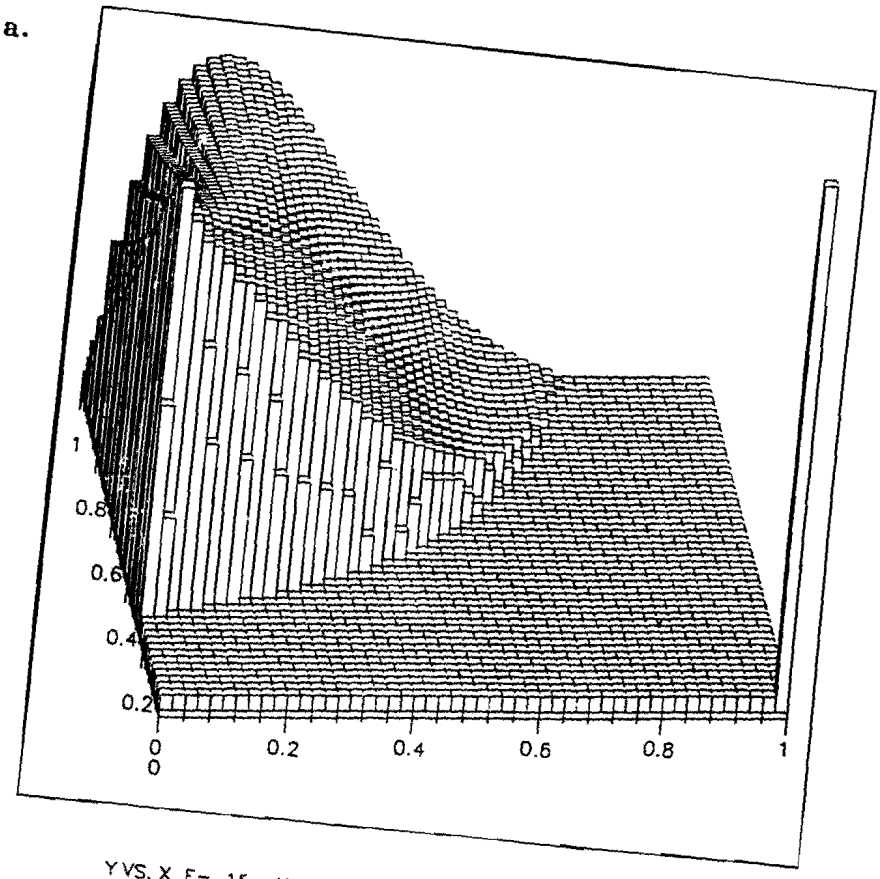

Y VS. X, E= 15. NU CHARM UD VAL KAPPA=.50 MC=1.50

b.

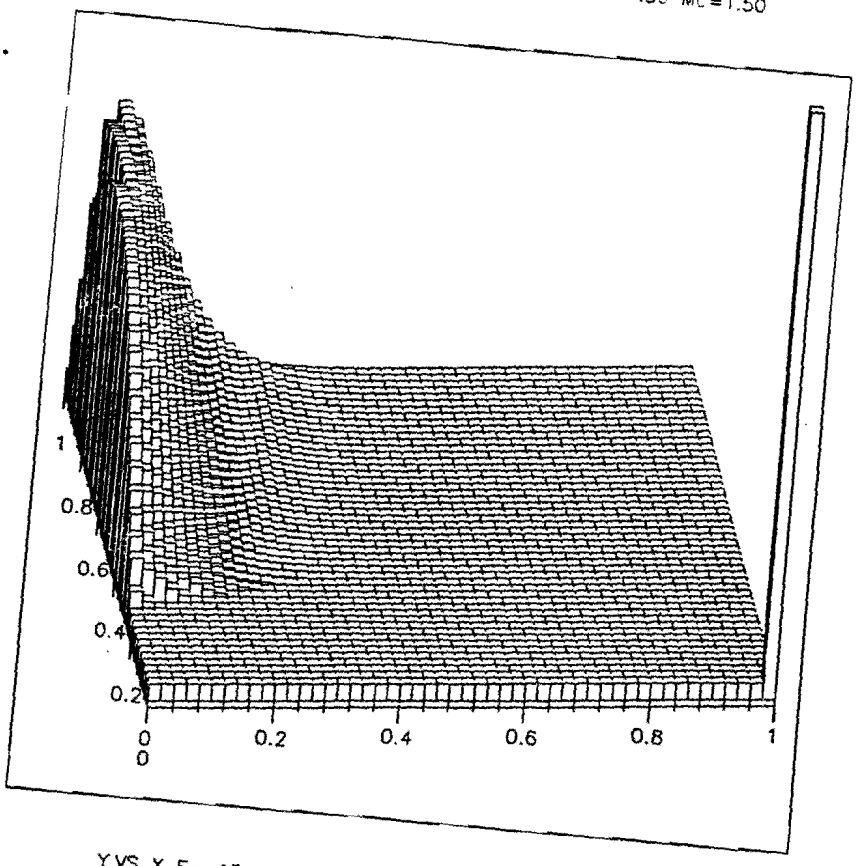

Y VS. X, E= 15. NU CHARM S SEA KAPPA=.50 MC=1.50

FIGURE B1. Lego plots showing the calculated ud valence (a) and strange sea (b) contributions to $d^2\sigma/dxdy$ for charm production by neutrinos at E_ν=15 GeV, with charm quark mass M_c=1.5 GeV. On these plots x is the nearly horizontal axis. The large single bin at (x,y)=(1,0) is a "ruler" for comparing the two plots.

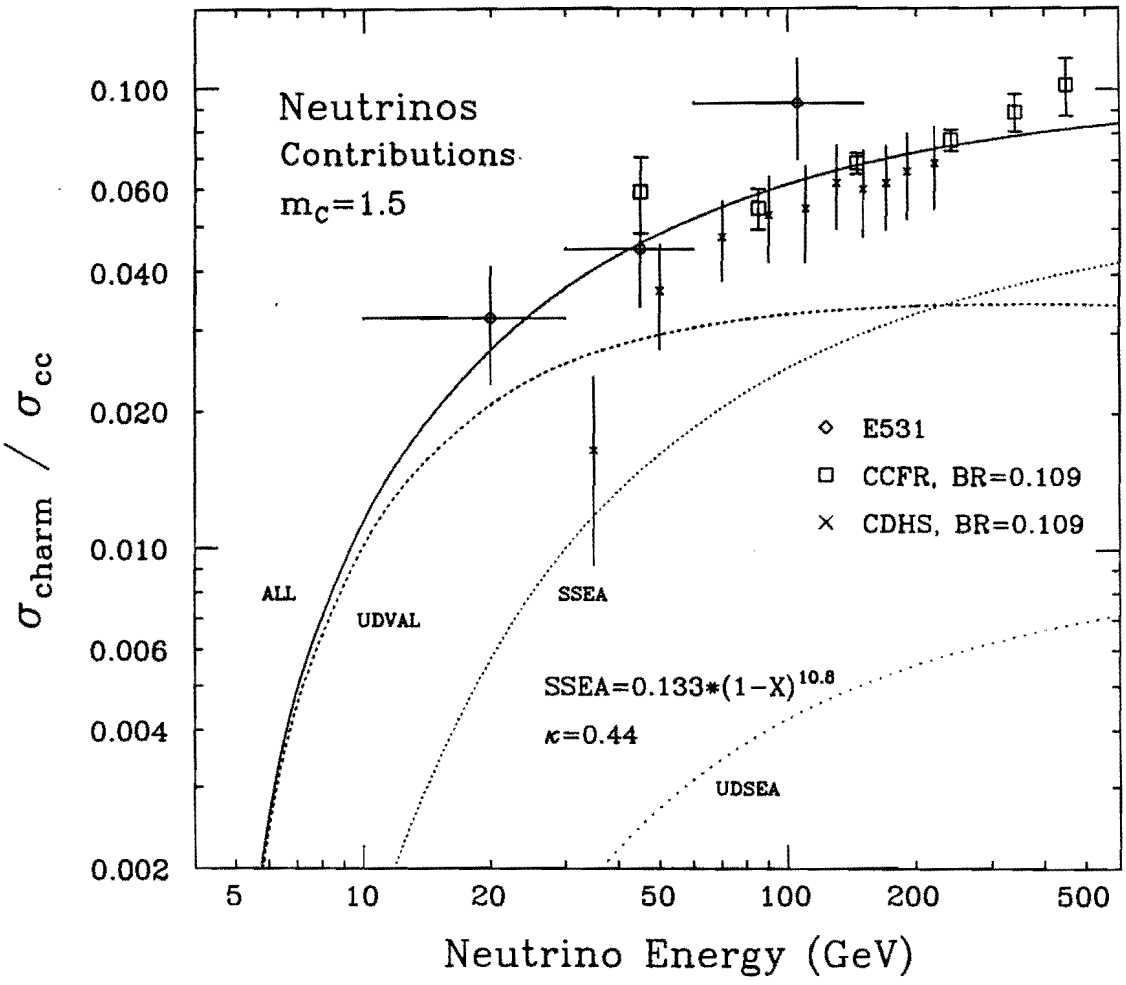

FIGURE B2. Calculated contributions to the cross section for $\nu + N \rightarrow C + X$ as a function of neutrino energy, using a charm quark mass M_C=1.5 GeV.

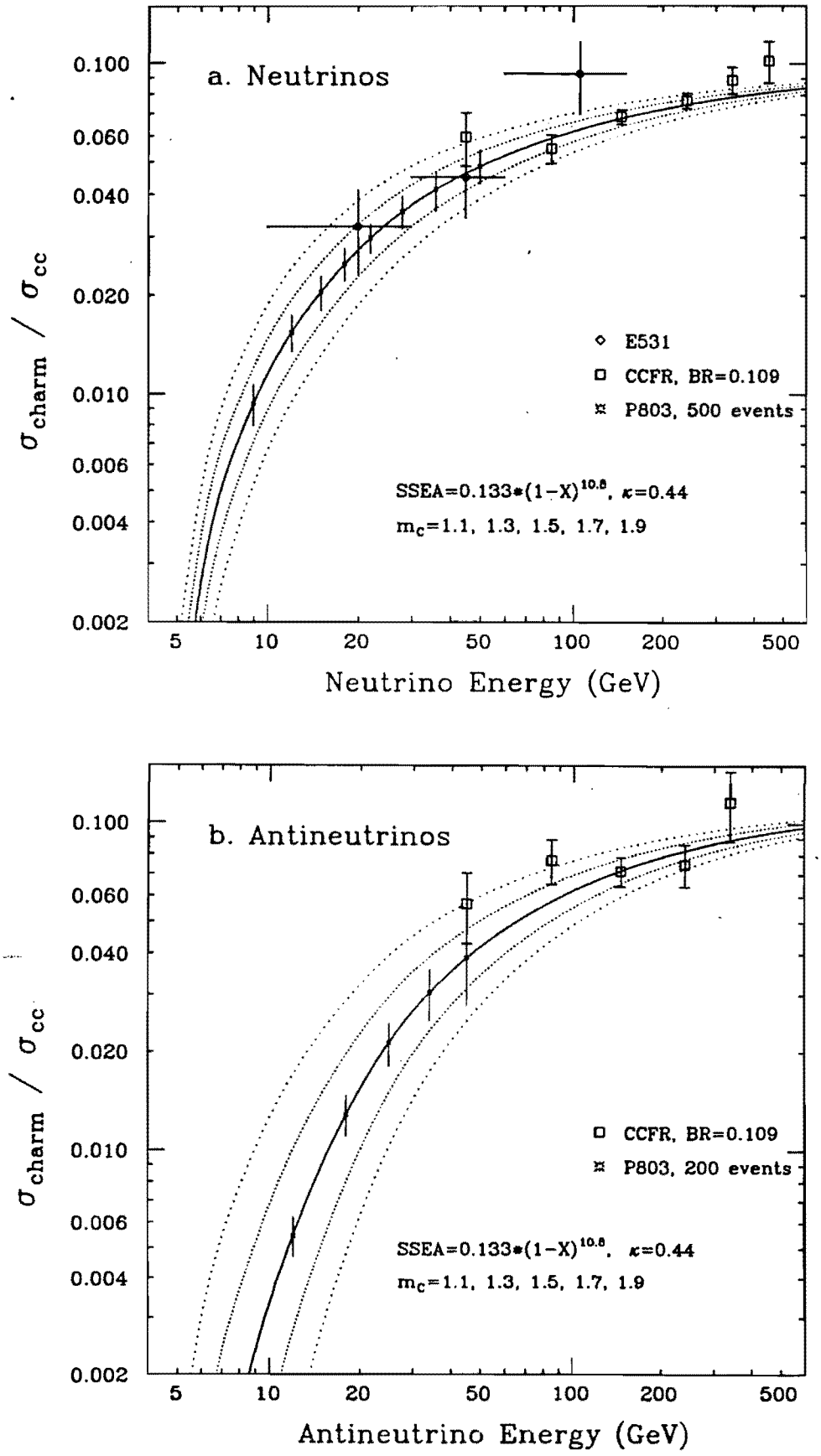

FIGURE B3. Sensitivity of ν (a) and $\overline{\nu}$ (b) production of charm to the charm quark mass parameter M_c. Data shown for P803 are simulated, based on a conservative estimate of the yield from the beams discussed in the proposal.

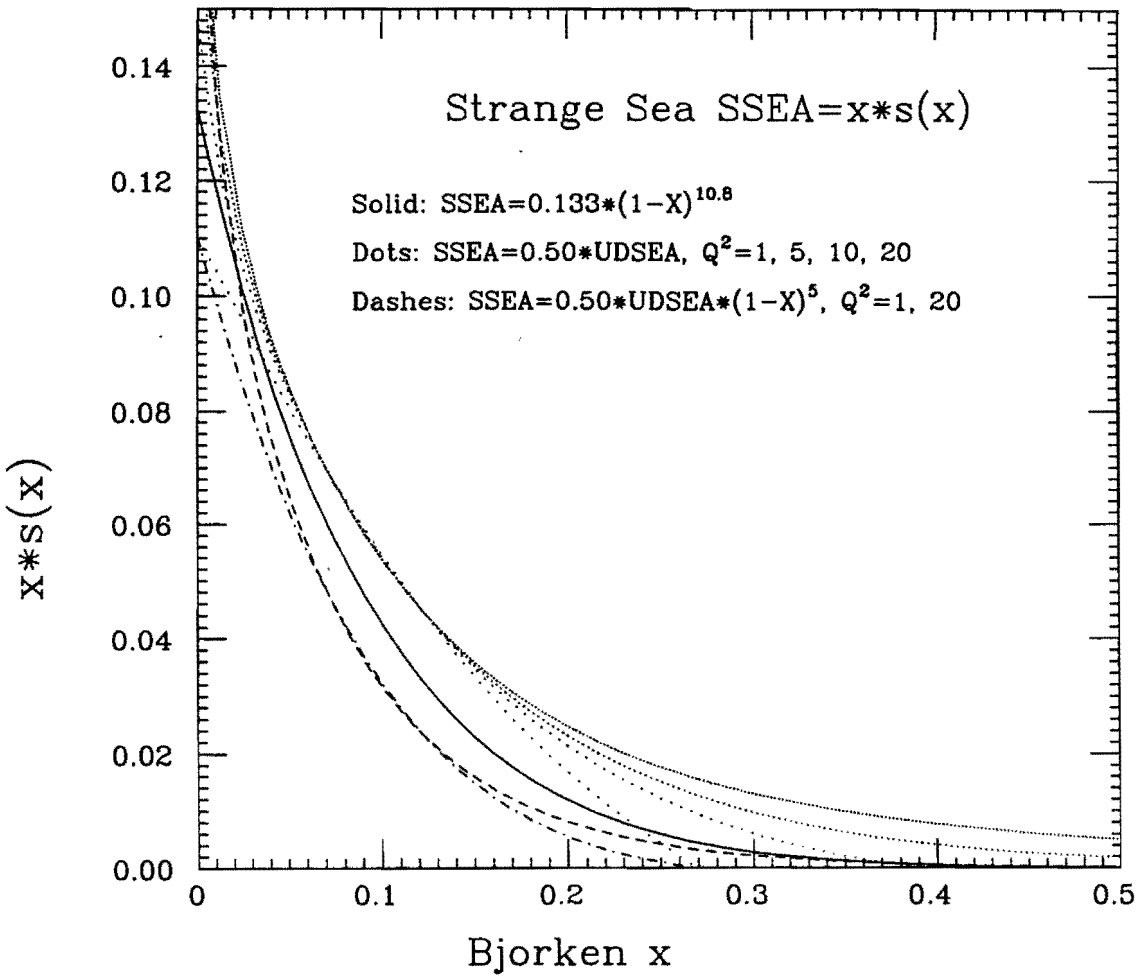

FIGURE B4. Parametrizations of the strange sea used in estimating systematic errors.

Appendix C

BACKGROUND FROM BEAM DUMP TAU NEUTRINOS

The source of the horn-focussed muon neutrinos for P803 is a 120 GeV proton beam passing through a 2.0 interaction length target 470 m upstream of the detector. The remaining protons are then stopped in an iron beam dump only 150 m from the emulsion. Real ν_τ's from the decay chain

$$\overline{D_s} \rightarrow \tau^- + \overline{\nu_{\tau 1}}, \qquad \tau^- \rightarrow \nu_{\tau 2} + X \tag{1}$$

are a potentially serious background to ν_τ's resulting from oscillation of ν_μ's.

In this Appendix we summarize a calculation of this direct ν_τ background which uses known production properties of charmed particles and Monte Carlo simulations of the decays (1) and

$$D \rightarrow \nu_\mu + X \tag{2}$$

to scale the results of the Fermilab E613 [1]. That experiment measured the yield of (2) from charm produced by dumping 400 GeV protons on a tungsten target. The calculation parametrizes charm production by

$$\sigma \propto (1 - x_F)^n e^{-1.0 p_T^2}, \tag{3}$$

and assumes that D_s and D production have the same x, p_T dependence at a given beam energy. The τ decay modes are taken from PDG 1992 [4].

Simulation of ν_μ Charged-Current Yield from E613

The simulation program was checked by calculating the absolute yield of ν_μ charged-current events from E613 [1]. E613 used a Pb and liquid scintillator neutrino target with a fiducial mass of 75 tons and a fiducial frontal area of 264 cm × 111 cm (2.3×10^3 gm/cm^2) located 56 m from the proton dump. This detector was offset horizontally so that the beam passed 24 cm inside one edge. The measured yield of ν_μ charged-current events with $E_\nu \geq 20$ GeV was 43.6±7.4 per 10^{16} protons, with an inferred $D\overline{D}$ production cross section from 400 GeV protons on tungsten of 57±2.9±8.5 μb/nucleon, n=3.2 (± approx. 1.0), and atomic weight dependence of $A^{0.75\pm0.05}$, essentially the same as $A^{0.72}$ for the absorption cross section of protons on nuclei. The experiment was insensitive to production at x_F below about 0.2.

For comparison, $D\overline{D}$ production data from LEBC for 400 GeV protons on hydrogen [5], sensitive to all positive x_F, finds a pair cross section of 30.2±3.3 μb and n=4.9±0.5; there are no events for $x_F > 6$. Since (3) is an empirical parametrization and no single experiment has good data over the full range of x_F, it is certainly

possible that the effective n is actually somewhat different for small and large x_F. Note that P803 is sensitive to large-x_F production.

The yield from E613 was calculated using several values of n and a $D\overline{D}$ crossection of 57 μb. The experimental corrections (total factor 0.83) specified in [1] have been applied. The resulting simulated absolute yields are in excellent agreement with the measured rate of 44 per 10^{16} protons for n$\approx$3.5; this gives us confidence that our simulation is valid.

Table 1. Calculated Yield of ν_μ Charged-Current Events from E613.

Assumed n-value	E613 Acceptance	$\overline{E_\nu}$ (GeV)	$\overline{x_F}$	E613 Yield per 10^{16} p
2.5	0.101	64.4	0.522	77.9
3.2	0.0824	55.3	0.464	54.3
4.0	0.0673	51.1	0.412	41.2
4.9	0.0552	32.5	0.367	21.5

In the estimates of direct ν_τ event yields for P803 in the next section which are scaled from E613, the E613 values of n and $D\overline{D}$ cross section, rather than those from LEBC, will be used, because a) the large-x_F data is more relevant; and b) if the A-dependence of high-x_F charm production is somewhat different than that of proton interactions, tungsten-target data will be a better approximation to an iron dump than hydrogen data.

Scaling to Direct ν_τ Event Yield for P803

A. Proton flux. This yields for this proposal are based on 13×10^{20} protons on a 2.0 interaction length, half-density 3 mm diameter target in which 80% of the protons interact, leaving 0.20 of these protons, or 2.6×10^{20}, to strike the dump. There should be no significant production of charm by secondaries from the production target because of the low energy of the beam.

B. Neutrino target mass/area. The emulsion target of P803 will have 0.206 tons/m^2, compared to 25.6 tons/m^2 in the fiducial volume of E613; the ratio is 0.0081.

C. Energy dependence of $D\overline{D}$ cross section. There is data from NA32 [6] on $D\overline{D}$ production on silicon by 200 GeV protons (9 events). The cross section (all x_F) is $3.0\pm1.4\pm0.2$ μb, with n about 5.5. Production data by π^- from the same experiment (with much better statistics) gives $5.1^{+0.6}_{-0.5}\pm0.3$ μb for $x_F>0$ and n=2.5 ± 0.3.

Another approach is to use theoretical calculations to extrapolate downward in energy. Results of two such calculations [7],[8], are shown in Figs. C1a and C1b; a conservative value of the decrease between 400 GeV ($\sqrt{s} = 27.4$) and 120 GeV ($\sqrt{s} = 15.0$) is a factor of 6 (0.17).

D. Ratio of D_s to D production. A preliminary measurement [3] from E653 (800 Gev protons) is $D_s/D \approx 0.2$, which we take as an upper estimate at 120 GeV.

E. Semileptonic branching ratios. We assume a branching ratio for $D_s \rightarrow \tau\ \nu_\tau$ of 3.7%, inferred from the measured [9] $D_s \rightarrow \mu\ \nu_\mu$ branching ratio, and a production-averaged semimuonic branching ratio for D of 10%. There is an additional factor of approximately 0.5 which arises as follows: we detect only τ^-, and are almost completely insensitive to the low-energy ν_τ's from $\overline{D_s}$ decay. In production of D_s, it is much more likely that a D_s will be produced as $D_s\overline{D}$ than as $D_s\overline{D_s}$. On the other hand, when E613 detects ν_μ, either member of the $D\overline{D}$ pair could have produced the neutrino. The scaling factor is then (0.037)(0.5)/(0.10)=0.19.

F. Angle and energy acceptance. The P803 detector subtends an angle of 6.0 mr from the dump, and is inefficient for detecting ν_τ's below 10 GeV. Geometric acceptances are presented for several values of n in Table 2 below; the acceptance is quite sensitive to n. Since n is generally observed to increase with energy, one expects n to be less than 3.2 at 120 GeV. For the best-guess value of n=2.5, the acceptance is 0.0051, compared to 0.0824 for E613, a ratio of 0.062.

G. Average neutrino energy, and energy dependence of $\sigma_{\nu_\tau}/\sigma_{\nu_\mu}$. The charged- current cross section is proportional to E_ν, which will be lower in the 120 GeV beam than its average value of 55 GeV for E613. In addition, ν_τ interactions are suppressed at low energy due to kinematic effects. The value of $\overline{E_\nu}$ for accepted events is a weak function of the assumed value of n. For n=2.5, $\overline{E_\nu}$=27 GeV, $\sigma_{\nu_\tau}/\sigma_{\nu_\mu}$=0.47; the ratio is (0.47)(27)/(55)=0.23.

H. Detection efficiency for ν_τ events. Beam dump ν_τ's are subject to the same event-finding losses and cuts as oscillation ν_τ's, a factor of approximately 0.15.

We now put these factors together for an assumed n=2.5. Results for other values of n are presented in Table 2.

Yield of beam dump ν_τ events = $(44/10^{16}\text{protons}) \cdot (2.6 \times 10^{20}\text{protons}) \cdot (0.0081)$

$\cdot\ (0.17) \cdot (0.2) \cdot (0.19) \cdot (0.062) \cdot (0.23) \cdot (0.15)$

= 0.13 detected events.

The uncertainty in this estimate is at least a factor of 2; however, direct ν_τ's do not appear to be a significant source of background. A factor 10 reduction in the already low direct ν_τ event rate could be obtained by deflecting the proton beam

before it strikes the dump.

Table 2. Calculated Yield of Direct ν_τ Events for P803.

Assumed n-value	P803 Acceptance	$\overline{E_\nu}$ (GeV)	$\sigma_{\nu_\tau}/\sigma_{\nu_\mu}$	$\overline{x_F}$	P803 Yield/ 2.4×10^{20} p
2.0	0.0065	28	0.48	0.66	0.17 events
2.5	0.0051	27	0.47	0.60	0.13 events
3.2	0.0039	26	0.46	0.55	0.10 events

REFERENCES FOR APPENDIX C

1. M. E. Duffy et al., Phys. Rev. **D38**, 2032 (1988).
2. J. C. Anjos et al., Phys. Rev. Lett. **61**,1587 (1989);
   J. C. Anjos et al., Phys. Rev. Lett. **62**,1587 (1989);
   J. Adler et al., Phys. Rev. Lett. **62**,1821 (1989).
3. Preliminary results from Fermilab E653, internal group communication.
4. Particle Data Group, Phys. Rev. **D45**, (1992).
5. M. Aguilar-Benitez et al., Z. Phys. **40C**, 321 (1988).
6. S. Barlag et al., Z. Phys. **39C**, 451 (1988).
7. R. K. Ellis, Preprint Fermilab-Conf-189/168-T (1989).
8. E. L. Berger, Proceedings of the Advanced Workshop on QCD Hadronic Processes, (B. Cox ed.), Plenum Press, p. 501 (1989).
9. S. Aoki et al., 'The First Observation of the Muonic Decay $D_s \rightarrow \mu\nu$', CERN-PPE/92-157 (1992).

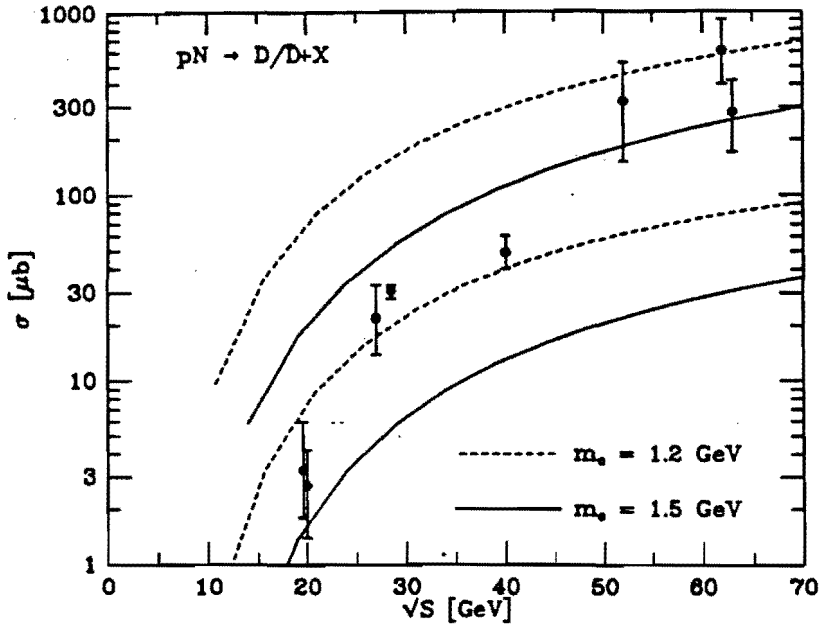

FIGURE C1a. Calculated energy dependence of charm production by protons from Ref. 7.

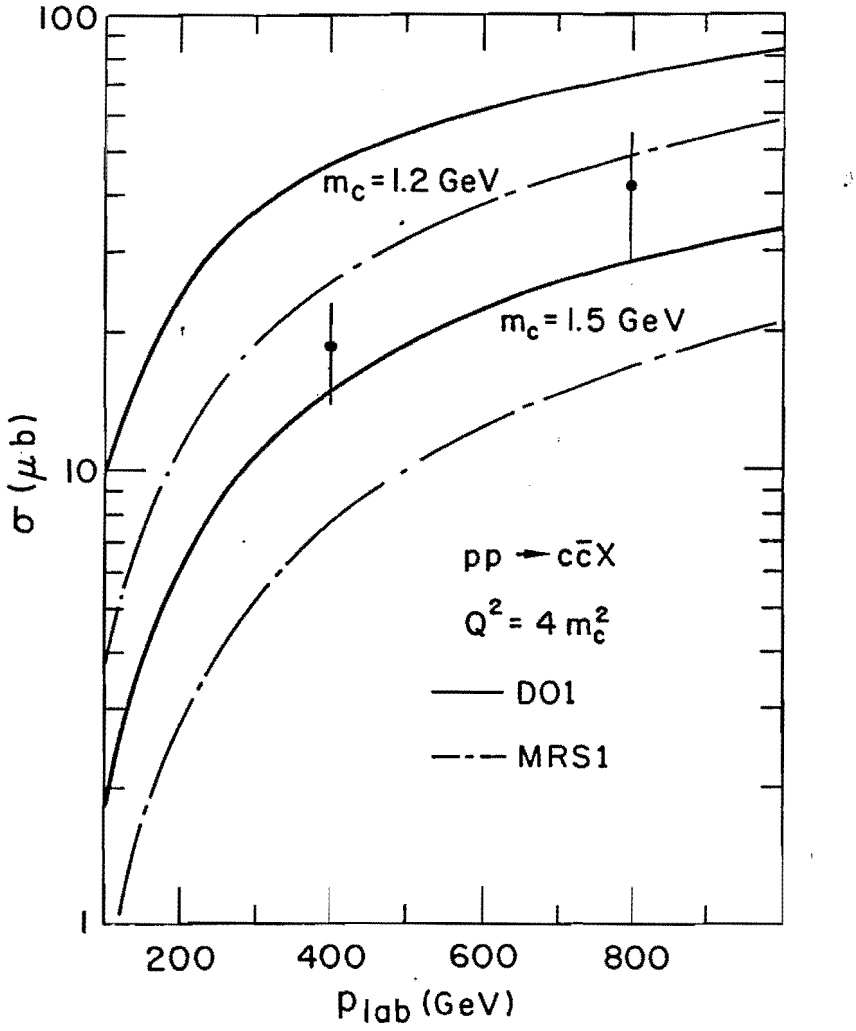

FIGURE C1b. Calculated energy dependence of charm production by protons from Ref. 8.

Appendix D

MEASUREMENT OF THE MEAN FREE PATH AND TRANSVERSE MOMENTUM DEPENDENCE OF WHITESTAR KINKS

The dominant background to hadronic τ decays in this experiment is expected to be single-prong interactions of tracks from the primary vertex which show no evidence of nuclear breakup, called whitestar kinks (WSK's). As discussed in the main body of the proposal, knowledge of the mean free path (mfp) for WSK's as a function of the transverse momentum p_T relative to the parent direction is essential for understanding the achievable sensitivity. An experiment has been performed at KEK by members of this collaboration to measure this quantity with π^- beams of 2 and 4 GeV/c.

The setup for the KEK experiment is shown in Fig. D1; it was performed in a magnetic field of 1.2 Tesla. The emulsion was divided into a main block which acted as a target and kink analyzer, and sheets separated by low-density spacers in which the secondaries were detected. The π^- beam was 2×2 cm^2 in area, and contained a 3% contamination of electrons. The emulsion was exposed to a density of 10^5 to 10^6 tracks/cm^2.

The 4 GeV/c sample has been scanned by both the beam-following and scan-back methods. The results presented here are based on an analysis which obtains the p_T of the kink from the product of kink angle and the parent momentum. Therefore, WSK's due to bremsstrahlung by the electron contamination in the beam have not been removed. Since the interest for P803 is in kinks with p_T above about 0.2 GeV/c, the scan was allowed to be inefficient for kinks with angle less than about 0.03 radians.

A total of 727 multiprong interactions, and 145 kink interactions with angle ≥ 0.2 radians, were found. These include 58 WSK's and 87 kinks with evidence of nuclear breakup (dark evaporation tracks or blobs). The 817 interactions correspond to the known mean free path of 50 cm for π^- in emulsion.

The p_T spectra of all kinks, and for WSK's, are shown in Fig. D2; there are no WSK events between 0.3 and 0.6 GeV/c, and one additional WSK event (off scale) with a $p_T > 0.6$ GeV/c. As shown in this figure, the total kink sample has a p_T dependence above 0.1 GeV/c of approximately e^{-10p_T}, while the WSK's have a much steeper dependence of about e^{-20p_T}. There are 8 WSK with $p_T \geq 0.2$ GeV/c, corresponding to a mfp of $(0.50 \text{ m}) \cdot (817)/(8 \pm 2.8) = (50 \pm 18)$ m. The exponential p_T dependence then implies a mfp of (370 ± 130) m for p_T above 0.3 GeV/c.

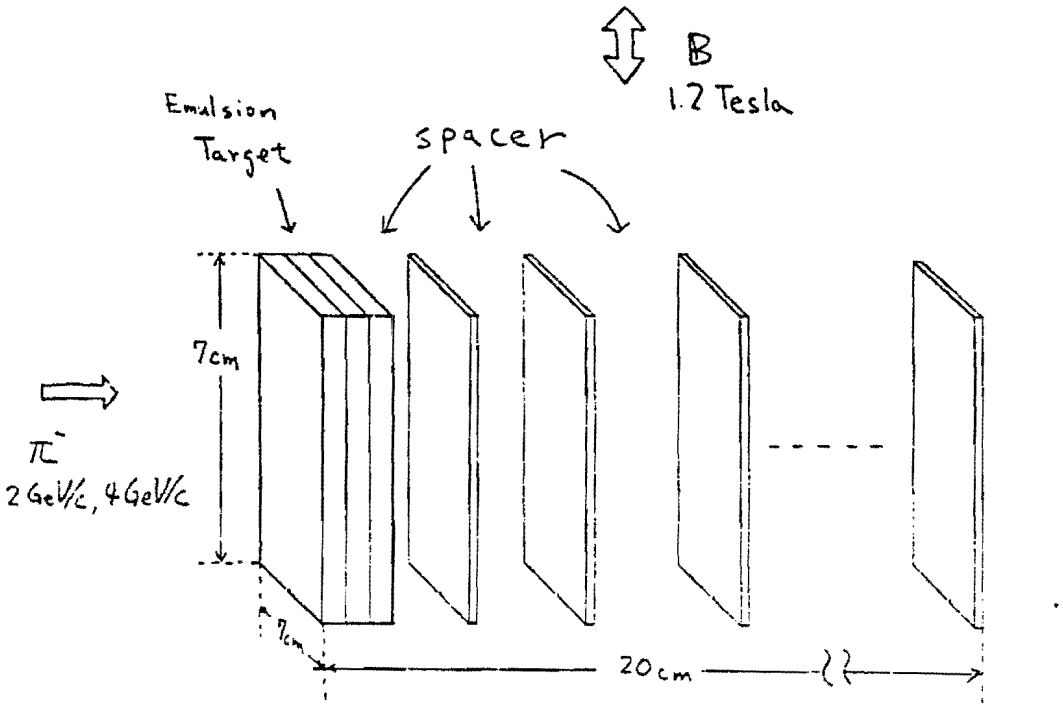

Fig 1.

FIGURE D1. Sketch of the experimental setup used in the KEK exposure.

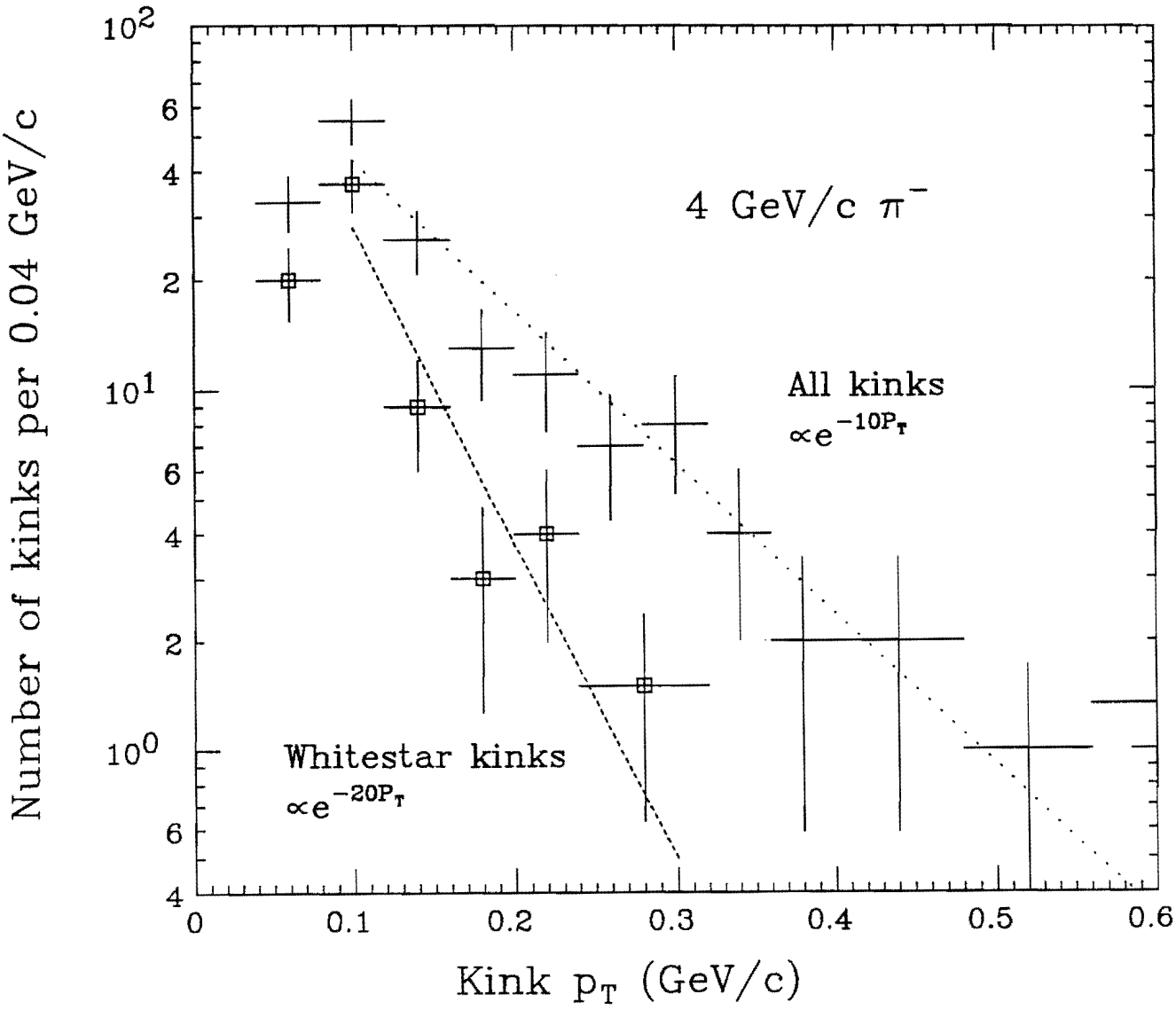

FIGURE D2. Preliminary results from the KEK exposure with 4.0 GeV/c π^-. Number vs. p_T for all kinks (crosses) and whitestar kinks (squares). There is one additional WSK event above 0.6 GeV/c. The p_T dependences for $p_T > 0.1$ GeV/c are indicated by the dotted and dashed lines.

ERRATA – P803 PROPOSAL

To avoid possible misunderstanding, we request readers to note and correct the following errors in the October, 1993 P803 proposal:

1. Page 17, third paragraph (electromagnetic calorimeter). The text should read

   > ... is approximately \$1.1M, including 15% EDIA and 25% contingency factors.

2. Page 24, Table 4: The heading of the final column should read

   > P803 Yield/13×10^{20} p

   The stated direct ν_τ backgrounds in this column correspond to 13×10^{20} protons.

3. Appendix C, Table 2: same correction (identical to Table 4 in the body of the proposal).